

Low Dimensional Magnetic Structures

By

ARNAB SINGH

PHYS05201404001

Saha Institute of Nuclear Physics, Kolkata

A thesis submitted to the

Board of Studies in Physical Sciences

In partial fulfilment of requirements

for the Degree of

DOCTOR OF PHILOSOPHY

of

HOMI BHABHA NATIONAL INSTITUTE



February, 2020

Homi Bhabha National Institute

Recommendations of the Viva Voce Committee

As members of the Viva Voce Committee, we certify that we have read the dissertation prepared by Arnab Singh entitled “**Low Dimensional Magnetic Structures**” and recommend that it may be accepted as fulfilling the thesis requirement for the award of Degree of Doctor of Philosophy.

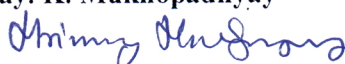
Chairman - Prof. Satyaranjan Bhattacharyya

Date: 06/02/2020



Guide / Convener - Prof. Mrinmay. K. Mukhopadhyay

Date: 06/02/2020



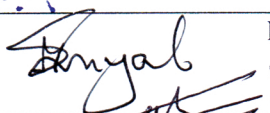
Examiner - Prof. Dipankar. D. Sarma

Date: 06/02/2020



Member 1 - Prof. Milan K. Sanyal

Date: 06/02/2020



Member 2- Prof. Krishnakumar S. R. Menon

Date: 06/02/2020



Member 3- Prof. Samita Basu

Date: 06/02/2020



Final approval and acceptance of this thesis is contingent upon the candidate's submission of the final copies of the thesis to HBNI.

I/We hereby certify that I/we have read this thesis prepared under my/our direction and recommend that it may be accepted as fulfilling the thesis requirement.

Date: 06 February, 2020

Place: Kolkata

Co-guide (if applicable)

Guide



STATEMENT BY AUTHOR

This dissertation has been submitted in partial fulfilment of requirements for an advanced degree at Homi Bhabha National Institute (HBNI) and is deposited in the Library to be made available to borrowers under rules of the HBNI.

Brief quotations from this dissertation are allowable without special permission, provided that accurate acknowledgement of source is made. Requests for permission for extended quotation from or reproduction of this manuscript in whole or in part may be granted by the Competent Authority of HBNI when in his or her judgment the proposed use of the material is in the interests of scholarship. In all other instances, however, permission must be obtained from the author.

Arnab Singh

Arnab Singh

06/02/2020

DECLARATION

I, hereby declare that the investigation presented in the thesis has been carried out by me. The work is original and has not been submitted earlier as a whole or in part for a degree / diploma at this or any other Institution / University.

Arnab Singh

Arnab Singh

06/02/2020

List of Publications arising from the thesis

Journals

1. “Scaling of domain cascades in stripe and skyrmion phases”, A. Singh, J.C.T Lee, K.E. Avila, Y. Chen, S.A. Montoya, E.E. Fullerton, P. Fischer, K.A. Dahmen, S.D. Kevan, M.K. Sanyal and S. Roy, *Nature Communications*, **2019**, 10:1988., 1-9.
2. “Evidence of two-dimensional anti-ferromagnetic ordering in rare-earth Langmuir Blodgett films”, A. Singh, M. K. Mukhopadhyay, M. K. Sanyal, G. Stenning and S. Langridge, *Journal of Physics: Condensed Matter*, **2019**, 31, 495803., 1-7.
3. “Modulated periodicities and Devil’s staircase in an amorphous magnetic thin film”, A. Singh, M.K. Sanyal, M. K. Mukhopadhyay, J.C.T Lee, E. E. Fullerton, P. Fischer, S.D. Kevan and S. Roy, *Submitted* (**2019**).
4. “Structural and optical properties of two-dimensional gadolinium stearate Langmuir monolayer”, S. Maiti, M. K. Sanyal, M. K. Mukhopadhyay, A. Singh, S. Mukherjee, A. Datta and P. Fontaine, *Chemical Physics Letter*, **2018**, 712., 172-183.

Conferences

1. “Resonant x-ray magnetic scattering study of domain morphology in FeGd thin film”, A. Singh, M. K. Sanyal, J. C. T. Lee, Y. Chen, S. Montoya, E. E. Fullerton, and S. Roy, *AIP Conference Proceedings*, **2018**, 1942, 130028., 1-4.

Others (under preparation)

1. “Polarized neutron reflectivity and sub-kelvin magnetization study of anti-ferromagnetic ordering in Holmium Stearate Langmuir-Blodgett films”, A. Singh, M. K. Sanyal, M. K. Mukhopadhyay, A. Carauna, T. Sakakibara and S. Langridge, (To be Submitted).
2. “In-situ X-ray and neutron reflectivity study of rare-earth Langmuir monolayers”, A. Singh, M. K. Mukhopadhyay, M. K. Sanyal, B. M. Murphy and J. Webster, (To be Submitted).

Arnab Singh

Arnab Singh

06/02/2020

DEDICATIONS

Every challenging work needs self efforts as well as guidance and support of elders those who were close to my hearts.

I dedicate to my caring and loving

Mother & Father,

Whose affection, love, encouragement and prayers made this journey a successful and memorable one.

Along with all the hard working and respected

Teachers

ACKNOWLEDGEMENTS

First of all, I would like to express my special appreciation and thanks to my thesis supervisors, **Prof. Milan K. Sanyal** and **Prof. Mrinmay K. Mukhopadhyay** for their constant support and proper guidance throughout my Ph.D course. Prof. Sanyal has been an inspirational figure for me and I am fortunate to have had the opportunity to study under his mentorship. He is always patient and encouraging when sharing his knowledge through invaluable discussions. His unparalleled enthusiasm in science and his wisdom toward life will always benefit me in the future and I owe him lots of gratitude for having me shown this way of research.

I would like to thank **Prof. Ajit K. Mohanty**, Director, Saha Institute of Nuclear Physics (SINP) for his support and cooperation during my Ph.D tenure. I would also like to thank all the members of my doctoral committee, **Prof Satyaranjan Bhattacharyya**, **Prof. Krishnakumar S. R. Menon** and **Prof. Samita Basu**.

This thesis work would not have been complete without the contribution of my principal collaborators and I would like to sincerely acknowledge **Dr. Sujoy Roy** of Advanced Light Source (ALS), USA, **Prof. Sean Langridge** of Rutherford Appleton Laboratory (RAL), UK, and **Prof. Toshiro Sakakibara** of Institute of Solid State Physics (ISSP), Japan, for providing their enormous amount of time and knowledge towards my research works.

I would like to acknowledge **Prof. Stephen D. Kevan**, director of Berkeley Lab's Advanced Light Source (ALS) for his help and useful discussions during my stay at ALS. I would like to thank **Prof. E. E. Fullerton**, CMRR, UC San Diego and **Prof. P. Fischer**, LBNL, UC Berkeley for their contributions in my research works. I would like to

acknowledge **Prof. Karin A. Dahmen** and **Dr. Karina Avila**, University of Illinois, Urbana (USA) for imparting useful discussions and help in theoretical statistical analysis part of my research work. I would also like to thank **Dr. Sudipta Bandyopadhyay**, Dept. of Physics, University of Calcutta for providing experimental help.

The experiments were carried out at several synchrotron sources like PF (Japan), ALS (USA), DESY (Germany) and neutron sources at RAL (UK). I would like to thank all the scientists and post docs at the beamlines, **Prof. Chandrabhas Narayan, Dr. Gangadhar Das, Dr. James Lee, Dr. Y. Chen, Dr. Robert Straubel, Prof. B. M. Murphy, Prof. A. Sundaresan, Prof. J. Webster, Dr. Andrew Carauna, Dr. Gavin Stenning and Dr. Florian Bertram**, who provided support and made the experiments possible.

The research work at the ALS, LBNL was supported by the Director, Office of Science, Office of Basic Energy. The research works at PF, DESY and RAL was financially supported by the **Department of Science and Technology (DST)**, India. I would also like to acknowledge the **Department of Atomic Energy (DAE)**, India for their cooperation and support in all my collaborative research work.

I am grateful to all my seniors and juniors at SINP particularly, Shirshendu da, Abhisakh da, Manjula di, Santanu da, Arpan da, Deboshree di, Arka da, Rajendra da, Gouranga da, Dipak, Sabyasachi, Subhadip and all my friends for making this journey bearable and a memorable one. I would also like to acknowledge Dr. Dirtha Sanyal, VECC, Kolkata for his support and encouragement during my research period.

I have received a major help in experiments from the scientific officers, Mr. Abhijit Das, Mr. Susanta Banerjee and Mr. Subir Roy and want to give thanks to them. I also acknowledge Mr. Mukul Chandra Das, Mr. Harendra Nath Jana, Mr. Gobardhan Jana and scientific assistant Mr. Ramkrishna Dev Das for their help during the research period.

A special thanks to my family and relatives. Words cannot express how grateful I am to my mother, my father and my sister for all the sacrifices that they've made on my behalf. Their prayer for me was what sustained me thus far. In addition, thanks to my friends and my pet for providing happy distraction to rest my mind outside of my research works. Finally, I thank my heavenly Father for letting me through all the difficulties during this period. I have experienced His guidance in every aspect of my life and will keep on trusting Him for my future.



Arnab Singh

Saha Institute of Nuclear Physics, Kolkata

February, 2020

The text in **Chapter 3** is based on the material published in:

A. Singh, J.C.T Lee, K.E. Avila, Y. Chen, S.A. Montoya, E.E. Fullerton, P. Fischer, K.A. Dahmen, S.D. Kevan, M.K. Sanyal and S. Roy. “**Scaling of domain cascades in stripe and skyrmion phases**”. *Nature Communications*, **10**:1988 (2019).

The text in **Chapter 4** is a reprint of the material submitted for publication:

A. Singh, M.K. Sanyal, M. K. Mukhopadhyay, J.C.T Lee, E. E. Fullerton, P. Fischer, S.D. Kevan and S. Roy. “**Modulated periodicities and Devil’s staircase in an amorphous magnetic thin film**”. *Submitted* (2019).

The content of **Chapter 5** is based on the manuscripts published in:

A. Singh, M. K. Mukhopadhyay, M. K. Sanyal, G. Stenning and S. Langridge. “**Evidence of two-dimensional anti-ferromagnetic ordering in rare-earth Langmuir Blodgett films**”. *Journal of Physics: Condensed Matter*, **31**, 495803 (2019).

S. Maiti, M. K. Sanyal, M. K. Mukhopadhyay, **A. Singh**, S. Mukherjee, A. Datta and P. Fontaine. “**Structural and optical properties of two-dimensional gadolinium stearate Langmuir monolayer**”. *Chemical Physics Letter*, **712**, 172-183 (2018).

CONTENTS

	Page No.
SYNOPSIS	13
LIST OF FIGURES	27
LIST OF TABLES	34
CHAPTERS	
1 Introduction.....	36
1.1 Types of magnetism.....	37
1.1.1 Weak Magnetism	37
1.1.2 Ferromagnetism	39
1.1.3 Anti-ferromagnetism	42
1.1.4 Ferrimagnetism	45
1.2 Low dimensional magnetism	46
1.2.1 Magnetic domains	46
1.2.2 Domain walls	51
1.3 Magneto-crystalline anisotropy	54
1.3.1 Magneto-crystalline anisotropic interaction	56
1.3.2 Long range magnetic order in presence of dipolar interaction	57
1.4 Two-dimensional (2D) spin textures	58
1.4.1 Stripe formation in 2D systems	58
1.4.2 Topological defects	60
1.4.3 Magnetic vortex, skyrmions and merons	61
1.5 Recent developments	65
1.6 Outline of the Thesis	70
References	72
2 Experimental methods.....	79
2.1 Magnetization measurements	79
2.2 Scattering techniques for Magnetic structures	82
2.3 Coherent X-ray scattering	92
2.3.1 Coherent-Beamline at Advanced Light Source (ALS)	98
2.3.2 Characterization of coherence	99
2.4 Langmuir-Blodgett (LB) deposition technique.....	103

2.4.1 Preparation of Langmuir monolayer	104
2.4.2 Deposition of LB films	110
2.4.3 X-ray reflectivity and GIXD techniques	114
References	125
3 Scaling of domain cascades in stripe and skyrmion phases	131
3.1 Introduction	132
3.2 Experimental details	137
3.2.1 Sample fabrication	137
3.2.2 Resonant coherent soft X-ray scattering (RSXS)	138
3.3 Results and discussions	142
3.3.1 RSXS in stripe and skyrmion phases	142
3.3.2 Determination of stochastic domain jumps	143
3.3.3 Scaling behaviour of stripe and skyrmion phases	149
3.4 Conclusion	155
References	158
4 Modulated periodicities and Devil's staircase in an amorphous magnetic thin film	161
4.1 Introduction	162
4.2 Commensurate phases, incommensurate phases and the Devil's staircase	164
4.3 Modulated periodicities in stripe phase of Fe/Gd thin film	171
4.3.1 Experimental details	175
4.3.2 Lorentz TEM data analysis	176
4.3.3 Experimental results	177
4.4 Discussions and conclusion	190
References	193
5 Two-dimensional magnetic ordering in rare-earth Langmuir-Blodgett films	198
5.1 Langmuir-Blodgett (LB) multilayer films	200
5.2 LB multilayer studies	207
5.2.1 X-ray reflectivity (XRR) study	208
5.2.2 Grazing incidence X-ray diffraction (GIXD) study	212
5.3 Magnetization measurements	213
5.4 Substrate magnetization and Secondary Ion Mass Spectrometry (SIMS)	216
5.5 Anti-ferromagnetic ordering in Ho-St LB multilayer films	224
5.6 Conclusion	227
References	229
6 Summary and outlook	232

SYNOPSIS

LOW DIMENSIONAL MAGNETIC STRUCTURES

ARNAB SINGH

*Surface Physics and Materials Science Division,
Saha Institute of Nuclear Physics, HBNI, 1/AF, Bidhan Nagar, Kolkata 700 064.*

Introduction:

During the last decade, much attention has been devoted to artificial layered magnetic materials which have revealed a large variety of fascinating new phenomena. The fundamental developments made such systems also of great interest from a technological point of view in the area of communication devices and storage media [1]. Stimulated by this physics resulting from the layering and reduction of the system size in the vertical direction, a natural extension was the venture into a further reduction of the lateral sizes and quite general into low dimensional systems of nanometer extend. Apart from the simple ferromagnetic, antiferromagnetic and ferrimagnetic domains as observed in bulk magnetic materials, complex domains of stripes, labyrinth, vortex, etc with competitive magnetic interactions has been observed in 2D magnetic systems and studied in great detail [2,3]. Very recently exotic spin structures like bubbles, skyrmions and merons has generated lot of interest in understanding the underlying interactions giving rise to such novel entity [4,5]. The control of the magnetic properties at nanometer lengthscales through a variation of the system dimensions has made these low dimensional magnetic structures interesting not only from a fundamental perspective, but also from a technological point of view. Research and development of new magnetic structures has largely benefited from the potential applications, particularly in energy efficient spinotronic devices [6]. With the advent of high brilliance synchrotron and neutron facilities around the globe, provide further insight into the structure and magnetic ordering in such nanometer sized objects both in real and reciprocal space which has not being realized before [7].

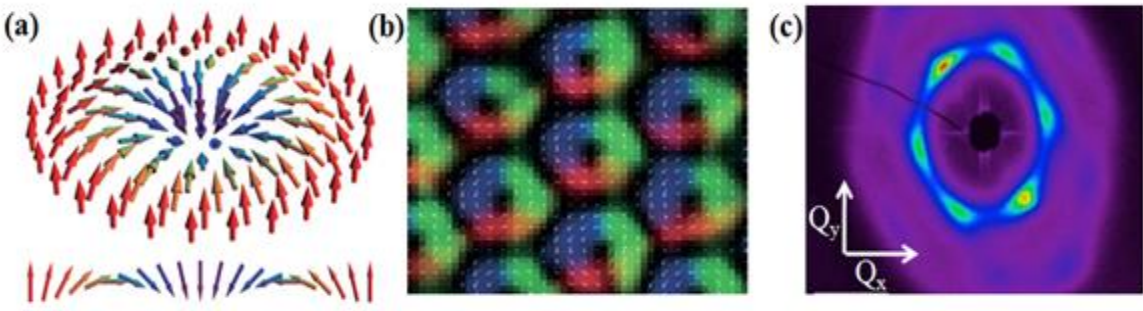


Fig 1: (a) Schematic of the spin configuration in a magnetic skyrmion [22]. (b) Real space image of skyrmions as observed in LTEM [23]. (c) Reciprocal space image of skyrmion lattice using resonant soft X-ray scattering [17].

Recently discovered magnetic skyrmions were first observed in bulk MnSi, FeCoSi and FeGe just a decade back ago [8]. These skyrmions are multi-atom vortex spin textures in which the atoms spin orientations change from one direction in the middle to the opposite direction at the periphery. These structures are topologically protected and manifest as hexagonal lattice of spin vortices (See Fig 1). Due to the topological stability from defects and pinning sites, skyrmions can be moved with 10^5 times lower current density than a conventional magnetic domains thereby making them technologically promising for energy efficient spinotronic applications such as skyrmion based ultra-dense storage, race track memory and magnetic random access memory etc [9,10]. In bulk, skyrmions are generally formed in B20 compounds with non-centrosymmetric crystal structure due to Dzyaloshinskii-Moriya (DM) interaction and exchange interaction. In thin films of FeGe, FeSi and FeGd skyrmions arises as a result of the dipolar interaction and magnetic anisotropy in presence of perpendicularly applied magnetic fields [11,12].

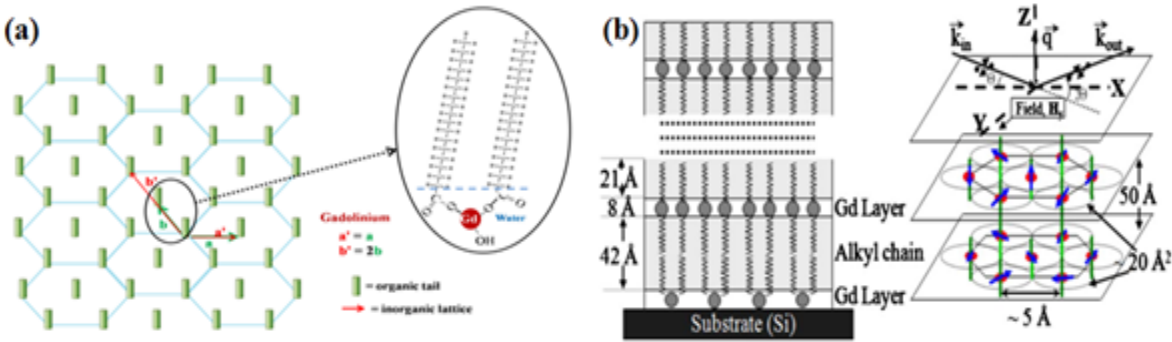


Fig 2: Schematic of the organic and metallic lattice of a LB monolayer at air-water interface along with the enlarged view of a metal-organic molecule. (b) Schematic of Gd-St multilayer LB film: out-of-plane stacking and layered arrangement of in-plane spins with specular reflectivity geometry [14].

Magnetic vortex structures have also been reported in rare earth based multilayer films deposited by Langmuir-Blodgett (LB) technique. Langmuir films of monolayer thickness are formed when amphiphilic (surfactants) molecules or nanoparticles are spread on water surface at the air–water interface. Multilayer stacks of amphiphilic fatty-acids attached with ions of rare-earth elements provide excellent 2D system to study low-dimensional magnetic ordering since the characteristic in-plane separations between metallic ions are an order of magnitude smaller than the out-of-plane layer-spacing decided by the hydrophobic tails (See Fig 2). It has been already reported that 2D short-range ferromagnetic order with no spontaneous magnetization occur in the gadolinium stearate (GdSt) LB films when a magnetic field is applied along any in-plane direction [13]. Further studies in gadolinium based LB films has predicted the existence of hexagonal lattice of spin vortices above a certain BKT transition temperature below which vortex and anti-vortex pairs annihilate to produce a homogenous phase with a saturation moment.

The magnetic properties of rare earth elements mainly in lanthanide series are generally determined by the localized 4f orbital and spin moments. The exchange interaction results in the long-range magnetic ordering here along with the existence of dipole-dipole long-range interaction among ions of a monolayer [14]. Apart from the ferromagnetic behaviour as observed in such systems, studies in MnSt LB films have also revealed about the existence of anti-ferromagnetic ordering occurring in these 2D structures [15].

Experimental Techniques:

Magnetic Characterization

Resonant coherent X-ray scattering: By tuning the energy of the incident photons (linearly polarized) to the metal L-edge of a constituent element greatly enhances the magnetic scattering intensity. The scattering provides information about spatial modulations of magnetically ordered structures. By making the beam coherent we can do correlation study as a function of time, field or temperature due to formation of speckle pattern in the magnetic Bragg peaks.

SQUID VSM: Magnetization measurement using the sensitivity of SQUID and speed of VSM together as a function of magnetic field and temperature.

Structural Characterization

X-ray Reflectivity: It is a surface sensitive technique used mainly in thin films and multilayers structures. It provides information about (i) film thickness, (ii) periodicity, (iii) electron density and (iv) surface and interfacial roughness. Reflectivity fitting was done using Parratt formalism [24].

Grazing angle X-ray Diffraction: It uses a small incident angle to study the surface properties of thin films or multilayer structures. The technique provides information about (i) in-plane and out-of plane lattice parameters, (ii) correlation length, (iii) tilt angle and (iv) surface roughness. GID data was analyzed using the Vineyard formalism [16].

Study of Skyrmions using magnetic scattering:

Spin, charge, and orbital motions can be affected by fluctuations, thereby generating entropy and losing information. Controlling and minimizing this decoherence holds a key feature of deploying quantum matter in emerging information technologies. An interesting example for such study is to employ a lattice of skyrmions. Due to the topological protection and existence of multiple length scale energetics, skyrmions scatter weakly from defects and can be moved relatively easily through the lattice.

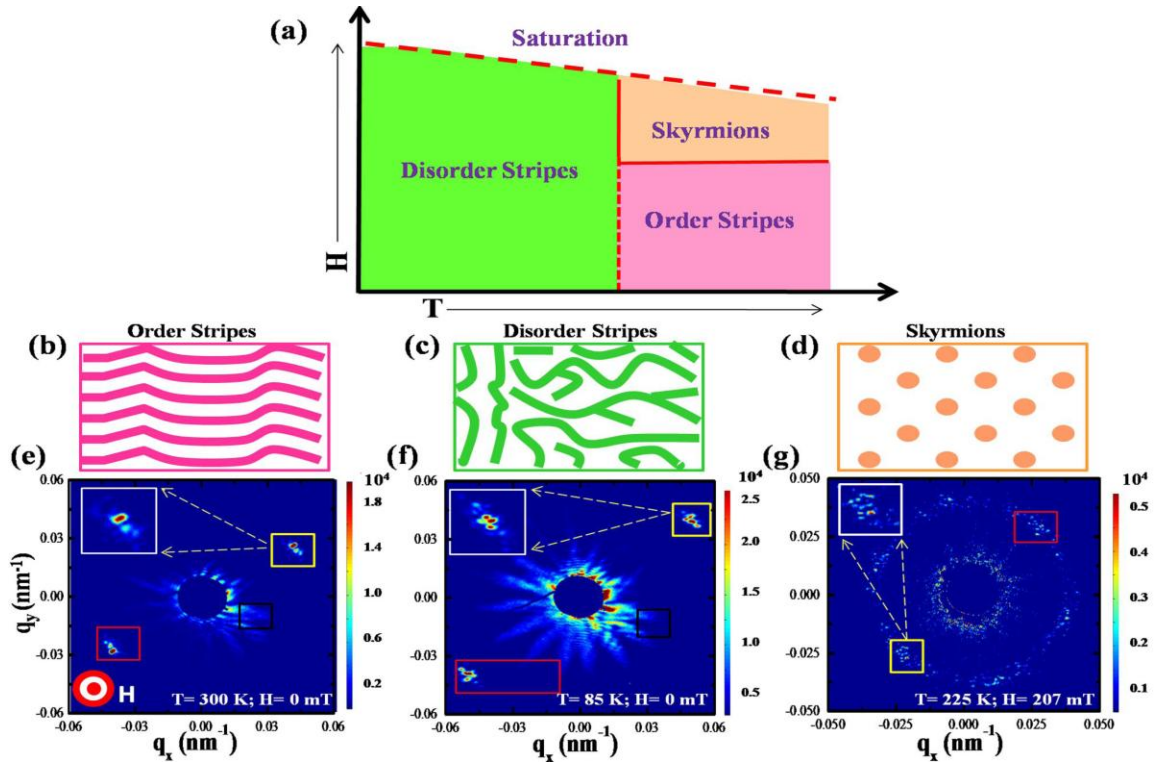


Fig 3: Schematic of phase diagram of the Fe/Gd sample as a function of temperature and applied magnetic field. (b-d) Schematic of order stripes, disorder stripes and skyrmion phase. (e-g) Magnetic diffraction spots in the three phases. The insets show enlarged image of the magnetic diffraction spots that are enclosed in yellow box. The red and black boxes are the regions of interest of magnetic diffraction and Airy fringes, respectively, for calculating the pair-wise correlation coefficients [21].

We have studied a Fe/Gd thin film heterostructure that exhibit highly tunable stripe and skyrmion phases using X-ray resonant coherent scattering as a function of magnetic field and temperature [17,18]. Both stripe and skyrmion peaks show modulation with speckles that indicate finite sized domain formation. At room temperature an ordered stripe domain with periodicity of 138 ± 5 nm forms at zero fields. Around 200 mT new peaks in the form of a distorted hexagonal pattern start to appear due to the onset of skyrmion formation. The periodicity of skyrmion hexagonal-lattice at 200 mT is 190 ± 5 nm (See Fig 3).

Resonant coherent soft X-ray scattering from a magnetic sample gives rise to speckle patterns due to the interference of randomly phase-shifted waves that are scattered by the magnetic domains. If the domain morphology changes either spontaneously or due to an external influence, then the speckle pattern will change as well. Such a change in an X-ray speckle pattern in reciprocal space provides a statistically significant measure of nanoscale changes in size, orientation and/or number density of the

magnetic domains in real space. We developed a statistical measure of field-induced domain jumps using the normalized pairwise correlation coefficient, a standard tool to measure the similarity of consecutive data sets.

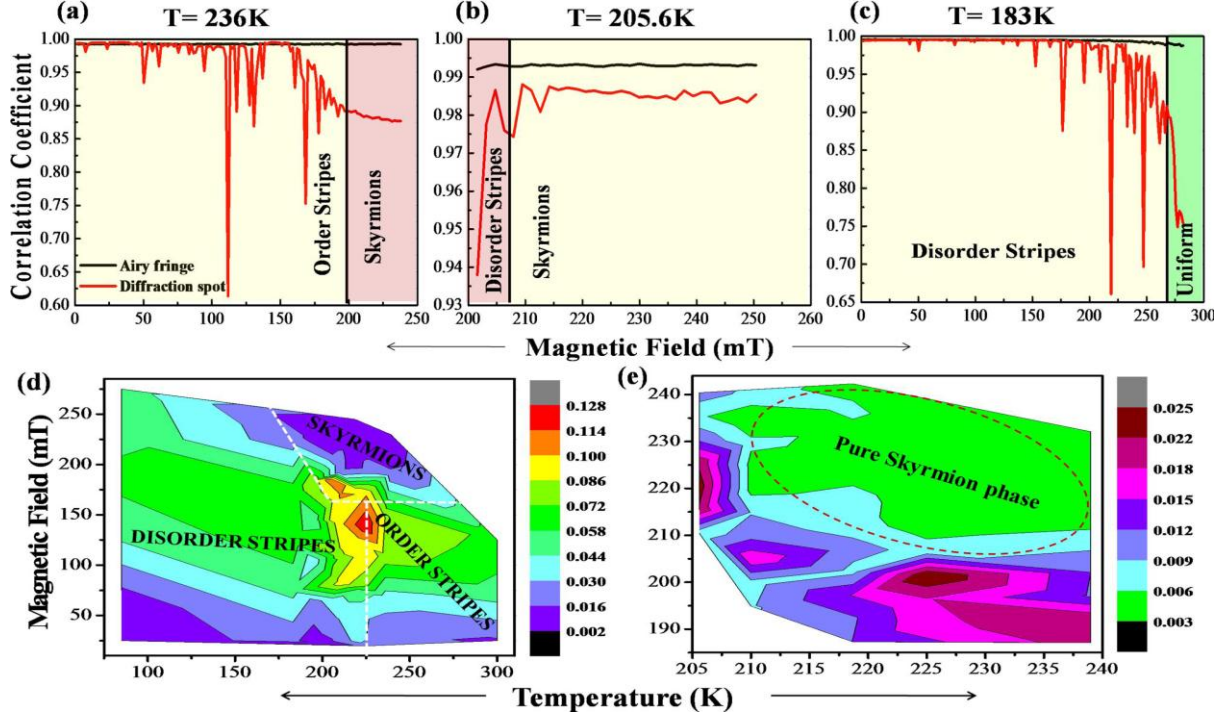


Fig 4: Plot of cross-correlation function (red line) versus magnetic field for (a) Stripe, (b) Skyrmion and (c) Disorder stripe diffraction spots. The black line in the figures corresponds to the correlation value from non-magnetic region (Airy fringes). Correlation between two consecutive image patterns was done for those regions as mentioned in Fig.3 with the corresponding color boxes. Color bar represents average jump size. Contour plot of average jumps size X as a function of field and temperature for (d) entire magnetic phase and (e) skyrmion phase only. A peak in the jump size in Fig. 4 (d) (red area ≈ 225 K, 150 mT) suggests a critical point [21].

We obtained direct experimental evidence that the magnitude and frequency of jumps in the skyrmion phase is significantly smaller compared to those in the stripe phase (for example, compare magnitude of jumps in Fig. 4 (b) with Fig. 4 (a) & (c)). The reduced jump size is most likely a consequence of the stability due to topologically protective nature of the skyrmions.

In Fig. 4 (d) a contour plot spanning all the three magnetic phases present in the sample is shown as a function of field and temperature. The contour plot shows that the average size of jumps increase with both temperature and field. It is observed that in the stripe phase, the average jump size shows a maximum value near the point $T \sim 225$ K and $H \sim 148$ mT, indicating the presence of a critical point in temperature and field around these values. The green region inside the contour plot (Fig. 4(e))

shows the temperature-field conditions where all the six peaks are of same intensity thereby representing the pure skyrmion phase. The magnitude of jumps is similar in both ordered and disordered stripes, however, the average jumps size in the skyrmion phase is almost an order-of-magnitude smaller than in the stripe phase.

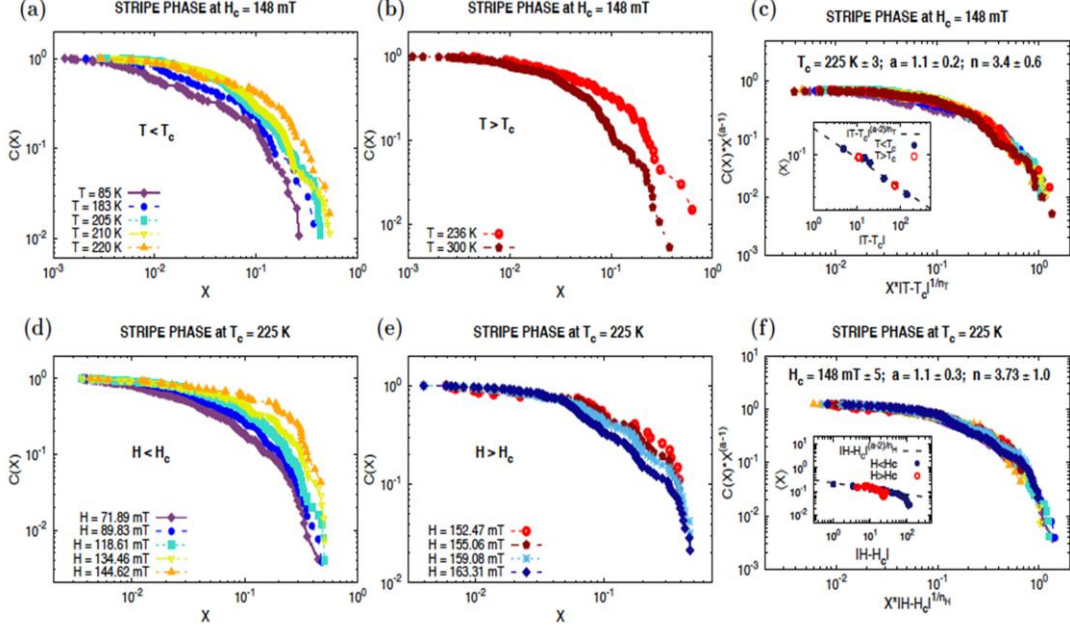


Fig 5: (a,d) and (b,e) Complementary cumulative distribution ($C(X)$) function of domain cascades in the stripe phase below and above the critical points. (c) and (f) The corresponding scaling collapse with the critical exponent values [21].

Our analysis was done according to the avalanche model using the scaling function of the form [19].

$$Z(X, T, H) = X^{-a} f_1 \left(X |T - T_c|^{\frac{1}{n_T}}, X |H - H_c|^{\frac{1}{n_H}} \right) \quad \dots 1$$

Where ‘X’ is the jump size and ‘ f_1 ’ is a universal function of temperature or field. Figure 5 and figure 6 clearly shows critical behavior for both stripes and skyrmion phase that is centred around different critical field and temperature. The critical exponent ‘ a ’ has a similar value for both phases, but exponent ‘ n ’ takes different value for stripes compared to skyrmions. Since all the critical exponents are not same for both the phases, this indicates that stripes and skyrmions belong to different universality classes.

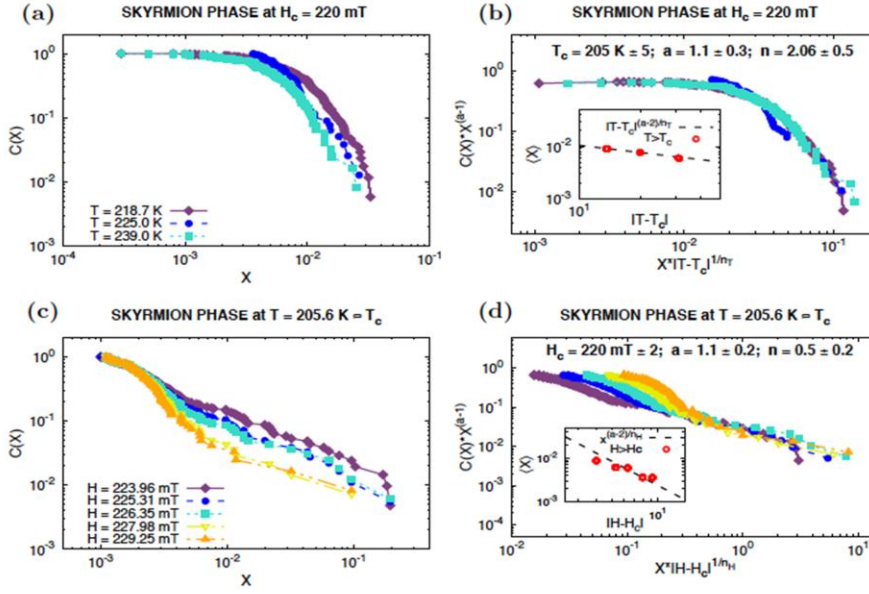


Fig 6: (a) and (c) Complementary cumulative distribution ($C(X)$) function of domain cascades in the skyrmion phase above the critical points. (b) and (d) The corresponding scaling collapse with the critical exponent values [21].

Anamolous expansion of stripe periodicity:

Self-organization of magnetic domains on surfaces and interfaces has attracted considerable recent interest, because it manifests in regular atomic scale structures, important in both fundamental and technological aspect. Self organized structures appear in nature whenever a system spontaneously chooses a preferred structure size and geometry due to minimization of energy. In thin films with perpendicular magnetic anisotropy (PMA), the dipolar interaction favours an in-plane magnetization, whereas the anisotropy prefers an out-of-plane magnetization. The competition between these two interactions results in periodic stripes in which the magnetization self organises in up and down magnetized bands.

The evolution of the diffractions spots from the stripe phase to skyrmions as a function of applied field at 225K in a thin film of FeGd is shown in fig 7(a). At zero fields, the sample is in stripe phase and the diffraction image corresponding to that phase is shown at the top-left corner inset of figure 7(a). Diagonally opposite two sharp spots in the inset image are due to the diffraction from the stripe magnetic domains whereas the streaks of intensity surrounding the beam stopper is due to the

diffraction from the pin hole placed before the sample. The line profile corresponding to the Bragg peak marked in the shaded cone shows a peak at $Q_1 (= 0.052 \text{ \AA}^{-1})$ as evident from the profile in the inset next to the image in figure 7(a). The increase in field leads to first the appearance of a satellite peak at Q_2 (lower than the Bragg peak at Q_1) and subsequently this satellite peak transforms into the main Bragg peak as shown by the symbols in figure 7(a). First appearance of satellite peak at Q_2 with less intensity and then the merger of the main Bragg peak to this Q_2 at a certain magnetic field indicates that the number of magnetic domains having periodicity $2\pi/Q_1$ decreases with increase in field while the number of domains having periodicity $2\pi/Q_2$ starts increasing and finally all the domains transforms to periodicity $2\pi/Q_2$. This sequence of events, changing Q values from Q_1 to Q_7 with similar mechanism of peak shifts is repeated for higher field values and ultimately ends in a structure when the skyrmion phase emerges which is represented by the six diffraction spots (due to hexagonal ordering) as shown by the image at the bottom-right corner inset of figure 7(a)

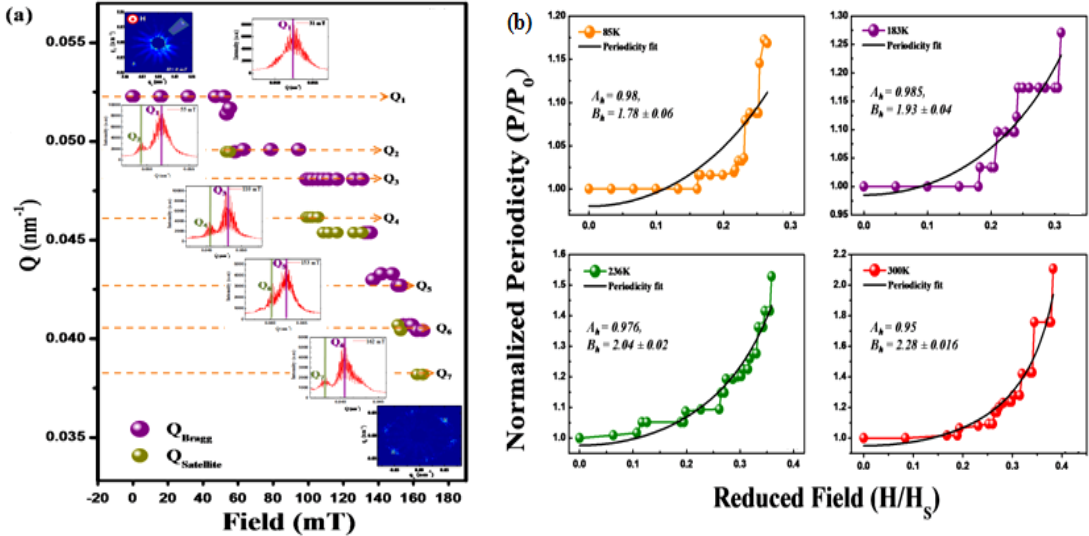


Fig 7: (a) The changes in the position of the diffractions peaks from the stripe phase to skyrmions as a function of applied field at 225K. The line profiles are extracted from the images of diffraction spots from the Fe/Gd multilayer structures. Two such images at stripe phase and skyrmion phase are shown at the top left and bottom right position of the figure.(b) The variation of the periodicity of the stripe domains normalised by the periodicity at remanence as a function of reduced fields (H/H_s) at different temperatures. Black lines are the theoretical fit to the experimental curve.

The periodicity ($2\pi/Q_1$) corresponding to the stripes at remanence is 119 ± 5 nm. At around 170 mT, new peaks are formed and a distorted hexagonal pattern starts to appear instead of only two diagonally opposite Bragg diffraction peaks indicating a transition to the skyrmion phase. The

periodicity of skyrmions at 193 mT is 233 ± 7 nm. At sufficiently high field (H_s) the diffraction pattern disappears as the film becomes uniformly magnetized

The periodicity of the stripe domains can be calculated simply from the position of the Bragg peak following the relation ($\tau_Q = 2\pi/Q$). The variation of the periodicity (τ) of the stripe domains normalised by the periodicity at remanence as a function of H/H_s at different temperatures 85 K, 183K, 236K and 300K are shown in figure 7(b) respectively. Also it is observed that the rate of change of τ with the variation in field increases with increase in the temperature. The solid lines in figure 7(b) show the fitting of a theoretical model following eq. (1) to the experimental data at different temperatures. The theoretical model was initially developed by Kooy, Enz and was later extended by Gehanno *et al* to make it applicable to films with thickness smaller than the domain period. This model gives a relationship between the periodicity of the stripes as a function of the applied field [20].

$$\tau(h) = A_h \sec[\arcsin(B_h h)] \quad \dots(2)$$

Here h is the reduced field (H/H_s), A_h and B_h are the terms whose value depends on the film thickness and susceptibility (at zero fields) of the material.

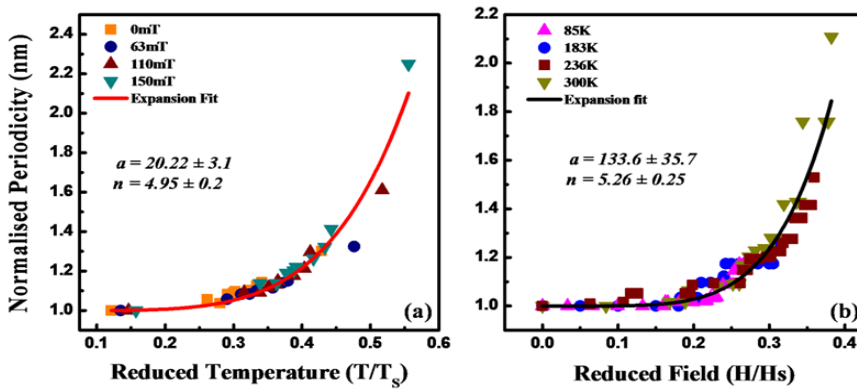


Fig 8: The collapse of normalised periodicity (symbols) as a function of (a) reduced temperature (T/T_s) and (b) reduced field (H/H_s). The solid lines are the fit with the expression as described in the text.

The periodicities extracted at different fields and temperatures after normalization can be collapsed to a single curve when plotted against the T/T_s (figure 8a) or H/H_s (figure 8b). The collapsed curve can be fitted with a simple expression similar to thermal expansion of solids as

$$\tau = 1 + a \cdot x^n \quad \dots(3)$$

Where x is the reduced temperature (t) for the temperature plot (figure 8a) or the reduced field (h) for the field plot (figure 8b).

Two dimensional magnetism in LB films:

Considerable interest in the 2D ferromagnetic and anti-ferromagnetic ordering has lead to several interesting neutron scattering measurements for understanding the nature of such ordering. In general it will be ideal if one can investigate in a system with minimal amount of structural change. 2D magnetic materials confined within ultrathin films and multilayered structures have always aroused considerable attention in understanding the underlying physics which may explain several interesting phenomena.

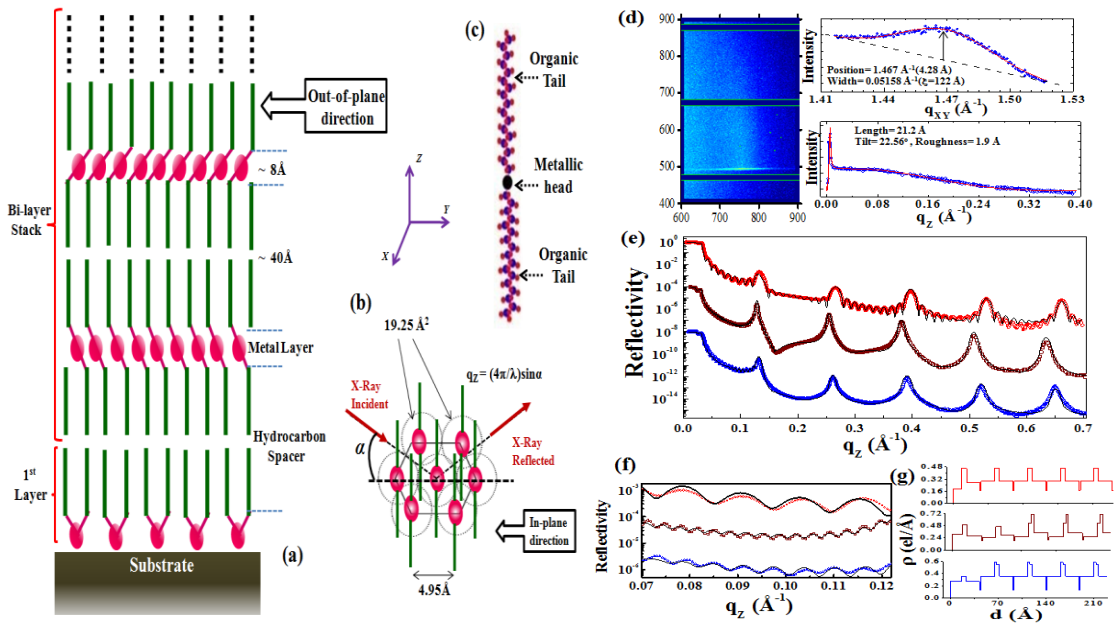


Fig 9: (a) Schematic of rare earth LB multilayer structure. (b) In-plane structure of multilayer Rare Earth LB film with the scattering geometry employed for the X-ray reflectivity measurements. All the molecules are in the same plane with the X-ray incident on the plane at an angle α . (c) amphiphilic molecule. (d) GID image of Gd-St multilayer LB film with q_{xy} and q_z plots along with their fits (red line). Specular X-Ray reflectivity of (d) Ho-St LB film (red color) with 21 monolayers, ErSt LB film (wine color) with 71 monolayers and Gd-St LB film (blue color) with 41 monolayers along with the corresponding fits. (f) Enlarged view of Kiessig fringes (with fit) in the above figure. (g) The electron density profile as a function of film thickness without roughness convoluted for initial few layers of Ho-St (red color), Er-St (wine color) and Gd-St (blue color) [25].

The metal-organic multilayer structures formed by Langmuir-Blodgett (LB) techniques provide an ideal platform to investigate 2D magnetic ordering. Here the magnetic metal ions are separated by approximately 5\AA within a monolayer that form a distorted hexagonal 2D lattice and in the out-of-plane direction the monolayers are separated from each other by 50\AA organic chains (See Fig 9).

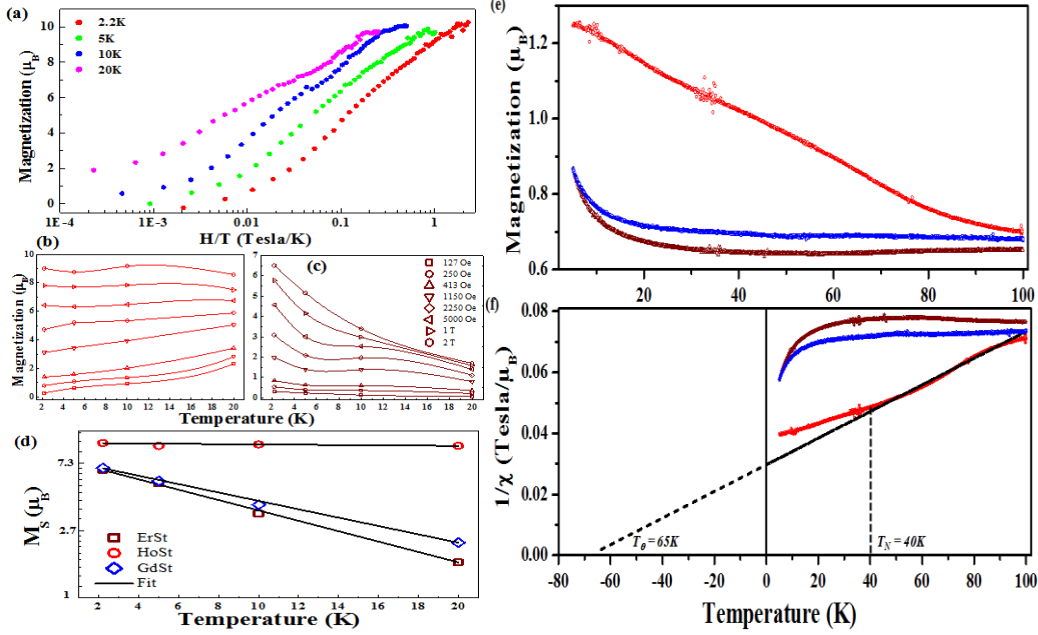


Fig 10: (a) Magnetization data for Ho-St LB film with 39 monolayers as a function of H/T (log scale) measured at 2.2 K (red), 5K (green), 10K (blue) and 20K (pink). Magnetization as a function of temperature at different field values derived from M-H curves for (b) Ho-St and (c) Er-St LB films. (d) Log-linear plot of the saturation magnetization M_s per RE (Gd, Er or Ho) ion at various temperatures and solid line is the linear fit. (e) The in-plane magnetization data for Ho-St (red), Er-St (wine) and Gd-St (blue) measured as a function of temperature T with an applied field H of 0.5 kOe. (f) Curie-Weiss plot of the inverse susceptibility vs temperature. The extrapolation of the high temperature data is shown by the dotted line which intercepts at a negative temperature only for Ho-St [25].

We observe different magnetic behaviour of HoSt LB films from both M-H and M-T data using SQUID VSM in the temperature range from 5K to 100K with field applied along the in-plane direction. Ferromagnetic behaviour in Gd-St LB films as previously reported is observed in Er-St films also. Whereas Ho-St LB film shows anti-ferromagnetic behaviour although the lattice structure of all the films are identical. The anti-ferromagnetic ordering temperature and Neel temperature is calculated to be 65K and 40K respectively (See Fig 10).

Conclusions:

It was shown in this thesis work, using coherent X-ray resonance scattering technique, that the domain fluctuations in one-dimensional (1D) magnetic stripe-phase are dramatically reduced in topologically protected two-dimensional (2D) skyrmion phase. Results of this study with a thin film of FeGd also show that the stripe and skyrmion phase follows different universality class [21]. Further observation of the periodicity of the stripe phase with applied magnetic-field has revealed a transition from discrete, staircase like behaviour at low temperatures to a smooth, continuous curve as we approach room temperature.

Through systematic X-ray reflectivity and magnetization studies of rare-earth LB films, it was shown that with similar structural configuration a ferromagnetic to anti-ferromagnetic crossover occur as the rare-earth ions of gadolinium or erbium is replaced by holmium ions in a LB films.

References:

- [1]. **Long range intrinsic ferromagnetism in two dimensional materials and dissipationless future technologies.** B. Shabbir *et al. Appl. Phys. Rev.*, **5**, 041105 (2018).
- [2]. **Layer-dependent ferromagnetism in a van der Waals crystal down to the monolayer limit.** B. Huang *et al. Nature* **546**, 270 (2017);
- [3]. **Domain shapes and patterns: The phenomenology of modulated phases.** M. Seul and D. Andelman. *Science*, **267**, 476 (1995)
- [4]. **Topological properties and dynamics of magnetic skyrmions.** N. Nagaosa and Y. Tokura. *Nature Nanotechnology*, **8**, 899 (2013).
- [5]. **Transformation between meron and skyrmion topological spin textures in a chiral magnet.** X. Z. Yu, W. Koshibae, Y. Tokunaga, K. Shibata, Y. Taguchi, Y.N. Nagaosa and Y. Tokura. *Nature* **564**, 95 (2018).
- [6]. **Magnetic skyrmions: advances in physics and potential applications.** A. Fert, N. Reyren and V. Cros. *Nature Review* (2017)
- [7]. **Coupled Skyrmion Sublattices in Cu₂OSeO₃.** M. C. Langner, S. Roy *et al. Phys. Rev Lett.* **112**, 167202 (2014).
- [8]. **Skyrmion Lattice in a Chiral Magnet.** S. Muhlbauer, B. Binz, F. Jonietz, C. Pfleiderer, A. Rosch, A Neubauer, R. Georgii and P. Boni. *Science*. **323**, 915 (2009)
- [9]. **Skyrmions on the track.** A. Fert, V. Cros and J. Sampaio. *Nature Nanotechnology*. **8**, 152 (2013).

- [10]. **Magnetic skyrmion logic gates: conversion, duplication and merging of skyrmions.** X.C. Zhang, M. Ezawa, Y. Zhou. *Scientific Reports*. **5**, 9400 (2014).
- [11]. **Chiral Symmetry Breaking in Magnetic Thin Films and Multilayers.** A.N. Bogdanov and U.K. Rossler. *Phys. Rev Lett.* **87**, 3 (2001).
- [12]. **Current-induced skyrmion dynamics in constricted geometries.** J. Iwasaki, M. Mochizuki and N. Nagaosa. *Nature Nanotechnology*. **8**, 742 (2013).
- [13]. **Field induced two-dimensional ferromagnetic ordering in a gadolinium stearate Langmuir-Blodgett film.** M. K. Mukhopadhyay, M. K. Sanyal, M. D. Mukadam, S. M. Yusuf and J. K. Basu. *Phys. Rev B* **68**, 174427 (2003).
- [14]. **Polarized neutron reflectivity study of spin vortices formed in Gd-based Langmuir-Blodgett films.** S. Gayen, M. K. Sanyal, A. Sarma, M. Wolff, K. Zhernenkov, and H. Zabel. *Phys. Rev B* **82**, 174429 (2010).
- [15]. **Antiferromagnetism of quasi two-dimensional manganese stearate.** A. Aviram and M. Pomerantz. *Solid State Communications*, **41**, 297 (1982).
- [16]. **Grazing-incidence diffraction and the distorted-wave approximation for the study of surfaces.** George H. Vineyard. *Phys. Rev B*. **26**, 8 (1982).
- [17]. **Synthesizing skyrmion bound pairs in Fe-Gd thin films.** J.C.T. Lee *et al.* *Appl. Phys. Lett.* **109**, 022402 (2016).
- [18]. **Resonant X-ray Magnetic Scattering Study Of Domain Morphology In FeGd Thin Film.** A. Singh, M. K. Sanyal, J. C. T Lee, Y. Chen, S. Montoya, E. E. Fullerton and S. Roy. *AIP Conference Proceedings* **1942**, 130028 (2018)
- [19]. **X-ray resonant magnetic scattering study of magnetic stripe domains in a-GdFe thin films.** J. Miguel, J. F. Peters, O. M. Toulemonde, S. S. Dhesi, N. B. Brookes and J. B. Goedkoop. *Phys. Rev B*. **74**, 094437 (2006).
- [20]. **Micromechanical Model for Deformation in Solids with Universal Predictions for Stress-Strain Curves and Slip Avalanches.** K. A. Dahmen, Y. Ben-Zion and J. T. Uhl. *Phys. Rev. Lett.* **102**, 175501 (2009).
- [21]. **Scaling of domain cascades in stripe and skyrmion phases.** A. Singh, J. C. T Lee, K. E. Avila, Y. Chen, S. A. Montoya, E. E. Fullerton, P. Fischer, K. A. Dahmen, S. D. Kevan, M. K. Sanyal and S. Roy. *Nature Communications*, **10**:1988 (2019).
- [22]. **Néel-type skyrmion lattice with confined orientation in the polar magnetic semiconductor GaV₄S₈.** I. Kézsmárki, S. Bordács, P. Milde, E. Neuber, L. M. Eng, J. S. White, H. M. Rønnow, C. D. Dewhurst, M. Mochizuki, K. Yanai, H. Nakamura, D. Ehlers, V. Tsurkan and A. Loidl. *Nature Materials* **14**, 1116–1122 (2015)
- [23]. **Real-space observation of a two-dimensional skyrmion crystal.** X. Z. Yu, Y. Onose, N. Kanazawa, J. H. Park, J. H. Han, Y. Matsui, N. Nagaosa and Y. Tokura. *Nature* **465**, 901–904 (2010).
- [24]. **Surface Studies of Solids by Total Reflection of X-Rays.** L. G. Parratt, *Phys. Rev.* **95**, 359 (1954).
- [25]. **Evidence of two-dimensional anti-ferromagnetic ordering in rare-earth Langmuir Blodgett films.** A. Singh, M. K. Mukhopadhyay, M. K. Sanyal, G. Stenning and S. Langridge. *Journal of Physics: Condensed Matter*, **31**, 495803 (2019).

List of figures

Chapter 1

Figure 1.1: (a) Ferromagnetic horse-shoe magnetic, (b) Two-dimensional arrangement of magnetic moments in ferromagnetic ordering and (c) behaviour of magnetic susceptibility (M/H) as a function of temperature. . . . 41

Figure 1.2: (a) Anti-ferromagnetic ordering, (b) Cr atoms in BCC lattice, (c) Fe atoms in SC lattice and (d) magnetic susceptibility of anti-ferromagnetic with temperature. 42

Figure 1.3: (a) Micrograph of a ferromagnetic surface, showing the crystal grains, each divided into several domains, with the magnetization in alternating directions (shown by red and green regions), (b) a ferromagnetic material divides into several small domains. 49

Figure 1.4: Different types of magnetic domain structure (a) labyrinth domain, (b) shape memory alloy domain structure and (c) magnetic bubble domains. 51

Figure 1.5: (a) Schematic of a domain wall and (b) different types of wall formations. 52

Figure 1.6: Neel and Bloch type of domain walls (a) front view and (b) 3D view. 54

Figure 1.7: Schematic diagram of spin configurations in case of (a) Bloch wall and (b) Néel wall. Topological magnetic domain texture of (c) vortex, (d) magnetic bubble, and (e) skyrmion 61

Figure 1.8: Illustration of diverse structures used for magnetic memory and storage based applications. They form the first generation of spintronics devices, as discussed in the context 62

Figure 1.9: (a) Schematic of the organic and metallic lattice of LB monolayers at air-water interface along with the enlarged view of a metal-organic molecule. (b) Schematic out-of plane and in-plane structure of Gd-St multilayer LB film. 63

Figure 1.10: (a) Schematic of spin configuration in a skyrmion, (b) real space image of skyrmions as observed in LTEM and (c) reciprocal image of skyrmion lattice as observed from resonant X-ray scattering. 63

Figure 1.11: LHS image, (a–d), Schematics of the magnetization textures of a core-up antimeron (a) and a core-down meron (b), each with a vorticity of +1, and a core-up meron (c) and a core-down antimeron (d), each with a vorticity of -1. Coloured arrows indicate directions of the magnetic moments. (e), Theoretically predicted square (anti)meron lattice. (f), Real-space magnetization textures of the square (anti) meron lattice, observed by using Lorentz TEM. RHS image, Upper panel: dissociation of a skyrmion into a meron and antimeron pair. Lower panel: a skyrmion covers the sphere, whereas a meron covers only half the sphere 65

Figure 1.12: A representative of a typical X-ray beamline at a third generation X-ray source. Bunches of charged particles (electrons or positrons) are circulated in a storage ring (typical diameter around 300 m). The ring is designed with straight sections, where an insertion device, such as undulator, is attached. The lattice of magnets in an insertion device makes the particles to execute small oscillations which produce intense beams of radiation. This radiation then passes through a number of optical elements, such as a monochromator, focusing device, etc., so that a beam of radiation with the required properties is delivered to the sample. Typical distances are indicated within the figure. 67

Chapter 2

Figure 2.1: (a) Phase difference of the current paths. (b) Schematic of a SQUID. 80

Figure 2.2: Graph showing the enhancement of the brightness of X-ray sources with time (*black*) in comparison to the development of the areal magnetic storage density in computers (*gray*). Moore's law, representing the doubling of the transistor density on an electronic chip every two years, is shown by the dotted curve. The brightness of X-ray is plotted as an average brightness on the left and has been aligned to the right scale of peak X-ray brightness at the point indicating 3rd generation synchrotron radiation sources. 82

Figure 2.3: Schematic of the scattering geometry in resonant X-ray scattering and the detailed picture of the scattering process at the electron level. 84

Figure 2.4: Summary of the quantum mechanical picture of the interaction of a photon with an atomic electron. (a) Photoelectric absorption and (b) Thomson scattering. (c) Resonant scattering is a second-order process and occurs via an intermediate electronic state. This picture should not be taken too literally, however, as resonant scattering is a virtual process, and does not occur in the two discrete steps suggested here. 85

Figure 2.5: Representative Gd M_3 resonant X-ray scattering patterns, square root scale. Scale bars represent a transfer momentum of 0.041 nm^{-1} . (a) Scattering from stripe domains with the first, second, and third order stripe peaks visible. Parts (b), (c) illustrate evolution of skyrmion bound pair lattice with magnetic field. . . . 88

Figure 2.6: A typical wavefunction and form factor of the 1s state for atomic number ($Z=1$ (dashed lines)) and $Z=3$ (solid lines). 89

Figure 2.7: Illustrations of longitudinal and transverse coherence lengths. (a) Two plane waves with different wavelengths are emitted along the same direction. For better understanding we have shown the waves displaced from each other in the vertical direction. After a distance LL , the longitudinal coherence length, the two are out of phase by a factor of π . (b) Two waves with the same wavelength are emitted from the ends of a finite sized source of height D 94

Figure 2.8: (a) Small Angle X-ray Scattering (SAXS) observation of a speckle structure in the diffraction ring of an Al-Li decomposed alloy. The central black region is the shadow of a beam stop to prevent the main beam from damaging the detector. (b) shows a typical profile observed across one side of the ring. (c) Image of the (001) superstructure peak from a Cu-Pd L12 ordering alloy. δq (in nm^{-1} units) is the distance from the superstructure peak position in the reciprocal lattice. Enlarged figures from each selection square are drawn at the right side in order to show the numerous speckles. 95

Figure 2.9: An image of the X-ray coherent beamline 12.0.2 at the advanced light source, USA. 98

Figure 2.10: Image of the beamline layout of the coherent soft X-ray beamline at the ALS. 98

Figure 2.11: Airy pattern and its cross section recorded using a $2.5\text{-}\mu\text{m}$ diameter pinhole at the focal plane of beamline 12.0.2 at the ALS. Picture was recorded at a wavelength of (a) 2.48 nm (500 eV) with an exposure time of 200 msec and (b) 2.07 nm (600 eV) with an exposure time of 1 s 99

Figure 2.12: Measured two-pinhole interference patterns at a photon energy of 500 eV (2.48 nm) and their respective lineouts for vertical pinhole separations of (a) $2 \text{ }\mu\text{m}$, (b) $6 \text{ }\mu\text{m}$, and (c) $8 \text{ }\mu\text{m}$. Each individual pinhole of the two-pinhole pairs has a diameter of 450 nm to ensure a spatially coherent wavefront over the individual pinhole. (d) Measured magnitude of the complex coherence function versus the pinhole separation. Least square error Gaussian curve is fitted to these data points. All data was taken on beamline 12.0.2 of the ALS. 101

Figure 2.13: Measured two-pinhole interference patterns at 500 eV , 600 eV , 700 eV , and 800 eV and their respective lineouts for a $5\text{-}\mu\text{m}$ vertical pinhole separation at a photon energy of (a) 600 eV (2.07 nm), (b) 700

eV (1.77 nm), and (c) 800 eV (1.56 nm). Note that airy envelope decreases for increasing energy. (d) Measured magnitude of the complex coherence function versus the pinhole separation. Least square error Gaussian curve is fitted to each energy's set of data points. All data was taken on beamline 12.0.2 of the ALS. Coherence length as calculated by (17) and (18) are 5.4 μm (500 eV), 4.9 μm (600 eV), 4.2 μm (700 eV), and 3.6 μm (800 eV). 102

Figure 2.14: Measured two-pinhole interference patterns at a photon energy of 500 eV (2.48 nm) and their respective lineouts for horizontal pinhole separations of (a) 1 μm , (b) 4 μm , and (c) 8 μm . (d) Measured magnitude of the complex coherence function versus the pinhole separation. Least square error Gaussian curve is fitted to these data points. All data was taken on beamline 12.0.2 of the ALS. 103

Figure 2.15: Schematic of a amphiphile - stearic acid and on the water surface. The polar group (head) is immersed in water and the hydrocarbon chain (tail) is pointing outwards to the water surface. 105

Figure 2.16: Wilhelmy plate, (a) front view, (b) side view. 106

Figure 2.17: Representative of (a) drop dispensing of the amphiphilic compound dissolved in a volatile solvent onto a polar liquid sub-phase filling a Langmuir trough, (b) Typical Pressure-Area isotherm showing the presence of all the distinct phases. 109

Figure 2.18: Schematic of the LB deposition mechanism in a alternating bath trough. 112

Figure 2.19: Schematic of various multi-layer LB deposition alternatives on hydrophobic and hydrophilic substrates. 114

Figure 2.20: Snell's law and the Fresnel equations can be derived by requiring continuity at the interface of the wave and its derivative. 115

Figure 2.21: Schematic (a) scattering geometry from a monolayer on a substrate and (b) of a multilayer consisting of a stack of bilayers. Each bilayer, as shown separately to the right has a homogeneous high electron density region of thickness $\Gamma\Lambda$, and a low density region. The total thickness of a bilayer is Λ 117

Figure 2.22: Geometry of a grazing incidence diffraction (GID) experiment from a solid single crystal surface at a synchrotron. The surface can be rotated around the surface normal \mathbf{n} , and the detector can be both rotated around \mathbf{n} in the vertical plane, and moved perpendicular to it so as to scan along the crystal truncation rods. 119

Figure 2.23: The Indian Beamline (BL-18B) at the photon factory, KEK, Japan. 123

Figure 2.24: Different experimental techniques used in this thesis at BL-18B, KEK, Japan 124

Chapter 3

Figure 3.1: (a) illustrative diagram of a single Bloch skyrmion and (b) skyrmion lattice. (c) Real-space Lorentz TEM image of skyrmion array and (d) SANS pattern from a skyrmion hexagonal lattice in reciprocal space.(e) magnetic helix state in B20 crystals. 133

Figure 3.2: Skyrmion structures with varying m and γ . The arrows indicate the direction of the in-plane spin component, and the brightness indicates the normal component to the plane, with white denoting the up direction and black the down direction. All the structures of the anti-skyrmions ($m = -1$) are equivalent on rotation in the x - y plane. The relative stability of each structure is determined by the mechanism or interaction generating the skyrmion. 134

Figure 3.3: Schematic of phase diagram of the Fe/Gd sample as a function of temperature and applied magnetic field. (b-d) Schematic of order stripes, disorder stripes and skyrmion phase. (e-g) Magnetic diffraction spots in the three phases. The insets show enlarged image of the magnetic diffraction spots that are enclosed in yellow box. The red and black boxes are the regions of interest of magnetic diffraction and Airy fringes, respectively, for calculating the pair-wise correlation coefficients. 138

Figure 3.4: Evolution of stripe and skyrmion phase: Azimuthal variation of scattered intensity for different field values at (a) 196 K and (b) 225 K. The black dotted arrows show the position of stripe and skyrmion peaks. (c), (d) Enlarged image of the diffraction spot for disordered stripes and ordered stripes, respectively. (e) Contour plot of angular full width half maximum (FWHM) of the stripe diffraction spot along the azimuthal direction as a function of field and temperature. Color bar represents the FWHM of the diffraction spot. The FWHM is related to degree of disorder of the stripe domains. The panel inset shows representative diffraction pattern as the temperature is changed. Clear evolution from a broad pattern to a strong diffraction peak is evident. . . . 140

Figure 3.5: Schematic experimental arrangement and expected diffraction patterns on the detector from stripe and skyrmion domains. As the data is taken at the absorption edge that enhances magnetic scattering, red spots denote basically the magnetic diffraction peaks. The central black dot indicates the shadow of the direct-beam stopper. 141

Figure 3.6: Data analysis scheme for extraction of pair-wise correlation coefficient as a function of magnetic field for the different magnetic phases. 143

Figure 3.7: Pair-wise correlation coefficient: Pair-wise correlation function (blue line) versus perpendicular magnetic field. We show the speckle pattern at $T = 236$ K for four consecutive field values that produces small and big jumps. The speckle patterns are represented within an area of 90 by 90 pixels. Large change in speckle pattern gives rise to large magnitude of jump indicating a large change of domain morphology. 145

Figure 3.8: Plot of cross-correlation function (red line) versus magnetic field for (a) Stripe, (b) Skyrmion and (c) Disorder stripe diffraction spots. The black line in the figures corresponds to the correlation value from non-magnetic region (Airy fringes). Correlation between two consecutive image patterns was done for those regions as mentioned in Fig.1 with the corresponding color boxes. Color bar represents average jump size. Contour plot of average jumps size X as a function of field and temperature for (d) entire magnetic phase and (e) skyrmion phase only. A peak in the jump size in Fig. 4 (d) (red area ≈ 225 K, 150 mT) suggests a critical point. 147

Figure 3.9: Plot of Correlation coefficient (PCC) between two consecutive diffraction images with variation of position. The x-axis corresponds to the image number which is assumed to vary due to applied magnetic field (1.575mT/image). The images below show the real space images and the corresponding diffraction pattern. The plots show the presence of sharp jumps. 149

Figure 3.10: Plot of Correlation coefficient between two consecutive diffraction images with variation to size and lattice parameter. The x-axis corresponds to the image number which is assumed to vary due to applied magnetic field (1.575mT/image). The real space images are shown below with the corresponding diffraction patterns. 149

Figure 3.11: (a) Histogram showing the number of Jumps as a function of Jump size. (b) Histogram of CCDF as a function of Jump size. 150

Figure 3.12: Above plots are shown for the stripe phase only. The first row corresponds to the critical field for temperatures below and above the critical value for $\frac{\langle X^2 \rangle}{\langle X \rangle}$, $\langle X \rangle$ and $\langle X^2 \rangle$, respectively. The second row is generated at the critical temperature for fields below and above the critical value. Similar procedures are followed for the skyrmion phase also. 152

Fig. 3.13: (a,d) and (b,e) Complementary cumulative distribution (C(X)) function of domain cascades in the stripe phase below and above the critical points. (c) and (f) The corresponding scaling collapse with the critical exponent values. 153

Fig. 3.14: (a) and (c) Complementary cumulative distribution (C(X)) function of domain cascades in the skyrmion phase above the critical points. (b) and (d) The corresponding scaling collapse with the critical exponent values. 154

Chapter 4

Figure 4.1: The one-dimensional FVdM model. The springs represent interactions between atoms, the wavy line the periodic potential. (a) Commensurate structure, (b) incommensurate structure, (c) chaotic structure. ... 164

Figure 4.2: Various types of staircase. (a) Continuous behaviour. (b) In-complete devil staircase. (c) Complete devil staircase. (d) Harmless staircase. 167

Figure 4.3: Krypton monolayer adsorbed on graphite. (a) Commensurate $\sqrt{3}$ structure⁴. The krypton atoms occupy 1/3 of the graphite honeycomb cells. (b) Incommensurate phase. 169

Figure 4.4: Stacking of metal (M) and graphite (A, B, C) layers in stage 2 graphite intercalation compounds such as CsC24. The intralayer ordering may be commensurate or incommensurate as shown in the previous figure. 169

Figure 4.5: Scattering from a 1D incommensurate chain. The top panel shows the position of atoms in a 1D chain with a commensurate, $\lambda m = 5a$, and an incommensurate, $\lambda m = (2/\sqrt{3})a$ modulation wavevector. The bottom panel is the calculated scattered intensity for a chain of $N=2000$ atoms, with positions given by Eq. (4.2), a modulation wavelength of $\lambda m = (2/\sqrt{3})a$, and a displacement amplitude of $u=0.2$. For simplicity it has been assumed that the atomic scattering length is unity, and independent of wavevector transfer Q 170

Figure 4.6: Temperature dependence of wavevector for sinusoidally modulated structure of cerium antimonide, CeSb (Fischer et al 1978). •, intense satellite; o, weak satellite. 170

Figure 4.7: Resonant X-ray scattering patterns due to (a) order stripes, (b) disorder stripes and (c) skyrmions. Insets show the enlarged view of the diffraction spot which shows speckle pattern. (d) Temperature Vs. magnetic field phase diagram of the Fe/Gd sample. 174

Figure 4.8: (a) & (d) Real space image of magnetic stripe domains using LTEM at fields F1 and F2 respectively ($F2 > F1$). (b) & (e) Line profile (yellow line in Fig. 3.16a, b) of the stripes at F1 and F2 respectively along with the Gaussian fit. (c) & (f) The fitting parameters of the Gaussian profile for all the peaks are listed in the corresponding tables (here width denotes FWHM). 176

Figure 4.9: The field vs. temperature phase map of the Fe/Gd multilayer films. The reciprocal space image (a) and the X-ray microscopy real space images (b) are shown for the disorder stripe, order stripe and the skyrmion phases. The red dotted lines show the resonant X-ray scattering measurements. 177

Figure 4.10: (a) Schematic of the experimental setup. (b) Evolution of the stripe phase at 236K at different applied magnetic fields. (c) The changes in the Q value of the diffraction peaks from the stripe phase to skyrmion phase as a function of applied field at 236K. The line profiles are extracted from the images of diffraction spots from the Fe/Gd multilayer structures. Two such images at stripe phase and skyrmion phase are shown at the top left and bottom right position of the figure. (d) The periodicity of the stripes as a function of

applied field at 236K. Also shown in the figure are the different rational steps indicating Devil staircase like behaviour. 179

Figure 4.11: Resonant X-ray scattering pattern at different fields (a-c) and the corresponding intensity profile of the diffraction spots as a function of Q 181

Figure 4.12: Schematic of the extraction of H_s and T_s from the phase boundary of the saturation magnetization in Fe/Gd multilayer films from the phase diagram [28]. The solid black and red lines are the line of extrapolation in the low and high temperature regions respectively. The dotted lines signify the measurement temperatures and fields for the films and the arrows mark the corresponding H_s and T_s 183

Figure 4.13: The variation of the periodicity of the stripe domains normalised by the periodicity at remanence as a function of reduced fields (H/H_s) at temperatures (a) 85 K, (b) 183K, (c) 236K and (d) 300K. 185

Figure 4.14: The variation of the periodicity of the stripe domains normalised by the periodicity at remanence as a function of reduced fields (T/T_s) at fields (a) 0mT, (b) 63mT, (c) 110mT and (d) 150mT. 186

Figure 4.15: The collapse of normalised periodicity (symbols) as a function of (a) reduced temperature (T/T_s) and (b) reduced field (H/H_s). The solid lines are the fit with the expression as described in the text. 187

Figure 4.16: Complementary cumulative distribution function (CCDF) of step height at temperatures (a) 236 K, & (c) 300 K and step width at (b) 236 K, & (d) 300 K. The distribution could be fitted with a power law. 188

Figure 4.17: (a) Periodicity of the magnetic stripes after normalization using equation 3 as a function of applied magnetic field at room temperature. Different spin configurations corresponding to a single stripe period for different rational fractions are shown inside. (b) Stripe periodicity at few commensurate states is drawn in contrast with the ground state. 192

Chapter 5

Figure 5.1: (a) Schematic of the experimental set-up and the scattering geometry including incident and scattered X-ray beam directions are indicated. (b) Typical π -A isotherm of GdSt Langmuir monolayer at the air-water interface is presented (refer text for details). 203

Figure 5.2: (a) XRR profiles of GdSt Langmuir monolayer on the water surface. (b) Corresponding R/R_f profiles. The profiles are shifted vertically for clarity. (c) Extracted electron density (ρ) profiles after fitting (line color same). (d) Derivative plot of EDP for $\pi=30$ mN/m. 205

Figure 5.3: (a) q_z -Integrated intensity profile of GIXD spectra as a function of q_{xy} of GdSt Langmuir monolayer; the profile is fitted by a linear background and two Lorentzian shape peaks, (b) q_{xy} - q_z map of GIXD spectra. (c) and (d) Intensity profile of the (02) and (11) peaks along q_z direction along with their fits [31]. 206

Figure 5.4: XRR profiles of GdSt LB films (a) monolayer (ML), (b) multilayer (9-ML) and their fits (black solid line). Corresponding AFM tomography images of GdSt LB films are in the insets. Extracted EDPs for (c) monolayer and (d) multilayer (without any roughness convolution) films. 209

Figure 5.5: Schematic diagram of the (a) out-of-plane and (b) in-plane structure of multilayer Rare-earth (Gd, Er & Ho) Stearate Langmuir-Blodgett films is shown with the scattering geometry employed for the X-Ray measurements. The x-z plane is the scattering plane and the magnetic field is applied along the +y direction. λ

and α are the wavelengths of the radiation and the angle of incidence, respectively. (c) Shows a single RE-St amphiphilic molecule where the central RE ion is connected to two hydrocarbon chains. 209

Figure 5.6: (a) Grazing Incidence Diffraction image of Gd-St (21ML) with the extracted q_{xy} and q_z plots along with their fits (red lines). Specular X-Ray reflectivity of (b) Ho-St LB film (open circle) with 21 monolayers, Er-St LB film (open square) with 71 monolayers and Gd-St LB film (open triangle) with 41 monolayers - the plots are shifted vertically for clarity. (c) Enlarged view of Kiessig fringes (with fit). (d) The electron density profile as a function of depth for initial few layers. Open coloured circles are experimental data points and solid lines are the fitted curves. 211

Figure 5.7: (a) Raw data of in-plane magnetization as a function of applied magnetic field taken at 2.2 K for 41 ML Ho-St LB film (open red square) and for bare Si substrate at 2.2K used here (open black square). The in-plane magnetization data after substrate correction in terms of Bohr magneton per unit Rare-earth atom at 2.2K (open square), 5K (open circles), 10K (open up-triangles) and 20K (open down-triangles) for (b) Ho-St LB film with 39 monolayers (red symbol) (c) Er-St LB film with 37 monolayers (violet symbol) and (d) Gd-St LB film with 41 monolayers (blue symbol). The black horizontal lines show the value of the respective saturation magnetization. 214

Figure 5.8: Raw magnetization data as a function of temperature, (a) Ho-St on Si (open red circles) and bare Si (open black circles) from 260 mK to 2.4 K and (b) Gd-St on Si (open blue circles) and bare Si (open black circles) from 2.2 K to 100 K. 216

Figure 5.9: (a) Image consisting of the different components of the SIMS instrument. (b) Sputtering from a sample using O_2 ion beam 217

Figure 5.10: Image of the SIMS instrument used for calculating the composition profile of the rare-earth based LB films at Saha Institute of Nuclear Physics, Kolkata, India. 219

Figure 5.11: (a) Image of the sample holder along with samples inside it. The red box shows the region to be studied. (b) Instrumental parameters of the ion beam (O_2) at the time of measurement. 219

Figure 5.12: Mass spectrum of Ho-St (red symbol) and Gd-St (blue symbol) LB films from mass number (a, c) 0 to 70 and (b, d) 150 (Gd) or 160 (Ho) to 170 respectively. 220

Figure 5.13: Intensity vs time profile in SIMS measurement of (a) Gd based LB film, (c) Er based LB film and (e) Ho based LB film. Depth vs Lateral distance profile as observed in Dektak instrument for (b) Gd based LB film, (d) Er based LB film and (f) Ho based LB film. All the samples were deposited on Si (100) substrates. 221

Figure 5.14: Plot of composition profile as a function of depth for (a) Gd-St LB film, (b) Er-St LB film and (c) Ho-St LB film. 223

Figure 5.15: (a) Magnetization data in terms of Bohr magneton for Ho-St LB film with 39 monolayers as a function of H/T (log scale) measured at 2.2 K (red), 5K (green), 10K (blue) and 20K (pink). Magnetization value as a function of temperature at different field values (shown within Fig. 4(c)) derived from M-H curves for (b) Ho-St (red colour) and (c) Er-St LB films (violet colour). (d) Log-linear plot of the saturation magnetization M_s expressed in Bohr magneton per RE (Gd, Er or Ho) ion as a function temperature and solid black line is the linear fit. 224

Figure 5.16: (a) The in-plane magnetization data for Ho-St (open red circles), Er-St (open violet triangles) and Gd-St (open blue squares) measured as a function of temperature T with an applied field H of 0.5 kOe. (b) Curie-Weiss plot of the inverse susceptibility vs temperature of Ho-St. The extrapolation of the high temperature data is shown by the dotted line which intercepts at a negative temperature. 226

List of tables

Table 2.1: Beamline summary giving spatially coherent flux delivered to the focal plane of the beamline. . . **99**

Table 2.2: Comparison of factors determining the interactions of neutrons, low energy (< 10 eV) electrons, X-rays, and optical photons with magnetic materials such as the ferromagnets Fe, Co, and Ni. Listed are the combined charge and magnetic cross sections and the magnetic contribution through a fractional value for the magnetic contrast P is given. Also the incident monochromatic flux per appropriate experimental bandwidth Φ , and the relative figure of merit per atom per second, defined as $\sigma\Phi P^2$ is indicated. **124**

Table 5.1: Parameters for GdSt Langmuir film on water; symmetric configuration are in bracket **207**

Table 5.2: X-ray reflectivity fitting parameters as used in Fig. 5.6. Each film is composed of first monolayer on the substrate followed by several bilayers stack having same parameters as shown below. **210**

Table 5.3: Constituent elements and their corresponding mass number considered for SIMS measurements from the mass spectrum results (see Fig. 5.8). **221**

Introduction

Ancient civilization relied on *energy and matter* to meet their daily needs and survive against any natural calamities. The knowledge of using it much more efficiently has evolved from generations to generations.

With the advent of modern civilization, the ever growing demand of *energy and matter* has increased considerably per capita in order to provide the latest facility and infrastructure. This has lead to the discovery of new materials where *energy and matter* can be used much more efficiently than ever before. From this perspective low dimensional materials in the *nanometer regime* has attracted our imagination due to their novel properties that are relevant not only from the technological aspect but also on our profound understanding of the *quantum mechanical nature of energy and matter*.

Exotic materials showing new physical properties have already been realized. But one such property which has remained from the ancient times and still amazes us is *magnetism*. Magnetism was observed as early as 800 BC long before the birth of Christ, in naturally occurring load stones and was used mainly for navigation purpose. Today, information technologies ranging from personal computers to main-frames employs magnetic materials to store and process information in tapes, floppies, pen drives and hard disks. Personal computers, laptops and many other electrical devices are now mainly powered by lightweight

switch-mode power supplies deploying new magnetic material technology that was unavailable 40 years ago [2, 36].

1.1 Types of Magnetism

The way the local atomic moments couple to each other, parallel, antiparallel, or not at all, provides an initial way of classifying magnetic materials. The individual atomic moments μ_m may be randomly oriented if they do not interact with each other. In such case $\sum \mu_m = 0$ at zero field. Such uncoupled magnetic moments may be aligned partially (depending on thermally induced agitation) in an applied magnetic field H . This weak field-induced magnetization behaviour defines a paramagnet. Alternatively, the atomic dipoles may couple somehow to each other and cooperatively align so $\sum \mu_m \neq 0$ even in the absence of an applied field. This defines an ordered magnetic material, examples of which are ferromagnets, antiferromagnets, and ferrimagnets [1-3, 36].

1.1.1 Weak Magnetism

Diamagnetic materials are repelled by external magnetic fields and the induced magnetization forms in the direction opposite to that of the applied magnetic field whereas paramagnetic and ferromagnetic materials are attracted by a magnetic field. Diamagnetism is a property that manifest in every kind of material, and always makes a minor contribution to the material's own response to applied magnetic field. However, the other types of magnetism (such as ferromagnetism or paramagnetism) are so much dominant that when multiple different forms of magnetism are present in a material, the diamagnetic signal is usually

negligible and suppressed. Substances in which the diamagnetic behaviour is the dominant effect are termed as diamagnetic materials, or diamagnets [4-6, 36].

Paramagnetism is another form of magnetism in which certain materials are weakly attracted by an externally applied magnetic field, and results in an internal, induced magnetic field in the direction of the applied magnetic field. Paramagnetism arises mainly due to the presence of unpaired electrons in the atoms constituting the material, implying that all atoms with incompletely filled atomic orbitals are paramagnetic [2, 3]. Due to their intrinsic spin, unpaired electrons have a magnetic dipole moment and act like tiny magnets. An external magnetic field induces the electrons' spins to align in the direction parallel to the field, causing a positive induced moment. Examples of paramagnetic materials include aluminium, oxygen, titanium, and iron oxide (FeO) [5, 6]. Paramagnetic material does not retain any net magnetization in the absence of an externally applied magnetic field unlike ferromagnetic material due to the thermal motion which randomizes the spin directions [36].

The magnetic susceptibility denoted by χ_m is usually used to describe weak magnetic responses to applied field H as in paramagnetic and diamagnetic materials. The magnitude of χ_m is usually $\pm 10^{-4}$ to 10^{-6} (dimensionless in SI). A material with a paramagnetic susceptibility of 10^{-5} would show a magnetization $M = 1$ A/m in a field of 10^{-5} A/m (applied field $B, = 0.1$ T). This value of magnetization corresponds to a flux density $\mu_0 M$ of order T, which is much less than the 1 T that our hydrogenic model suggests for fully aligned moments. What is keeping the moments in a paramagnet from aligning in an external field? Perhaps it is thermal energy, $k_B T$ [9, 10].

The degree to which a paramagnetic material will respond to a field can be understood by considering the potential energy U of the moment μ_m in an applied field B :

$$U = -\mu_m \cdot \mathbf{B} \quad (1.1)$$

$$U = -\mu_m \cdot \mathbf{H} \text{ (in cgs unit)} \quad (1.2)$$

[In mks units the energy is written as $\mu_m \cdot \mathbf{B}$ because the factor μ_0 needed to relate μ_m to a flux density has been put with the field \mathbf{H} . If μ_m were defined as $\mu_0 \mathbf{IA}$ (Wb/m²), then the energy would be $-\mu_m \cdot \mathbf{H}$].

Using the value of $\mu_m \approx 10^{-23}$ Am² as calculated for a hydrogenic orbit gives $U \approx 9.3 \times 10^{-24}$ J = 6×10^{-5} eV (for $B = 1$ T, i.e., $\mathbf{H} = 8 \times 10^5$ A/m). This energy is negligibly small in comparison to the thermal energy at room temperature, $k_B T \approx 4 \times 10^{-21}$ J = 1/40 eV, so it is not expected for a 1T field to produce much magnetic response in a paramagnet. One can even crudely calculate the fraction of saturation moment that would be measured in a thermally disordered paramagnet by multiplying $n\mu_m$ with the scale factor $(U/k_B T) = \mu_m B/B T$; $\chi_m = M/H \approx n\mu_m(U/k_B T)/(B/\mu_0) = \mu_0 n\mu_m / k_B T \approx 9.3 \times 10^{-4}$. This shows why paramagnetic susceptibilities are so small. The field tends to have only a weak linear effect in aligning the moments because thermal energy is large in comparison to the magnetic energy [3-7, 36].

1.1.2 Ferromagnetism

Ferromagnetic materials are generally characterized by a long-range ordering of their atomic magnetic moments, even without the presence of an external field. This spontaneous, long-range magnetization is observed to exist only below an ordering temperature known as the Curie temperature T , (Fig. 1.1).

The relative magnetic permeability $\mu_r = \mu/\mu_0 (= 1 + \chi_m)$ is more commonly used than the susceptibility to describe the magnetic response of a ferromagnetic material to an external magnetic field. This is due to the reason that ferromagnets are useful in electromagnetic

devices where it is B , particularly $\partial B/\partial t$, that is important in generating a voltage (see Faraday's law). Ferromagnets are efficient because a large $B \approx 1-2$ can be produced by a fairly small field, $H \approx 100$ A/m ($B \approx 10^{-4}$ T = 1 gauss). The full magnetization of ferromagnets $M \approx B/\mu_0$ is of the order 10^6 A/m for fully aligned moments. The important question here is that where the energy for magnetic alignment in a ferromagnet is originated. For a paramagnet, M is of order $n\mu_m(U/k_B T)$ which raises the question whether the moment-disordering effect due to thermal energy just as strong in a ferromagnetic solid or could there be something else rather than the external field contributing towards the tendency to align the local moments? One of the pioneers in this field, Pierre Weiss thought long and hard about this inconsistency and eventually concluded that in ferromagnetic materials there must be a presence of a giant "molecular" field, H_{molec} which exists even when no external field H_{ext} is applied: $H = H_{ext} + H_{molec}$. H_{molec} aids in overcoming the thermal fluctuation and essentially aligns all the atomic moments in a ferromagnet so that $M = n\mu_m = M_s$ instead of $M \approx n\mu_m(U/k_B T)$ as in the case of a paramagnet [9,10,33]. But then another fundamental question arise that since ferromagnets have such strong magnetizations, why do not two pieces of iron attract each other the way they are attracted by a permanent magnet? What is reason for iron getting magnetized or demagnetized? Weiss came up with a hypothesis for that, too. He predicted the existence of magnetic domains, regions (ranging in size upwards from approximately $0.1 \mu\text{m}$) in a ferromagnetic material within which all moments are essentially aligned parallel (see Fig. 1.1). Each domain is separated from one another by domain walls, surfaces over which the orientation of μ_m changes relatively abruptly (within about 10-100 nm) from one direction to the other. The domain walls will be discussed in more details in later sections. The magnetizations in different domains have different orientations so that over the whole sample the vector sum of the net magnetic moment may vanish. Figure 1.3 shows an image of the magnetic domains at the surface of a body-centered cubic (BCC) 3%

SiFe crystal. (The image was taken with a scanning electron microscope). In that figure the (100) directions of the crystal are parallel to the figure edges. It is not a coincidence that M inside the domains is parallel to these crystallographic directions. The coupling of the direction of M to the crystal axes is called magnetocrystalline anisotropy. Note also that domains often form so as to create closed flux loops. This minimizes magnetostatic energy.

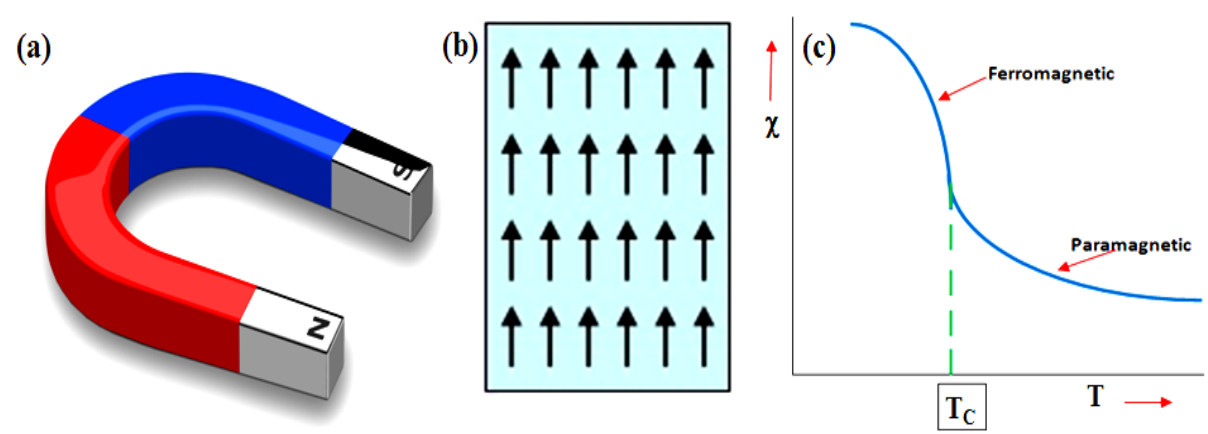


Figure 1.1: (a) Ferromagnetic horse-shoe magnetic, (b) Two-dimensional arrangement of magnetic moments in ferromagnetic ordering and (c) behaviour of magnetic susceptibility (M/H) as a function of temperature [101].

In an ideal magnet, it does not matter much where the domain wall lies. If the potential energy of a domain wall were independent of its position, it would only take a relatively weak field to move the wall, much as it is relatively easy to move a ripple in a carpet. In some soft magnetic materials, domain walls can be moved with fields of order 0.1 A/m. However, defects such as grain boundaries and precipitates cause the wall energy to depend on position, so in most materials, higher fields are required to move domain walls. It is now possible to understand, at least qualitatively, the B-H loops of ferromagnets and connect them with domain wall motion and other magnetization processes. But before describing the B-H loop of a ferromagnet, the classification of strongly magnetic materials needs to be completed [2].

1.1.3 Antiferromagnetism

In some magnetically ordered materials (i.e., materials with atomic magnetic moments having long-range correlation in their orientations) the atomic moments couple in antiparallel arrangements with zero net moment, rather than parallel as in a ferromagnet. Such materials are called *antiferromagnets*.

When no external field is applied, the antiferromagnetic structure corresponds to a very small or nearly zero value of total magnetization. In an external magnetic field, a kind of ferrimagnetic behavior may be observed in the antiferromagnetic phase, due to the absolute value of one of the sublattice magnetizations differing from that of the other sublattice, resulting in a net nonzero value of net magnetization. Ideally the net magnetization should be zero at absolute zero, the effect of spin canting in some cases often causes a small net magnetization to develop, as seen for example in hematite.

The magnetic susceptibility of an antiferromagnetic material is characterized by a maximum at the Néel temperature. In contrast, the susceptibility will diverge at the transition between the ferromagnetic to the paramagnetic phases. In the antiferromagnetic case, a divergence is seen in the staggered susceptibility.

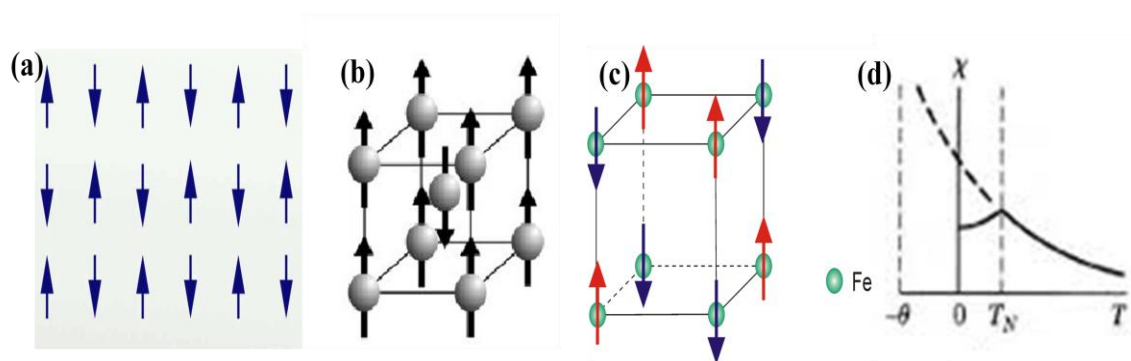


Figure 1.2: (a) Anti-ferromagnetic ordering, (b) Cr atoms in BCC lattice, (c) Fe atoms in SC lattice and (d) magnetic susceptibility of anti-ferromagnetic with temperature [41, 102].

Various microscopic (exchange) interactions between the magnetic moments or atomic spins give rise to antiferromagnetic structures. In the simplest picture, one can consider an Ising model on a binary lattice, e.g. the simple cubic lattice, with interactions between spins at nearest neighbour sites. Depending on the sign of that coupling, ferromagnetic or antiferromagnetic order will prevail. Geometrical frustration or competing ferro- and antiferromagnetic interactions can lead to different and, perhaps, more complicated magnetic structures [1-5].

Antiferromagnetic materials occur more among transition metal compounds, especially oxides. Examples of antiferromagnetic materials include hematite, metals such as chromium, alloys like iron manganese (FeMn), and oxides such as nickel oxide (NiO). There are also numerous examples among high nuclearity metal clusters. Organic molecules can also exhibit antiferromagnetic coupling under rare circumstances, as seen in radicals such as 5-dehydro-m-xylylene [4, 5].

In a crystalline material, the structure dictates how the anti-parallel spins are arranged. Many transition metal monoxides assume the rocksalt structure and are antiferromagnetic with alternate (111) planes oppositely magnetized.

Chromium has the BCC structure with the body-center atoms having one direction of spin (parallel to $\langle 100 \rangle$) and the corner atoms having the opposite direction. (Actually, the period of the magnetic fluctuation is incommensurate with the crystal lattice by about 5%) (see Fig. 1.2b).

Antiferromagnets can couple to ferromagnets, for instance, through a mechanism known as exchange bias, in which the ferromagnetic film is either grown upon the antiferromagnet or annealed in an aligning magnetic field, causing the surface atoms of the ferromagnet to align with the surface atoms of the antiferromagnet. This provides the ability

to "pin" the orientation of a ferromagnetic film, which provides one of the main uses in so-called spin valves, which are the basis of magnetic sensors including modern hard drive read heads. The temperature at or above which an antiferromagnetic layer loses its ability to "pin" the magnetization direction of an adjacent ferromagnetic layer is called the blocking temperature of that layer and is usually lower than the Néel temperature [36].

Magnetic frustrations

Unlike ferromagnetism, anti-ferromagnetic interactions can lead to multiple optimal states (ground states- states of minimal energy). In one dimension, the anti-ferromagnetic ground state is an alternating series of spins: up, down, up, down, etc. Yet in two dimensions, multiple ground states can occur.

Let us consider an equilateral triangle with three spins, one on each vertex. If each spin can take on only two values (up or down), there are $2^3 = 8$ possible states of the system, six of which are ground states. The two situations which are not ground states are when all three spins are up or are all down. In any of the other six states, there will be two favorable interactions and one unfavorable interaction. This illustrates frustration: the inability of the system to find a single ground state. This type of magnetic behavior has been found in minerals that have a crystal stacking structure such as a Kagome lattice or hexagonal lattice [13].

Antiferromagnets have limited technical application because their net magnetization is zero; they produce no external field and the direction of the atomic moments is not easily affected by an external field. Antiferromagnetism plays a crucial role in giant magnetoresistance, as had been discovered in 1988 by the Nobel prize winners Albert Fert and Peter Grünberg (awarded in 2007) using synthetic antiferromagnets.

1.1.4 Ferrimagnetism

When the two antiferromagnetically coupled sublattices in a material have unequal opposite moments - usually happens when two different species are found on the different sites making the net moment non- zero. Such materials are known as ferrimagnets and are characterized by consecutive atoms with opposing magnetic moments but the opposing moments are unequal in magnitude thereby resulting in a net spontaneous magnetization. This happens when the populations are exhibited by the presence of different materials or ions (such as Fe^{2+} and Fe^{3+}).

Ferrimagnetism is generally found in ferrites and magnetic garnets with the oldest known example being magnetite, Fe_3O_4 . There the Fe ions of different valence appear at sites of different coordination, originally it was classified as a ferromagnet before Néel's discovery of antiferromagnetism and ferrimagnetism in 1948 [1-3].

Ferrimagnets are technologically very important because of their good high-frequency properties. Below the Curie temperature they possess a spontaneous magnetization and show absence of any magnetic ordering (as in case of paramagnet) above this temperature. However, at very low temperature below the Curie point when the two opposing moments are almost equal which results in a vanishingly small net magnetic moment; this is called the magnetization compensation point. This compensation point is readily observed in garnets and rare-earth–transition-metal alloys (RE-TM). Additionally, ferrimagnets may also show an angular momentum compensation point, at which the net angular momentum is zero. This compensation point is vital for achieving high speed magnetization reversal in magnetic memory devices [12, 10, 33].

1.2 Low-dimensional Magnetism

In one of a pioneering work, Mermin and Wagner in 1966 showed theoretically, that long-range ferromagnetic or antiferromagnetic ordering ceases to exist in one or two dimension considering isotropic exchange interactions between spins [14]. Later, some other studies also revealed the same for Heisenberg and xy spin systems by including RKKY type of interactions and showing that long-range order decreases as $R^{-\alpha}$, with suitably large exponent ' α ' [15].

But the presence of anisotropy, resulting either from crystalline order or from long-range dipolar interactions, is intrinsic in two- dimensional solids and thus plays a leading role in determining the long-range magnetic order in real 2D systems [16-19]. In this section and further, the domain theory along with the theory of two-dimensional solids will be discussed in a greater detail.

1.2.1 Magnetic Domains

A magnetic domain corresponds to a region inside a magnetic material whereby the magnetization is along a uniform direction. When a piece of ferromagnetic material is cooled below a certain temperature called the Curie temperature, the magnetization spontaneously divides into multiple small regions called magnetic domains. Although the magnetization within each of these domains points in a uniform direction, but the magnetization of different domains may orient in different directions. Structure of the magnetic domains are responsible for the magnetic behavior of different ferromagnetic materials like iron, cobalt, nickel and their alloys, and ferrimagnetic materials like ferrite [34]. This also includes the development of permanent magnets and the behaviour (attraction) of ferromagnetic materials in response

to an external magnetic field. The regions separating these magnetic domains are known as domain walls, in which the magnetization self rotates coherently from the particular orientation in one domain to that same direction in the next domain. The study of the behaviour of magnetic domains in the sub-micrometer regime is called micromagnetics [28, 30, 31, 32].

Magnetic domains appear in materials due to the magnetic ordering. This results in the spontaneous alignment of the dipoles due to the exchange interaction. These are the observed in ferromagnetic, ferrimagnetic and antiferromagnetic materials. In paramagnetic and diamagnetic materials the dipoles starts' aligning in response to an external applied magnetic field but the alignment is lost once the field is removed; hence do not have magnetic domains.

Once domains starts forming, the orientation of the magnetic moments within each domain and the size of each domains are determined by interactions due to magnetostatic, magnetoelastic, crystal anisotropy and domain wall energy. Formation of all domain structure in a magnetic material involves minimization of the appropriately selected energies. Figure 1.3 shows the process of subdivision of a uniformly saturated sample (a), having high magnetostatic energy, into one composed of increasingly more number of domains. The changes in energy for each case are depicted in the Fig. 1.3. First, the large magnetostatic energy arising due to the end poles in the case shown at left is reduced as a result of the formation of two domains of opposite magnetization. The integral of H_z in the region outside the sample decreases in the second panel because the field lines now close at the ends of the neighbouring domains; the flux lines takes the path of low reluctance R , and thereby low energy. This process goes on from figure 1.3b (1) to (3) with the increase in the number of domains proceeding and ultimately this process ends when the energy cost of adding another

180° domain wall is greater than the magnetostatic energy saved. There is always some magnetostatic energy cost for 180° wall formation in such a finite sample. If the material has cubic anisotropy, or if the uniaxial anisotropy is not too strong, the sample may form closure domains at its end surfaces. These closure domains allow the flux to be fully contained within the sample, thus completely eliminating the magnetostatic energy contribution. However, there is a cost to formation of these closure domains in terms of magnetic anisotropy energy (for a uniaxial material) and in terms of elastic energy if the magnetostriction is not zero. In this section, analytic estimates of these energies will be required for samples of various geometries. Here the demagnetizing field will be approximated in many cases, so the estimates of the energies are useful only to the extent that the sample geometry meets the assumptions of the approximate demagnetizing factors. In ellipsoidal samples the demagnetizing field approximations fail near charged surfaces [29-33].

Magnetic domain theory was first developed by French physicist Pierre-Ernest Weiss [38] who, in 1906, suggested the existence of magnetic domains in ferromagnets [5]. He suggested that large number of atomic magnetic moments were aligned in the same direction. The direction of alignment varies from domain to domain in a more or less random manner, although certain crystallographic axis may be preferred by the magnetic moments, called easy axes. Weiss still had to explain the reason for the spontaneous alignment of atomic moments within a ferromagnetic material, and he came up with the so-called Weiss mean field. He assumed that a given magnetic moment in a material experiences a very high effective magnetic field due to the magnetization of its neighbours. In the original Weiss theory the mean field was proportional to the bulk magnetization M , so that

$$H_e = \alpha M \tag{1.3}$$

where α is the mean field constant. However this is not applicable to ferromagnets due to the variation of magnetization from domain to domain. In this case, the interaction field is

$$H_e = \alpha M_s \tag{1.4}$$

Where M_s is the saturation magnetization at 0K.

Later, the quantum theory made it possible to understand the microscopic origin of the Weiss field. The exchange interaction between localized spins favours a parallel (in ferromagnets) or an anti-parallel (in anti-ferromagnets) state of neighbouring magnetic moments [3, 4, 5, 34, 35].

Magnetic materials such as iron spontaneously split into separate domains to minimize the free energy, rather than existing in one homogeneous phase.

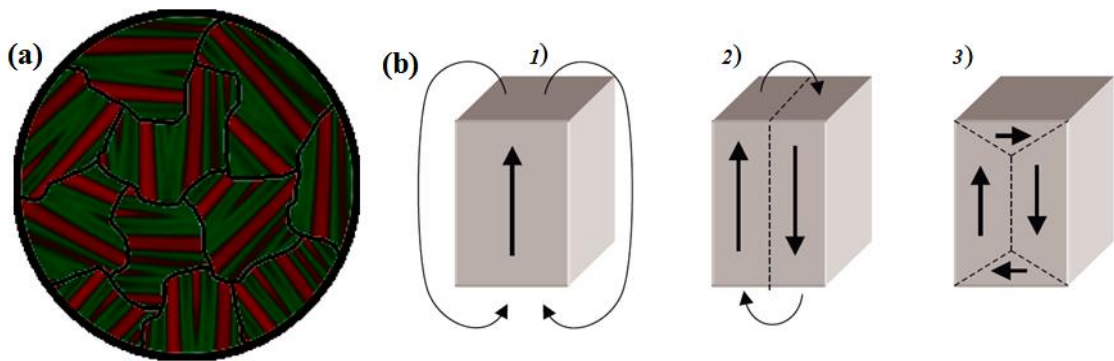


Figure 1.3: (a) Micrograph of a ferromagnetic surface, showing the crystal grains, each divided into several domains, with the magnetization in alternating directions (shown by red and green regions), (b) a ferromagnetic material divides into several small domains [103].

To reduce the field energy further, each of these domains can split also, resulting in smaller parallel domains with magnetization in alternating directions, with smaller amounts of field outside the material (see Fig. 1.3(b), right).

The domain structure of actual magnetic materials does not generally form by the process of large domains dividing into smaller ones as described previously. When a sample is cooled below the Curie temperature, for example, the equilibrium domain configuration simply appears. But domains can split, and the description of domains splitting is frequently used to reveal the energy tradeoffs in domain formation.

As explained above, a domain which is too big is unstable, and will divide into smaller domains. But a small enough domain will be stable and will not split, and this describes the size of the domains created in a material. This size depends on the balance of several energies inside the material [11]. Each time a region of magnetization splits into two or more domains, it creates a domain wall between the domains, where magnetic dipoles (molecules) with magnetization pointing in different directions are adjacent. The exchange interaction which creates the magnetization is a force which tends to align nearby dipoles so that they point in the same direction. Forcing adjacent dipoles to orient in different directions requires energy. Therefore, a domain wall requires additional energy, called the domain wall energy, which is proportional to the area of the domain wall.

Thus the net amount of energy that is reduced when a domain splits is equal to the difference between the magnetic field energy saved, and the additional energy required to create the domain wall. The field energy is proportional to the cube of the domain size, while the domain wall energy is proportional to the square of the domain size. As the size of the domains gets smaller, the net energy saved by splitting decreases. The domains keep dividing into smaller domains until the energy cost of creating an additional domain wall is just equal to the field energy saved. Then the domains of this size are most stable. In most materials the domains are microscopic in size, around 10^{-4} - 10^{-6} m. The different types of observation techniques used to study magnetic domain structure are [35, 36, 38].

1) Real Space Imaging (See Fig. 1.4)

(a) Magneto-optic Kerr effect (MOKE), (b) Lorentz force microscopy (LTEM) and (c) Magnetic force microscopy (MFM).

2) Reciprocal Space Observations

(a) Small angle neutron scattering (SANS) and (b) Resonant soft X-ray scattering (RSXS).

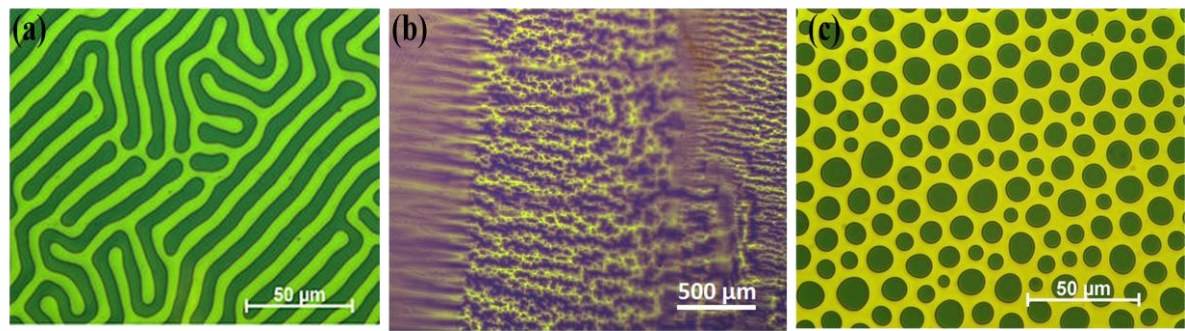


Figure 1.4: Different types of magnetic domain structure (a) labyrinth or stripe domain, (b) shape memory alloy domain structure and (c) magnetic bubble domains [103].

1.2.2 Domain Walls

In magnetism, a domain wall is an interface separating the magnetic domains. It is a transition between different magnetic moments and usually undergoes an angular displacement of 90° or 180°. A domain wall is a gradual reorientation of the material’s individual moments across a finite distance (See Fig.1.5 (a)). The domain wall thickness depends on the anisotropy of the material, but on average spans across around 100–150 atoms [33, 36, 41].

The energy of a domain wall is simply the difference in the magnetic moments before and after the creation of domain wall. This value is usually expressed as energy per unit wall area.

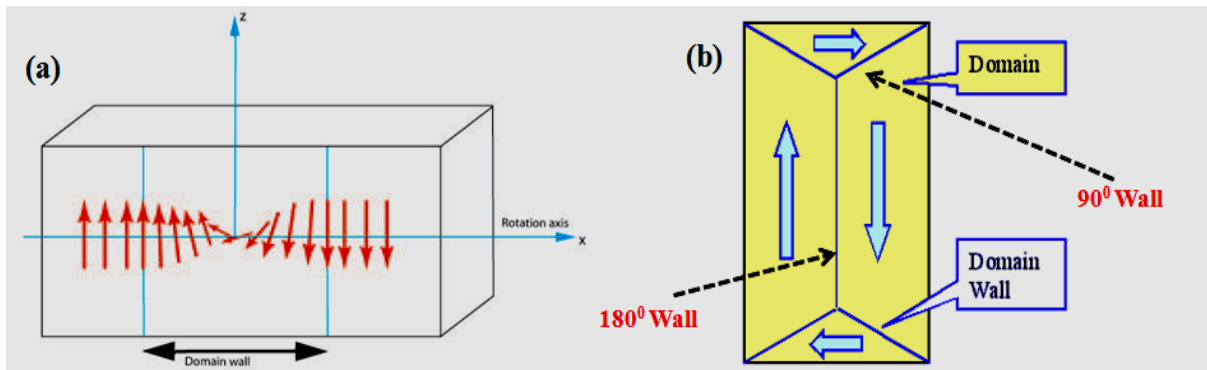


Figure 1.5: (a) Schematic of the magnetic moments within a domain wall and (b) different types of wall formations [104].

The width of the domain wall depends on the two opposing energies that create it: the magnetocrystalline anisotropy energy and the exchange energy (J_{ex}), both of which tend to be as minimum as possible so as to be in a more favourable energetic state. The anisotropy energy is least when the individual magnetic moments are aligned along the crystal lattice axes thus reducing the width of the domain wall. Also, the exchange energy is reduced when the magnetic moments are aligned parallel to each other and therefore makes the wall thicker, due to the repulsion between them (whereby anti-parallel alignment would bring them closer, tends to reduce the wall thickness). In the end equilibrium is restored between the two and the domain wall's width is set as such [36, 37].

An ideal domain wall would be fully independent of position, but the domain structures are not ideal and so get stuck on inclusion sites inside the medium, also known as crystallographic defects. These consist of missing or different (foreign) atoms, oxides, insulators and even stresses within the crystal. This prevents the formation of domain walls and also hinders their propagation through the medium. Thus a greater applied magnetic field is required to overcome these sites.

Non-magnetic inclusions in the volume of a ferromagnetic material, or dislocations in crystallographic structure, can result in "pinning" of the domain walls. Such pinning sites

cause the domain wall to stay in a local energy minimum and an external field is required to "unpin" the domain wall from its pinned position. The act of unpinning will cause sudden drastic movement of the domain wall and abrupt change of the volume of both neighbouring domains; this is known as Barkhausen effect.

It is therefore energetically much more favourable to align the magnetic moments gradually over a region at the interface: the domain wall. There exist two kinds of domain walls as shown in Fig. 1.6 that differ in the direction of canting. The more common one is the Bloch wall, but in thinner films a Neel wall is often preferred.

Bloch Wall

A Bloch wall is a slender transition region at the boundary between magnetic domains, within which the magnetization changes from its value in one domain to that in the next, named after the Swiss-American physicist Felix Bloch. The magnetization rotates out of the plane of the domain wall, in contrast to Néel walls. Figure 1.6 below shows an example of a Bloch and Néel wall.

Bloch domain walls are commonly observed in bulk materials, i.e. when sizes of magnetic material are significantly larger than domain wall width [39]. In this case energy of the demagnetization field does not impact the micromagnetic configuration of the wall. Mixed cases are possible as well when demagnetization field changes the magnetization direction in domains but not the domain walls [40].

Neel wall

A Neel wall is a narrow transition section between magnetic domains, named after the French physicist Louis Neel. In the Neel wall, the magnetization rotates smoothly from the direction of magnetization within the first domain to the direction of magnetization within the

next. In contrast to Bloch walls, the magnetization changes in plane of the domain wall. It consists of a core with fast varying rotation and two tails where the rotation logarithmically decays. Néel walls are the common type of magnetic domain wall in very thin films where the exchange length is very large compared to the thickness. Néel walls tend to spread across the whole volume if not for magnetic anisotropy [37, 41].

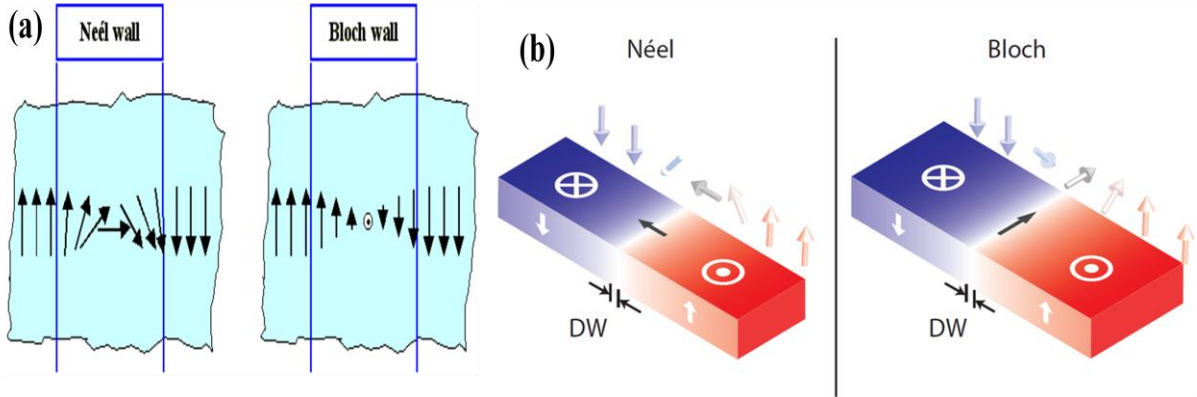


Figure 1.6: Neel and Bloch type of domain walls (a) front view and (b) 3D view [104].

1.3 Magnetocrystalline anisotropy

Magnetic anisotropy represents the preference of an object's magnetic properties to be different depending on direction. In the simplest situation, there is usually no preferential direction to the object's magnetic moment. It will respond to an applied magnetic field in the same way, irrespective of which direction the external field is applied. This is known as magnetic isotropy. In contrast, it will be easier or harder for a magnetically anisotropic material to magnetize it in any particular direction. For most magnetically anisotropic materials, there exist two easy directions of magnetization, which are a 180° rotation apart. The line parallel to these directions is described as the easy axis. In other words, the easy axis corresponds to the energetically favourable direction of spontaneous magnetization. Since the two opposite directions along an easy axis are usually equivalent, hence easy to magnetize

along, and the actual direction of magnetization can just as easily orient into any one of the two directions, which also corresponds to an example of spontaneous symmetry breaking [8-10, 21, 22, 36].

When the physical property of a system is dependent on the direction, that property is said to exhibit anisotropy. As mentioned already the preference for the magnetic moments within a material to align in a particular direction is called magnetic anisotropy. Parameter describing the magnetization process could be the permeability or the susceptibility. Magnetic anisotropy can originate due to the sample shape, stress, crystal symmetry, or directed atomic pair ordering [8, 10, 23].

The spin-orbit coupling is the main source of magnetocrystalline anisotropy. Basically the orbital motion of the electrons interacts with crystal electric field giving rise to the first order contribution to magnetocrystalline anisotropy. The second order contribution arises due to the mutual interaction of the magnetic dipoles [10, 24, 25, 36].

For example, in Fe having BCC crystal structure, the magnetization process is generally easy along the $\langle 100 \rangle$ directions and hard in the $\langle 111 \rangle$ directions; this is because, the field needed to magnetize iron to saturation is much easier in the $\langle 100 \rangle$ directions than along any others directions. Whereas, in FCC Ni, the case is just the opposite with $\langle 111 \rangle$ being the easy direction, $\langle 100 \rangle$ hard, and the strength of the applied magnetic field required for saturation along the hard directions is smaller for Ni than for Fe. Cobalt is hexagonal lattice, with the easy direction of magnetization being the c axis; saturating the sample along the basal plane is very difficult and requires more than an order of magnitude harder than in the $\langle 111 \rangle$ directions in Fe [22, 26].

After attaining the saturation value, reduction of the field to zero leaves more of the magnetization remaining in the direction parallel to which the field had been applied if it

happens to be the easy axis as opposed to the hard direction. In the absence of an external applied magnetic field, the magnetization prefers to align along the easy directions. It should be noted that the value of the magnetization remaining at zero field ($H = 0$), is called the remanence which is non-zero for Ni and Fe when they are magnetized along the hard directions whereas it is zero in case of Co when magnetized in the hard direction. A quantifiable measure of the strength of the magnetocrystalline (or any other) anisotropy is the field, H_a , required to saturate the magnetization along the hard direction. This field is called the anisotropy field [27, 36].

1.3.1 Magneto-crystalline anisotropic interaction

Magneto-crystalline anisotropy originates from the spin-orbit interactions [44, 45, 46]. The electron orbits are linked to the crystalline structure and their interaction with the spins which makes the spins to align in preferred well-defined crystallographic axes. In this direction, it is easier to magnetize for a crystal than in the other directions, and is called the easy-axis for magnetization of the crystal. Like the dipolar interactions, the magneto-crystalline anisotropy is also weak compared to the exchange interactions but the direction of the magnetization is determined only by this anisotropy, as exchange is isotropic in space.

Exchange interactions always try to align the spins parallel to each other and the anisotropy tries to align them along a crystallographic axis. Anisotropy of a crystal will be a function of the angle θ with respect to the normal to the layer (z-axis) and ϕ , the angle with respect to the x-axis within the layer. For a simplification, if we now assume the anisotropic term of the Hamiltonian depends on either θ or ϕ , then the anisotropic energy term can be expanded in the series [44, 45, 46],

$$H_K = \sum_m K_m \cos m\theta \quad (1.5)$$

It is known from the experimental observations that the anisotropic contributions are of even order. Then, if $K_2 < 0$, the out-of-plane anisotropy favours a magnetization direction perpendicular to the xy-plane. Without an external field, the spontaneous magnetization will orient the spins along the perpendicular direction which is the case for Fe/Gd thin films heterostructure discussed in chapter 3 and 4.

1.3.2 Long-range magnetic order in presence of dipolar interaction

Theoretical calculations for determining ferromagnetic ordering is not taken into account while considering dipolar interaction since it is comparatively weak than the exchange interactions. The long-range nature of the dipolar interactions plays a crucial role in two-dimensional systems for stabilizing long-range magnetic order. Such two-dimensional systems are characterized by a uniaxial anisotropy favoring an easy-magnetization axis [18]. The competition between the different on-site, short-range and long-range interactions results in the rich variety of novel magnetic properties within these systems.

The contribution of the dipolar interactions to the system Hamiltonian is -

$$H_D = \frac{1}{2} (g\mu_B)^2 \sum_{i,j}' \left(\frac{\mathbf{S}_i \cdot \mathbf{S}_j}{r_{ij}^3} - 3 \frac{(\mathbf{S}_i \cdot \mathbf{r}_i)(\mathbf{S}_j \cdot \mathbf{r}_j)}{r_{ij}^5} \right) \quad (1.6)$$

$$= \frac{1}{2} C \sum_{i,j}' (\mathbf{S}_i \cdot \mathbf{S}_j - 3((\mathbf{S}_i \cdot \hat{\mathbf{r}}_i)(\mathbf{S}_j \cdot \hat{\mathbf{r}}_j))) \quad (1.7)$$

where $C = (2\mu_B)^2/a^3$ and the sum is over all the possible pairs of sites on the lattice and $\mathbf{r}_{ij} = (a\hat{\mathbf{r}}_{ij})$ is the joining vector between sites i and j. An estimate of the relative strength of the dipolar to the exchange energy can be obtained by comparing a typical dipolar energy E_D

$= 4\pi\alpha\mu_B M_0$ [55, 56], where $M_0 (= 2\mu_B S/a^3 = CS/\mu_B)$ is the saturation magnetization and ' α ' is spin-wave stiffness constant reflects the discreteness of the lattice. For a Gd hcp lattice having spin 7/2, the value of E_D/k_B will come out to be 1.66 K. The exchange energy J for a monolayer is not known, either experimentally or theoretically. However, we can approximately calculate the exchange from Rushbrooke-Wood mnemonic formula which gives a fairly good approximation for the transition temperature of a three-dimensional Heisenberg ferromagnet [57]

$$\frac{K_B T_C}{J} = \frac{5}{96} (z - 1) [11S(S + 1) - 1] \quad (1.8)$$

where z is the number of nearest neighbours. For example, bulk Gd has $T_c=292$ K which gives for centered hexagonal bravais lattice $J/k_B \approx 3$ K, a value less than twice that of E_D . Actually the physically meaningful parameter with which to compare E_D is with $4SJ$. Then the ratio $(E_D/(4SJ))$ is 1/25 for Gd hcp lattice, which is not very small whereas this value is 1/600 for spin 1/2 ions with same T_c . So it is clear that the effect of dipolar interactions can be important when S is large.

1.4 Two dimensional spin textures

1.4.1 Stripe formation in 2D systems

As a result of exchange, long-range dipolar and magneto-crystalline anisotropic interactions a variety of spontaneous formation of domain structures have been predicted in 2D systems [48]. Physically, the stability of the stripe domains can be understood as a compromise between the increment in exchange energy due to the formation of domain walls

and the decrease in dipolar energy due to the interaction between magnetization currents generated at the domain walls [49, 50].

For $0 < |\mathbf{K}_{\text{eff}}| < \pi^2 g^2 / (6J)$ in-plane spins cannot stabilize in a homogeneous phase as magneto-crystalline anisotropy becomes large enough to pull some of the spins in the out-of-plane direction and create ripple like instability. It is known that both average magnetization $M(T)$ as well as initial susceptibility $\chi(T)$ is proportional to the physical extent of ordered phase l^* that minimizes the zero-field energy [55] and can be written as

$$M \propto H l^* \quad \text{where } l^* \propto \exp(-\gamma T) \quad (1.9)$$

then

$$M \propto \exp(-\gamma T) \quad (1.10)$$

γ is a parameter depends on the exchange interaction. So then,

$$\chi = \frac{\partial M}{\partial H} \propto l^* \propto \exp(-\gamma T) \quad (1.11)$$

It is likely that at low enough temperature l^* reaches a saturation either because l^* become comparable to sample size or due to the freezing of ripple walls. For systems having large exchange coupling to produce bulk Curie temperatures of several hundred Kelvin, the ground state stripe width is predicted to be much larger than any practical laboratory sample size and thus can show a net ferromagnetic moment at low temperatures [48, 51].

As the temperature is increased, a critical temperature will be reached where the domain width will become comparable to the sample size of the system and for further rise in temperature the net magnetization of the sample goes to zero due to the formation of stripe domain with alternating orientations within the sample. Monte Carlo simulation studies on 2D spin system [49] with strong uniaxial anisotropy shows the transition of the stripe domain

structure to a randomly oriented multiple domain structure through a number of stages. First, at low temperature, the sample will be a single-domain phase in which the system has a net magnetic moment. But as the temperature increases, the system loses the magnetic moment due to the onset of multiple domains in the striped phase and the magnetization decreases exponentially due to exponential increase in number of domains with increasing temperature. As a matter of fact the susceptibility follows the law as in Eq. (1.11). There is also one phenomena, called the reorientation transition, involved in these patterned formed systems which is explained below.

Typically a saturation magnetization in the perpendicular direction has been observed in a number of sufficiently thin films which decays following Eq. (1.11) until a region essentially on an average zero magnetization is reached. As the temperature is increased further, an onset of magnetization in the in-plane direction in a number of systems has been observed [52, 53, 54]. This phenomenon has also been observed with increasing thickness of the films. This phenomenon is known as the reorientation transition of the spin systems.

1.4.2 Topological defects

Topological defects are a class of entity in a system with continuous broken symmetry and are generally characterized by some core region (like point or line) where order is destroyed. Topological defects have wide variety of names depending on the nature of symmetry, like vortices in magnetic systems, superfluid helium or 2D xy-models, dislocations in periodic crystals, and disclinations in nematic liquid crystals. A topological defect plays a crucial role in determining the mechanical properties of bulk systems and particularly a crucial part in the phase transitions of two-dimensional materials.

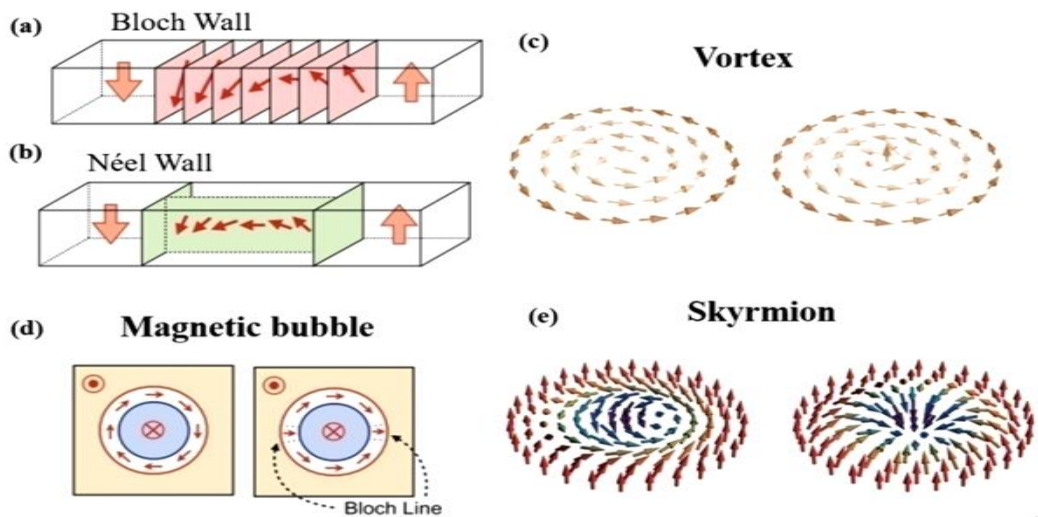


Figure 1.7: Schematic diagram of spin configurations in case of (a) Bloch wall and (b) Néel wall. Topological magnetic domain texture of (c) vortex, (d) magnetic bubble, and (e) skyrmion [59, 60, 61].

1.4.3 Magnetic vortex, skyrmions and merons

Vortices occurs whenever a flow field ‘whirls’ around a one-dimensional core, are among the simplest topological structures, prevalent in many branches of physics. In the crystalline state, vortex formation is very uncommon, due to the presence of long-range interactions: in ferroic materials (ferromagnetic and ferroelectric), vortices are observed mainly when the effects of the dipole–dipole interaction are modified due to confinement at the nanoscale, or when the parameter associated with the vorticity does not couple directly with strain (See Fig.1.7).

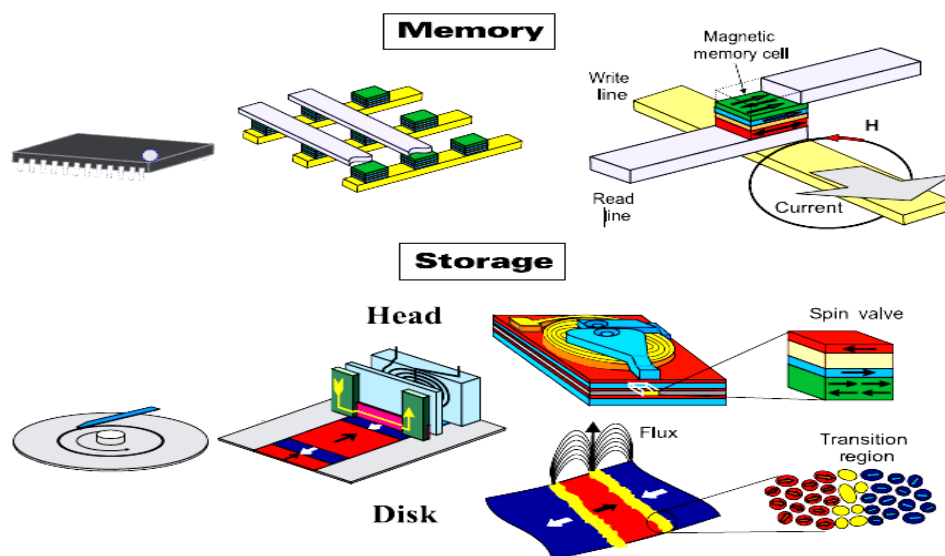


Figure 1.8: Illustration of diverse magnetic structures used for magnetic memory and storage based applications. They form the first generation of spintronics based devices [98].

Magnetic vortex structures have already been reported in rare earth based multilayer films deposited by Langmuir-Blodgett (LB) technique [75]. Langmuir films of monolayer thickness are formed when amphiphilic (surfactants) molecules or nanoparticles are spread on water surface at the air–water interface. Multilayer stacks of amphiphilic fatty-acids attached with ions of rare-earth elements provide excellent 2D systems to study low-dimensional magnetic ordering since the characteristic in-plane separations between metallic ions are an order of magnitude smaller than the out-of-plane layer-spacing given by the hydrophobic tails (See Fig.1.9).

It has been reported that 2D short-range ferromagnetic order with no spontaneous magnetization occur in the gadolinium stearate (Gd-St) LB films when a magnetic field is applied along any in-plane (xy plane) direction, whereas the moments remains paramagnetic if the field is applied along the out-of plane direction (z direction) [74].

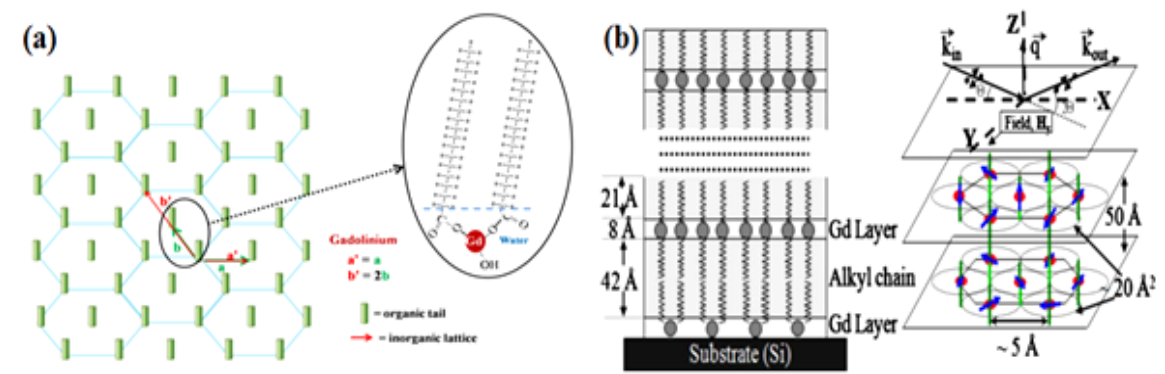


Figure 1.9: (a) Schematic of the organic and metallic lattice of LB monolayers at air-water interface along with the enlarged view of a metal-organic molecule. (b) Schematic out-of plane and in-plane structure of Gd-St multilayer LB film [75].

Further studies in gadolinium based LB films have predicted the existence of hexagonal lattice of spin vortices above a certain BKT transition temperature below which vortex and anti-vortex pairs annihilate to produce a homogenous phase with a saturation moment [75]. The magnetic properties of rare earth elements mainly in lanthanide series are generally determined by the localized 4f orbital and spin moments. The exchange interaction mediated by the hybridized 6s and 5d conduction electrons results in long-range magnetic ordering along with the existence of dipole-dipole long-range interaction among ions of a monolayer [75]. Apart from the ferromagnetic behaviour as observed in such systems, studies in Mn-St LB films have also revealed about the existence of anti-ferromagnetic ordering occurring in these 2D structures [76].

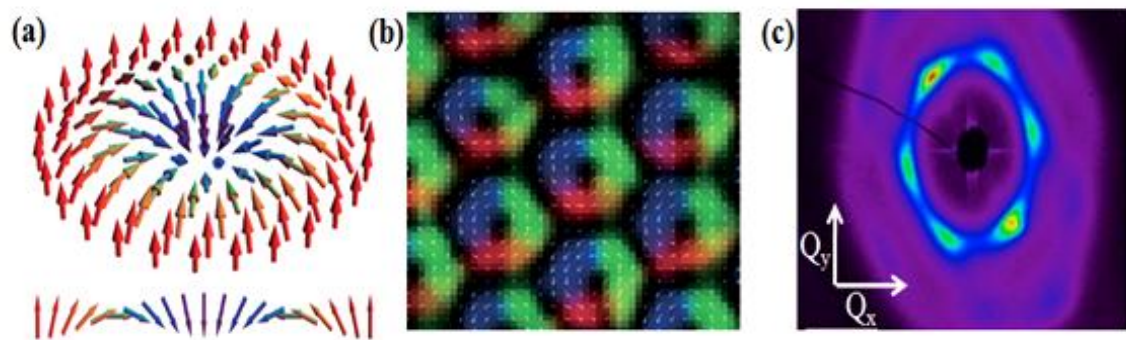


Figure 1.10: (a) Schematic of spin configuration in a skyrmion [105], (b) real space image of skyrmions as observed in LTEM [106] and (c) reciprocal image of skyrmion lattice as observed from resonant X-ray scattering [107].

Recently discovered magnetic skyrmions were first observed in bulk MnSi, FeCoSi and FeGe just a decade back ago [69]. These skyrmions are multi-atom vortex spin textures in which the atoms spin orientations change from one direction in the middle to the opposite direction at the periphery (See Fig.1.10). These structures are topologically protected with a topological number $N \geq 1$ and manifest as hexagonal lattice of spin vortices. Due to the topological stability from defects and pinning sites, skyrmions can be moved with 10^5 times lower current density than conventional magnetic domains thereby making them technologically promising for energy efficient spinotronic applications such as skyrmion based ultra-dense storage, novel memory and logic applications as shown in Fig. 1.8 [70,71] . These structures are formed in very few magnetic materials till date in their bulk or in magnetic thin films. In bulk, skyrmions are generally formed in B20 compounds with non-centrosymmetric crystal structure due to Dzyaloshinskii-Moriya (DM) interaction and exchange interaction. In thin films of FeGe, FeSi and FeGd skyrmions arises as a result of the dipolar interaction and magnetic anisotropy in presence of perpendicularly applied magnetic fields [72, 73].

Skyrmions with topological number, $N = -1$ have been discovered in chiral and polar magnets and at ferromagnetic interfaces, in which the antisymmetric spin exchange interaction arises from relativistic spin-orbit coupling (Dzyaloshinskii-Moriya interaction). In a skyrmion, whole magnetic moments swirl from the south pole at the core to the north pole at the perimeter, encompassing a sphere. The hexagonal skyrmion lattice is thermodynamically stabilized by the hybridization of three helices lying within the plane perpendicular to the magnetic field in chiral-lattice magnets [99].

Merons ($N = -1/2$) and antimerons ($N = +1/2$) are topologically distinct from skyrmions ($N = -1$) and antiskyrmions ($N = +1$); in merons and antimerons, the magnetic moments in the core region point upwards or downwards, and those near the perimeter align

in-plane, producing degrees of freedom for magnetic helicity and polarity (Fig. 1.11a–d). The topological number N of skyrmions and antiskyrmions is determined by the product of the vorticity (the rotation direction of the in-plane component of the magnetic moments) and the direction of the magnetic moment in the core [99,100].

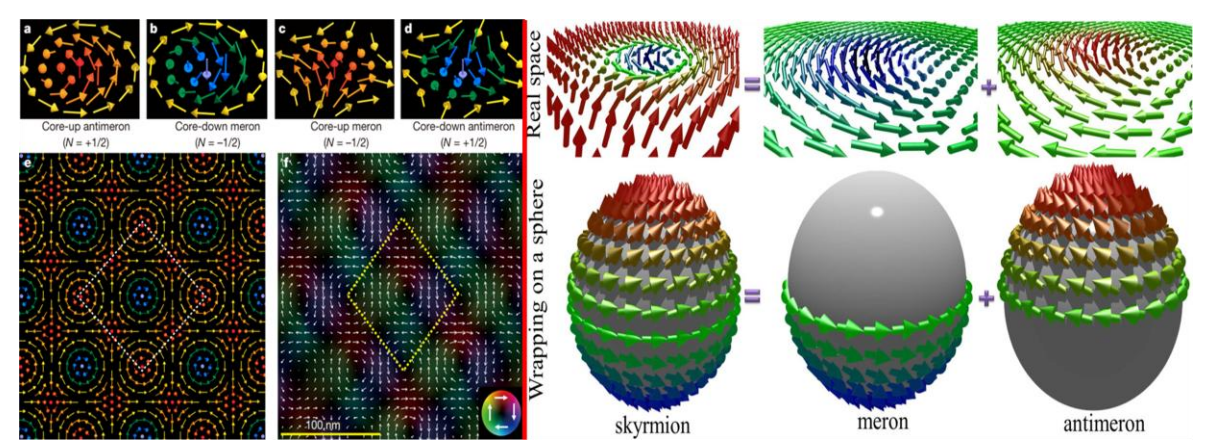


Figure 1.11: LHS image, (a–d), Schematics of the magnetization textures in a core-up antimeron (a) and a core-down meron (b), each having a vorticity of +1, and a core-up meron (c) and a core-down antimeron (d), each with a vorticity of -1 . Coloured arrows indicate directions of the magnetic moments. (e) Theoretically predicted square (anti)meron lattice structure. (f), Real-space magnetization textures of the square (anti)meron lattice, observed through a Lorentz TEM [99]. RHS image, Upper panel: dissociation of a skyrmion lattice into a meron and antimeron pair. Lower panel: a skyrmion covers the sphere, whereas a meron covers only half the sphere [100].

1.5 Recent Developments

During the last decade, much attention has been devoted to artificial layered magnetic materials which have revealed a large variety of fascinating new phenomena. The fundamental developments made such systems also of great interest from a technological point of view in the area of communication devices and storage media [62]. Stimulated by this physics resulting from the layering and reduction of the system size in the vertical direction, a natural extension was the venture into a further reduction of the lateral sizes and quite general into low dimensional systems of nanometer extent [109]. Apart from the simple ferromagnetic, antiferromagnetic and ferrimagnetic domains as observed in bulk magnetic materials complex domains of stripes, labyrinth, vortex, etc with competitive magnetic

interactions in the nanometer regime has been observed in 2D magnetic systems and studied in great detail [63, 64]. Very recently exotic spin structures like bubbles, skyrmions and merons has generated a lot of interest in understanding the underlying interactions giving rise to such novel entity [65, 66]. The control of the magnetic properties at nanometer length scales through a variation of the system dimensions has made these low dimensional magnetic structures interesting not only from a fundamental perspective, but also from a technological point of view. In contrast a variety of tantalizing new possibilities for devices, structured from magnetic low dimensional systems has only been reported in the literature over the last few years. Research and development of new magnetic structures has largely benefited from these potential applications, particularly in energy efficient spinotronic devices [67].

With the advent of high brilliance synchrotron and neutron facilities around the globe, provide further insight into the structure and magnetic ordering in such nanometer sized objects both in real and reciprocal space which has not being realized before [69]. The major part of this thesis work is done by using X-ray scattering techniques in synchrotron facilities. In Fig. 1.12 we have shown a schematic of such a synchrotron storage ring showing the different components required for delivering X-ray photons with the desired specifications to the sample for investigating its various physical properties. In the storage ring the charged particles are bent into a circular path by a magnetic field produced by a bending magnet. Insertion device like Undulators are used for increasing the brightness of synchrotron radiation. It consists a succession of magnets of alternating polarity and is used as being inserted at the straight section between bending magnets. Light produced by a storage ring is introduced to the experimental endstations known as beamlines. There are many common components called “optics” in the beamline for arranging the light, such as “slit” to cut it, “mirror” to focus it and “monochromator” to get only specific wavelength of it.

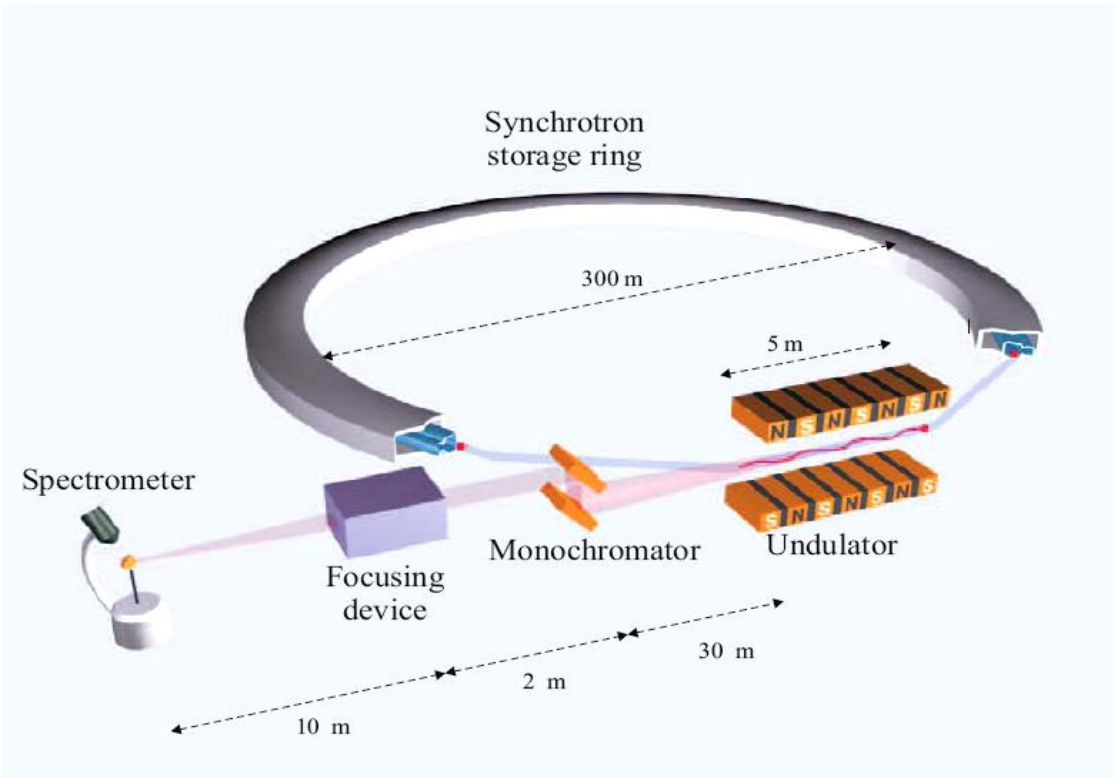


Figure 1.12: A representative of a typical X-ray beamline using a third generation X-ray source. Bunches of charged particles (electrons or positrons) are circulated inside a storage ring (typical diameter around 300 m). The ring is designed with straight sections, where an insertion device, such as undulator, is attached. The lattice of magnets in an insertion device makes the particles to perform small oscillations which produce intense beams of radiation. This radiation then passes through a number of optical elements, such as a monochromator, focusing device, etc., so that a beam of radiation with the requisite properties is delivered to the sample. Typical distances are shown within the figure [108].

A wide diversity of two- and three-dimensional physical-chemical systems exhibit domain patterns in equilibrium. The different phases which give rise to a particular variety of domain patterns are stabilized by competing interactions and are described by periodic spatial variations of the relevant order parameter. The corresponding modulation period in general displays a dependence on temperature and applied fields. The prevalence of a small number of morphological features leads to patterns of remarkably similar appearance, regardless of the aspects of microscopic structure and interactions. Linear arrays of stripes and hexagonal arrays of bubbles are a universal feature in thin magnetic films, ferrofluids and also in Langmuir films. The modulation period is set by the relative magnitudes of the competing

interactions and can be modulated by varying parameters such as temperature and external magnetic, electric, or other fields. Apart from controlling the period of these condensed phases, the balance between the different competing interactions also determines the stability of the shapes realized by individual, isolated domains [77].

Another area of magnetism known by nanomagnetism, together with the understanding and design of complex multi-component novel magnetic nanostructures, is currently one of the promising frontiers in magnetism. Driven by the motivation of using the exchange bias effect for tuning the device characteristics in giant-magnetoresistance systems, strong efforts to study antiferromagnetic (AFM) films adjacent to ferromagnetic ones are currently being underway. This arrangement has lead to a wide variety of complex magnetic structures, such as, antiferromagnetism, spin-density waves, and frustrated spin-structures which constitutes the magnetic properties at the surfaces of thin films. Surface-sensitive techniques providing both high spatial resolution (< 10 nm) in real space along with a sufficient degree of magnetic sensitivity could give a great deal of insight into these phenomena. Unfortunately at present, such techniques are not routinely available. This makes understanding of domain boundaries or two-dimensional (2D) antiferromagnetism still novel field of research. Eventually the lower limit of a 2D AFM consists of a single magnetic monolayer (ML) of chemically equivalent atoms, where magnetic moments of the adjacent atoms at nearest-neighbor sites have opposite directions, deposited on a nonmagnetic substrate. Nearly a decade ago, Blugel *et al.* [78] predicted the existence of such 2D antiferromagnets, on the basis of first-principles calculations such as V, Cr, and Mn on noble-metal substrates, However, experimental verification still possess a great scientific challenge because the antiferromagnetism is at the atomic scale plus the total magnetization is zero, and the Neel-temperature T_N is unknown. Although there have been a large number of attempts to

verify that antiferromagnetism does exist in these structures and some supporting evidence [79] has been reported till date, unambiguous proof is still required.

Layered van der Waals structures have shown sharp variations of their physical properties as they are thinned down to a single mono-molecular layer. These include: (1) transitions involving indirect to a direct bandgap material, thus opening new opportunities for optoelectronic based applications; (2) variations of multi-body quantum criticalities, such as charge density wave (CDW) or superconducting transitions; and (3) field tunability of many-body systems. The rich variety of physical properties available in two-dimensional (2D) materials and the potential to arbitrarily combine materials of atomically sharp interfaces makes them promising candidate for designing heteromaterials that exhibit novel properties or enabling new device architectures [80-91].

Ferromagnetic materials of monolayer thickness are an important addition to the family of 2D materials. Such materials have great future in spintronics based devices, which makes the use of the spin degree of freedom of electrons rather than their electrical charge. As a result devices rely on nanomaterials of dimensions smaller than the spin relaxation length and controlled interface properties. This potential was realized soon after the discovery of graphene, the first true 2D material, and further attempts have been made to induce magnetism by introduction of ferromagnetic materials, adsorption, defects or doping of 2D materials. However due to low magnetic moments such disordered systems are not suitable for applications. Accordingly, layered materials having intrinsic magnetic ordering have been sought, mainly focusing on materials with dominant ferromagnetic interaction in the bulk. Recent advances in thinning such bulk-ferromagnetic materials to achieve single or bilayer thickness have demonstrated the existence of ferromagnetic order even to the ultrathin limit, despite pioneering work by the Mermin–Wagner theorem that demonstrates that long-range magnetic order cannot exist at finite temperatures in 2D materials [92-97].

1.6 Outline of the Thesis

Different experiments and the consequent theories outlined in the previous sections indicate the development of low dimensional magnetic ordering both from the fundamental and applications point of view. It is also understood that recently considerable amount of attention has been given to layered magnetic Van-der Waals structures especially in anti-ferromagnetic systems. Another fascinating subject that we have discussed consists of topologically protected magnetic state of vortex structures arising due to long range dipole interaction in 2D systems. This topologically protected magnetic structure has attracted tremendous interest due to their applications in energy efficient spintronic devices. In this Ph.D work the morphology and magnetic properties of low dimensional magnetic structures present in magnetic thin films are investigated and a short outline of the different chapters present in context of the scientific investigations are discussed in the subsequent paragraphs.

This thesis work covers two distinct systems, first one is a Fe/Gd multilayer structure grown by DC magnetron sputtering technique and the second one consists of rare earth (Gd, Er and Ho) multilayer thin films grown by Langmuir-Blodgett (LB) method. For this, first in chapter 2 I have given the detailed description of the various experimental tools used in this thesis work to characterize the two different systems with special emphasis given on resonant coherent magnetic X-ray scattering technique.

The behaviour of magnetic domains in stripe and skyrmion phases of a Fe/Gd multilayer film as a function external field and temperature has been discussed in chapter 3. A detailed X-ray scattering investigation for studying domain fluctuations along with the scaling behaviour in both stripe and skyrmion phases has been carried out for the first time which gives insights into the morphology of the different magnetic structures. We

demonstrate the existence of phase boundaries and underlying critical points in the stripe and skyrmion phases. The magnitude and frequency of abrupt domain jumps observed in the stripe phase are dramatically reduced in the skyrmion phase owing to its topological protection. We found that distinct scaling and universality classes are associated with these domain topologies. Our results provide an incisive way to probe and understand phase stability in systems exhibiting complex spin topologies.

To understand the incommensurate-commensurate transitions and its significance in Devil's staircase like systems we have analysed the evolution of the magnetic stripe phase as a function of applied magnetic fields at different temperatures of a Fe/Gd thin film in chapter 4. We observe modulated periodicities in the stripe phase as the field is varied and the staircase structure smears out with temperature in conformation with theoretical predictions. The behaviour of the stripe periodicity shows discrete random behaviour reminiscent to Devil's staircase like features which has been observed in very few systems till date will also be discussed.

To investigate the nature of magnetic interactions present in rare earth multilayer LB films when the magnetic head group of the molecules are changed from gadolinium, erbium to holmium, we have done a detailed study covering both the structural and magnetic properties of the different LB multilayer systems in chapter 5. We show there that 2D magnetic ordering along the in-plane direction of multilayered LB films changes from ferromagnetic to anti-ferromagnetic as the rare-earth magnetic ion is changed from Gadolinium (Gd) to Holmium (Ho) even though both are iso-structural. The results of the magnetization study presented here show that the Ho based LB films exhibit an in-plane anti-ferromagnetic ordering and unlike Gd the saturation moment is found to be almost independent of temperature indicating the possibility of absence of spin vortex structures.

References:

- [1]. Chikazumi, S. *Physics of Magnetism*, Wiley, New York, 1965.
- [2]. Bozorth, R. M. *Ferromagnetic Materials*, Van Nostrand, New York, 1955; IEEE Press, New York, 1993.
- [3]. Chikazumi, S. *Physics of Ferromagnetism*, Oxford Univ. Press, Oxford, 1997.
- [4]. Craik, D. *Magnetism: Principles and Application*, Wiley, New York, 1996.
- [5]. Cullity, B. D. *Introduction to Magnetic Materials*, Addison Wesley, New York, 1973.
- [6]. Jiles, D. C. *Introduction to Magnetism and Magnetic Materials*, Chapman & Hall, London 1991.
- [7]. Mattis, D.C. *Theory of Magnetism*, Harper & Row, New York, 1965.
- [8]. Akulov, N. Z. *Phys.* **100**, 197 (1936).
- [9]. Aschroft, N. W. and Mermin, N. D. *Solid State Physics*, W. B. Saunders, Philadelphia, PA, 1976.
- [10]. Bozorth, R. M. *Ferromagnetic Materials*, IEEE Press, New York, 1993.
- [11]. Feynman, R. P., Leighton, R. and Sands M. *The Feynman Lectures on Physics*, Vol. **2**. Addison-Wesley. pp. Ch. 37, (1963).
- [12]. Spaldin, N. A. *Magnetic materials: fundamentals and applications* (2nd ed.). Cambridge: Cambridge University Press. pp. 113–129, (2010).
- [13]. Néel, L. *Propriétés magnétiques des ferrites; Férrimagnétisme et antiferromagnétisme*, Annales de Physique (Paris) **3**, 137–198 (1948).
- [14]. Mermin, N. D. and Wagner, H. *Phys. Rev. Lett.* **17**, 1133 (1966); **17**, 1307 (1966).
- [15]. Bruno, P. *Phys. Rev. Lett.* **87**, 137203 (2001).
- [16]. De'Bell, K., Maclsaac, A. B. and Whitehead, J. P. *Rev. Mod. Phys.* **72**, 225 (2000).
- [17]. Bruno, P. *Phys. Rev. B* **43**, 6015 (1991).

- [18]. Male'ev, S. V. *Sov. Phys. JETP* **43**, 1240 (1976).
- [19]. Gelfert, A. and Nolting, W. *J. Phys. Condens. Matter* **13**, R505 (2001).
- [20]. Carey, R. and Isaac, E.D. *Magnetic domains and techniques for their observation*, The English University Press Ltd, London, (1966).
- [21]. Goodenough, J. B. *Magnetism and the chemical Bond*, Wiley, New York.
- [22]. Hall, R. C. *J. Appl. Phys.* **30**, 816 (1959).
- [23]. Pauthenet, R., Barnier, Y. and Rimlet, G. *J. Phys. Soc. Jpn.* **17**, Suppl. B-1, 309 (1962).
- [24]. Slonczewski, J. C. *Magnetism*, Vol. **3**, G. Rado and H. Suhl, eds., Academic Press, New York, 1963.
- [25]. Van Vleck, J. H. *Phys. Rev.* **52**, 1178 (1937).
- [26]. Victoria, R. H. and McLaren J. H. *Phys. Rev. B.* **47**, 11583 (1993).
- [27]. Yamada, M., Kato, H., Yamamoto, H. and Nakagawa, Y. *Phys. Rev. B.* **38**, 620 (1988).
- [28]. Aharoni, A. and Jakubovics, J. P. *Phys. Rev. B.* **43**, 1290 (1991).
- [29]. Bloch, F. *Z. Phys.* **74**, 295 (1932).
- [30]. Chapman, J. N. *J. Phys. D., Appl. Phy.* **17**, 623 (1984).
- [31]. Craik, D. J. and Tebble, R. S. *Ferromagnetism and Ferromagnetic Domains* (North Holland, Amsterdam, 1965).
- [32]. Hubert, A. and Schiifer, R. *Magnetic Domains*, Springer-Verlag, Berlin, 1998, p. 294.
- [33]. Kittel, C. *Rev. Mod. Phys.* **21**, 541 (1949); Kittel, C. and Galt, J. K. *Solid State Phys.* **3**, 437 (1956).
- [34]. Oepen, H. P. and Kirschner, J. *Phys. Rev. Lett.* **62**, 819 (1989).
- [35]. Scheinfein, M. R., Unguris, J., Celotta, R. B. and Pierce, D. T. *Phys. Rev. Lett.* **63**, 668 (1989); *Phys. Rev. B* **43**, 3395 (1991).

- [36]. O’Handley, R. C. *Modern Magnetic Materials: Principles and Applications*. Wiley, New York (2000).
- [37]. Chaikin, P. M. and Lubensky, T. C. *Principles of Condensed Matter Physics*, (Cambridge University Press, New Delhi, 1999).
- [38]. Weiss, P. *La variation du ferromagnetisme du temperature*, *Comptes Rendus*, **143**, p.1136-1149, (1906) cited in Cullity, 2008, p.116
- [39]. Lilley, B.A. "LXXI. Energies and widths of domain boundaries in ferromagnetics". The London, Edinburgh, and Dublin Philosophical Magazine and Journal of Science. **41** (319), (2010).
- [40]. D’yachenko, S. A., Kovalenko, V. F., Tanygin, B. N. and Tychko, A. V. *Physics of the Solid State*. **50** (1): 32–42, (2011).
- [41]. Kittel, C. *Introduction to Solid State Physics*, Wiley, 2010.
- [42]. Shang-Keng Ma. *Modern Theory of Critical Phenomena*, (Perseus Books, Massachusetts, 1976).
- [43]. Kosterlitz, J. M. and Thouless, D. J. *J. Phys. C*. **6**, 1181 (1973).
- [44]. Schneider, C. M. and Kirschner, J. *Handbook of surface science* (eds. K. Horn, and M. Scheffler), 511, (Elsevier, Amsterdam, 2000).
- [45]. Elmers H. J. *Intern. J. Mod. Phys. B*. **9**, 3115 (1995).
- [46]. Aharoni, A. *Introduction to the Theory of Ferromagnetism*, (Oxford University Press, New York, 2000).
- [47]. Kashuba, A. and Pokrovsky, V. L. *Phys. Rev. Lett.* **70**, 3155 (1993).
- [48]. Whitehead, J. P. and De’Bell, K. *J. Phys.: Condens. Matter*. **6**, L731 (1994).
- [49]. Booth, I., MacIsaac, A. B., and Whitehead, J. P. and De’Bell, K. *Phys. Rev. Lett.* **75**, 950 (1995).
- [50]. Kwok-On Ng and Vanderbilt, D. *Phys. Rev. B*. **52**, 2177 (1995).
- [51]. Kashuba, A. and Pokrovsky, V. L. *Phys. Rev. Lett.* **70**, 3155 (1993).

- [52]. Elmers, H. J. *Intern. J. Mod. Phys. B.* **9**, 3115 (1995).
- [53]. Arnold, C. S., Johnston, H. L. and Venus, D. *Phys. Rev. B.* **56**, 8169 (1997).
- [54]. Allenspach, R. and Bischof, A. *Phys. Rev. Lett.* **69**, 3385 (1992).
- [55]. De'Bell, K., Maclsaac, A. B. and Whitehead, J. P. *Rev. Mod. Phys.* **72**, 225 (2000).
- [56]. Yafet, Y., Kwo, J. and Gyorgy, E. M. *Phys. Rev. B* **33**, 6519 (1986).
- [57]. Rushbrooke, G. S. and Wood, P. J. *Mol. Phys.* **1**, 257 (1958).
- [59]. Seki, S. and Mochizuki, M. *Skyrmions in Magnetic Materials*, New York Springer (2016).
- [60]. Streubel, R., Han, L., Im, M. Y., Kronast, F., Rößler, U. K., Radu, F., Abrudan, R., Lin, G., Schmidt, O. G., Fischer, P. and Makarov, D. *Sci. Rep.* **5**, 8787 (2015).
- [61]. Kézsmárki, I., Bordács, S., Milde, P., Neuber, E., Eng, L. M., White, J. S., Rønnow, H. M., Dewhurst, C. D., Mochizuki, M., Yanai, K., Nakamura, H., Ehlers, D., Tsurkan, V. and Loidl, A. *Nat. Mater.* **14**, 1116 (2015).
- [62]. Shabbir, B., Nadeem, M., Dai, Z., Fuhrer, M. S., Xue, Q. K., Wang, X. and Bao, Q. *Appl. Phys. Rev.* **5**, 041105 (2018).
- [63]. Huang, B., Clark, G., Navarro-Moratalla, E., Klein, D. R., Cheng, R., Seyler, K. L., Zhong, D., Schmidgall, E., McGuire, M. A., Cobden, D. H., Yao, W., Xiao, D., Jarillo-Herrero P. and Xu, X. *Nature* **546**, 270 (2017);
- [64]. Seul, M. and Andelman. D. *Science*, **267**, 476 (1995)
- [65]. Nagaosa, N., and Tokura. Y., *Nature Nanotechnology*, **8**, 899 (2013).
- [66]. Yu, X. Z., Koshibae, W., Tokunaga, Y., Shibata, K., Taguchi, Y., Nagaosa Y.N. and Tokura, Y. *Nature* **564**, 95 (2018).
- [67]. Fert, A., Reyren, N. and Cros, V. *Nature Review* (2017).
- [68]. Langner, M. C., Roy, S., Mishra, S. K., Lee, J. C. T., Shi, X.W., Hossain, M. A., Chuang, Y.-D., Seki, S., Tokura, Y., Kevan, S. D. and Schoenlein R.W. *Phys. Rev Lett.* **112**, 167202 (2014).

- [69]. Muhlbauer, S., Binz, B., Jonietz, F., Pfleiderer, C., Rosch, A., Neubauer, A., Georgii R. and Boni. P. *Science*. **323**, 915 (2009)
- [70]. Fert, A., Cros V. and Sampaio, J. *Nature Nanotechnology*. **8**,152(2013).
- [71]. Zhang, X.C. Ezawa, M., Zhou. Y. *Scientific Reports*. **5**, 9400 (2014).
- [72]. Bogdanov, A.N. and Rossler, U.K. *Phys. Rev Lett*. **87**, 3 (2001).
- [73]. Iwasaki, J., Mochizuki, M. and Nagaosa, N. *Nature Nanotechnology*. **8**, 742 (2013).
- [74]. Mukhopadhyay, M. K., Sanyal, M. K., Mukadam, M. D., Yusuf, S. M. and Basu, J. K. *Phys. Rev. B*. **68**, 174427 (2003).
- [75]. Gayen, S., Sanyal, M. K., Sarma, A., Wolff, M., Zhernenkov, K. and Zabel. H. *Phys. Rev. B*. **82**, 174429 (2010).
- [76]. Aviram, A. and Pomerantz, M. *Solid State Communications*, **41**, 297 (1982).
- [77]. Seul, M. and Andelman, D. *Science*, **267**, 476 (1995)
- [78]. Blügel, S., Weinert, M. and Dederichs, P. H. *Phys. Rev. Lett*. **60**, 1077 (1988).
- [79]. Krembel, C., Hanf, M. C., Peruchetti, J. C., Bolmont, D. and Gewinner, G. *J. Magn. Mater.* **93**, 529 (1991).
- [80]. Mak, K. F., Lee, C., Hone, J., Shan, J. and Heinz, T. F. *Phys. Rev. Lett*. **105**, 136805 (2010).
- [81]. Splendiani, A., et al. *Nano Lett*. **10**, 1271–1275 (2010).
- [82]. Xi, X. et al. *Nat. Nanotech*. **10**, 765–770 (2015).
- [83]. Kolekar, S., Bonilla, M., Ma, Y., Coy Diaz, H. & Batzill, M. *2D Mater*. **5**, 015006 (2017).
- [84]. Tsen, A. W. et al. *Nat. Phys*. **12**, 208–212 (2016).
- [85]. McCreary, K. M., Swartz, A. G., Han, W., Fabian, J. and Kawakami, R. K. *Phys. Rev. Lett*. **109**, 186604 (2012).
- [86]. van Bruggen, C. F. and Haas, C. *Solid State Commun*. **20**, 251–254 (1976).

- [87]. Bayard, M. and Sienko, M. J. *J. Solid State Chem.* **19**, 325–329 (1976).
- [88]. Xia, F., Wang, H., Xiao, D., Dubey, M. and Ramasubramaniam, A. *Nat. Photon.* **8**, 899–907 (2014).
- [89]. Yu, Y. et al. *Nat. Nanotech.* **10**, 270–276 (2015).
- [90]. Soumyanarayanan, A., Reyren, N., Fert, A. and Panagopoulos, C. *Nature* **539**, 509–517 (2016).
- [91]. Li, L. J. et al. *Nature* **529**, 185–189 (2016).
- [92]. Geim, A. K. and Grigorieva, I. V. *Nature* **499**, 419–425 (2013).
- [93]. Novoselov, K. S., Mishchenko, A., Carvalho, A. and Castro Neto, A. H. *Science* **353**, 9439 (2016).
- [94]. Gonzalez-Herrero, H. et al. *Science* **352**, 437–441 (2016).
- [95]. Nair, R. R. et al. *Nat. Phys.* **8**, 199–202 (2012).
- [96]. Avsar, A. et al. *Nat. Commun.* **5**, 4875 (2014).
- [97]. Sun, Y., Zhou, Z., Wu, X. and Yang, J. *Nano Lett.* **17**, 2771–2777 (2017).
- [98]. Stöhr, J. and Siegmann, H.C. *Magnetism from Fundamentals to Nanoscale Dynamics*. Springer (2006).
- [99]. Yu, X. Z., Koshibae, W., Tokunaga, Y., Shibata, K., Taguchi, Y., Nagaosa, N. and Tokura, Y. *Nature* **564**, 95 (2018).
- [100]. Lin, Shi-Zeng., Saxena, A. and Batista, C. D. *Phys. Rev. B* **91**, 224407 (2015).
- [101]. www.advancedmagnetsource.com, www.electrical4u.com.
- [102]. Bödeker, P., Schreyer, A. and Zabel, H. *Phys. Rev. B* **59**, 9408 (1999).
- [103]. https://en.wikipedia.org/wiki/Magnetic_domain.
- [104]. www.doitpoms.ac.uk/tlplib/ferromagnetic/walls.php, www.tf.uni-kiel.de/matwis/amat/elmat_en/kap_4/backbone

- [105]. Kézsmárki, I., Bordács, S., Milde, P., Neuber, E., Eng, L. M., White, J. S., Rønnow, H. M., Dewhurst, C. D., Mochizuki, M., Yanai, K., Nakamura, H., Ehlers, D., Tsurkan, V. and Loidl, A. *Nature Materials* **14**, 1116 (2015).
- [106]. Yu, X. Z., Onose, Y., Kanazawa, N., Park, J. H. Han, J. H., Matsui, Y., Nagaosa, N. and Tokura, Y. *Nature* **465**, 901 (2010).
- [107]. J.C.T. Lee *et al.* *Appl. Phys. Lett.* **109**, 022402 (2016).
- [108]. Als-Nielsen, J. and McMorrow, D. *Elements of Modern X-ray Physics*, (John Wiley and Sons, New York, 2000).
- [109]. Ziese, M and Thornton, M. J. *Spin Electronics*, Springer (2001).

Experimental Methods

In the last few decades significant improvement in experimental techniques related to structural, electrical and magnetic properties of ultra-thin films along with the development of sophisticated technology for growing ultra-thin films with precision of sub-monolayer level has led to a outstanding development in low-dimensional physics. In this chapter we will discuss about the different experimental techniques, used in the thesis work and their basic working principle related to growth and characterization of magnetic thin films. Firstly we will discuss in the subsequent sections about the characterization techniques used for investigating the magnetic properties and magnetic structure in multilayer magnetic thin films.

2.1 Magnetization measurement

SQUID VSM

SQUID-VSM is a hybrid system that couples together the sensitivity of the SQUID and speed of VSM to measure the magnetic moment. A SQUID magnetometer is one of the most efficient and sensitive method of measuring magnetic properties. In particular, it is the

only method which directly allows one to determine the overall magnetic moment of a sample in terms of its absolute units. The superconducting quantum interference device (SQUID) consists of two superconductors separated by thin insulating layers to form two parallel Josephson junctions.

The main components of the SQUID magnetometer as shown in Fig. 2.1(b) are:

- (a) Superconducting magnet (with programmable bipolar power supply);
- (b) Superconducting detection coil which is coupled inductively to the sample;
- (c) A SQUID connected to the detection coil.
- (d) Console panel with necessary electronics to amplify and display the signal.

Principle: The measure of the flux change through a pick-up coil system associated with a SQUID is based on the flux quantization within a superconducting loop. This signal depends on the magnetic moment produced by a sample which gets magnetized in the magnetic field produced by a superconducting magnet.

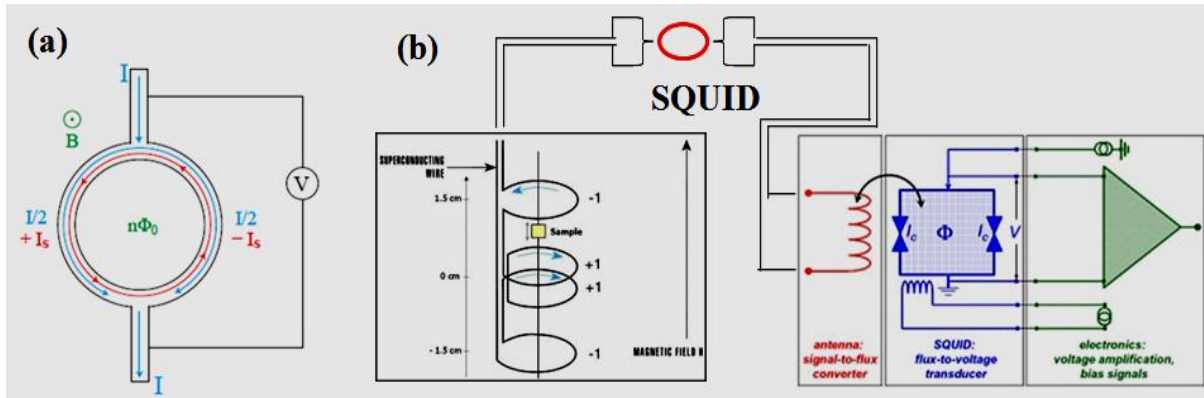


Figure 2.1: (a) Phase difference of the current paths. (b) Schematic of a SQUID [88].

The phase difference of two current paths around a loop in Figure 2.1 is based on the flux through the loop (See Fig.2.1 (a)):

$$\Delta\phi = \frac{q\phi}{\hbar}, \quad (2.1)$$

To avoid scattering of these two paths, the difference must be multiples of 2π , thus limiting the flux allowed within the superconducting loop to multiples of Φ_0 .

$$\phi = \frac{nh}{q} = \frac{nh}{2e} = n\phi_0 = 2.07 \times 10^{-15} \text{ Weber}, \quad (2.2)$$

The magnitude of flux quantum (called also as fluxon) is tiny. Therefore, the sensitivity of the SQUID is very high.

Working method: As the sample is moved up and down it generates an alternating magnetic flux in the pick-up coil. The magnetic signal of the sample is obtained via a superconducting pick-up coil with 4 windings (Fig. 2.1(a)). This coil is, together with a SQUID antenna (red in Fig. 2.1(b)), part of a whole superconducting circuit transferring the magnetic flux from the sample to an rf SQUID device which is located away from the sample in the liquid helium bath. This device acts as a magnetic flux-to-voltage converter (blue in Fig. 2.1(b)). This voltage is then amplified and read out by the magnetometer's electronics (green in Fig. 2.1(b)).

VSM: This method is governed by the Faraday's law of electromagnetic induction [163] which states that the e.m.f. induced in a circuit is equal to the rate of change of magnetic flux linking the circuit having cross-sectional area A and N number of turns, i.e.,

$$V = -N A \frac{dB}{dt} \quad (2.3)$$

where B is the magnetic induction in the coil. Now if the coil vibrates, then the e.m.f. generated can be obtained by integrating above equation over a time period –

$$\int V dt = -NA \int dB = NA\mu_0 M \quad (2.4)$$

This principle of magnetic flux measurement is utilized in Vibrating Sample Magnetometer (VSM).

2.2 Scattering techniques for Magnetic structures

An important aspect of any magnetic system is to understand its morphology from both structural and magnetic point of view. Low dimensional magnetic structures can be studied through different scattering techniques by employing X-ray photons, neutrons or electrons. Here in this section we will mainly discuss about resonant X-ray scattering technique while a brief overview of the polarized neutron reflectivity (PNR) and Lorentz TEM will be presented at the end.

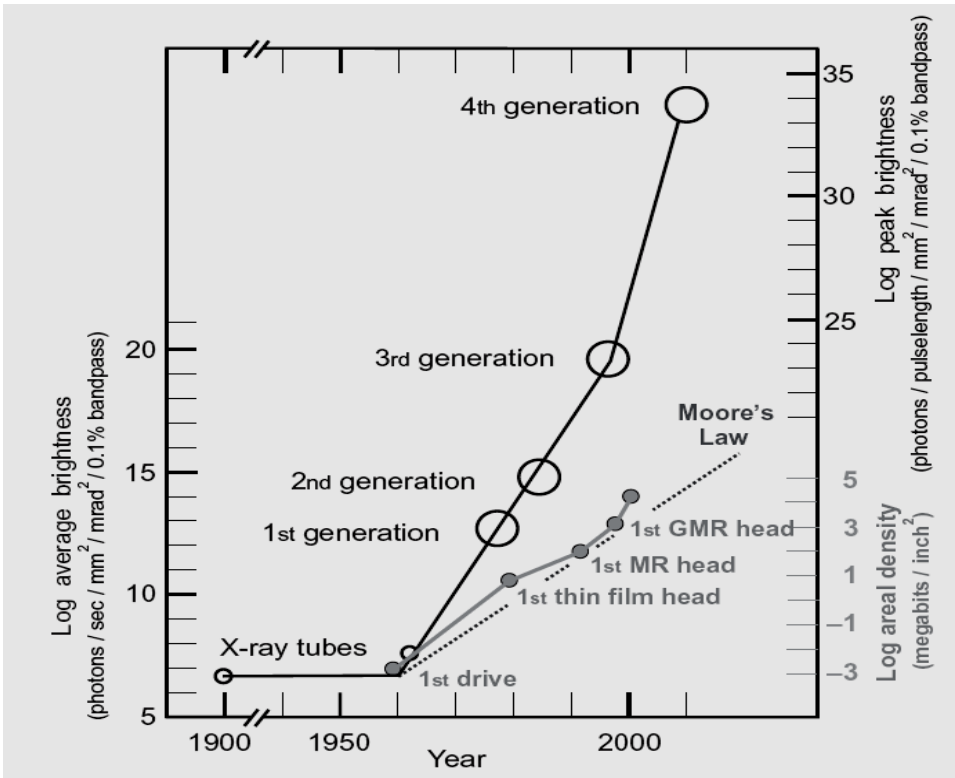


Figure 2.2: Graph showing the enhancement of the brightness of X-ray sources with time (*black*) in comparison to the development of the areal magnetic storage density in computers (*gray*). Moore’s law, representing the doubling of the transistor density on an electronic chip every two years, is shown by the dotted curve. The brightness of X-ray is plotted as an average brightness on the left and has been aligned to the right scale of peak X-ray brightness at the point indicating 3rd generation synchrotron radiation sources [66].

Resonant X-ray Scattering

It is well known that although charge scattering remains the most dominant mechanism, the electric and magnetic field of the X-ray also interact with the magnetic moment of electron giving rise to magnetic scattering. The magnetic scattering cross section was calculated for the first time by Gell-Mann and Goldberger [15]. Later Platzman and Tzoar calculated the dependence of scattering cross section on the scattering vector and predicted the possibility to observe magnetic structures by using X-rays [16]. Ultimately in the year of 1972, magnetic X-ray scattering was for the first time experimentally observed by de Bergevin and Brunel in AFM NiO [17]. In comparison to charge scattering cross section, the magnetic scattering cross section is reduced by a factor of $(h\nu/m_0c^2)^2$ for a single electron. For typical X-ray energies of 10 keV this factor is of the order of 10^{-4} . Scattering from atoms further reduces the magnetic-scattering cross section because only unpaired electrons take part in the magnetic-scattering process. Taking all these factors into account, the magnetic scattering intensity is typically 5 to 6 orders of magnitude less than the charge scattering intensity. Despite this serious drawback, magnetic X-ray scattering has made a rapid progress within the last few decades with the routine availability of high brilliance synchrotron radiation sources (See Fig.2.2). Tunability of the photon energy of synchrotron radiation has given rise to new technique of resonant (magnetic) X-ray scattering (see Fig. 2.3), which makes use of the large enhancement of the scattering cross section near absorption thresholds.

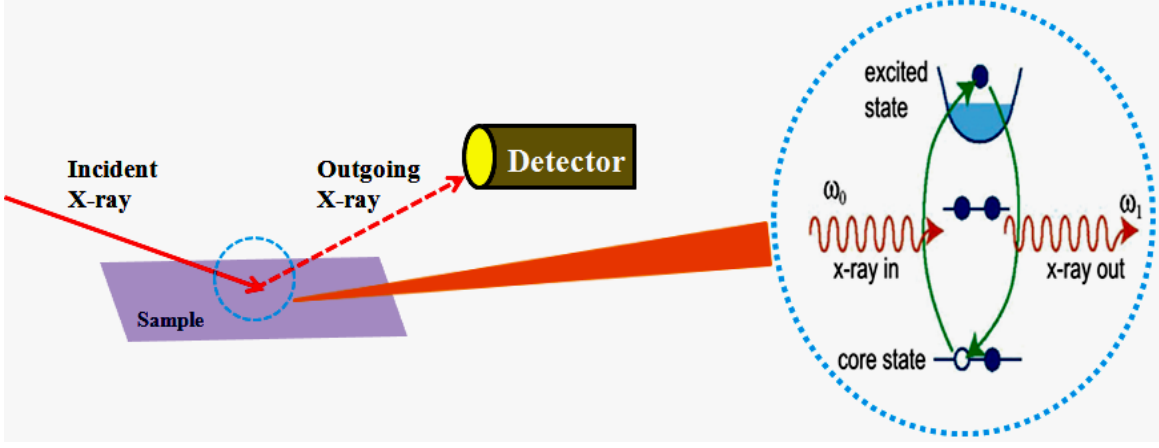


Figure 2.3: Schematic of the scattering geometry in resonant X-ray scattering and the detailed picture of the scattering process at the electron level [90].

The theoretical description of magnetic scattering process follows the treatment and the notation by M. Blume using quantum mechanical basics of magnetic scattering [18]. The detailed derivation of the scattering cross-section can be found in the paper by M. Blume. The scattering cross-section is derived by a perturbation treatment to second order of the transition probability of the interaction Hamiltonian (H_{int}) given by the golden rule:

$$S_C = \frac{2\pi}{\hbar} |\langle f | H_{int} | i \rangle + \sum_n \frac{\langle f | H_{int} | n \rangle \langle n | H_{int} | i \rangle}{E_i - E_n}|^2 \delta(E_i - E_f) \quad (2.5)$$

with the initial state $|i\rangle$, the final state $|f\rangle$, the intermediate states $|n\rangle$ and the corresponding energies E_i , E_f , E_n respectively. Equation 2.5 gives rise to resonant scattering with a huge contribution if the energy denominator in the equation becomes very close to resonance. The excitation of inner core electrons into vacant intermediate states makes the scattering dependent on the constituent element and its chemical surroundings (See Fig.2.3). As a result of magnetic exchange splitting and spin polarization terms, resonant scattering cross-section is also sensitive to magnetism. This magnetic scattering cross-section part will be discussed in more details in the following sections.

Most of the magnetic scattering experiments in this thesis were carried out by utilizing resonance. At resonance condition, when the photon energy is tuned very close to an absorption edge, there is an extra contribution of \widehat{F}_{res} to the scattering amplitude. Within a simple one-electron framework, an incident photon stimulates an inner-shell electron to an empty state above the Fermi level. The excited electron decays through emission of a scattered photon of the same energy as the incident photon. Figure 2.4 below shows the different possible phenomena that happen when a photon interacts with an atomic electron.

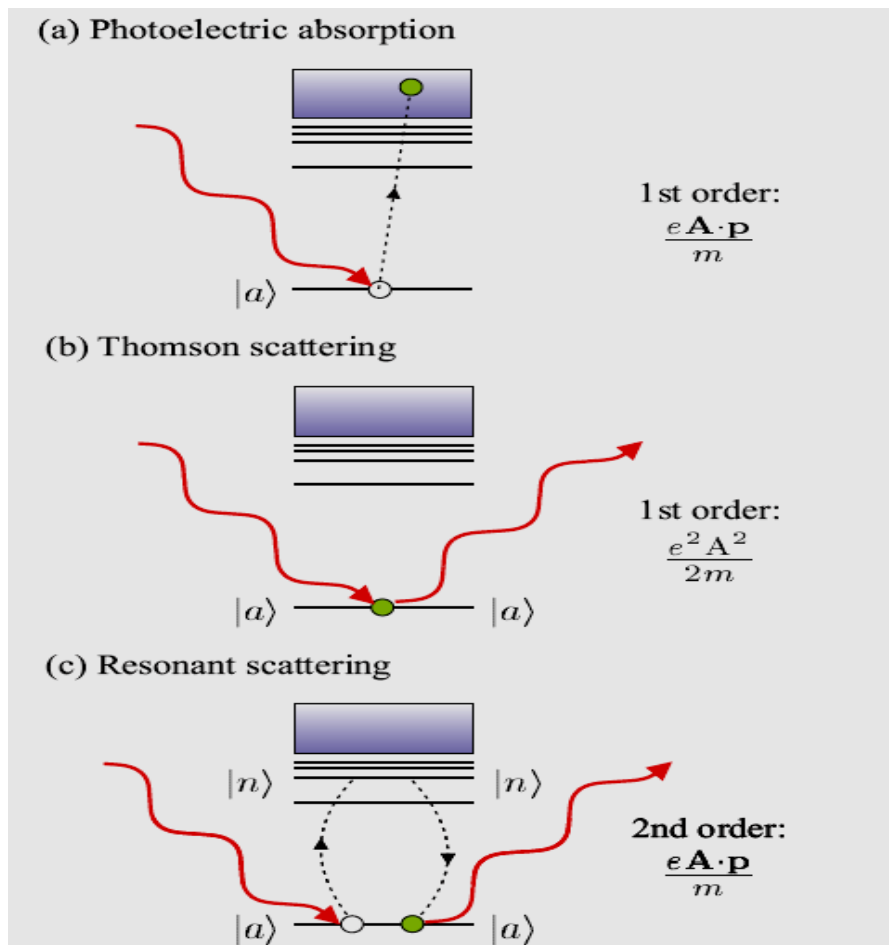


Figure 2.4: Description of the quantum mechanical picture of the interaction of a photon with an atomic electron. (a)Photoelectric absorption and (b)Thomson scattering. (c)Resonant scattering is a second-order process and happens via an intermediate electronic state. However, as resonant scattering is a virtual process, and does not occur in the two discrete steps as suggested here [70].

In comparison to non-resonant magnetic scattering, calculation of the resonant-scattering amplitude is not so trivial. In case of electric dipole transitions E1, [84], the scattering amplitude can be written as the sum of three separate terms [96].

$$\widetilde{F}_{res}^{E1}(h\vartheta) = \widetilde{F}_0(h\vartheta) + \widetilde{F}_{circ}(h\vartheta) + \widetilde{F}_{lin}(h\vartheta) \quad (2.6)$$

Where

$$\widetilde{F}_0(h\vartheta) = -\left(\frac{3}{4\pi k}\right)(\hat{\mathcal{E}}' \cdot \hat{\mathcal{E}})[F_{+1}^1 + F_{-1}^1] \quad (2.7)$$

$$\widetilde{F}_{circ}(h\vartheta) = -i\left(\frac{3}{4\pi k}\right)(\hat{\mathcal{E}}' \times \hat{\mathcal{E}}) \cdot \hat{m}[F_{-1}^1 - F_{+1}^1] \quad (2.8)$$

$$\widetilde{F}_{lin}(h\vartheta) = -\left(\frac{3}{4\pi k}\right)(\hat{\mathcal{E}}' \cdot \hat{m})(\hat{\mathcal{E}} \cdot \hat{m})[2F_0^1 - F_{+1}^1 - F_{-1}^1] \quad (2.9)$$

here, the F_ℓ^1 are energy-dependent dimensionless resonant oscillator terms for dipole transitions due to change in the magnetic quantum number ℓ . The first term, $\widetilde{F}_0(h\vartheta)$, is independent of the local magnetic direction \hat{m} . Similarly like that of Thomson scattering it does not change the polarization direction, and is expressed as the inner product of the polarization vectors of the incoming and the outgoing light, $\hat{\mathcal{E}}$ and $\hat{\mathcal{E}}'$ respectively. This gives rise to $\sigma \rightarrow \sigma'$ or $\pi \rightarrow \pi'$ scattering, where σ signifies the X-ray-polarization direction perpendicular and π denotes parallel to the scattering plane spanned by the wave vectors of the incident and scattered X-rays. This contribution leads to what is known as anomalous scattering. The second term arises due to the difference in the resonant oscillator strengths, F_ℓ^1 , where ℓ is the projection of the photon spin on the local magnetic axis \hat{m} (unit vector). With the selection rule for photon absorption $\ell = \Delta M_J = \pm 1$, this term is of circular dichroic nature. After scattering, the direction of polarization is rotated by some angle, leading to finite contributions in σ' or π' components of the scattered light ($\sigma \rightarrow \pi'$ or $\pi \rightarrow \sigma'$ scattering). The scattering amplitude contains \hat{m} as a linear term, leading to peaks at the same

points in reciprocal space as those arising from the non-resonant scattering, which is also linear in \hat{m} as well. The last term appearing in the scattering amplitude is of linear dichroic nature. While the projection on local magnetic axis appears twice, this contribution is quadratic in \hat{m} [96].

The resonant E2 or the electric quadrupole amplitude contains terms in \hat{m} from zero up to fourth order with 13 different contributions. Therefore, E2 resonant scattering can contribute to the main Bragg reflections and satellites up to the fourth order [84]. Hence the scattering amplitude is the coherent sum of contributions from E1, E2, . . . events. In case of strong dipole resonances like the $M_{IV,V}$ absorption thresholds of the lanthanides, the contributions due to the electric quadrupole or higher transitions are very weak as compared to E1 and can be neglected. By tuning the energy of the photon to a resonance, an enhancement in the magnetic-scattering signal happens if there is a difference in the cross section between spin-up and spin-down electronic states. This difference can arise due to number of ways making the identification of the exact mechanism not as straightforward as in case of non-resonant scattering. The first and most apparent reason is the finite spin polarization of the partially filled electronic states into which the core electron is excited. If there are more unoccupied states of one spin direction in comparison of the other, then there is a higher transition probability to the first ones, leading to magnetic contrast in the scattering cross section. This is exactly the case for the 3d states of 3d-transition metals ($L_{II,III}$ absorption thresholds) and also for the 4f and 5f states of lanthanides and actinides ($M_{IV,V}$ absorption thresholds), respectively, where a resonant enhancement of the magnetic-scattering signal can be expected. A second possible reason for the enhancement in magnetic signal arises due to the difference of overlap integrals between spin-up and spin-down states. This occurs from polarization via hybridization by another strongly polarized state [85]. It was found by Van Veenendaal *et al.* that the difference in the spatial extent of the spin-up and

spin-down 5d states owing to interaction with the strongly polarized 4f states makes a dominant contribution to the observed signal at the Ho $L_{II,III}$ thresholds. Excitation into polarized 5d states results in resonant enhancement of the magnetic signal by a factor of 50 as compared to off-resonant scattering. In fact, it was the L_{III} threshold of Ho at which the first observations of resonant magnetic scattering were made by Gibbs et al. [81]. Finally, if the resonant excitation energies, or lifetimes of the spin-up and spin-down channels are different, there might also be a magnetic contrast, i.e. an enhancement of the magnetic signal can occur as is seen in case of a Fe/Gd thin film (See Fig.2.5). Apart from the situations described above, this can occur even with a totally empty intermediate state, where the assignment of a finite polarization in the valence shell might not be correct [86]. Experimental evidence of this effect has been observed at the K threshold of Mn in the orbitally-ordered material LaMnO_3 [87].

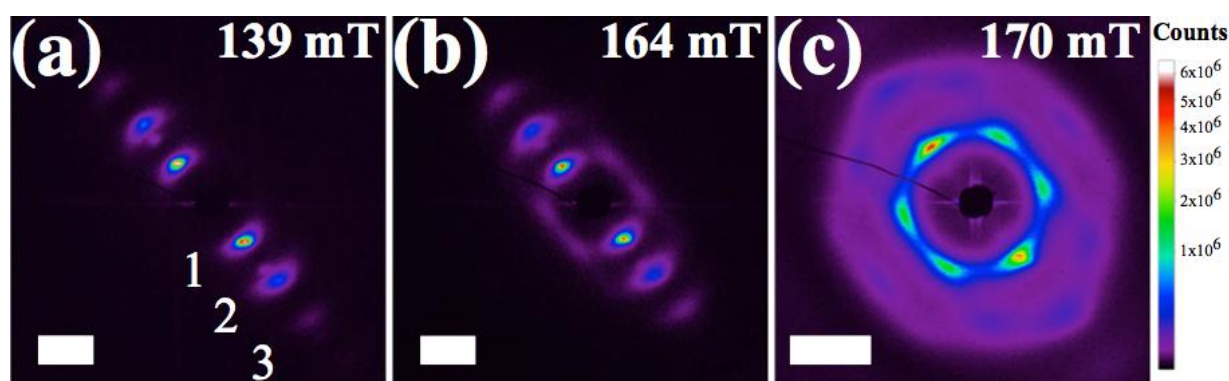


Figure 2.5: A Representation of Gd M_5 resonant X-ray scattering patterns, square root scale. Scale bars represent a transfer momentum of 0.041 nm^{-1} . (a) Scattering from stripe domains with the first, second, and third order stripe peaks visible. Parts (b), (c) illustrate evolution of skyrmion bound pair lattice with magnetic field [89].

In an interesting work published by M. Blume (1985), the cross section for X-ray scattering was calculated by including magnetic terms and is derived in a way that allows the effects of electron binding to be taken into consideration. By starting with the nonrelativistic Hamiltonian equation for electrons [to order $(v/c)^2$] and the quantized electromagnetic field, they produce a general formula for the cross section including virtually all types of scattering

phenomena within proper limits (in the "kinematic" or Born approximation), including Thomson, Rayleigh, Bragg, thermal diffuse, Raman and magnetic scattering, and also anomalous dispersion.

The pure charge scattering by X-ray photons is greater than that of pure magnetic scattering by a factor given by [18]

$$\frac{\sigma_{mag}}{\sigma_{charge}} \cong \left(\frac{\hbar\omega}{mc^2}\right)^2 \frac{N_m^2}{N^2} \langle s \rangle^2 \frac{f_m^2}{f^2} \quad (2.10)$$

where ' N_m ' is the number of magnetic electrons per atom and ' N ' is the number of electrons per atom. ' f_m ' and ' f ' are the magnetic and charge form factors. For Fe and 10-keV photons,

$$\frac{\sigma_{mag}}{\sigma_{charge}} \cong 4 \times 10^{-6} \langle s \rangle^2$$

Also, it is understood that the magnetic form factor ' f ' of an atom decreases much more rapidly than the charge form factor as the magnetization density is more diffuse spatially than is the charge density which reduces the ratio even further. Finally, the term ' $\langle s \rangle$ ', which goes to zero at the Curie temperature, is unity only at low temperatures.

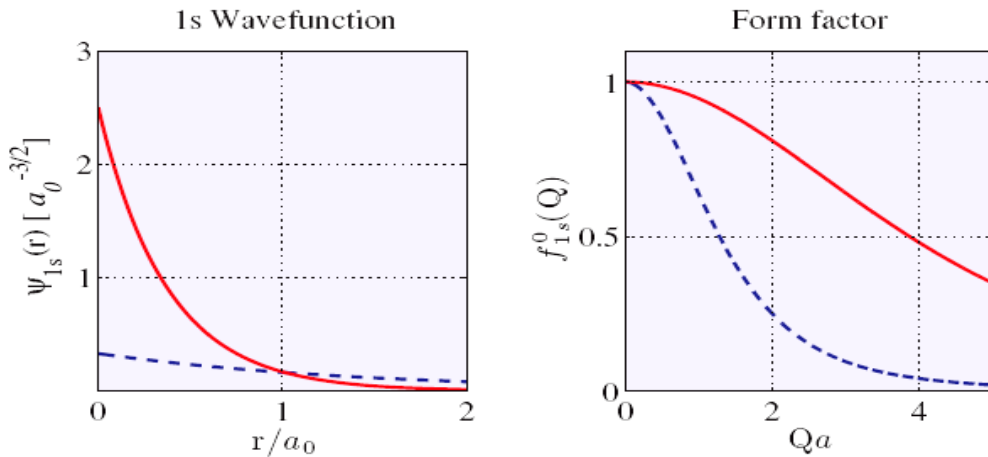


Figure 2.6: A typical wavefunction and form factor plots of the 1s state for atomic number ($Z=1$ (dashed lines)) and $Z=3$ (solid lines) [70].

On the other hand the ratio of magnetic terms for X-rays and neutrons is approximately

$$\frac{I_0^x \sigma_{mag}^x}{I_0^n \sigma_{mag}^n} \cong \frac{1}{4} \left(\frac{\hbar\omega}{mc^2}\right)^2 \frac{I_0^x}{I_0^n} \approx \frac{1}{4} \times 10^{-4} \frac{I_0^x}{I_0^n} \quad (2.11)$$

Neutron sources can produce 10^8 neutrons/sec on a sample. An X-ray source usually gives 10^{12} photons/sec (monochromatic) will give comparable X-ray and neutron peaks.

The X-ray pure magnetic scattering should be observed clearly in structures (like antiferromagnets or spirals) in which the Bragg peaks do not occur at the same point in Q-space where the dominant charge scattering happen. The detailed analysis scheme for calculating the scattering cross-section is given in the paper by M.Blume (1985). Here we have given the final simplified representation of the scattering cross-section by taking into account only the spin-dependent terms. Thus the magnetic scattering amplitude is proportional to

$$[\hbar^2 \omega^2 / c^2] \langle f | \mathbf{H}^+(\mathbf{k}') | m \rangle \langle m | \mathbf{H}(\mathbf{k}) | i \rangle / (E_a - E_c + \hbar \omega - i \Gamma/2) \quad (2.12)$$

At resonance conditions; $\hbar \omega \approx E_a - E_c$, so the scattering amplitude reduces to

$$2[\hbar \omega / c] \langle f | \mathbf{H}^+(\mathbf{k}') | m \rangle \langle m | \mathbf{H}(\mathbf{k}) | i \rangle \times (i \frac{\hbar \omega}{\Gamma c}) \quad (2.13)$$

The factor $\frac{\hbar \omega}{\Gamma c}$ can be as large as 10^4 .

Polarized Neutron Reflectivity (PNR)

Neutron scattering techniques have contributed a lot to our knowledge regarding the microscopic magnetic and structural properties of solids, starting with the pioneering work on anti-ferromagnetic system [85]. Polarized neutron reflectivity (PNR) has been used [67, 75-84] to investigate the magnetization profiles along the out-of plane direction as a function of depth in thin films and multilayer structures by comparing the reflected intensity due to two anti-parallel neutron spin states. The interaction of the incoming neutrons with the scattering systems is generally comprised of two parts, [67-74, 84], viz

(1) Incident neutron interacts with the nuclei of the target system through purely nuclear forces, and

(2) Interaction arising due to the magnetic moment of the neutron and the magnetic moment of the electrons present in the target system.

The interaction between the neutron magnetic moment and the Coulomb field of the electrons and nuclei in most cases can be neglected with respect to the purely nuclear and magnetic interactions as detailed above.

In a PNR experiment, the incident neutrons are polarized either parallel (+) or antiparallel (-) to an externally applied magnetic field H . The magnetization in the sample induces a change in spin state of the scattered neutrons. The final state of the neutrons is analyzed in terms of the polarization of the incident neutrons. As a result four reflectivities R^{++} , R^{--} , R^{+-} , R^{-+} can be measured depending on the spin state of the incident and scattered neutrons [67, 75-83].

The reflected neutrons thereby carry information regarding the refractive index, $n^{\pm}(z)$ of the system. The refractive index profile containing both the nuclear and magnetic scattering terms and is expressed as

$$n^{\pm}(z) = 1 - \frac{\lambda^2}{2\pi} \left(\frac{b}{v} \pm c\mu \right) \quad (2.14)$$

where b/v is the complex nuclear scattering amplitude per unit volume, $c = m_n \mu_n / 2\pi \hbar^2$ ($= 2.3 \times 10^{-10} \text{ \AA}^{-2} \text{ Oe}^{-1}$) and $\mu(\mu_x, \mu_y, \mu_z)$ is the magnetization.

Lorentz TEM

Around 40 years ago TEM was first used to observe magnetic domain structures using the Fresnel or defocus mode. Since then Lorentz microscopy has been extensively used to study magnetic domain in magnetic thin films and multilayer structures [86].

Magnetic structures are most commonly explored in the TEM by utilizing one of the modes of Lorentz microscopy. This standard name is used to describe all the imaging modes in which the contrast is generated due to the deflection experienced by electrons as they pass through a region of magnetic induction \mathbf{B} [87]. The Lorentz deflection angle β_L is given by

$$\beta_L = e\lambda t(\mathbf{B} \times \mathbf{n})/h \quad (2.15)$$

here \mathbf{B} is the induction averaged in the direction of an electron trajectory, \mathbf{n} is a unit vector parallel to the incident beam, t is the specimen thickness and λ is the wavelength of electron.

2.3 Coherent X-ray Scattering

Microstructure plays a dominant role in determining physical properties of metals. Most of the recent advances in material technology consist of innovative treatments designed to control and improve this microstructure. X-rays scattering studies, in particular, provides us a direct probe to the nature of microstructure. The availability of high brilliance synchrotron sources comprising of sufficient volume of coherent X-ray flux to perform time-resolved diffraction experiments has been perceived in the last few decades. These measurements have allowed further insights into the morphology and dynamics of microstructure. Generally in a diffraction experiment, one observes interference due to scattered waves coming from a small 3-dimensional volume, known as coherence volume. For typical X-ray scattering geometry, the detected intensity results due to an addition of the contributions from a large number of coherence volumes and each such volume has dimensions of less than a micron. In most cases, the local configuration of each coherence volume cannot be determined exactly since the experiment measures an ensemble average of the sample properties over the irradiated region. Information regarding the morphology of the structure is available by choosing the diffraction volume equal to the coherence volume. In a simplified image, this corresponds to the observation of the Fourier transform of the sample's real space configuration. The intensity in the momentum space has presence of strong fringes, irregular resulting due to summing a set of random amplitudes, called "speckles", provided one has sufficient diffracted amplitude. The coherence volume is generally divided into

transverse A_t and longitudinal A_l (or temporal) coherence parts (See Fig.2.7). A_t is related to the divergence (ε) of the beam. A rough generalization, valid for diffraction limited beams coming through a slit or pinhole gives [25]:

$$\varepsilon \times A_t \approx \lambda/2 \quad (2.16)$$

For X-rays with $\lambda \approx 1.5 \text{ \AA}$ and $\varepsilon \approx 10 \text{ \mu rad}$, A_t is 10 \mu m .

A_l is directly related to the monochromaticity of the X-ray photons:

$$A_l \approx \lambda^2 / (2 \cdot \delta\lambda) \quad (2.17)$$

Where $\delta\lambda/\lambda$ is the relative bandwidth, which yields A_l of the order of 0.5 \mu m with a Si(111) monochromator. Nowadays synchrotron radiation source (SRS) provides beams of high intensities in this angular range and thus makes it possible of carrying out experiments with fully (or at least partially) coherently irradiated samples [26]. A simple expression connecting the available coherent intensity I_c to the SRS brilliance B is given by:

$$I_c = B (\lambda/2)^2 (\delta\lambda/\lambda) \quad (2.18)$$

For an undulator beamline using third generation sources (APS, ESRF, Spring 8, Soleil, Petra III, Diamond, SLS, . . .), $B \sim 10^{20} \text{ ph/(mrad}^2\text{mm}^2 \text{ s)}$ for a 0.1% bandwidth. This gives an approximate of $I_c \sim 10^{11} \text{ ph/s}$ with a Si(111) monochromator at $\lambda = 1.5 \text{ \AA}$. In practice, $I_c \approx 10^{10} \text{ ph/s}$, but coherent experiments can still be carried out with as little as $I_c \approx 10^6 \text{ ph/s}$.

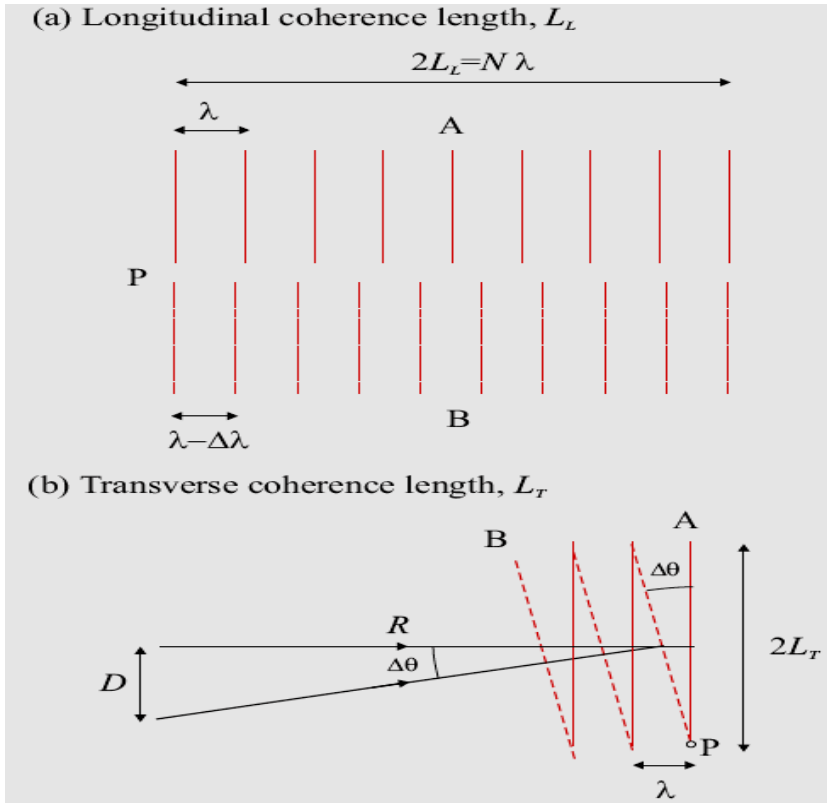


Figure 2.7: Representations of longitudinal and transverse coherence lengths. (a) Two plane waves with different wavelengths are emitted along the same direction. For better understanding we have shown the waves displaced from each other along the vertical direction. After a distance L_L , the longitudinal coherence length, the two are out of phase by a factor of π . (b) Two waves with the same wavelength are emitted from the ends of a finite sized source of height D [70].

Observation of speckles

In a typical coherent experiment, the irradiated volume is kept generally of the order of the coherence volume. For maintaining transverse coherence condition, either small size samples are studied (from a few μm to a few nm) or by limiting the size of the transverse beam by slits or pinholes of diameter $\varphi \approx \lambda$. Longitudinal coherence allows one to limit the size of the irradiated region such that path length differences across the irradiated sample ΔL remains of the order of λ .

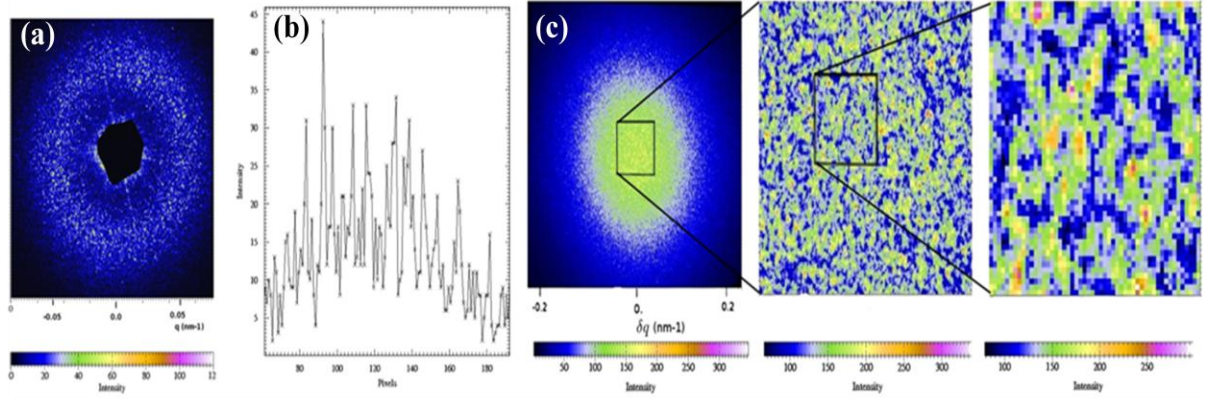


Figure 2.8: (a) Small Angle X-ray Scattering (SAXS) observation of a speckle structure in the diffraction ring of an Al–Li decomposed alloy. The central black region is the shadow due to the beam stop to prevent the main beam from damaging the detector [28–31]. (b) shows a typical profile observed across one side of the ring. (c) Image of the (001) superstructure peak from a Cu–Pd $L1_2$ ordering alloy. δq (in nm^{-1} units) is the distance from the superstructure peak position in the reciprocal lattice. Enlarged figures from each selection square are drawn at the right side in order to show the numerous speckles [35].

Detection

The interference pattern resulting in the speckles, gives them a typical angular size which primarily depends on the beam divergence and also on the domain size. Thus for the observation of these speckles, one requires a high resolution detector having an angular aperture ε' of the order of the beam divergence ε . In such small solid angle, the detected intensity may be low and the use of area detectors is highly recommended. Pixel sizes of 20 μm are standard for a CCD chip and direct illumination CCDs are frequently used in coherent scattering experiments [25–27]. These CCDs are characterized by low readout frequencies (less than a few MHz) and degrade slightly with radiation exposure.

Speckles in small angle X-ray scattering

In material science problems, small angle scattering (SAXS in the case of X-rays) gives important information on the size of inclusions which contribute to sample

strengthening. In a SAXS experiment, with transmission geometry, two terms contribute to ΔL :

$$\Delta L = 2 \cdot \varphi \times \theta \quad (2.19)$$

and

$$\Delta L = 2 \cdot e \times \theta^2 \quad (2.20)$$

Where ΔL is the length of the sample irradiated, φ is the beam size, θ is the scattering angle and e is the thickness of the sample.

Using a Si (111) monochromator with ΔL smaller than λ , SAXS experiments can still be carried out by using the 1% bandwidth “pink beam” obtained by filtering a harmonic of an undulator [32–34].

When the diffraction volume is large in comparison to the coherence volume than the beam is said to be partially coherent. Such beams results in reduced fluctuations in their speckle pattern. An incoherent beam can be considered due to the outcome of large size of the diffraction volume that the speckle contrast cannot be observed. Speckle contrast β can be estimated from the variations of the intensity, as compared to an incoherent SAXS intensity $S(\vec{q})$. For isotropic scattering

$$1 + \beta(q) = \frac{\langle I(q)^2 \rangle - S(q)^2}{S(q)^2} \quad (2.21)$$

In this equation, the “1” arises because of Poisson noise and the averages are over regions with the same magnitude, $|\vec{q}|$. This means that $S(\vec{q})$ has to be measured under equivalent conditions.

In some papers, the speckle “visibility” is defined, as $\sqrt{\beta}$. These speckles correspond to averaging over $1/\beta \approx 5$ coherence volumes. In experiments involving speckles, improving the coherence significantly lowers the available intensity, and thus optimizing the setup can considerably improve the signal to noise ratio [24].

Speckles at large angle

In the locality of a Bragg peak, at large θ , the condition implied by Eq. (2.20) is satisfied only if the longitudinal dimension of the diffracting volume is a few microns. This can be achieved for thin enough samples or by studying strongly absorbing samples in the Bragg reflection geometry. If the absorption length is μ^{-1} , one writes:

$$\Delta L = 2 \times \mu^{-1} \sin^2 \theta \quad (2.22)$$

An example is given by the superlattice peak of the Cu–Pd ordering alloy [35]. In this alloy, the L12 ordered structure induces a (001) superstructure peak. The ordering dynamics is slow, and in a conventional diffraction experiment, the (001) peaks are broadened by the presence of various antiphase domains. In a coherent scattering experiment, this superlattice peak displays speckles as shown in Fig. 2.8(c).

In Fig. 2.8(c), incoherent scattering is varying slowly as the domains coarsen. An approximation of $\beta \approx 0.044$ can be obtained from Eq. (2.21) by studying the speckle variations of a single image (see Fig. 2.8(c)). Here, $\Delta L \approx 1 \mu\text{m}$ from Eq. (2.22), which is appreciably larger than $\Lambda_1 \approx 0.5 \mu\text{m}$, and this reduces β from 0.25, as measured in a SAXS configuration to 0.044.

2.3.1 Beamline 12.0.2 at ALS

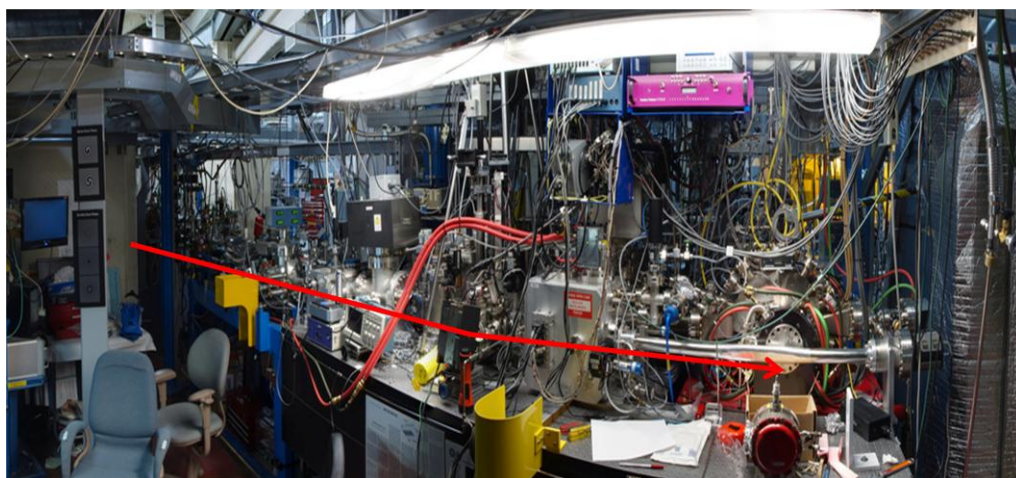


Figure 2.9: An image of the X-ray coherent beamline 12.0.2 at the advanced light source, USA.

The availability of high-power spectrally and spatially coherent soft X-rays would facilitate a wide variety of experiments as this energy region contains several important K and L absorption edges. Specifically, there are the carbon and oxygen K edges that are critical for biological imaging in the water window and the L edges of magnetic materials iron, nickel, and cobalt for which imaging and scattering studies can be performed. The coherent end-station beamline at ALS is a high tunable, spatially and spectrally coherent soft X-ray undulator branchline (See Fig.2.9 and Fig. 2.10). Using the third harmonic from an 8-cm period undulator, this branch delivers coherent soft X-rays with photon energies ranging from 200 to 1000 eV.

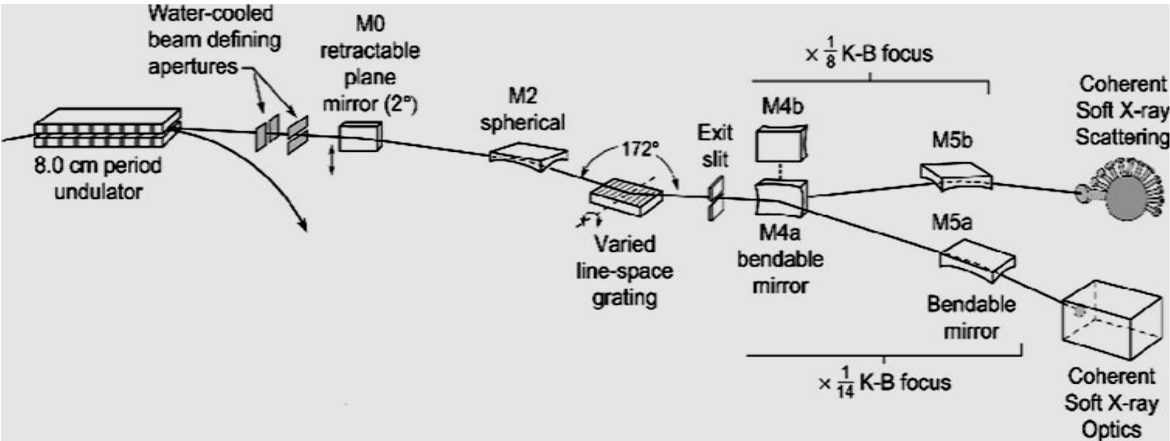


Figure 2.10: Image of the beamline layout of the coherent soft X-ray endstation at the ALS [91].

TABLE 2.1

BEAMLINE SUMMARY GIVING SPATIALLY COHERENT FLUX DELIVERED TO THE FOCAL PLANE OF THE BEAMLINE [91]

Energy (eV)	λ (nm)	K	$\theta_{cen}(\mu rad)$ $n=3, \sigma^l=0$ finite K	Spatially coherent flux- F_{sp} $BW=1/nN$, finite σ'	Beamline efficiency - η	Spatially coherent flux at focal plane ($BW=0.1\%$)
500	2.48	1.77	33.57	4.69E+13	0.00567	4.39E+10
600	2.07	1.51	30.65	2.88E+13	0.00534	2.54E+10
700	1.77	1.29	28.37	1.68E+13	0.00433	1.20E+10
800	1.55	1.1	26.54	9.11E+12	0.00251	3.80E+09

2.3.2 Characterization of coherence

A wave normally incident on a circular aperture will produce an airy intensity distribution in the far field if it has a sufficient level of spatial coherence [37]. As a first-order measurement of the spatial coherence of the beamline, we will look at the far-field patterns generated by the 2.5- μm diameter pinhole. The far-field patterns are recorded on a 1" \times 1", 1024 \times 1024 pixel (24.8 μm /pixel) charge-coupled device (CCD) camera (See Fig.2.11).

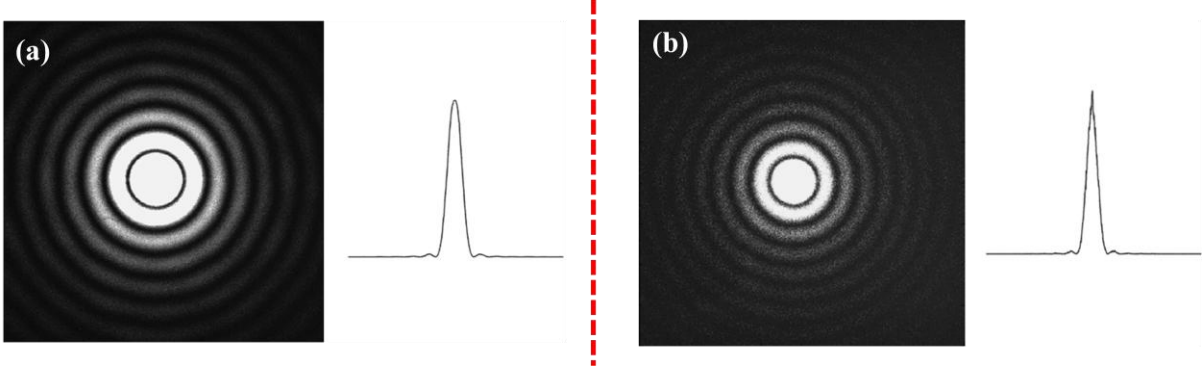


Figure 2.11: Airy pattern and its cross section recorded using a 2.5-μm diameter pinhole at the focal plane of beamline 12.0.2 at the ALS. Picture was recorded at a wavelength of (a) 2.48 nm (500 eV) with an exposure time of 200 msec and (b) 2.07 nm (600 eV) with an exposure time of 1s [91].

Double-Pinhole Characterization

The magnitude of the complex coherence factor of the soft X-ray branchline was measured using the classical Thompson and Wolf experiment [38] using the Young's double-slit setup [39] as has been discussed at short wavelengths by [40-44]. In this experiment, the Young's slits are replaced by pinhole pairs placed at the focal plane of the beamline to better characterize the two-point spatial coherence. The soft X-rays pass through the pinholes and then propagate 1.44 m to the far-field region where they are detected on the 1" × 1" CCD camera.

The visibility can be described as the sharpness of the fringes or [45]

$$\text{Visibility} = \frac{I_{\max} - I_{\min}}{I_{\max} + I_{\min}} = \frac{2\sqrt{I^{P1}I^{P2}}}{I^{P1} + I^{P2}} |\mu_{12}| \quad (2.23)$$

for the quasi-monochromatic case of undulator radiation passed through a monochromator where I_{\max} and I_{\min} are the maximum and minimum intensity of the fringe pattern, respectively, and $I^{(P1)}$ and $I^{(P2)}$ are the intensities on each of the pinholes. If the double pinholes are centered about the incident radiation such that $I^{(P1)} = I^{(P2)}$, then the visibility is

simply equal to the magnitude of the complex coherence factor μ_{12} . Figure 2.12-2.14 shows a detailed description of the measured double pin-hole pattern as function of pin-hole separation, energy and pin-hole diameter.

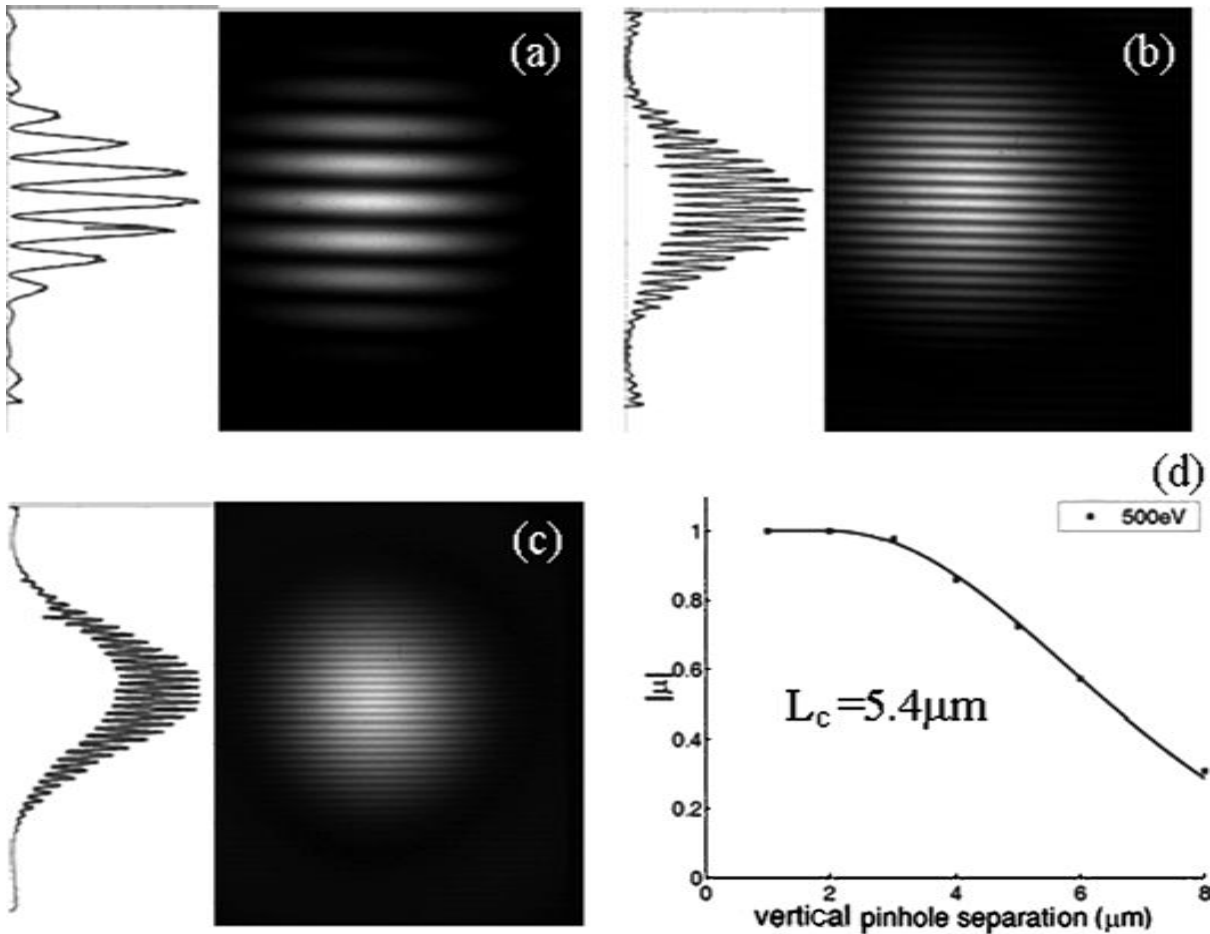


Figure 2.12: Measured two-pinhole interference patterns at a photon energy of 500 eV (2.48 nm) and their respective lineouts for vertical pinhole separations of (a) 2 μm , (b) 6 μm , and (c) 8 μm . Each individual pinhole of the two-pinhole pairs has a diameter of 450 nm to ensure a spatially coherent wavefront over the individual pinhole. (d) Measured magnitude of the complex coherence function versus the pinhole separation. Least square error Gaussian curve is fitted to these data points. All data were taken on beamline 12.0.2 of the ALS.

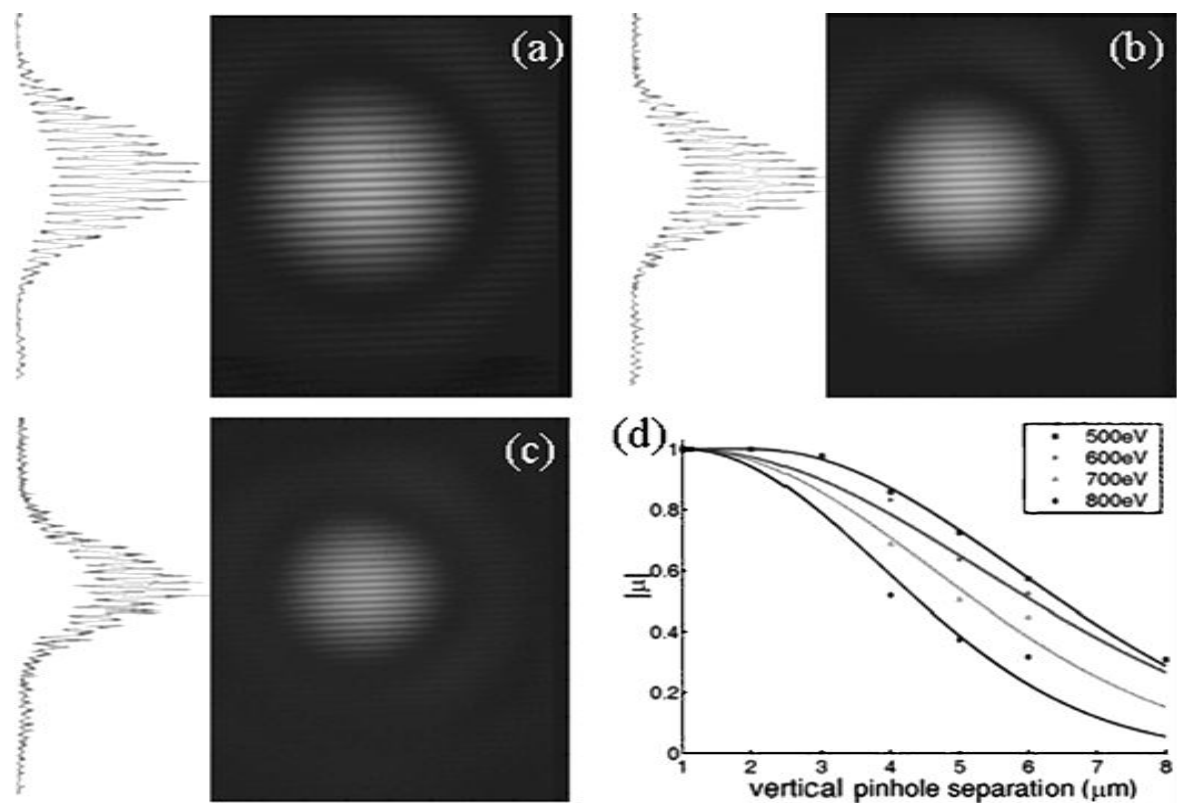


Figure 2.13: Measured two-pinhole interference patterns at 500 eV, 600 eV, 700 eV and 800 eV and their respective lineouts for a 5- μm vertical pinhole separation at a photon energy of (a) 600 eV (2.07 nm), (b) 700 eV (1.77 nm), and (c) 800 eV (1.56 nm). Note that airy envelope decreases for increasing energy. (d) Measured magnitude of the complex coherence function versus the pinhole separation. Least square error Gaussian curve is fitted to each energy's set of data points. All data was taken on beamline 12.0.2 of the ALS. Coherence length calculated are 5.4 μm (500 eV), 4.9 μm (600 eV), 4.2 μm (700 eV), and 3.6 μm (800 eV) [91].

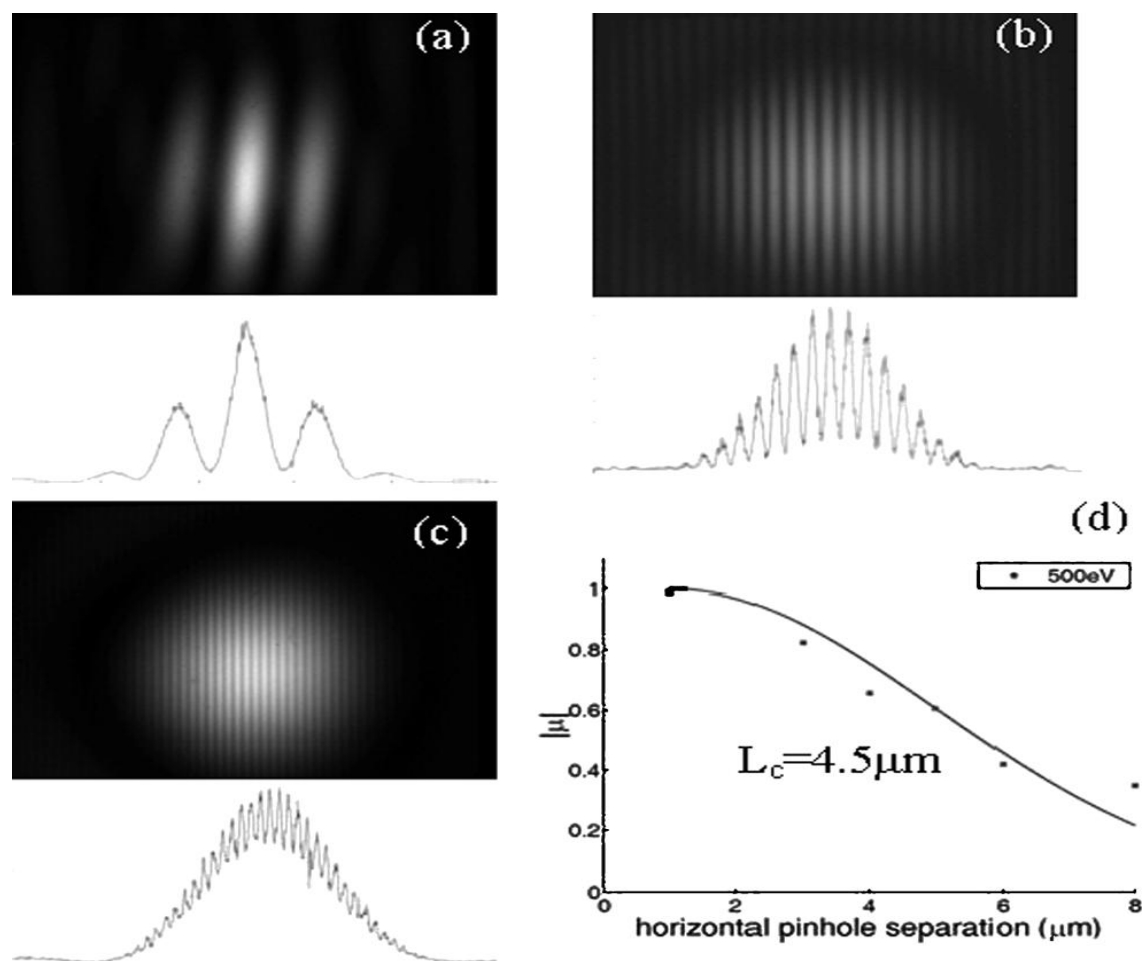


Figure 2.14: Measured two-pinhole interference patterns at a photon energy of 500 eV (2.48 nm) and their respective lineouts for horizontal pinhole separations of (a) 1 μm, (b) 4 μm, and (c) 8 μm. (d) Measured magnitude of the complex coherence function versus the pinhole separation. Least square error Gaussian curve is fitted to these data points. All data were taken on beamline 12.0.2 of the ALS [91].

2.4 Langmuir-Blodgett (LB) deposition technique

The Langmuir-Blodgett technique was first introduced by Irving Langmuir and applied extensively by Katherine Blodgett while working in Research and Development for General Electric Co. It involves the vertical deposition of a monolayer film formed at the air-water interface onto a solid substrate. The as-formed monolayer film on water surface is known as Langmuir monolayer. The oil monolayer film on water surface was first observed and is named as Langmuir monolayer but the history of this oil film started with the

pioneering work of Benjamin Franklin in the year 1774 of making an oil film on Clapham pond [1]. However the importances of this monolayer was not realized at that time and further not much scientific work was done on it. About hundred years later Rayleigh, predicted that the layer can be one molecule thick while observing the maximum extent of the oil film on water surface. Around the same time with the help of her kitchen sink, Agnes Pockles introduced the idea of using barriers on top of the water surface which controls the quantitative measurements on this monomolecular layer. She added that surface tension changes with contamination of water [2]. Langmuir started performing systematic studies on mono- layer and developed the theoretical background of these insoluble monolayers on water surface [3]. Later Katherine Blodgett first demonstrated the detailed description of sequential transfer of monolayer from the air-water interface onto solid substrates [4]. These built-up monolayer assemblies are therefore named as Langmuir-Blodgett films.

2.4.1 Preparation of Langmuir monolayer

All compounds may be roughly divided into two broad categories, one those that are soluble in water and two, those that are not soluble in water. The former type of materials generally carries an uneven distribution of charge and hence termed as polar group. The materials which do not dissolve in water are commonly known as non-polar materials. The molecules of majority monolayer forming materials are composed mainly of two parts, one is polar and hence have positive affinity to water and other part is non-polar and have negative affinity (suffer repulsion) from water surface. The soluble part is termed as hydrophilic and the insoluble part as hydrophobic as a result these molecules are known as amphiphiles. It is the competition between the hydrophilic and hydrophobic forces that determines the monolayer forming abilities of the amphiphilic molecules on water surface. If for example, the hydrocarbon chain was too short, or the polar group too strong, then the material would

have simply immersed in the subphase. The amphiphilic nature of the molecules controls their orientation at the air-water interface in such a way that the polar head group always remains beneath the water surface and the long hydrocarbon chain (tail) is standing above the water surface. In Fig. 2.15 the structure and orientation of a amphiphilic molecule (stearic acid) at the air-water interface is shown.

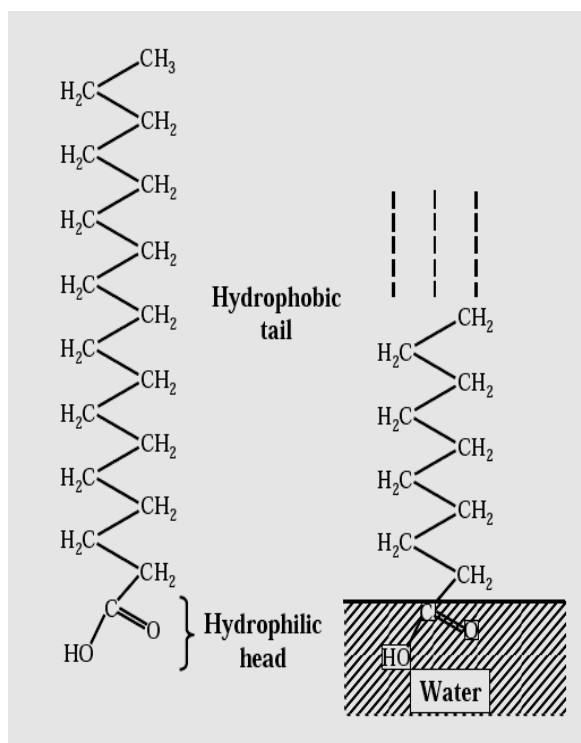


Figure 2.15: Schematic of a amphiphile - stearic acid on the water surface. The polar group (head) is immersed in water and the hydrocarbon chain (tail) is pointing outwards to the water surface [92].

The surface tension is one of the significant properties to characterize the formation of monolayer on water surface [5-8]. In presence of a monomolecular film on a liquid surface the surface tension will change. Surface pressure is measured mainly in monolayer experiments and is defined as,

$$\Pi = \gamma_0 - \gamma \quad (2.24)$$

where γ_0 is defined as the surface tension of the pure liquid and γ as the surface tension of the

film covering the surface. The two most common methods for monitoring the surface pressure are the Langmuir balance and the Wilhelmy plate or paper plate.

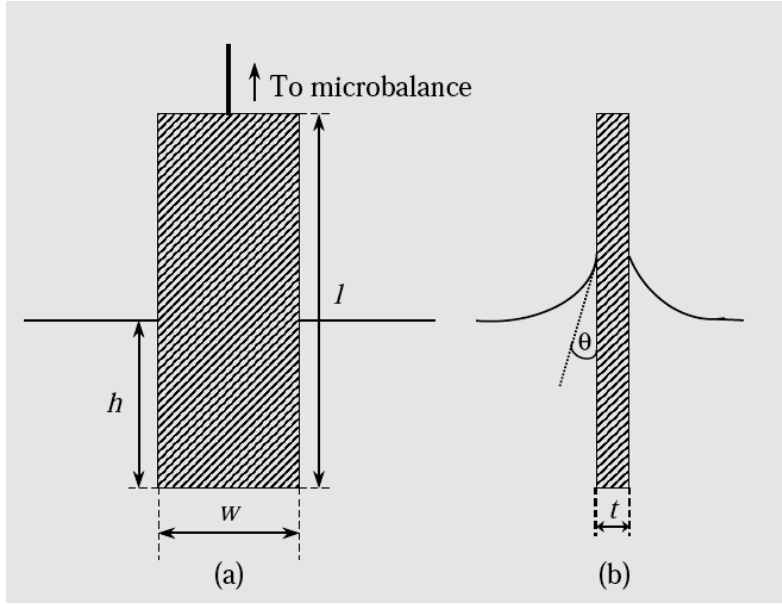


Figure 2.16: Wilhelmy plate, (a) front view, (b) side view [92].

Use of Wilhelmy plate or paper plate is perhaps the most popular and in this method the force due to surface tension exerted on a suspended plate which is partially immersed in the subphase is measured. The dominant forces acting on the plate are due to gravity and surface tension in the downward direction and buoyancy, due to displaced water in the upward direction. For a rectangular plate having dimensions l , w and t (as marked in Fig. 2.16) and the density of the material is ρ_w immersed to a depth h in a liquid having density ρ_L , the net downward force F acting on the plate is given by,

$$F = \rho_w glwt + 2\gamma(t + w) \cos \theta - \rho_L g t w h \quad (2.25)$$

where γ is the surface tension due to the liquid, θ is the contact angle of the liquid with the solid plate and g is the gravitational constant. The usual practice of a plate that is completely

wetted by the liquid (i.e. $\theta=0$) and measure the change in F with respect to a stationary plate.

The change in force ΔF related to the change in surface tension $\Delta\gamma$ is given by,

$$\Delta\gamma = \Delta F / 2(t + w) \quad (2.26)$$

if the plate is sufficiently thin so that $t \ll w$

$$\Delta\gamma = \Delta F / 2w \quad (2.27)$$

Thus the sensitivity can be increased by using very thin plate and often very thin plate of platinum, glass, quartz, mica or paper can be used.

Most monolayer forming materials are formed on the subphase first by dissolving it in a suitable solvent (like chloroform) and then spreading it on the subphase. The solvent should have the unique properties to disperse the molecules of the film forming material on the subphase and then quickly evaporate completely from the subphase surface so that the subphase does not get contaminated. That is the reason for choosing a solvent which is both volatile and insoluble in the liquid subphase as the spreading solvent like chloroform on water surface. Extremely volatile solvent is not chosen as a spreading solvent because it hinders accurate measurement of the solution concentration. Generally solvents having boiling temperature in the nearby ambient range 30°C to 70°C are generally preferred for spreading. If a liquid droplet is placed on a solid or another liquid, the drop will spread or wet the surface in accordance to Young's equation

$$\gamma_{LG} \cos \theta = \gamma_{SG} - \gamma_{SL} \quad (2.28)$$

where the γ 's corresponds to the surface tensions at the various interfaces between the solid (S), liquid (L) and gas (G) phases. θ is the contact angle between liquid and solid surface. For completely wet surface, θ is nearly equal to zero, implying that the liquid spreads

completely on the solid surface. The spreading coefficient of two immiscible liquids a and b can be calculated as,

$$S_{b/a} = \gamma_a - \gamma_b - \gamma_{ab} \quad (2.29)$$

where $S_{b/a}$ corresponds to the spreading coefficient for liquid b on liquid a , γ_a and γ_b denotes the respective surface tensions and γ_{ab} is the interfacial surface tension between two liquids. If $S_{b/a} > 0$ then the liquid b will simply spread over liquid a , but when $S_{b/a} < 0$ liquid b will tend to dewet and form droplet on the surface of the liquid a . Chloroform was used as the mixing solvent in our experiments and measured amount of solution is gently spread on water subphase with the help of a micro-syringe by keeping the syringe close to the water subphase without touching it (See Fig.2.17 (a)).

As the monolayer is slowly compressed on the water surface by the barriers, it will go through several phase transitions [9]. These are almost analogues to the three-dimensional gas, liquid and solid phases according to the density variation. The phase changes may be recognized by observing kink in pressure-area isotherm.

Such a typical pressure-area isotherm for a long chain amphiphilic fatty acid is shown in Fig. 2.17(b). In this phase diagram the area generally implies to the area/molecule, i.e., total film area divided by the total number of molecules present in the monolayer. In the gaseous phase, the molecules are wide apart from each other on the water surface so that they exert little force on one another. As the surface area of the monolayer is decreased, the hydrocarbon chains will start to interact and a mixed phase called the liquid-expanded monolayer phase will appear in the isotherm.

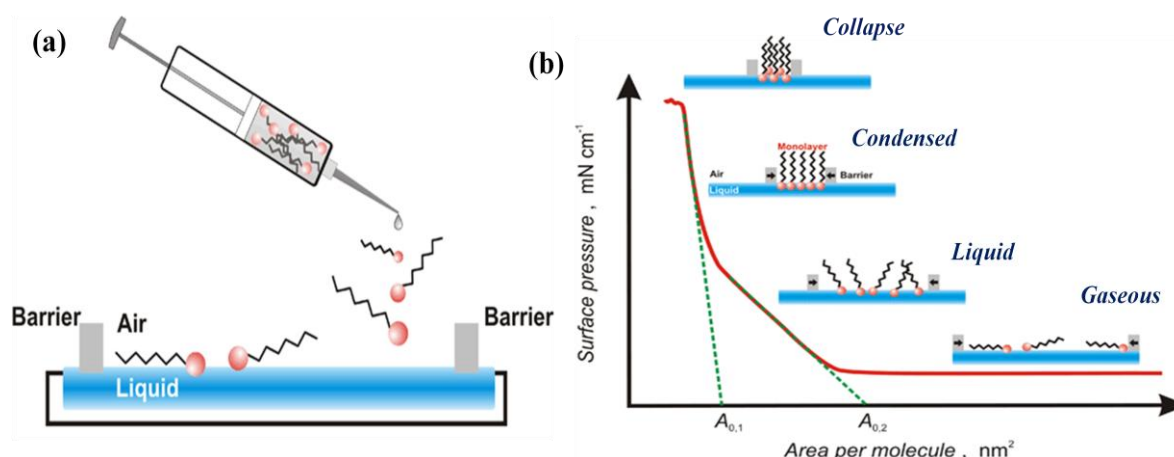


Figure 2.17: Representative of (a) drop dispensing of the amphiphilic molecules dissolved in a volatile solvent onto a polar liquid sub-phase filling the Langmuir trough, (b) Typical Pressure-Area isotherm showing the presence of all the distinct phases [93].

The hydrocarbon chains of the molecules in this phase are in arbitrary positions, instead of a regular orientation, with their polar groups in contact with the subphase. From this condition as the molecular area is decreased further, a tilted condensed phase will emerge where the hydrocarbon chains are symmetrically tilted.

Further compression will lead to a condensed phase where the molecules in the monolayer on the water surface are closely packed and hydrocarbon chains are oriented vertically. If the monolayer is compressed more, finally a point will reach where it is not possible to increase the surface pressure and may result in sharp decrease in area per molecule without variation in monolayer pressure or pressure falls as the area decreases. This is referred as collapse state of the monolayer. When this collapse occurs, molecules are forced out of the monolayer state and can form multilayer structures on the water surface (See Fig.2.17 (b)). Other types of structures are also possible for amphiphilic molecules having dominant polar head group, where the molecules join together and form micelles above a certain concentration (critical micelle concentration) [10].

2.4.2 Deposition of LB Films

LB multilayer film deposition takes place by dipping a substrate upwards and downwards through a Langmuir monolayer. A layer is deposited on the substrate during each upstroke and downstroke through the monolayer. The instrument which is used to prepare the Langmuir monolayer and within which subsequent LB film deposition occurs is called a LB trough.

Today's LB troughs are much sophisticated with total computer control movement of every component, than the trough initially developed by Agnes Pockels. The essential constituents of a LB trough are (a) TEFLON (PTTE) made bath, (b) movable barriers for altering monolayer area and hence monolayer surface pressure (c) balance for measuring surface pressure and (d) dipper for deposition with the substrate.

Here we have used a KSV5000 alternating bath trough for depositing LB films [11]. In Fig. 2.18, a schematic of the deposition process along with a close view of the dipper part of the trough is shown. In normal single bath trough, there is only one dipper arm. But the advantage of the double bath trough is that here there are two dipping arms and these two dipping arms can facilitate the interchange of the substrate from one arm to another. So one can spread two dissimilar types of materials separately in the two baths and deposit ABAB..... or ABBA.....types of films. The effective area of each bath was $120 \times 357.5 \text{ mm}^2$ with two independent barriers sets made of a special hydrophilic material called DELRIN to ensure that the monolayer material does not go underneath the barrier during compression. The speeds of the barriers are controlled through a micro-step driven stepper motor and the minimum and maximum speeds are 0.5 mm/min and 85 mm/min respectively. In addition each bath also contains a pressure sensor consisting of Wilhelmy plate made from sandblasted platinum. An elevator is provided to position these plates inside the subphase and

usually one third of the plates remain submerged in the sub-phase. The schematic of LB deposition mechanism is shown in Fig. 2.18. The substrate is attached to the upper arm clip and it brings the substrate near the sub-phase and then transfers it to the lower arm clip. The upper arm always remains above the sub-phase and lower arm always stay inside the subphase. Furthermore the dipper arms are controlled by independent stepper motors. We have used millipore (Milli-Q) water of $18.2 \text{ M}\Omega/\text{cm}$ resistivity as the subphase in our experiments. The temperature of the bath is adjusted by circulating water from an external temperature controlled water bath through the circulator fitted underneath the trough. The subphase temperature can be varied from 10^0 C to room temperature. It is evident from Π -A isotherm shows different molecular phase in the monolayer and deposition of LB films are done in the untilted condensed phase of the monolayer [9]. During the deposition process a constant monolayer pressure is maintained and this monolayer pressure can vary on the composition of different monolayers depending on the Π -A diagram. In our experiment, fatty acid salts of stearic acid are used which can be formed by gently spreading fatty acid on water containing dissolved metal salt like gadolinium acetate (Gd-Ac), erbium acetate (Er-Ac) or holmium acetate (Ho-Ac). It is reported that preparation of LB films using this method and direct transfer of the substance is expected to give similar result but the isotherms are reported to be somewhat different in these two cases as observed for ferric stearate salt monolayer and stearic acid monolayer containing ferric ion in water [12]. Here mainly three types of LB films are studied which are gadolinium stearate (Gd-St), erbium stearate (Er-St) and holmium stearate (Ho-St). Separate LB films were prepared by spreading stearic acid (Aldrich, 99%) mixed in chloroform on water subphase containing dissolved Gd-Ac, Er-Ac or Ho-Ac salt. The surface pressure was maintained at a constant pressure of 30 mN/m and at a temperature 15^0 C . The pH of the water subphase was unadjusted. The films were deposited at a surface pressure 30 mN/m at unadjusted pH and at 15^0 C temperatures.

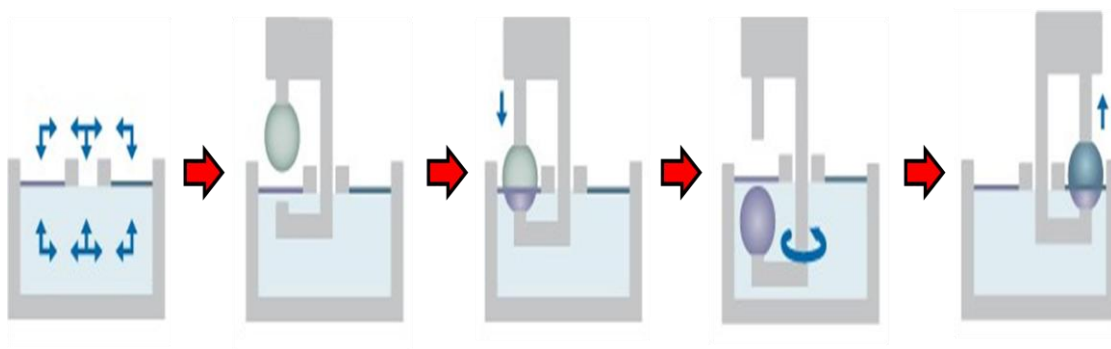


Figure 2.18: Schematic of the LB deposition mechanism in an alternating bath trough [94].

The dipping speed of the substrates was kept at 3 mm/min and the drying time during up and down stroke was varied between 30-500 secs. The substrates used for LB deposition were Si (001) hydrophilized by special treatment for good transfer of multiple monolayer onto the substrates. During the deposition process of multilayered LB films, the monolayer on water gets deposited first on the substrate and as a result the surface area of the LB monolayer on the water subphase decreases. This percentage of transfer can be defined through the transfer ratio, which is the ratio of the total surface area decrease in Langmuir monolayer to the total surface area of the film deposited on substrate [5-8]. In the ideal case this transfer ratio must be unity for perfect transfer. This ideal condition assumes that the amphiphilic molecules simply form a model of the structure on water surface onto the substrate. But in actual reality this ratio may differ from unity due to imperfect transfer or loss of molecules during deposition. Also different packing of the molecules on the substrate makes the difference from unity transfer ratio. This transfer of molecules to a great extent depends on the hydrophilicity or hydrophobicity of the substrates. Both silicon and quartz type of substrates have been used to deposit the LB films. Silicon (100) single crystals were used as a primary choice of substrate and this silicon substrate were hydrophilized using RCA cleaning procedure. According to this standard substrate cleaning method, first the substrates were treated in aqueous solution containing 30% NH_4OH and 30% H_2O_2 for 20 mins. Then

substrates were rinsed with acetone and alcohol and ultimately washed with copious amount of water. On the other hand silicon substrates can be made hydrophobic by first boiling in 'piranha' solution (conc. H_2SO_4 : 30% H_2O_2 = 70:30 by volume) for half an hour. After cooling, the substrate is subjected to the RCA cleaning procedure, washed, dried and then immersed in very dilute solution of octadecyltrichlorosilane (OTS) in acetone for 20 minutes in inert gas atmosphere to form a monolayer of OTS on this silicon. This silicon is again washed with copious amounts of acetone till no visible white condensation is observed.

In LB deposition the hydrophilic or hydrophobic part of the amphiphilic molecules simply adhere to the substrate depending on the substrate-molecule interaction. In hydrophilic substrate the head part will get attached to the substrate and so first stroke will be upstroke. For hydrophobic substrate the opposite scenario will happen and the tail part of the molecules will get attached to the substrate first. So here downstroke will be the first stroke. Depending on these situations, normally three different modes of deposition is possible, (a) Y type deposition - both upstroke and downstroke occur, (b) X type deposition - only downstroke occurs and (c) Z type deposition - only upstroke occurs [5, 6]. One might expect that by depositing X or Z type deposition, the monolayer structure can be manufactured. But it is already well known that bilayer structure is the basic unit of the LB multilayer structure of divalent or trivalent fatty acid salt except in the first layer. X and Z type of deposition of divalent or trivalent actually produce the same structure as in Y type deposition [13, 14] (See Fig. 2.19).

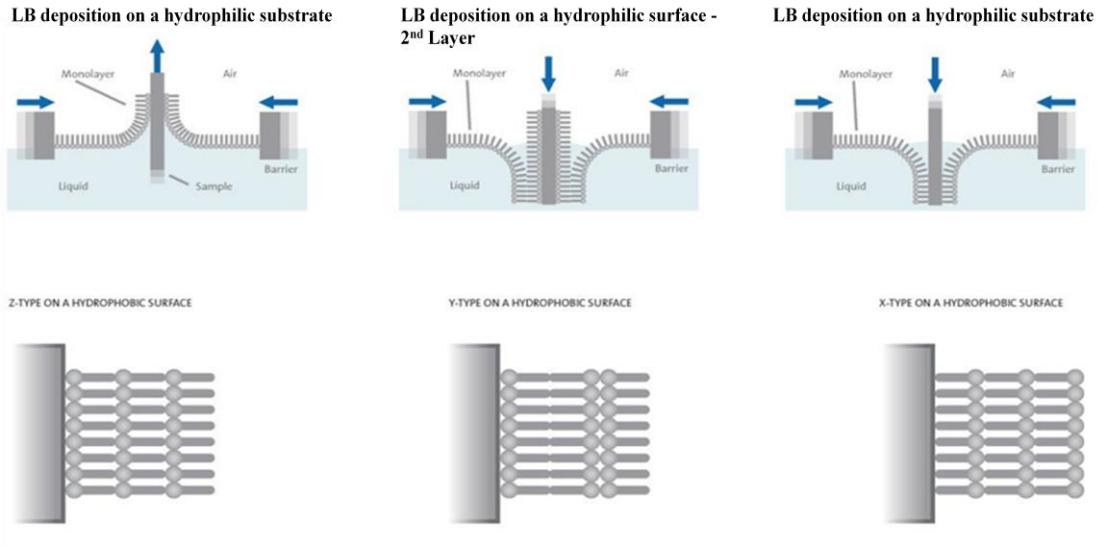


Figure 2.19: Schematic of various multi-layer LB deposition alternatives using hydrophobic and hydrophilic substrates [94].

2.4.3 X-ray reflectivity and GIXD techniques

X-Ray reflectivity method

X-ray and neutron reflectivity are generally same in principle [46,68] but their interaction with material is fundamentally different for each other. The refractive index of a material is slightly less than unity for X-ray or neutron and can be written as [48-50]

$$n = 1 - \delta + i\beta \quad (2.30)$$

The imaginary component denotes the absorption in the medium. Away from absorption edge for X-ray of the medium, in terms of electron density ρ_{el} , and mass absorption coefficient μ , these terms can be rewritten as

$$\delta_x = \frac{r_0 \lambda^2}{2\pi} \rho_{el} \quad (2.31)$$

$$\beta_x = \frac{\mu \lambda}{4\pi} \quad (2.32)$$

For neutrons

$$\delta_n = \frac{\lambda^2}{2\pi} \left[N_A \sum_i \frac{\rho_i}{A_i} b_i - \frac{m}{2\pi\hbar^2} \boldsymbol{\mu}_n \cdot \mathbf{B} \right] \quad (2.33)$$

where N_A is Avogadro's number, r_o is the classical electron radius (2.82×10^{-13} cm), λ is the wavelength of incident radiation, where b_i is the scattering length of the element i and μ_n and \mathbf{B} are the neutron magnetic moment and the induced magnetization in the medium. The magnetic contribution in neutron reflectivity will not be discussed in this section. Here we will explain the nonmagnetic part of the scattered neutron only. In most of the cases neutron absorption coefficient (β_n) is relatively small and can be neglected in reflectivity calculation. But for elements like Li, B, Cd, Sm, Gd and their isotopes with significant absorption coefficient this β_n cannot be neglected.

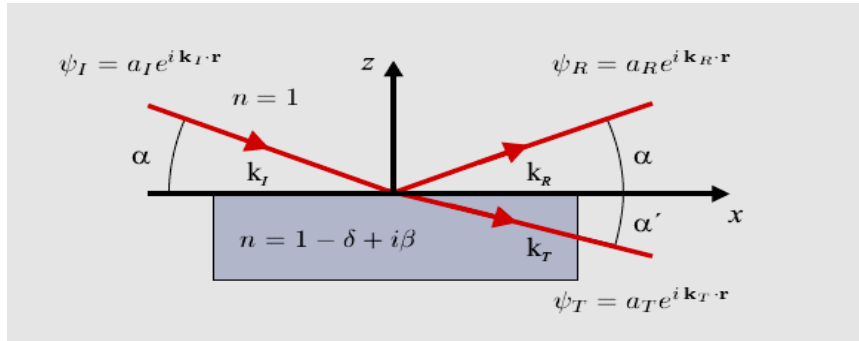


Figure 2.20: Snell's law and the Fresnel equations can be derived by requiring continuity at the interface of the wave and its derivative [70].

If a sample is irradiated by a plane wave of X-rays with incident and scattered wave vector \mathbf{k}_i and \mathbf{k}_f respectively, the momentum transfer vector is $\mathbf{q} = (\mathbf{k}_f - \mathbf{k}_i)$. In vacuum, the z component of the momentum transfer vector is,

$$q_z = \frac{2\pi}{\lambda} (\sin\theta_i - \sin\theta_r) = k_0 (\sin\theta_i - \sin\theta_r) \quad (2.34)$$

where θ_i and θ_r are incident and scattered angle (as shown in Fig. 2.20). In specular condition $\theta_i = \theta_r$, only q_z component of the momentum transfer vector q will survive (i.e., $q_x = q_y = 0$).

At air/medium interface, from Snell's law of refraction

$$\cos\theta_i = (1 - \delta)\cos\theta_r \quad (2.35)$$

As $\delta \sim 10^{-6}$, the critical angle θ_c for total reflection (i.e., when $\theta_c = 0$) will be very small and under this approximation, we can write

$$\theta_c \approx \sqrt{2\delta} \quad (2.36)$$

Using Eq. (2.36) in Eq. (2.31), the critical value of momentum transfer vector q_c can be written as,

$$q_c^2 = \left(\frac{4\pi}{\lambda}\right)^2 \theta_c^2 = 16\pi\varrho_s \quad (2.37)$$

where ϱ_s is the scattering length density of the medium and is equal to $(r_0\rho_{el})$ for X-rays and (b) for neutrons.

The reflected intensity (I_R) falls off rapidly with q^{-4} for scattering angles large compared to the critical angle $\theta_c = \sqrt{2\delta}$ [75]. A general description of reflection from N stratified homogeneous slabs is given by Parratt [72]. The situation is sketched in figure 2.21(b). In this case, the evaluation of the boundary conditions leads to a recursive formula for the reflectance of the interface, $r_{j-1,j}$, between the j^{th} and the $(j-1)^{\text{th}}$ slab.

$$r_{j-1,j} = a_{j-1}^4 \left[\frac{r_{j+1,j} + F_{j-1,j}}{r_{j+1,j} F_{j-1,j} + 1} \right], \quad (2.38)$$

where $a_j = \exp(-iq_j d_j/4)$ is the phase factor and $F_{j-1,j} = (q_{j-1} - q_j) / (q_{j-1} + q_j)$ are the Fresnel coefficients for a reflection from the interface $j-1$ and j , described by the complex momentum transfer q_j . Starting from the substrate slab N with infinite thickness and therefore with

reflectance $r_{N-1,N} = a_{N-1}^4 F_{N-1,N}$, and defining the phase factor on the vacuum side $a_1 = 1$, the recursive solution leads to the intensity reflected from the surface (See Fig. 2.21).

$$\frac{I_r}{I_0} = |r_{1,2}|^2, \quad (2.39)$$

with the incident intensity I_0 .

Since scattering at grazing angles is sensitive to the change of the index of refraction, it is sensitive to the exact electron-density profile at the surface and the interfaces of the sample.

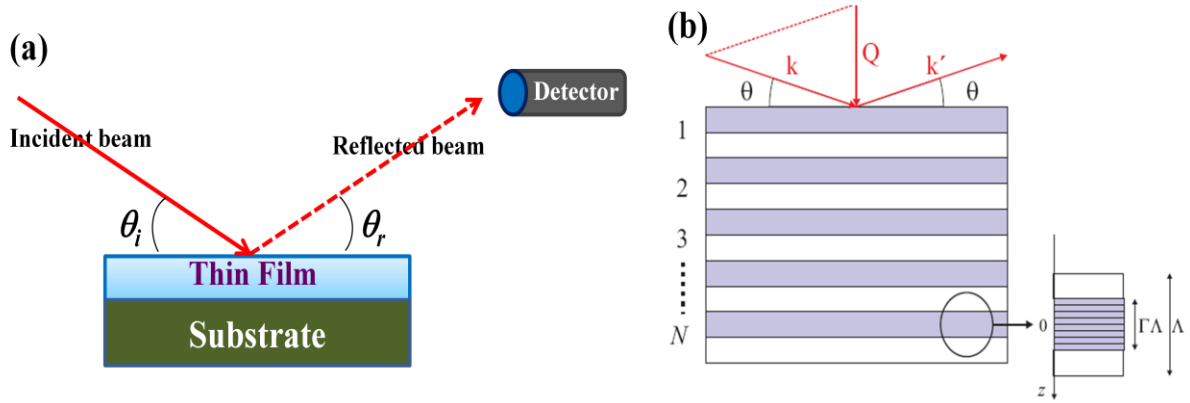


Figure 2.21: Schematic (a) scattering geometry from a monolayer on a substrate and (b) of a multilayer consisting of a stack of bilayers. Each bilayer, as shown separately to the right has a homogeneous high electron density region of thickness $\Gamma\Lambda$, and a low density region. The total thickness of a bilayer is Λ [70].

Thus, it is important to include surface and interface roughness into the model. The simplest expression can be derived in kinematical approximation, which describes the reflectivity by the Fourier transform of the electron-density profile perpendicular to the surface. While a sharp surface is described by an abrupt change of the electron-density profile, a rough surface with a height variation described by a Gaussian distribution of width σ_{rms} leads to a Debye-Waller-like damping of the reflected intensity [71, 75]

$$I_R = I_R^{\text{Fresnel}} [\exp(-q^2 \sigma_{\text{rms}}^2)], \quad (2.40)$$

The value of σ_{rms} (root-mean-square roughness) is conventionally used to express surface and interface roughness.

Grazing Incidence X-ray Diffraction (GIXD)

X-ray diffraction for studying thin films is not generally performed using laboratory X-ray sources due to low flux. With the introduction of intense and well collimated X-ray beams of tunable energy from synchrotron sources, it has become feasible to obtain direct structural information from thin films [54, 55, 56, 57, 58]. When X-rays are made to fall on a sample at an incidence angle θ_i smaller than the critical angle θ_c of the sample, the beam is subjected to total reflection and only an evanescent wave propagates [60, 61, 62]. In this grazing incidence condition, the penetration depth of the X-rays is only upto few tens of Angströms and X-rays cannot traverse further inside the medium. In this situation, X-rays become surface sensitive [54, 55, 56, 57, 58], i.e., allowing it to probe the crystalline structure in the vicinity of the surface (See Fig. 2.22). If the X-ray is incident on the sample at an angle higher than critical angle θ_c , it will get refracted from higher depth of the sample and the scattering signal will be dominated by the undesirable background noise.

The Structure Factor

As discussed in the previous section, if a sample is illuminated by a plane wave of X-rays having incident and scattered wave vector \mathbf{k}_i and \mathbf{k}_f respectively, the momentum transfer vector will be $\mathbf{q} = (\mathbf{k}_f - \mathbf{k}_i)$. Then the phase difference due to the two scattered rays from lattice points \mathbf{r}_i and \mathbf{r}_j will be $\mathbf{q} \cdot (\mathbf{r}_i - \mathbf{r}_j)$. The amplitudes of the two rays will differ by a term $\exp(i\mathbf{q} \cdot (\mathbf{r}_i - \mathbf{r}_j))$.

The amplitudes of the rays scattered at positions $\mathbf{r}_1, \mathbf{r}_2, \mathbf{r}_3, \dots, \mathbf{r}_n$ are in the ratios $e^{i\mathbf{q} \cdot \mathbf{r}_1}, e^{i\mathbf{q} \cdot \mathbf{r}_2}, e^{i\mathbf{q} \cdot \mathbf{r}_3}, \dots, e^{i\mathbf{q} \cdot \mathbf{r}_n}$, with a prefactor $f_1(\mathbf{q}), f_2(\mathbf{q}), f_3(\mathbf{q}), \dots, f_n(\mathbf{q})$ respectively for taking into

consideration the scattering contribution from different atoms. $f_j(\mathbf{q})$ represents the atomic form factor of the j^{th} atom. Hence the resultant X-ray scattered by the entire primitive cell is the sum of all individual rays and will therefore have an amplitude containing factor

$$S_q = \sum_j f_j(\mathbf{q}) e^{i\mathbf{q} \cdot \mathbf{r}_j} \quad (2.41)$$

Where S_q denotes the structure factor. In the continuum limit, the structure factor can be represented as an integration of scattered wave from every infinitesimal elements contained in volume dV by the expression,

$$S_q = \int \rho(\mathbf{r}) e^{i\mathbf{q} \cdot \mathbf{r}} d^3r \quad (2.42)$$

$\rho(\mathbf{r})$ being the electron density at position \mathbf{r} . The corresponding intensity of the Bragg peak from a lattice plane will be proportional to the square of the amplitude containing a factor $|S_q|^2$.

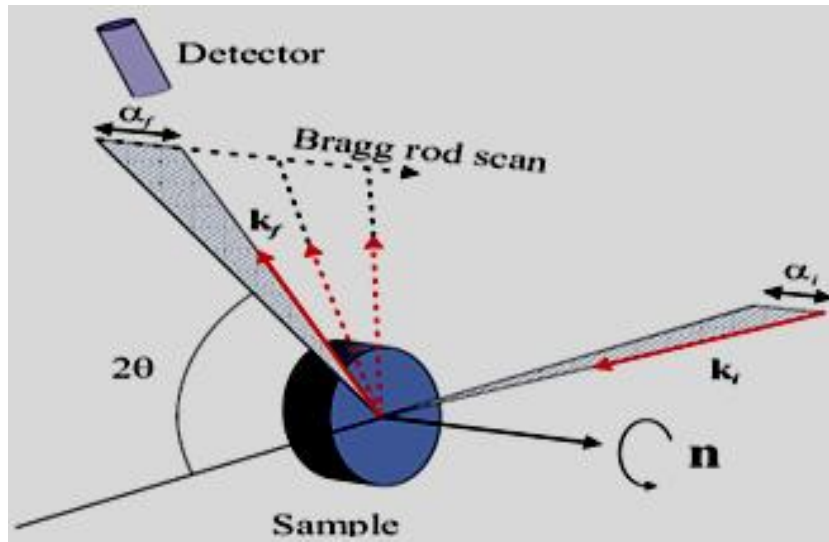


Figure 2.22: Geometry of a grazing incidence diffraction (GID) experiment from a solid single crystal surface at a synchrotron. The surface can be rotated around the surface normal 'n', and the detector can be both rotated around 'n' in the vertical plane and moved perpendicular to it so as to scan along the crystal truncation rods [70].

Surface Crystallography

The momentum transfer vector \mathbf{q}_{hk} , for an (hk) reflection, is calculated by $\mathbf{q}_{hk} = h\mathbf{a}^* + k\mathbf{b}^*$, where \mathbf{a}^* and \mathbf{b}^* represents the primitive translation vectors in the reciprocal space. If the primitive lattice vectors in real space are given by \mathbf{a} and \mathbf{b} , the intensity I_{hk} will thus be maximum when the two conditions (the Laue equations) are satisfied concurrently,

$$\mathbf{q} \cdot \mathbf{a} = 2h\pi \quad (2.43)$$

$$\mathbf{q} \cdot \mathbf{b} = 2k\pi \quad (2.44)$$

Most of the LB films of fatty acid salts which are our interest of study, have a distorted hexagonal in-plane lattice structure in room temperature [64, 58, 59]. These LB films are powder-like along the in- plane, hence \mathbf{q}_x and \mathbf{q}_y component of the momentum transfer vector \mathbf{q} cannot be determined separately, but only the combination $\mathbf{q}_{xy} = \sqrt{\mathbf{q}_x^2 + \mathbf{q}_y^2}$ can be considered. As a result, a few peaks with different (hk) may overlap in the diffraction pattern. Usually two types of unit cells are considered for analyzing the diffraction pattern in hexagonal lattice and these are the primitive parallelogram and the non-primitive centered rectangle. In our case the primitive parallelogram has been preferred for the analysis of GID data. If the molecules are ordered in a hexagonal lattice (i.e., $|\mathbf{a}| = |\mathbf{b}|$ and $\gamma = 60^\circ$), simply a triply degenerate first order peak will be observed and can be indexed as $(10 + 01 + 1\bar{1})$. On the other hand if the molecules are arranged in distorted hexagonal lattice, two first order peaks will be observed containing the doubly degenerate peak assigned to $(01 + 1\bar{1})$ peak and the nondegenerate peak as (10) peak. Finally, for molecules arranged in a oblique unit cell ($|\mathbf{a}| \neq |\mathbf{b}|$ and $\gamma \neq 60^\circ$), three non-degenerate peaks will be observed. The indexing scheme is usually assigned for the low-order peaks at first and confirmed by the

positions of higher-order peaks later. The lattice constants and A , the area per molecule, can be calculated from the relations,

$$\gamma = \cos^{-1} \frac{q_1}{2q_2} \quad (2.45)$$

$$a = \frac{2\pi}{q_1 \sin \gamma} \quad (2.46)$$

$$b = \frac{2\pi}{q_2 \sin \gamma} \quad (2.47)$$

And

$$A = ab \sin \gamma \quad (2.48)$$

where q_1 and q_2 gives the positions of the degenerate and non-degenerate peaks respectively. In the case of two-dimensional lattice of point particles, there is absence of periodicity in the direction perpendicular to the lattice plane in real-space, and hence, there is no condition to be satisfied by the out-of-plane component \mathbf{q}_z of the diffracted wave vector. In reciprocal space, this lattice will represent a two-dimensional array of vertical lines, as they are simply called ‘rods’ that extends upto infinity in the direction normal to the lattice plane. But the LB film does not consist of point like particles and the molecules have the variation in electron density along the length of the molecules and also have periodicity between different layers. The molecular degrees of freedom are tilt, orientation of the molecular structure and lattice distortion. The tilt and tilt azimuth of the unit-cell, can be calculated from the Bragg rod scan, by keeping \mathbf{q}_{xy} fixed at a peak position in \mathbf{q}_{xy} scan and scanning the \mathbf{q}_z component.

Bragg Rods

Now let us assume a cylindrical rod of length 'L' having constant electron density ρ and define \hat{n} as the unit vector along the rod length. Following Eq. (2.42), the structure factor for one such cylinder will be $[f(\mathbf{q}) \mathbf{s}_q]$, where $f(\mathbf{q})$ is the form factor for the cylinder and

$$\mathbf{s}_q = \left| \int_{-L/2}^{+L/2} e^{ix\mathbf{q} \cdot \hat{n}} dx \right| = L \left[\frac{\sin \frac{L}{2} \mathbf{q} \cdot \hat{n}}{\frac{L}{2} \mathbf{q} \cdot \hat{n}} \right] \quad (2.49)$$

This function is peaked when $\frac{L}{2} \mathbf{q} \cdot \hat{n} = 0$ and will lead to a diffraction pattern along q_z , whenever \hat{n} is tilted from the surface normal. When \hat{n} is tilted the factor $\mathbf{q} \cdot \hat{n} = u = [q_z \cos \theta - q_x \sin \theta]$, where θ is the tilt angle and q_x is the component along tilt direction. Explicitly, $q_x = |\mathbf{G}_{hk}| \cos \psi_{hk}$, where \mathbf{G}_{hk} is the reciprocal lattice vector and ψ_{hk} is the angle from \mathbf{G}_{hk} to the tilt direction \hat{n} . More detailed analysis can be done in a similar way by dividing the vertical stack of molecules in a number of cylinders of constant electron densities. Let the molecular stack be divided in a number of cylinder each of length l_j having constant electron density ρ_j and centered at $z = c_j$. Then the intensity for (hk) reflection,

$$I_{hk}(qz) = |V(x)S(\mathbf{G}_{hk}, qz)|^2 \exp[-q_z^2 \sigma^2] \quad (2.50)$$

Then the structure factor as defined above will be $S(\mathbf{G}_{hk}, qz) = \sum_j \rho_j l_j S'_j(u)$, where $S'_j(u) = \exp(-ic_j u) \sin(0.5l_j u)/(0.5l_j u)$. The Vineyard function $V(x)$ describes the interference between the diffracted and subsequently reflected waves. It show a peak at $q_z = q_c/2$. Explicitly, $V(x) = 2x$ for $x < 1$ and $= 2x/[x + (x^2 - 1)^{1/2}]$ for $x > 1$, where $x = q_z/q_c$.

The Debye-Waller factor $\exp[-q_z^2 \sigma^2]$ accounts for the surface roughness.

Indian Beamline, Photon Factory, KEK, Japan



Figure 2.23: The Indian Beamline (BL-18B) at the photon factory, KEK, Japan [95].

GID measurements were carried out at BL-18B, Photon Factory, KEK, Japan with monochromatic X-ray beam [175] (See Fig.2.23). The Photon Factory is an accelerator-based light source facility, as a part of the High Energy Accelerator Research Organization (KEK) Japan. The Photon Factory operates two storage rings; the 2.5-GeV PF Ring and the 6.5-GeV PF Advanced Ring (PF-AR). The Photon Factory supplies brilliant X-rays and VUV light, which provide the means to understand the function of materials and life. BL-18B beamline is operated by DST, India is a multi-purpose monochromatic hard X-ray station operating within 7-20 KeV. The Indian beamline at Photon Factory synchrotron radiation facility (in Japan) has been set up successfully to cater the needs of Indian scientists and research fellows in a wide variety subject areas. The project is sponsored by Department of Science and Technology (DST), Govt. of India, with Saha Institute of Nuclear Physics and Jawaharlal Nehru Centre for Advanced Scientific Research being the nodal institutes implementing the same.

GID experiments were carried using Pilatus 2D detector placed in direction to the incident X-ray beam and then moved in the horizontal direction to get the GID pattern from the sample placed on the 1st goniometer. The different components of the beamline used for the reflectivity and GID measurements are shown in Fig.2.24.

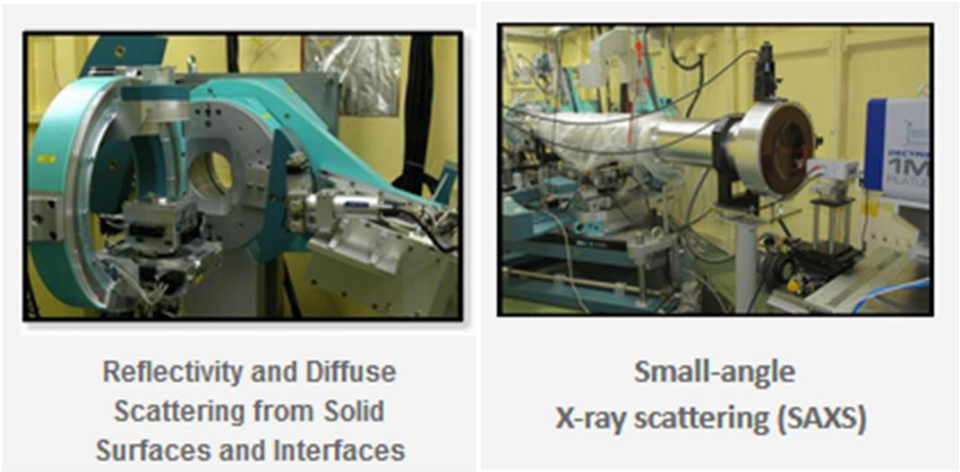


Figure 2.24: Different experimental techniques used in this thesis available at BL-18B, KEK, Japan [95].

TABLE 2.2 Comparison of factors determining the interactions of neutrons, low energy (< 10 eV) electrons, X-rays, and optical photons with magnetic materials such as the ferromagnets Fe, Co, and Ni. Listed are the combined charge and magnetic cross sections and the magnetic contribution through a fractional value for the magnetic contrast P is given. Also the incident monochromatic flux per appropriate experimental bandwidth Φ , and the relative figure of merit per atom per second, defined as $\sigma\Phi P^2$ is indicated. [66].

	technique	atomic cross-section σ [barn/atom] ^a	magnetic contrast P	incident flux Φ ^b [s ⁻¹ cm ⁻² BW ⁻¹]	figure of merit 10 ⁻⁷ $\sigma\Phi P^2$
neutrons	El. Scatt. ^c	1	1	1 × 10 ⁷	1
electrons	El. Scatt	1 × 10 ⁸	0.5	1 × 10 ¹⁰	2.5 × 10 ¹⁰
X-rays	El. Scatt.	5 × 10 ⁻²	1	1 × 10 ¹²	5 × 10 ³
	Res. El. Scatt. ^d	5 × 10 ³	0.5	1 × 10 ¹²	1.25 × 10 ⁸
	Res. Abs. ^d	5 × 10 ⁶	0.3	1 × 10 ¹²	4.5 × 10 ¹⁰
light	Kerr Effect	5 × 10 ⁶	0.01	1 × 10 ¹⁶	5 × 10 ¹¹

^a 1 barn = 10⁻²⁴ cm²

^bWe have used monochromatic fluxes with appropriate experimental bandwidths (BW). The BWs are 1% for neutrons and 0.1% for electrons and photons.

^c The nuclear and magnetic neutron cross sections are about the same.

^d Total resonant cross-section at 3d transition metal L-edge.

References:

- [1]. Franklin., B. *Phil. Trans. R. Soc.* **64**, 445 (1774).
- [2]. Pockels., A. *Nature* **46**, 418 (1891).
- [3]. Langmuir, I. *J. Am. Chem. Soc.* **39**, 1848 (1917).
- [4]. Blodgett., K. B. *J. Am. Chem. Soc.* **57**, 1007 (1935); Blodgett., K. B. and Langmuir., I. *Phys. Rev.* **51**, 964 (1937).
- [5]. Gaines., G. L. *Insoluble Monolayers at Liquid-Gas Interfaces*, (Interscience, New York, 1966).
- [6]. Ulman., A. *Introduction to Ultrathin Organic Films*, (Academic, New York, 1991).
- [7]. Roberts., G. G. *Langmuir-Blodgett Films* (Plenum Press, New York, 1990).
- [8]. Petty., M. C. *Langmuir-Blodgett Films, an introduction*, (Cambridge university press, New York, 1996).
- [9]. Kaganer., V. M., MÄohwald., H. and Dutta., P. *Rev. Mod. Phys.* **71**, 779 (1999).
- [10]. Harkins., W. D. *Physical Chemistry of Surface Films*, (Reinhold, New York, 1952).
- [11]. See the webpage, <http://www.ksvlt.com>
- [12]. Datta., A., Kundu., S., Sanyal., M. K., Daillant, J., Luzet., D. and Blot., C. *Phys. Rev. E* (in press).
- [13]. Schwartz, D. K. *Surf. Sci. Rep.* **27**, 245-329 (1997).
- [14]. Sanyal., M. K., Mukhopadhyay, M. K., Mukherjee., M., Datta, A., Basu., J. K. and Penfold., J. *Phys. Rev. B* **65**, 033409 (2002).
- [15]. Gell-Mann, M. and Goldberger, M. L. *Phys. Rev.* **96**, 1433 (1954).
- [16]. Platzman, P. M. and Tzoar, N. *Phys. Rev. B* **2**, 3556 (1970).
- [17]. De Bergevin, F. and Brunel, M. *Phys. Lett. A* **39**, 141 (1972).

- [18]. Blume, M. *J. Appl. Phys.* **57**, 3615 (1985).
- [19]. Hannon, J. P., Trammell, G. T., Blume, M. and Gibbs, D. *Phys. Rev. Lett.* **61**, 1245 (1988).
- [20]. Gibbs, D., Harshman, D. R., Isaacs, E. D., McWhan, D. B., Mills, D. and Vettier, C. *Phys. Rev. Lett.* **61**, 1241 (1988).
- [21]. Kao, C., Hastings, J. B., Johnson, E. D., Siddons, D. P., Smith, G. C. and Prinz, G. A. *Phys. Rev. Lett.* **65**, 373 (1990).
- [22]. Sacchi, M., Hague, C. F., Pasquali, L., Mirone, A., Mariot, J.-M., Isberg, P., Gullikson, E. M. and Underwood, J. H. *Phys. Rev. Lett.* **81**, 1521 (1998).
- [23]. Dürr, H. A., Dudzik, E., Dhesi, S. S., Goedkoop, J. B., van der Laan, G., Belakhovsky, M., Mocuta, C., Marty, A. and Samson, Y. *Science* **284**, 2166 (1999).
- [24]. Tonnerre, J. M., Sève, L., Raoux, D., Soullié, G., Rodmacq, B. and Wolfers, P. *Phys. Rev. Lett.* **75**, 740 (1995).
- [25]. Livet, F. *Acta Crystallogr. A* **63** 87 (2007).
- [26]. Sutton, M., Mochrie, S. G. J., Greytak, T., Nagler, S. E., Berman, L. E., Held, G. E. and Stephenson, G. B. *Nature* **352** 608 (1991).
- [27]. Livet, F., Bley, F., Mainville, J., Sutton, M., Mochrie, S., Geissler, E., Dolino, G., Abernathy, D. and Grübel, G. *Nucl. Instr. Meth. A* **451** 596 (2000).
- [28]. de Vries, R., Weijers, S., Bethke, K., Kogan, V., Vasterink, J., Kharchenko, A., Fransen, M. and Bethke, J. *Nucl. Instr. Meth. A* **576** 164 (2007).
- [29]. Ponchut, C., Clément, J., Rigal, J. -M., Papillon, E., Vallerger, J., LaMarra, D. and Mikulec, B. *Nucl. Instr. Meth. A* **576** 109 (2007).
- [30]. Livet, F. and Bloch, D. *Scripta Met.* **10** 1147 (1985).
- [31]. Livet, F., Bley, F., Létoublon, A., Simon, J. P. and Bérar, J. F. *J. Synchr. Rad.* **5** 1337 (1998).
- [32]. Abernathy, D. L., Grübel, G., Brauer, S., McNulty, I., Stephenson, G. B., Mochrie, S. G. J., Sandy, A. R., Mulders, N. and Sutton, M. *J. Synchr. Rad.* **5** 37 (1998).

- [33]. Malik, A., Sandy, A. R., Lurio, L. B., Stephenson, G. B., Mochrie, S. G. J., McNulty, I. and Sutton, M. *Phys. Rev. Lett.* **81** 5832 (1998).
- [34]. Dufresne, E. M., Nurushev, T., Clarke, R. and Dierker, S.B. *Phys. Rev. E* **65** 061507 (2002).
- [35]. Ludwig, K., Livet, F., Bley, F., Simon, J. P., Caudron, R., Bolloc'h, D. L. and Moussaid, A. *Phys. Rev.* **72** 144201 (2005).
- [36]. Livet, F. and Sutton, M. *C. R. Physique* **13** 227 (2012).
- [37]. Goodman, J. W. *New York: McGraw-Hill*, 1996, pp. 77–78.
- [38]. Thompson, B. J. and Wolf, E. *J. Opt. Soc. Amer.*, **47** 10 (1957).
- [39]. Young, T. *Course of Lectures Natural Philosophy Mechanical Arts I*.
- [40]. Chang, C., Naulleau, P., Anderson, E. and Attwood, D. *Opt. Commun.*, **182** 1 (2000).
- [41]. Bartels, R. A., Paul, A., Murnane, M. M., Kapteyn, H. C., Backus, S., Liu, Y. and Attwood, D. T. *Opt. Lett.*, **27** 9 (2002).
- [42]. Ditmire, T., Tisch, J., Gumbrell, E. T., Smith, R. A., Meyerhofer, D. D. and Hutchinson, M. H. R. *Appl. Phys. B—Lasers Opt.*, **B65** 3 (1997).
- [43]. Takayama, Y., Hatano, T., Miyahara, T. and Okamoto, W. *J. Synchrotron Radiation*, **5** 4 (1998).
- [44]. Coisson, R. *Appl. Optics*, **34** 5 (1995).
- [45]. Goodman, J. W. *New York: Wiley*, pp. 163–176 (2000).
- [46]. Russell, T. P. *Mat. Sci. Rep.* **5**, 171 (1990).
- [47]. Daillant, J. and Gibaud, A. *X-ray and Neutron Reflectivity: Principles and Applications*, (Springer, Berlin, 1999).
- [48]. Born, M. and Wolf, E. *Principles of optics*, (Pergamon Press, New York, 1985).
- [49]. Griffiths, D. J. *Introduction to Electrodynamics*, (Prentice Hall, New Jersey, 1989); Jackson, J. D. *Classical Electrodynamics*, (John Wiley and Sons, New York, 1998).

- [50]. Lekner, J. *Theory of Reflection*, (Nijhoff/Kluwer, 1987).
- [51]. Gallet, F., Deville, G., Valdes, A. and Willams, F. I. B. *Phys. Rev. Lett.* **49**, 212 (1982).
- [52]. Murray, C. A. and Wenk, R. A. *Phys. Rev. Lett.* **62**, 1643 (1989).
- [53]. Pini, M. G., Rettori, A., Pescia, D., Majlis, N. and Selzer, S. *Phys. Rev. B* **45**, 5037 (1992).
- [54]. Als-Nielsen, J., Jacquemain, D., Kjaer, K., Leveiller, F., Lahav M. and Leiserowitz, L. *Phys. Rep.* **246**, 251 (1994).
- [55]. Robinson I. K. and Tweet, D. J. *Rep. Prog. Phys.* **55**, 599 (1992).
- [56]. Dosch, H. *Evanescent X-ray and Neutron Scattering*, Springer Tracts in Modern Physics, 126, (Springer, Berlin, 1992).
- [58]. Jacquemain, D., Wolf, S. G., Leveiller, F., Lahav, M., L. Leiserowitz, Deutsch, M., Kjaer, K. and Als-Nielsen, J. *Collo. de Physique*, **C7**, 29 (1989).
- [59]. Böhm, C., Leveiller, F., Jacquemain, D., MÄohwald, H., Kjaer, K., Als-Nielsen, J., Weiss- buch, I. and Leiserowitz, L. *Langmuir*, **10**, 830 (1994).
- [60]. Warren, B. E. *X-ray Diffraction*, (Dover Publ., New York, 1990).
- [61]. James, R. W. *The Optical Principles of the Diffraction on X-rays*, (G. Bell and sons, London, 1948).
- [62]. Cowley, J. M. *Diffraction Physics*, (North Holland, Amsterdam, 1984).
- [63]. Als-Nielsen, J., Jacquemain, D., Kjaer, K., Leveiller, F., Lahav M. and Leiserowitz, L. *Phys. Rep.* **246**, 251 (1994).
- [64]. Kaganer, V. M., Möhwald, H. and Dutta, P. *Rev. Mod. Phys.* **71**, 779 (1999).
- [65]. See the webpage <http://www.saha.ac.in/web/photon-factory-home> for details.
- [66]. Stöhr, J. and Siegmann, H.C. **Magnetism: From Fundamentals to Nanoscale Dynamics**. Springer (2006).
- [67]. Felcher, G. P. *Phys. Rev. B* **R24**, 1595 (1981).

- [68]. daillant J. and Gibaud, A. *X-ray and Neutron Reflectivity: Principles and Applications*, (Springer, Berlin, 1999).
- [69]. Tolan, M. *X-ray Scattering from Soft-Matter Thin Films*, Springer Tracts in Modern Physics, 148, (Springer, Berlin, 1999).
- [70]. Als-Nielsen, J. and McMorrow, D. *Elements of Modern X-ray Physics*, (John Wiley and Sons, New York, 2000).
- [71]. Penfold, J. and Thomas, R. K. *J. Phys.: Condens.matter* **2**, 1369 (1990).
- [72]. Squires, G. L. *Introduction to the Theory of Thermal Neutron Scattering*, (Cambridge, London, 1978).
- [73]. Marshall, W. and Lovesey, S. W. *Theory of Thermal Neutron Scattering*, (Clarendon Press, Oxford, 1971).
- [74]. Lovesey, S. W. *Theory of Thermal Neutron Scattering from Condensed Matter*, (Clarendon Press, Oxford, 1984).
- [75]. Wiesler, D. G. and Zabel, H. *J. Appl. Phys.* **63**, 3554 (1988).
- [76]. Blundell. S. J. and Bland, J. A. C. *Phys. Rev. B* **46**, 3391 (1992).
- [77]. Dosch, H. *Physica B* **192**, 163 (1993).
- [78]. Zabel, H. *Physica B* **198**, 156 (1994).
- [79]. Bland, J. A. C., Daboo, C., Heinrich, B., Celinski, Z. and Bateson, R. D. *Phys. Rev. B* **51**, 258 (1995).
- [80]. Anker, J. F. and Felcher, G. P. *J. Mag. Mag. Mat.* **200**, 741 (1999).
- [81]. Kepa, H., Kutner-Pielaszek, Twardowski, J. A., Majkrzak, C. F., Sadowski, J., Story, T. and Giebultowicz, T. M. *Phys. Rev. B* **64**, 121302 (2001).
- [82]. Vettier, C. *J. Mag. Mag. Mat.* **1053**, 226 (2001).
- [83]. Mazkrzak, C. F. *Physica B* **156/157**, 619 (1989).

- [84]. Dietrich, S. and Wagner, H. *Z. Phys. B* **59**, 35 (1985).
- [85]. Shull, C. G. and Smart, J. S. *Phys. Rev.* **76**, 1256 (1949).
- [86]. Hale, M.E., Fuller, H.W. and Rubinstein, H. *J. Appl. Phys.* **30**, 789 (1959).
- [87]. Chapman, J.N. and Scheinfein, M.R. *J. Mag. Mag. Mat.* **200**, 729 (1999).
- [88]. <https://www.wmi.badw.de/methods/squid.htm>.
- [89]. Lee, J. C. T. et al. *Appl. Phys. Lett.* **109**, 022402 (2016).
- [90]. <https://www.chem.ubc.ca/resonant-soft-x-ray-scattering>
- [91]. Rosfjord, K. M., Liu, Y. and Attwood, D. T. *IEEE journal of selected topics in quantum electronics*, **10**, 6 (2004).
- [92]. Mukhopadhyay, M. K. “*Phase Transitions in Ultra-Thin Organic Films*”, Ph.D-Thesis (2005).
- [93]. <http://groups.ichf.edu.pl/kutner/research>.
- [94]. <https://www.biolinscientific.com/measurements/langmuir-and-langmuir-blodgett>.
- [95]. <http://www.saha.ac.in/web/photon-factory-home>.
- [96]. Ott, H. “*Magnetic Structures and Phase Transitions in Thin and Ultrathin Films of Heavy Lanthanide Metals Investigated by Resonant Magnetic X-Ray Scattering*”, Ph.D-Thesis (2004)

Scaling of domain cascades in stripe and skyrmion phases

In order to explain the stability of particles which is a nontrivial issue, Skyrme in 1960 proposed that the particles can be topologically protected. His theoretical formalism showed that such particles are designated by a topological number that cannot be varied by a continuous deformation of the field configuration. The particles satisfying this model are called skyrmions and have been proposed to explain hadrons in nuclear physics. Later on, such entity has also been attributed to condensed-matter systems such as the quantum Hall system, Bose condensate and liquid crystals. Around 1980 it was theoretically predicted that topologically protected particles referred to as magnetic skyrmions can also be realized in chiral magnets in the form of stable spin textures (See Fig. 3.1). Following these pioneering theoretical works, large number of recent experiments using neutron scattering, X-ray magnetic scattering, Lorentz transmission electron microscopy (LTEM) and spin-resolved scanning tunnelling microscopy has experimentally demonstrated the existence of magnetic skyrmion phases. In this chapter through a soft X-ray speckle metrology technique we have studied in detail regarding the stability of the magnetic stripe and skyrmion lattice as the external field was varied.

3.1 Introduction

Magnetic skyrmions were first experimentally discovered in MnSi sample (2009) and are multi-atom vortex-like nanometre-sized spin-swirling objects where the atoms' spin orientations change from one direction at the centre to the reverse direction at the periphery. They are topologically protected and manifest as a hexagonal lattice of spin vortices (See Fig. 3.1). Due to the presence of properties like novel Hall effects, current-driven motion with ultra-low current density and multiferroic behaviour, they are envisaged as technologically promising candidates for energy-efficient spintronic devices [6].

Various mechanisms can give rise to a skyrmion phase in a magnetic system. These are:

(1) Long-ranged dipole-dipole interactions: In thin films with perpendicular magnetic anisotropy, the dipolar interaction favours an in-plane orientation of the atomic spins, whereas the anisotropy prefers an out-of-plane direction. The competition between these two interactions results in periodic stripes in which the magnetization direction rotates in the plane perpendicular to the thin film. A magnetic field applied perpendicular to the film turns the stripe phase into a hexagonal ordering of magnetic bubbles or skyrmions.

(2) The relativistic Dzyaloshinskii–Moriya (DM) interaction: In non-centrosymmetric bulk magnets such as MnSi, $\text{Fe}_{1-x}\text{Co}_x\text{Si}$, FeGe and $\text{Mn}_{1-x}\text{Fe}_x\text{Ge}$, the transformation from the helical spiral into the triangular-lattice skyrmion crystal under an external magnetic field occurs due to the DM interaction and exchange interaction [6].

(3) Frustrated exchange interactions or (4) four-spin exchange interaction, which can lead to atomic-sized skyrmion structures.

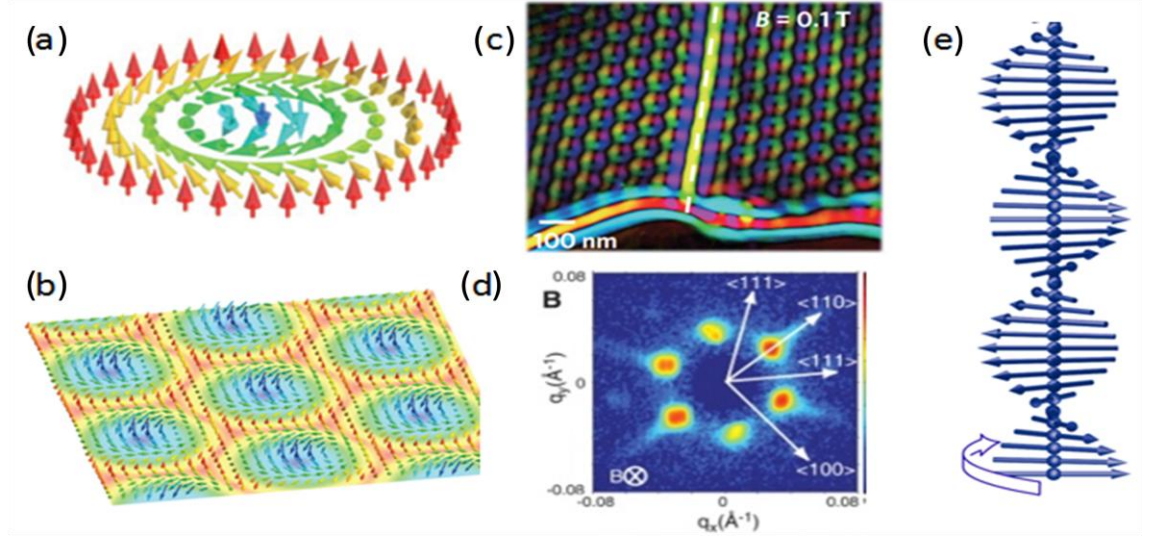


Figure 3.1: (a) illustrative diagram of a single Bloch skyrmion and (b) skyrmion lattice. (c) Real-space Lorentz TEM image of skyrmion array [36] and (d) SANS pattern from a skyrmion hexagonal lattice in reciprocal space [16]. (e) magnetic helix state in B20 crystals [19].

Skyrmion number

The swirling structure of a skyrmion is characterized by the topological skyrmion number defined by [6]

$$N_{\text{sk}} = \frac{1}{4\pi} \iint d^2\mathbf{r} \mathbf{n} \cdot \left(\frac{\partial \mathbf{n}}{\partial x} \times \frac{\partial \mathbf{n}}{\partial y} \right) \quad (3.1)$$

as the integral of the solid angle, and counts how many times $\mathbf{n}(\mathbf{r}) = \mathbf{n}(x,y)$ wraps the unit sphere [14,15]. Using the symmetry of the skyrmion, one can write

$$\mathbf{n}(\mathbf{r}) = (\cos\Phi(\varphi)\sin\Theta(r), \sin\Phi(\varphi)\sin\Theta(r), \cos\Theta(r)) \quad (3.2)$$

where we introduce the polar coordinates $\mathbf{r} = (r\cos\varphi, r\sin\varphi)$.

Putting this form into Eq. (3.1), we obtain

$$N_{\text{sk}} = \frac{1}{4\pi} \int_0^\infty dr \int_0^{2\pi} d\varphi \frac{d\Theta(r)}{dr} \frac{d\Phi(\varphi)}{d\varphi} \sin\Theta(r) = [\cos\Theta(r)]_{r=0}^{r=\infty} [\Phi(\varphi)]_{\varphi=0}^{\varphi=2\pi} \quad (3.3)$$

Accordingly, one can classify the skyrmion structures as follows. Suppose the spins point up at $r \rightarrow \infty$ while they point down at $r = 0$. Then, $[\cos\theta(r)]_{r=0}^{r=\infty} = 2$. Now, there are several possibilities for $\Phi(\varphi)$. The vorticity is defined by the integer $m = [\Phi(\varphi)]_{\varphi=0}^{\varphi=2\pi} / 2\pi$. Therefore, the vorticity determines the skyrmion number as $N_{\text{sk}} = m$, once the boundary condition at $r \rightarrow \infty$ is fixed. We further define the helicity by the phase γ appearing in

$$\Phi(\varphi) = m\varphi + \gamma \quad (3.4)$$

We show in Fig. 3.2 various skyrmion structures corresponding to vorticity $m = \pm 1$, and $\gamma = 0, \pm\pi/2$ and π , first image of Fig. 3.2 corresponds to $m = 1$ and $\gamma = \pi/2$.

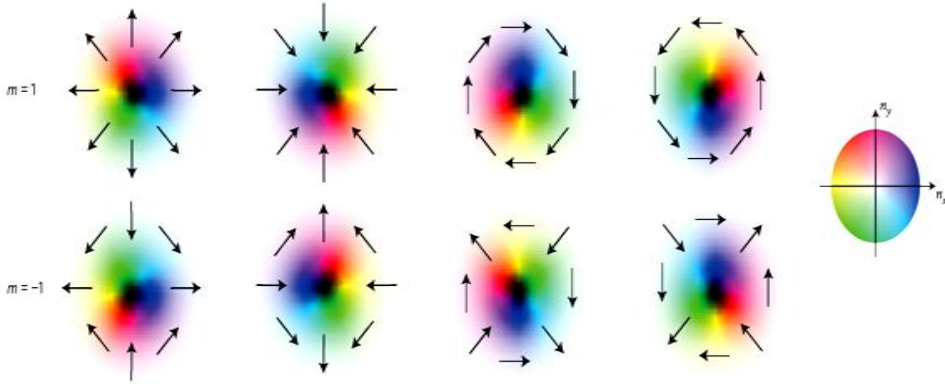


Figure 3.2: Representative of skyrmion structures with varying m and γ . The arrows indicate the direction of the in-plane spin component, and the brightness denotes the normal component to the plane, with white indicating the up direction and black the down direction. All the spin structures of the anti-skyrmions ($m = -1$) are equivalent on rotation in the x - y plane. The relative stability of each configuration is determined by the mechanism or interaction generating the skyrmion [6].

The Fe/Gd sample which we have studied comprises of disorder stripe phase, order stripe phase and also shows the presence of topologically protected phase of skyrmion lattices. Here the Gd and Fe moments are ferrimagnetically aligned and Gd provides the dominant moment within the temperature of interest. Resonant coherent X-ray scattering (RCXS) measurements were performed starting from the magnetic stripe phase observed at remanence. The remanent order stripe period is 138 ± 5 nm at room temperature. At

remanence odd-order diffraction peaks are dominated indicating that the up and down domains are nearly of equal widths. By applying an out-of-plane magnetic field resulted in appearance of both even and order diffraction peaks due to breaking of the equality. At fields around 170 mT, the intensity of all order peaks due to the stripe phase gradually started diminishing and eventually new peaks started to appear in the form of an approximately hexagonal pattern. Around 200 mT the nominally hexagonal scattering pattern became more distinct and resulted in six peaks of similar intensity. At still higher fields, the film became uniformly magnetized and all diffraction peaks disappeared.

It is well known that spin, charge, and orbital motions can be scattered by fluctuations due to external sources and leads to loss of information. Controlling and minimizing this decoherence plays a vital role in deploying quantum matter in emerging information technologies. An interesting and possible solution for such study is to employ a lattice of skyrmions. Due to the topological protected nature and existence of multiple length scale energetics, skyrmions scatter weakly from defects and can be moved relatively easily through the lattice. For this purpose we have carried out a detailed RCXS measurement within the entire magnetic phase as a function of applied field and temperature of the Fe/Gd sample to study the nature of magnetic fluctuations in topologically protected skyrmion phase and topologically trivial stripe phase [1-9].

Magnetic skyrmions provide an ideal system to probe the effect of topology on fluctuations and scaling. Skyrmions have already been found relevant in various condensed matter systems ranging from liquid crystals [12], 2D quantum Hall systems [10, 11], multiferroics [13], ferroelectrics [14] to even Bose condensates [15]. Interestingly, skyrmions in 2D magnetic systems provide unusual flexibility in measuring the behaviour of nanoscale topological features under applied fields [6, 16-18]. The topology of a skyrmion is defined in terms of its winding number, which is a quantized and conserved quantity. The topological

protection allows it to move through defects and pinning sites much more easily in comparison to the trivial stripe domains, and makes skyrmions a potential candidate for dissipation less technology and logic applications [18, 19]. Since the stability of a device depends crucially on fluctuations, it is important to understand that how topology affects the nature of abrupt domain jumps and avalanches as the applied magnetic field or the external temperature is varied. In spite of a lot of advances in materials discovery for skyrmions, still the role of it on topics pertaining to stability, abrupt jumps, domain stability have not been addressed in detail. There are very few studies which have focused on this topic, for example, in a recent theoretical study, it has been predicted through simulations that skyrmions do exhibit avalanches with power law distribution and the context of universality has been discussed [20]. Magnetic structures, such as bubble domains which are topologically trivial, have been discussed in the context of avalanches and scaling behaviour where, under the application of external magnetic field the bubble domains were found to self organize in a sub-critical state [21].

Crucial to the understanding of scaling and critical behaviour is to determine the existence of power law behaviour. Power law variation and the absence of characteristic scales are of paramount significance in understanding the emerging macroscopic properties from microscopic stochastic events [27-33]. The power laws are generally governed by different parameters such as, material microstructure, external stress, demagnetizing field, etc. If power laws obtained at different conditions over many scales share the same behaviour and can be collapsed to a unique scaling behaviour, the system is said to exhibit universality. Scaling and universality suggest that the relevant symmetries, interactions, and conservation laws affect the behaviour of the system, while many other quantitative aspects are irrelevant.

We have used resonantly tuned coherent X-ray scattering technique because it provides a unique platform to execute element-specific studies of stochastic events to

quantitatively characterize fluctuations. We have used a Fe/Gd thin film heterostructure exhibiting highly tunable stripe and skyrmion phases [22, 23] to address the topic of phase boundaries and underlying critical point in the context of topologically trivial stripe phase and topologically protected skyrmion phase. Our study has shown that even within a stripe phase an order and disorder phase is distinguished by critical points. It was observed that in the pure skyrmions phase, magnitude and frequency of domain cascades were dramatically reduced. The distribution of the cascade size although followed similar pattern as in the case of stripe phase. The divergence of correlation length was found to vary much faster for the stripes near the critical point than for the skyrmions, implying a higher degree of criticalness for skyrmions. Through a detailed analysis of the data within the framework of statistical mechanics we show that the distribution of fluctuations could be collapsed to a unifying scale. By collapsing the data over a large range of the length scale we found that the scaling parameters were distinct in the stripes and skyrmions phases indicating the presence of two separate universality classes [35]. Now all these will be discussed in much greater detail in the subsequent sections.

3.2 Experimental details

3.2.1 Sample fabrication

The samples studied were nominally $[\text{Fe} (0.34 \text{ nm})/\text{Gd} (0.4 \text{ nm})] \times 80$ multilayers deposited on Si_3N_4 membranes using DC magnetron sputtering in an ultrahigh vacuum (UHV) environment under a 3 mTorr argon environment with a 20 nm Ta seed and capping layers.

3.2.2 Resonant coherent soft X-ray scattering (RSXS)

The incident photon was linearly polarized and tuned to the Fe L3 edge (≈ 707 eV photon energy or 1.75 nm photon wavelength). Resonant coherent soft X-ray magnetic scattering patterns of the Fe/Gd multilayer are shown in Fig. 3.3e–g. Both stripe and skyrmion peaks are modulated with speckles that indicate finite-sized domain formation. We used the following field protocol consistently throughout the experiment to get to the specific phases. The sample was subjected to a magnetic field that was first raised to 500 mT, then reversed to -500 mT and finally reduced to zero before taking the measurements. The field ramp rate for the first two segments was 13 mT/s while the final drop of field from -500 mT to 0 mT took place at a rate of 380 mT/s. We started our measurement at this zero-field condition and proceeded to measure diffraction data as a function of applied magnetic field using a ramp rate of 1.575 mT/s. The above protocol was repeated at different temperatures between 85 and 300 K.

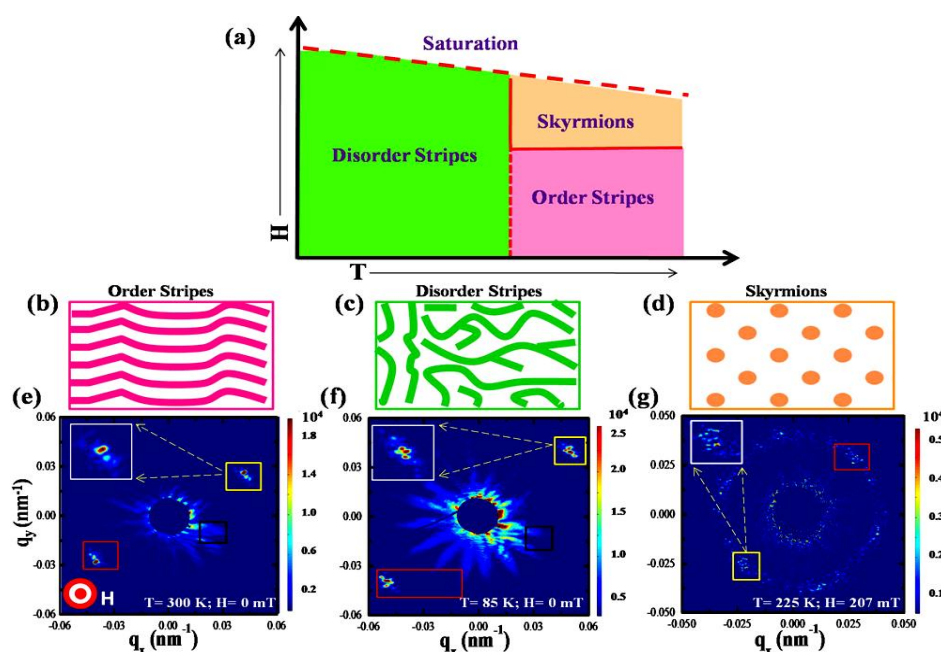


Figure 3.3: Schematic of phase diagram of the Fe/Gd sample as a function of temperature and applied magnetic field. (b–d) Schematic of order stripes, disorder stripes and skyrmion phase. (e–g) Magnetic diffraction spots in the three phases. The insets show enlarged image of the magnetic diffraction spots that are enclosed in yellow box. The red and black boxes are the regions of interest of magnetic diffraction and Airy fringes, respectively, for calculating the pair-wise correlation coefficients [35].

At room temperature an ordered stripe domain with periodicity of 138 ± 5 nm forms at zero field. Around 200 mT new peaks in the form of a distorted hexagonal pattern start to appear due to the onset of skyrmion formation. The periodicity of skyrmion hexagonal-lattice at 200 mT is 190 ± 5 nm. The ordering of the stripe was found to decrease as we lowered the temperature. At the lowest measured temperature of 85 K, we start with a disordered phase at zero-field condition. As the field is increased the diffraction spots smear into arcs indicative of formation of meandering or labyrinth stripes. The amount of field-dependent rotation of the diffraction spots decreases with increasing temperature, and stops eventually at some higher temperature where hexagonal Bragg spots appear due to the formation of skyrmions. Consequentially, there must exist a minimum temperature where there is a field-driven transition from stripe to skyrmion phase, which we have identified as $T = 205$ K. The rotation and movement of the diffraction pattern gives a hint about the presence of temperature and applied field dependent instability in the system.

To illustrate how the structure evolves from stripe to skyrmion phase, we plot in Fig. 3.4(a), 3.4(b) line scans of the diffraction data along the azimuthal direction (constant scattering momentum contour) as a function of applied magnetic field. At $T = 196$ K (near the stripe–skyrmion phase boundary), we initially obtain two diffraction spots corresponding to an ordered stripe state. The two spots persist to around 200 mT when two additional new spots appear 50° in azimuthal angle away from the original spot position. The intensity of the original spot diminishes although it does not disappear. In effect this means the stripes predominantly rotate while some stripes persist in the original direction. In contrast, the skyrmion phase at $T = 226$ K (Fig. 3.4(b)) starts with two diffraction spots corresponding to stripes and develops as field increases into six spots characteristic of the skyrmion phase.

Thus, as skyrmions form, four diffraction spots appear in addition to the two diffraction spots due to the stripes without involving any further rotations. In Fig. 3.4(c),

3.4(d) we show that diffraction peaks at zero field are much more spread out in the azimuthal direction in reciprocal space at 85 K compared to 300 K, indicating a shorter correlation length and hence a larger degree of disorder in the stripes. A contour plot of the full width half maximum (FWHM) of the stripe diffraction peak as a function of applied field and temperature in Fig. 3.4(e) shows that the degree of disorder is highest at the lowest measured temperature and decreases continuously till 230 K after which the FWHM becomes constant.

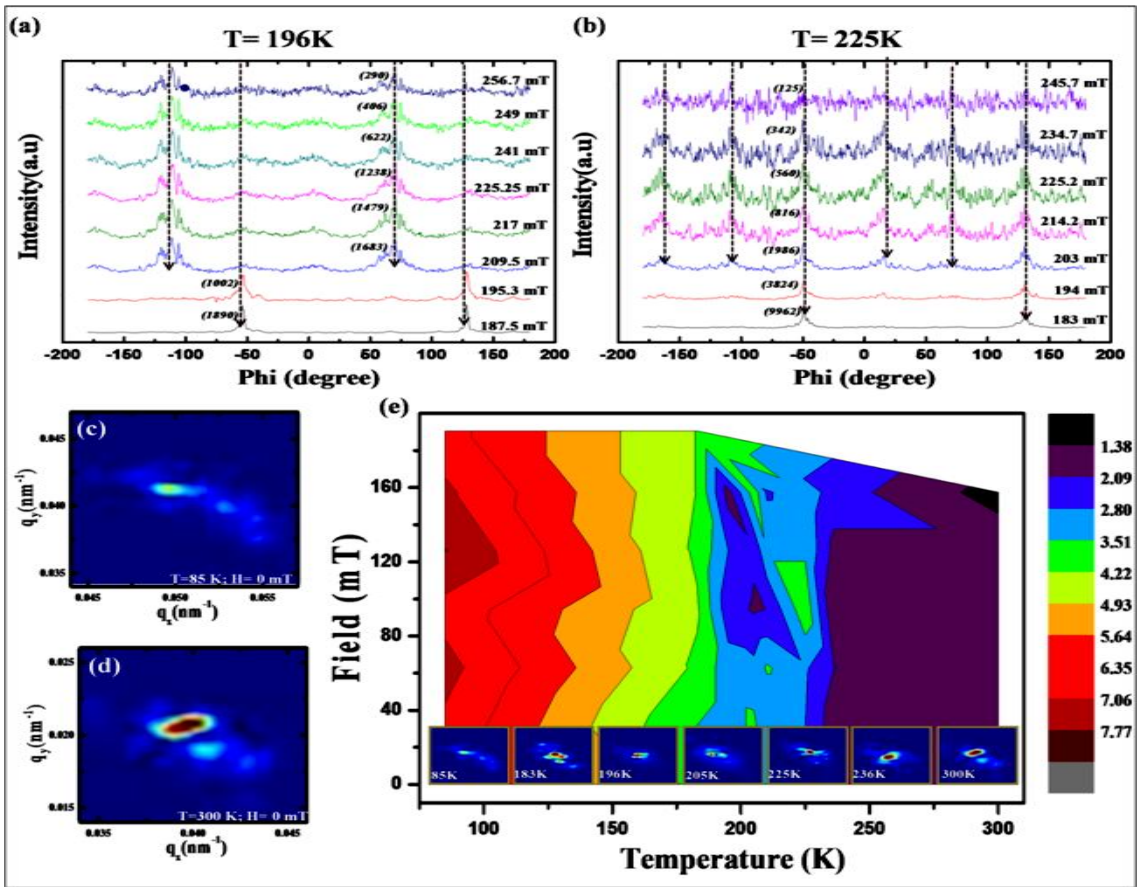


Figure 3.4: Evolution of stripe and skyrmion phase: Azimuthal variation of scattered intensity for different field values at (a) 196 K and (b) 225 K. The black dotted arrows show the position of stripe and skyrmion peaks. (c), (d) Enlarged image of the diffraction spot for disordered stripes and ordered stripes, respectively. (e) Contour plot of angular full width half maximum (FWHM) of the stripe diffraction spot along the azimuthal direction as a function of field and temperature. Color bar represents the FWHM of the diffraction spot. The FWHM is related to degree of disorder of the stripe domains. The panel inset shows representative diffraction pattern as the temperature is changed. Clear evolution from a broad pattern to a strong diffraction peak is evident [35].

Around $T = 230$ K a transition from disordered to ordered stripe is observed. We therefore conclude that our Fe/Gd undergoes a transition from disordered to ordered stripe phase at $(T_{\text{Cstripe}}, H_{\text{Cstripe}}) \equiv (230 \text{ K}, 148 \text{ mT})$ and stripe-to-skyrmion transition at $(T_{\text{Csk}}, H_{\text{Csk}}) \equiv (205 \text{ K}, 220 \text{ mT})$. The importance of these transition temperatures and fields in context of criticality will be discussed below.

The schematic of real and reciprocal space representation of stripe and skyrmion lattice is shown in the figure 3.5 below. Linear arrangement of stripes results in two intense diffraction spots. The skyrmions are arranged as hexagonal lattice in real space that manifests as six-fold diffraction pattern.

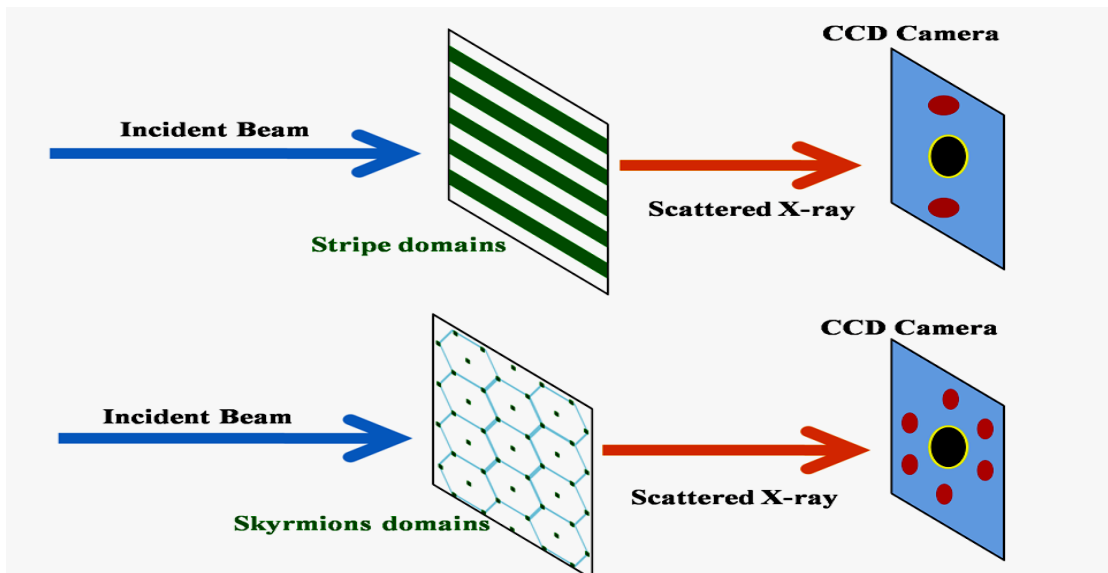


Figure 3.5: Schematic experimental arrangement and expected diffraction patterns on the detector from stripe and skyrmion domains. As the data is taken at the absorption edge that enhances magnetic scattering, red spots denote basically the magnetic diffraction peaks. The central black dot indicates the shadow of the direct-beam stopper [35].

3.3 Results and discussions

3.3.1 RSXS in stripe and skyrmion phase

A Fe/Gd thin film heterostructure exhibiting highly tunable stripe and skyrmion phases is studied using X-ray resonant coherent scattering as a function of magnetic field and temperature. Both stripe and skyrmion diffraction peaks are modulated with speckles that indicate finite sized domain formation. Resonant coherent soft X-ray scattering of a magnetic sample results in the appearance of speckle patterns due to the interference from randomly phase-shifted waves that are scattered by the magnetic domains. A speckle pattern in the reciprocal space is like a fingerprint which is unique to the specific domain configuration illuminated by the X-ray beam. If the morphology of the domains changes either spontaneously or due to an external influence, then the speckle pattern in the reciprocal space will change as well. Such a change in an X-ray speckle pattern in reciprocal space assigns a statistically significant measure of nanoscale variations in size, orientation and/or number density of the magnetic domains in real space. We have developed a statistical measure of the field-induced domain jumps by using the normalized pairwise correlation coefficient, p , a standard tool to measure the similarity of consecutive data sets.

Pairwise correlation coefficient (PCC) is calculated using the relation

$$PCC = \frac{\sum_m \sum_n (A_{mn} - \bar{A})(B_{mn} - \bar{B})}{\sqrt{(\sum_m \sum_n (A_{mn} - \bar{A})^2)(\sum_m \sum_n (B_{mn} - \bar{B})^2)}} \quad (3.5)$$

where, A_{mn} = Intensity value at m^{th} row and n^{th} column of the first image (A), \bar{A} = Average intensity value of the first image (A). B_{mn} and \bar{B} are defined in the same way for the second image (B).

The value of p is 1 for correlated and 0 for uncorrelated images A and B. For two partially correlated images we get $0 < p < 1$.

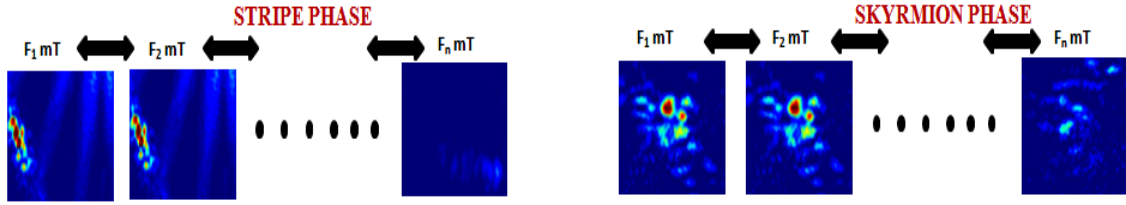


Figure 3.6: Data analysis scheme for extraction of pair-wise correlation coefficient as a function of magnetic field for the different magnetic phases.

3.3.2 Determination of stochastic domain jumps using speckle metrology

Resonant coherent soft X-ray scattering from a magnetic sample gives rise to speckle patterns due to the interference of randomly phase-shifted waves that are scattered by the magnetic domains. A speckle pattern is a fingerprint, unique to the specific domain configuration illuminated by the X-ray beam. If the domain morphology changes either spontaneously or due to an external influence, then the speckle pattern will change as well. Such a change in an X-ray speckle pattern in reciprocal space provides a statistically significant measure of nanoscale changes in size, orientation and/or number density of the magnetic domains in real space. We developed a statistical measure of field-induced domain jumps with the normalized pairwise correlation coefficient, p , a standard tool to measure the similarity of data sets (See Fig. 3.6(a)). Specifically, we correlated consecutive speckle patterns, collected near the magnetic Bragg peaks discussed above, as the field was swept. If $p = 1$ for particular pairs of consecutive speckle patterns, then the domain patterns are the same and no jump has occurred. By contrast, $p < 1$ indicates a change in speckle pattern and domain morphology, and the magnitude of the drop of p from unity quantifies the magnitude

of change in the domain morphology. This is shown graphically in Fig. 3.7 for a large domain jump with $p = 0.61$, for which the change in the speckle pattern is readily apparent. The evolution of domain states under applied magnetic fields results through a collection of different physical mechanisms. If we were to perform pair correlations that take into account all potential field-dependent (e.g. stripe domain phase, coexisting stripe, and skyrmion phase) domain morphologies, then the resulting scaling laws would be complex and the dynamics from each phase could not be distinguished. (In Figs. 3.9 and 3.10 we show simulation of jumps appearing due to position change and size change of domains.) Here, we performed analysis of pair correlations in distinct pure phases, namely stripe phases and the skyrmion phase using a well-established mean field model of avalanche dynamics. A magnetic material magnetizes in a phase through a series of jumps under slowly changing external field with no characteristic size scale, similar crackling happens in many systems when pushed slowly. The statistical formalism used here has been making rapid progress to predict behavior of such systems on long scales of length and time, independent of many microscopic details.

Figure 3.8(a) – 3.8(c) shows the variation of the pairwise correlation coefficient of two consecutive datasets as a function of magnetic field in the ordered stripe, skyrmion, and disordered stripe phases, respectively. The correlation curve of stripe phase shows multiple sharp drops (jumps) indicating abrupt changes in the topological configuration of domains (red curve in Fig. 3.8(a)). The onset of the jump is the point at which the slope of the correlation curve changes from zero or positive to negative while the position of a jump is defined as the value of the magnetic field where the slope of the correlation curve sharply changes its sign from negative to positive. The correlation curves were repeated for more than 100 hysteresis loops at each temperature to build up statistics. The appearance of the abrupt jumps is reminiscent of domain avalanches/cascades observed in Barkhausen events.

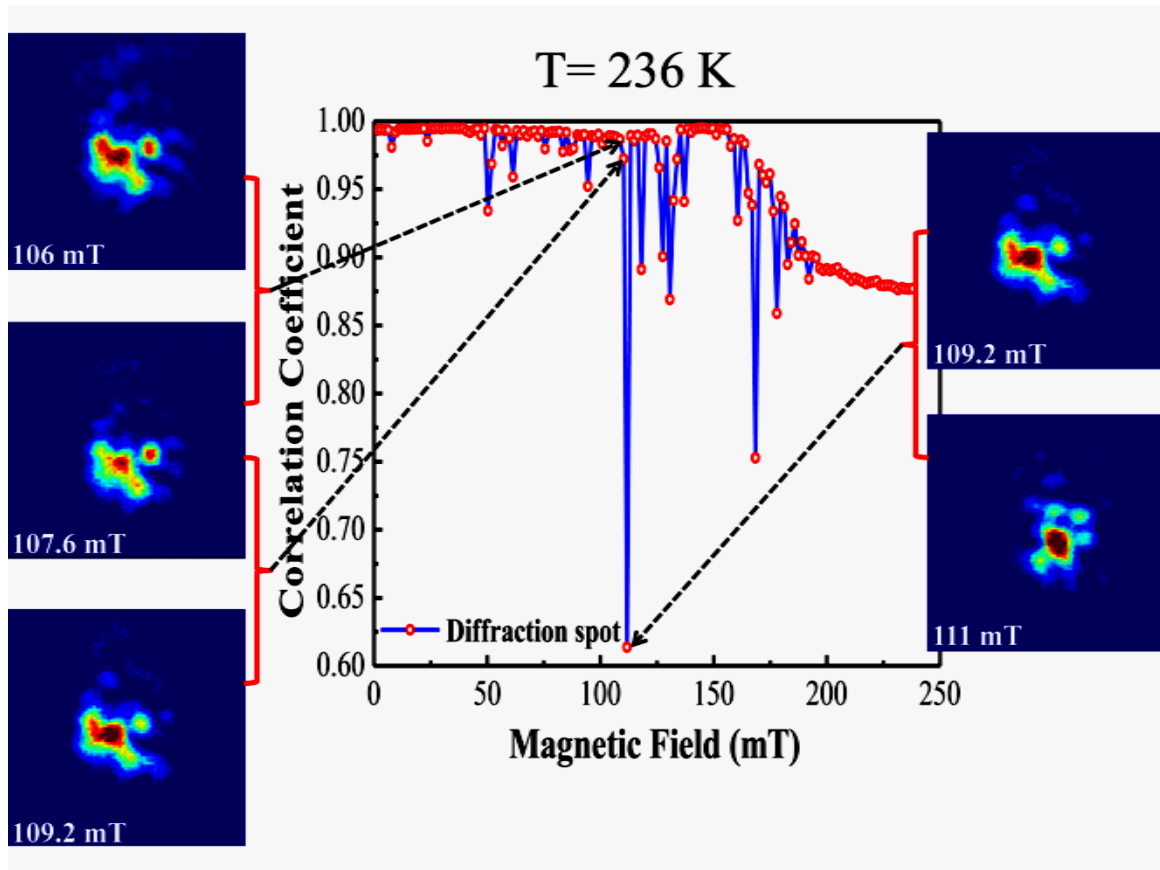


Figure 3.7: Pair-wise correlation coefficient: Pair-wise correlation function (blue line) versus perpendicular magnetic field. We show the speckle pattern at $T = 236$ K for four consecutive field values that produces small and big jumps. The speckle patterns are represented within an area of 90 by 90 pixels. Large change in speckle pattern gives rise to large magnitude of jump indicating a large change of domain morphology [35].

By using the above relation of *PCC* we obtained direct experimental evidence that the magnitude and frequency of jumps in the skyrmion phase is significantly reduced in comparison to those in the stripe phase, both order and disorder (for example, compare magnitude of jumps in Fig. 3.8(b) with Fig. 3.8(a) and 3.8(c)). The reduced jump size and jump frequency is most likely the outcome of the stability due to topologically protective nature of the skyrmions.

In the disordered stripe phase the size of the jumps are smaller at lower field values, but at higher applied field large jumps dominate (Fig. 3.8(c)). Interestingly, large and more cascades appear in the same field region where the skyrmions would appear for $T \geq 205$ K.

Since the characteristics of jumps are representative of a phase, a change in average jump size indicates a phase change and may have an underlying critical point.

A contour plot of the average jump size $\langle X \rangle$ as a function of field and temperature is a simple way to visualize the jump characteristics and ascertain probable presence of critical points. In Fig. 3.8(d) a contour plot is shown spanning all the three magnetic phases present in the sample as a function of field and temperature. The contour plot depicts that the average size of jumps increase with both temperature and field. By approaching from any direction in the contour plot it is observed that in the stripe phase, the average jump size shows a maximum value near the point $T \sim 225$ K and $H \sim 148$ mT, indicating the presence of a critical point in temperature and field around these values. The green region inside the contour plot (Fig. 3.8(e)) shows the temperature-field conditions where all the six peaks are of same intensity thereby representing the pure skyrmion phase. The pure skyrmion phase is surrounded by bigger jumps indicating presence of mixed phases, which is in close agreement with the line scan shown in Fig. 3.8(a). As shown before in the line scans (Fig. 3.8(a-c)), the magnitude of jumps is similar in both ordered and disordered stripes, however, the average jumps size in the skyrmion phase is almost an order-of-magnitude smaller than in the stripe phase. The stability of the incident beam is indicated by the horizontal black line in Figs. 3.8 (a-c) in all the three phases. The pair-wise correlation function from the region occupied by Airy fringes shows nearly perfect correlation between consecutive frames with negligible fluctuations. This confirms the stability of the beam throughout the experimental time.

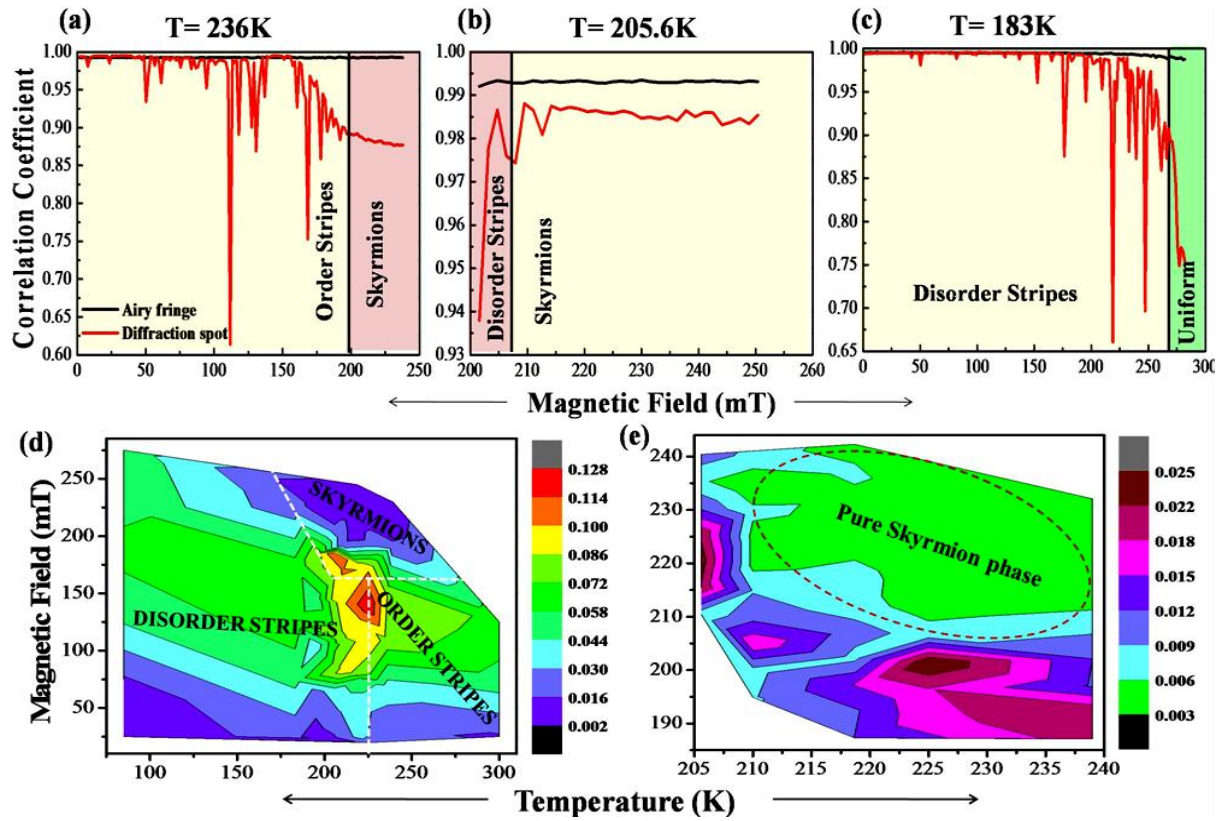


Figure 3.8: Plot of cross-correlation function (red line) versus magnetic field for (a) Stripe, (b) Skyrmion and (c) Disorder stripe diffraction spots. The black line in the figures corresponds to the correlation value from non-magnetic region (Airy fringes). Correlation between two consecutive image patterns was done for those regions as mentioned in Fig.3.3 with the corresponding color boxes. Color bar represents average jump size. Contour plot of average jumps size X as a function of field and temperature for (d) entire magnetic phase and (e) skyrmion phase only. A peak in the jump size in Fig. 3.8 (d) (red area \approx 225 K, 150 mT) suggests a critical point [35].

In order to understand the specific role of the changes in size, orientation and/or number density of the magnetic domains in real space we have carried out simple simulations. We have carried out simulations to calculate the pair-wise correlation coefficient (PCC) using a model comprising of two magnetic domains of rectangular shape in real space (See Fig. 3.9 and 3.10 below). Each yellow rectangular box corresponds to an intensity normalized to one while the blue background has zero intensity. Next we performed Fourier transform (FT) of the 2D real space image of the rectangular magnetic domains and generated the corresponding 2D diffraction pattern in the reciprocal space. The reciprocal image was generated within a region of 1024 by 1024 pixels. By varying the position and size of the

domains separately through random number generation we have created diffraction patterns for 100 different images. Furthermore, by changing the centre of the diffraction pattern which corresponds to a change in the lattice parameter, we have created a set of real space images and the FT of those real space images was generated. Then a small region was selected about the centre of the diffraction pattern and the pair-wise correlation coefficient was calculated between two such regions of consecutive images with variation to size, position and centre separately for 100 images. The generated correlation plots resemble the PCC plots obtained from the experimental data.

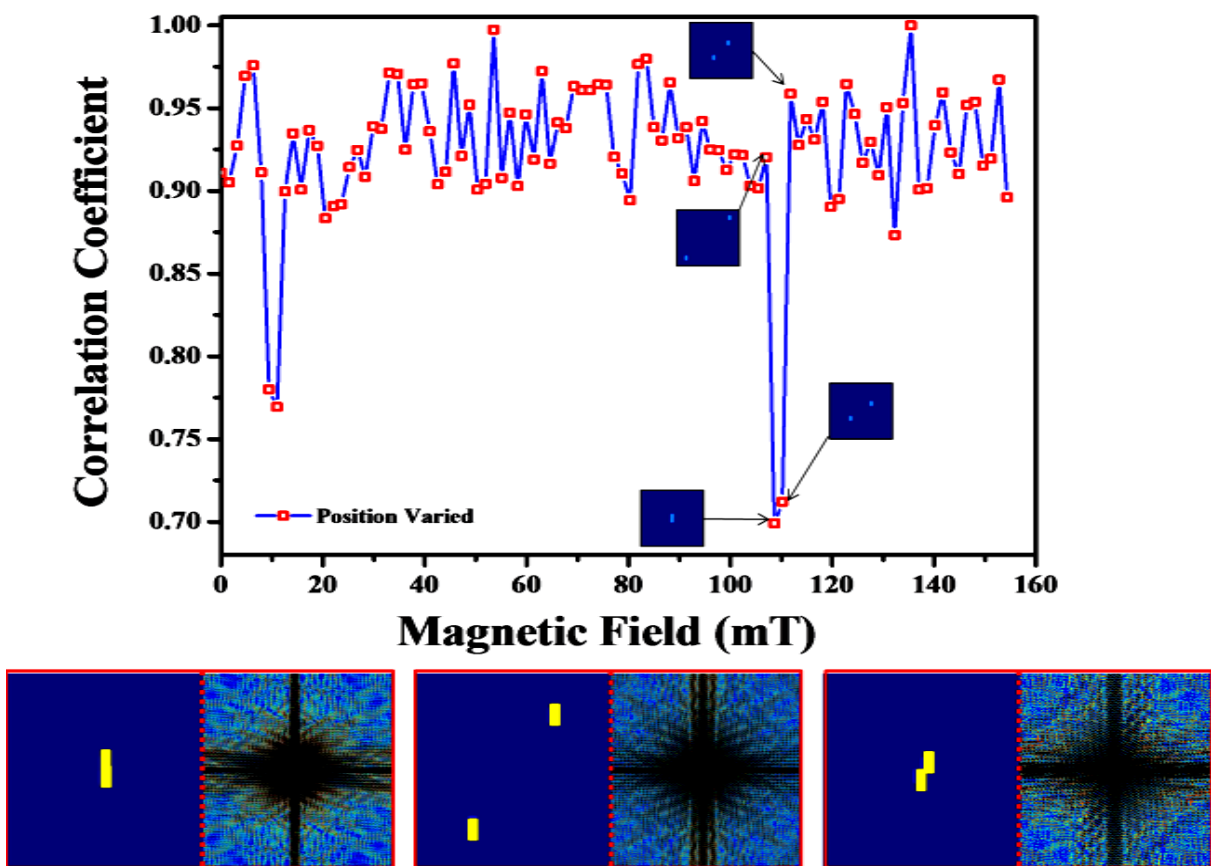


Figure 3.9: Plot of Correlation coefficient (*PCC*) between two consecutive diffraction images with variation of position. The x-axis corresponds to the image number which is assumed to vary due to applied magnetic field (1.575mT/image). Insets inside the plot shows a sequence of real space images comprising of two stripes (light blue squares) whereby there is a drastic change in the value of the simulated correlation coefficient. The images below show the real space images and the corresponding diffraction pattern. The plots show the presence of sharp jumps [35].

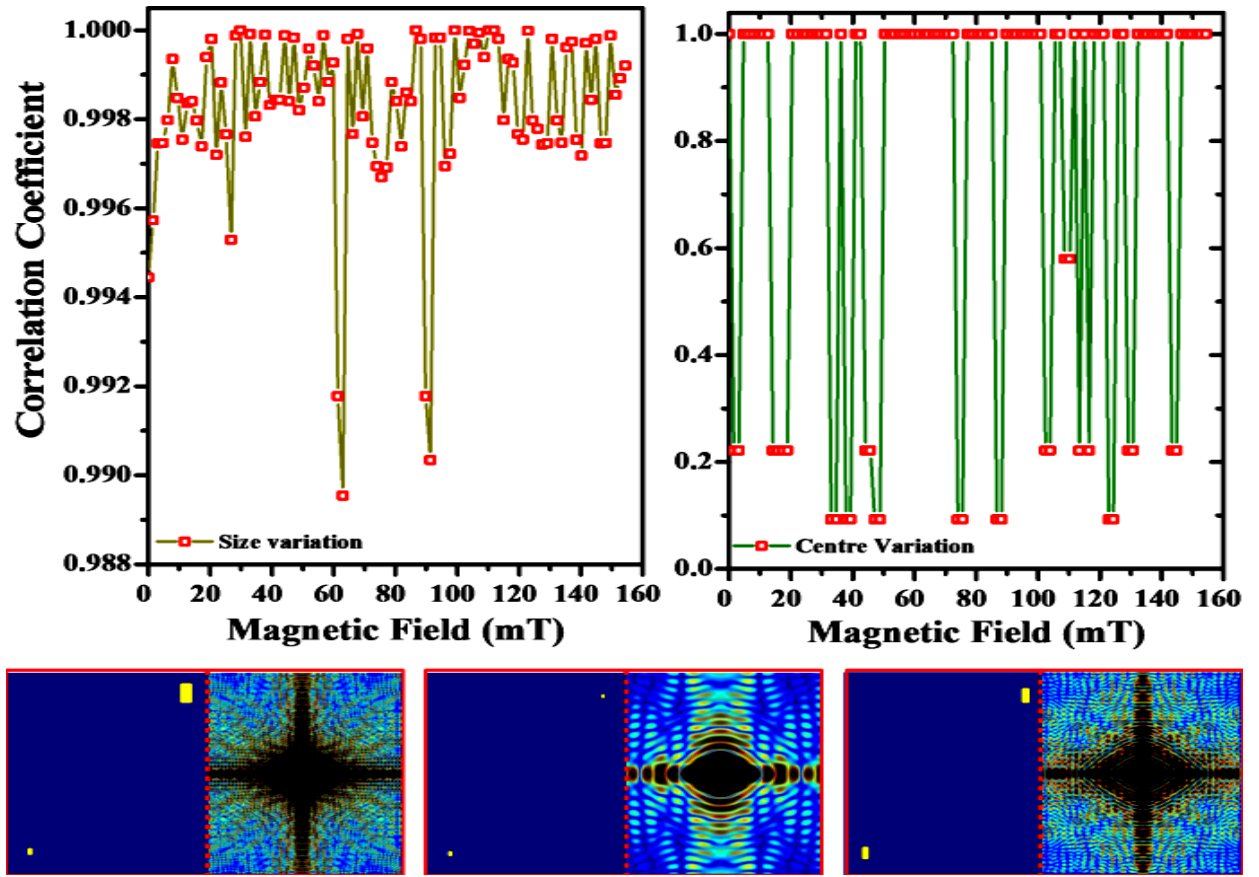


Figure 3.10: Plot of Correlation coefficient between two consecutive diffraction images with variation to size and lattice parameter. The x-axis corresponds to the image number which is assumed to vary due to applied magnetic field (1.575mT/image). The real space images are shown below with the corresponding diffraction patterns [35].

3.3.3 Scaling behaviour of stripe and skyrmion domains

Distribution of the Jumps as a function of its size at 300 K is shown in figure 3.11 below. The number of Jumps is extracted from the pair-wise correlation plots from over 100 field cycles. From the distributions we have calculated the cumulative distribution function (CDF) and the complementary cumulative distribution function (CCDF), defined a

$$P_n = \frac{c_n}{\sum_{n=1}^N c_n} \quad (3.6)$$

$$CDF = \sum_{n=1}^N P_n \text{ \& } CCDF = 1 - CDF$$

Where, C_n = Number of counts at the n^{th} bin, N = total number of bins in the histogram and P_n = probability distribution function of the n^{th} bin. In order to make the scaling function independent of the bin size and to minimise the effect of fluctuations at low counts we have done the statistical part using the complementary cumulative distribution function (CCDF) analysis scheme.

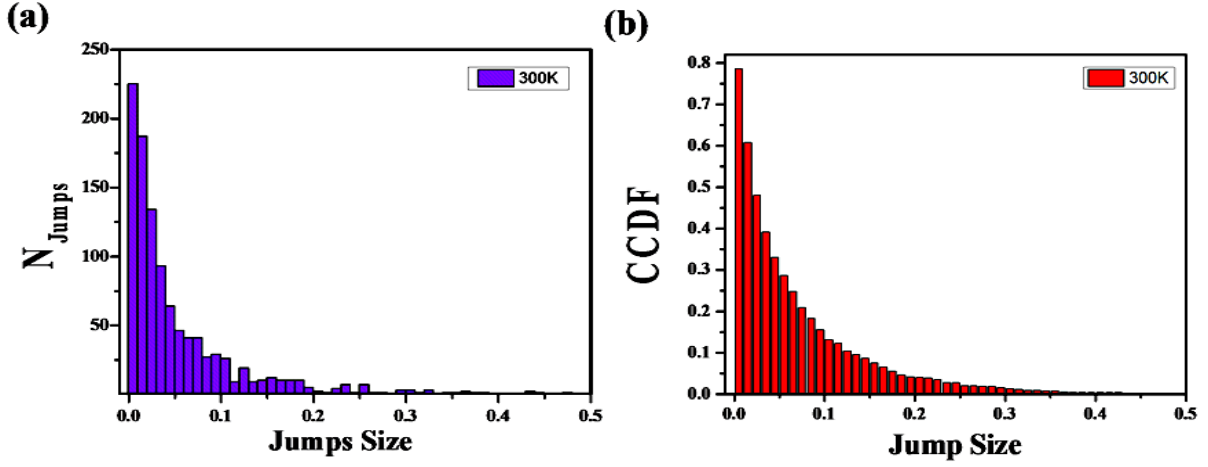


Figure 3.11: (a) Histogram showing the number of Jumps as a function of Jump size. (b) Histogram of CCDF as a function of Jump size [35].

To test criticality, we make an assumption that there is presence of a critical point where the moments of the avalanche size distribution become maximum. If there is an existence of a critical point, i.e. a non-equilibrium phase transition, then the mean field model for avalanche dynamics can be used in such case according to Ref. [34], which has already been tested in several systems like earthquakes, nanocrystals, and granular materials [33]. According to the avalanche model, the distribution of jump sizes is expected to have the following general behaviour

$$Z(X, T, H) = X^{-a} f_1(X|T - T_c|^{\frac{1}{n_T}}, X|H - H_c|^{\frac{1}{n_H}}) \sim X^{-a} f\left(\frac{X}{X_{max}}\right) \quad (3.7)$$

where X denotes the jump size T_C , H_C corresponds to the critical temperatures and fields, respectively, and, n_T and n_H are critical cut-off exponents, respectively, and $X_{max} \sim (\xi(T-T_C, H-H_C))^{1/\sigma\nu}$ is the maximum (cutoff) jump size with $\xi(t, h)$ denoting the correlation length that diverges at the critical point, with $t \equiv |T - T_C| \rightarrow 0$ and $h \equiv |H - H_C| \rightarrow 0$. The critical exponents n_T and n_H are related to how the correlation length grows as one approaches the critical point along the T or H direction. $1/\sigma\nu$ is the fractal dimension of the jumps, and the universal scaling function $f(x)$ is expected to decay exponentially as $f(x) = Ae^{-Bx}$, with A and B being non-universal constants.

According to Eq. (3.7), the distributions follow a power law up to the maximum jump size cut off values given by $X_{Tmax} \sim |T - T_C|^{\frac{1}{n_T}}$ for $H = H_C$ and $X_{Hmax} \sim |H - H_C|^{\frac{1}{n_H}}$ for $T = T_C$.

Further, we can also obtain cumulative distribution function (CCDF) given by,

$$CC(X, T, H) = X^{-(a-1)} g_1\left(\frac{X}{X_{Tmax}}, \frac{X}{X_{Hmax}}\right) \sim X^{-(a-1)} g\left(\frac{X}{X_{max}}\right) \quad (3.8)$$

where, $g(x) \sim x^{a-1} \int_x^\infty e^{-A't} \cdot t^{-a} dt$, with A' being a non-universal constant.

From eqn. (3.7) we can derive the relation for the average size of the jumps, $\langle X(T) \rangle = \int_0^\infty X Z(X, T) dX$, which at $H = H_C$ is given by $\langle X(T) \rangle \sim |T - T_C|^{(a-2)/n_T}$. Analogously, for temperature $T = T_C$ we obtain $\langle X(H) \rangle \sim |H - H_C|^{(a-2)/n_H}$.

We have calculated the CCDF of the Number of Jumps (NOJ) *i.e.* $CCDF = 1 - CDF$ and plotted it as function of Jump Size in log-log scale (Details are given in Fig. 3.11). Figures 3.13(a) and 3.13(b) show the CCDF for the stripe phase, at a fixed magnetic field $H_{C \text{ stripe}}$, for temperatures below and above $T_{C \text{ stripe}}$ respectively. Similarly, the CCDF at fixed temperature $T_{C \text{ stripe}}$ for fields below and above $H_{C \text{ stripe}}$ are shown in Fig. 3.13(d) and 3.13(e), respectively.

The average value of the jumps and jumps squared was determined. First, we used the equations below to fit our data to obtain the critical exponents ‘ a ’ and ‘ n ’ (See Fig. 3.12). After that, we used the obtained critical exponents to collapse the data as shown in Fig. 3.13 and Fig. 3.14 in this chapter for stripes and skyrmions, respectively

$$\frac{\langle X^2 \rangle}{\langle X \rangle} \propto \Delta^{-1/n} \quad (3.9)$$

$$\langle X^2 \rangle \propto \Delta^{(a-3)/n} \quad (3.10)$$

$$\langle X \rangle \propto \Delta^{(a-2)/n} \quad (3.11)$$

where,

$$\Delta = |T - T_C|, \text{ or } \Delta = |H - H_C|$$

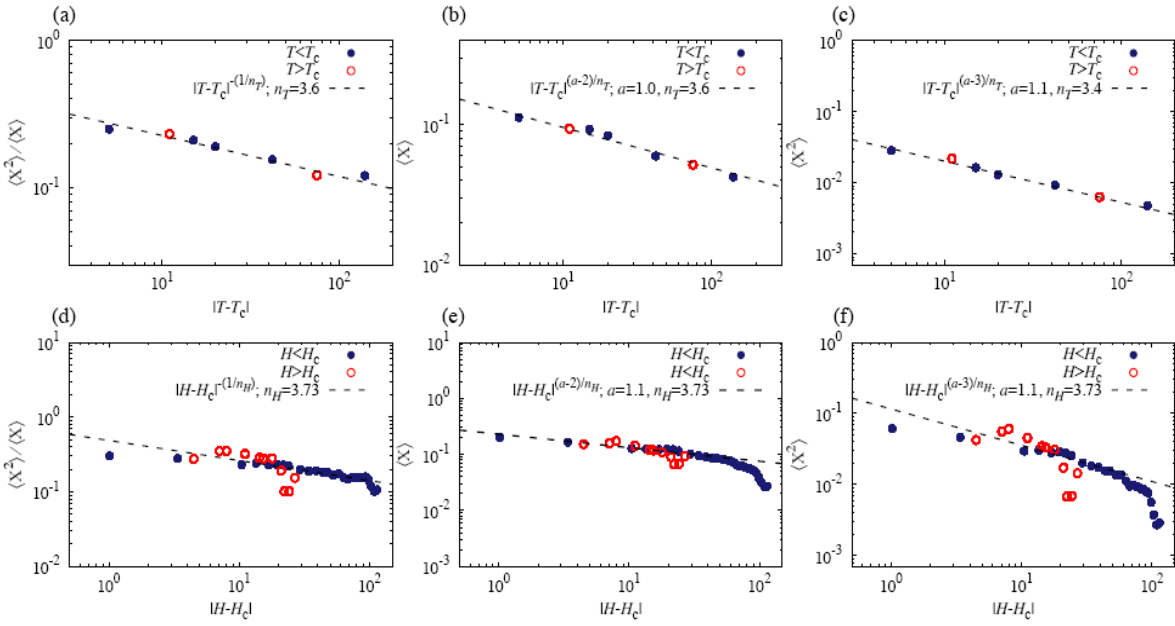


Figure 3.12: Above plots are shown for the stripe phase only. The first row corresponds to the critical field ($H_c=148$ mT) for temperatures below and above the critical value for $\frac{\langle X^2 \rangle}{\langle X \rangle}$, $\langle X \rangle$ and $\langle X^2 \rangle$, respectively. The second row is generated at the critical temperature ($T_c=225$ K) for fields below and above the critical value. Similar procedures are followed for the skyrmion phase also [35].

In the inset of Fig. 3.13(c) we plot $\langle X(T) \rangle$ versus $|T - T_{C \text{ stripe}}|$ at $H = H_{C \text{ stripe}}$, and fit the data to obtain the critical exponents $a_{T \text{ stripe}} = 1.1 \pm 0.2$ and $n_{T \text{ stripe}} = 3.4 \pm 0.6$. We find same critical exponents for both $T < T_{C \text{ stripe}}$ and $T > T_{C \text{ stripe}}$ cases. The obtained values of

critical exponents were used to collapse the data using eqn. (3.8). Fig. 3.13(c) shows the collapse for all the distributions presented in Fig 3.13(a) and 3.13(b). Similar results are shown as a function of H for the case of $T = T_{C \text{ stripe}}$ in the inset and main panel of Fig. 3.13(f), where the critical exponents were found to be $a_{H \text{ stripe}} = 1.1 \pm 0.3$ and $n_{H \text{ stripe}} = 3.73 \pm 1.0$.

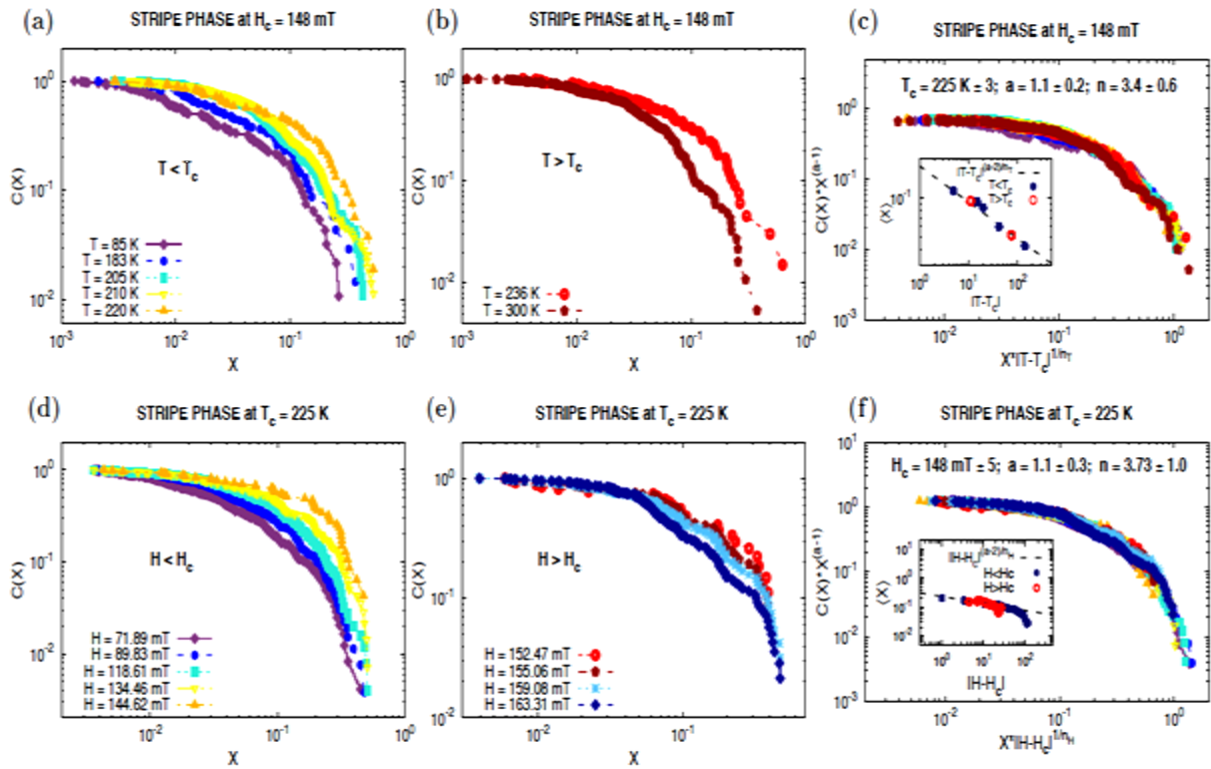


Fig. 3.13: (a,d) and (b,e) Complementary cumulative distribution ($C(X)$) function of domain cascades in the stripe phase below and above the critical points. (c) and (f) The corresponding scaling collapse with the critical exponent values [35].

A similar analysis was performed for the skyrmion phase (shown in Fig. 3.14). We found that the critical exponents that collapsed the data best at $H = H_{C \text{ sk}} = 220$ mT are $a_{T \text{ sk}} = 1.1 \pm 0.3$ and $n_{T \text{ sk}} = 2.06 \pm 0.5$, while at $T = 205$ K $\sim T_{C \text{ sk}}$, we obtained the critical exponents values of $a_{H \text{ sk}} = 1.1 \pm 0.2$ and $n_{H \text{ sk}} = 0.5 \pm 0.2$.

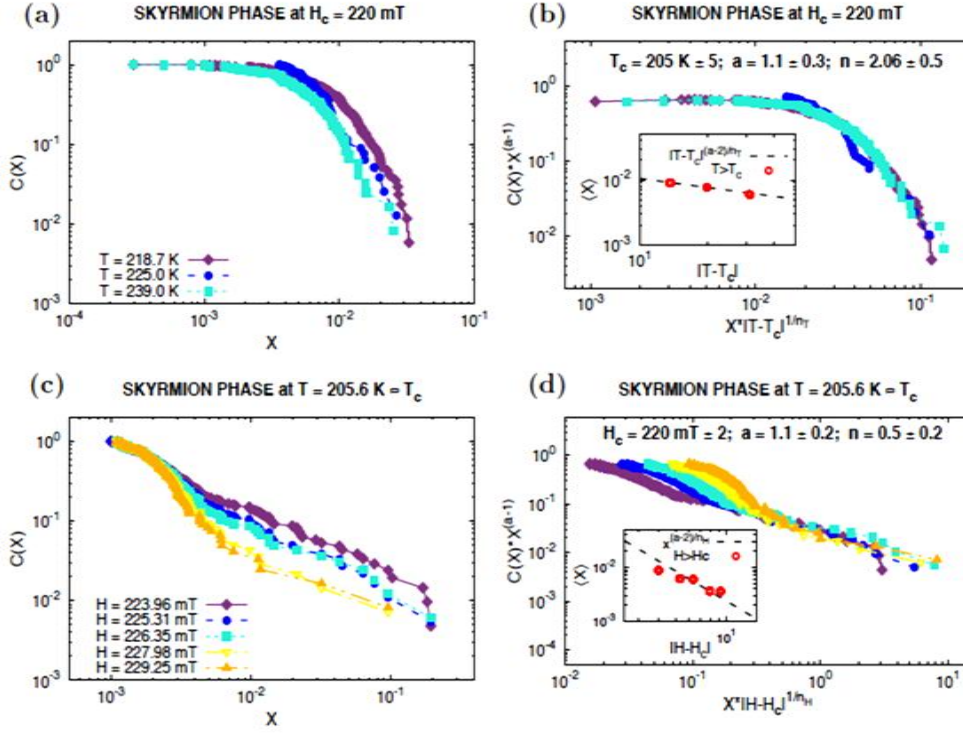


Fig. 3.14: (a) and (c) Complementary cumulative distribution ($C(X)$) function of domain cascades in the skyrmion phase above the critical points. (b) and (d) The corresponding scaling collapse with the critical exponent values [35].

Our analysis was done according to the avalanche model and it clearly shows critical behaviour for both stripes and skyrmion phase that is centred on different critical field and temperature. The critical exponent ' a ' has a similar value for both phases, but exponent ' n ' takes different value for stripes compared to skyrmions. The similarity of the exponent ' a ' suggests that near the critical point the distribution of avalanche sizes for both stripes and skyrmions follows roughly the same power law distribution although the magnitudes are much different. The difference in the n_H and n_T exponents between stripes and skyrmion, on the other hand, suggests that the divergence of the correlation length is much faster in one case than the other. Since all the critical exponents are not same for both the phases, this indicates that stripes and skyrmions belong to different universality classes.

3.4 Conclusion

One of the most important findings of this work from the behavior of the jumps or cascades is that once the skyrmion phase sets in there is hardly any noticeable evidence of sudden or drastic change in the periodicity, orientation or number density of the distorted hexagonal lattice as is the case in stripe phase where sharp changes are observed in both order and disorder states. Till date experimental studies have not reported the exact nature of changes occurring in such topologically protected skyrmion phase relative to the size, morphology or number density. It is most likely that due to the topological protection that allows skyrmions to move easily through the lattice is also the reason that the domain walls are not pinned and consequently show smaller magnitude and frequency of jumps with respect to the stripe phase.

Our theoretical analysis of the jump data on the basis of mean field avalanche model clearly shows critical behavior for both stripes and skyrmion phase that is positioned around different critical field and temperature. It is observed that the critical exponent a has a similar value for both stripe and skyrmion phases, whereas the cut-off exponent n_H have different value for stripes in contrast to skyrmions. The similarity of the exponent a in the scaling function suggests that close to the critical point the size distribution of the avalanche in both stripe and skyrmion phase roughly follows the same power law behaviour even though the magnitudes are much different. Since long-range dipolar interactions play an important role in the Fe/Gd heterostructure [22], it is not surprising that the value of the exponent a comes out to be similar in all the magnetic phases. It is reported that dipolar interaction in addition to frustration lead to small power law exponents a in other avalanche type systems: for

example the Sherrington Kirkpatrick avalanche model gives an exponent value of $a = 1 \pm 0.1$, which is very close to our findings [37].

On the other hand the difference in the n_T and n_H exponents between stripes and skyrmion, suggests that the correlation length diverges much more rapidly in one case than the other. Since all the critical exponents of the scaling function are not identical for both the phases, this indicates that stripes and skyrmions belong to different universality classes. Apart from average size of the jumps, which is a non-universal quantity, we can therefore use the avalanche statistics and universal exponents n_H for distinguishing stripes and skyrmions.

Distinctly separate critical fields H_C and temperatures T_C indicate differences in energetic that govern the formation of stripes and skyrmions. It is well established that stripe and skyrmion lattice have different symmetry and dimensionality. One can conclude that the reasons for anomaly in jump size and critical exponents could be attributed to differences in dimensionality. A stripe represents a one-dimensional structure whereas a skyrmion is a two-dimensional lattice. Results in Fig. 3.8 suggest that under the application of an external magnetic field, stripe domains undergo large avalanches while skyrmions become locally distorted. Since it is known that the skyrmion winding number needs to be conserved, which makes them move relatively smoothly through lattice, the domain walls are weakly pinned leading to a small magnitude of jumps. As a consequence, topology and dimensionality affects the dynamic behavior of stripe and skyrmion phases.

Apart from field induced domain fluctuation that was observed, thermal fluctuations are most likely to get enhanced near the critical temperature. Future studies will be focused more towards understanding the nature of the disorder-order transition particularly that involves meron and skyrmion spin textures [38]. Indeed, study of magnetic fluctuations as a function of time will enable us to determine “correlation function” that may shed light into

formation of skyrmions. It will be exciting and important to perform similar such studies on a Dzyaloshinskii-Moriya based skyrmion system and evaluate the critical nature of the helical and skyrmion state. Beyond magnetic systems, our X-ray based versatile technique can be applied to a wide variety of condensed matter system such as liquid crystals, polymers, ferroelectrics to directly study stochasticity and scaling behavior at the nanometer scale regime.

References:

- [1]. Salje, E. K. H. and Dahmen, K. A. *Annu. Rev. Condens. Matter Phys.* **5**, 233–254 (2014).
- [2]. Middey, S. et al. *Annu. Rev. Mater. Res.* **46**, 305–334 (2016).
- [3]. Tokura, Y. (CRC Press, 2000).
- [4]. Kivelson, S., Bindloss, I. and Fradkin, E. *Rev. Mod. Phys.* **75**, 1201–1241 (2003).
- [5]. Torchinsky, D. H., Mahmood, F., Bollinger, A. T., Božović, I. and Gedik, N. *Nat. Mater.* **12**, 387–391 (2013).
- [6]. Nagaosa, N. and Tokura, Y. *Nat. Nanotech.* **8**, 899–911 (2013).
- [7]. Huang, E. W. et al. *Science* **358**, 1161–1164 (2017).
- [8]. Laliena, V. and Campo, J. *Phys. Rev. B* **96**, 134420 (2017).
- [9]. Sethna, J. P., Dahmen, K. A. and Myers, C. R. *Nature* **410**, 242–250 (2001).
- [10]. Sondhi, S. L., Karlhede, A., Kivelson, S. A. and Rezayi, E. A. *Phys. Rev. B* **47**, 16419–16426 (1993).
- [11]. Lilliehöök, D., Lejnell, K., Karlhede, A. and Sondhi, S. L. *Phys. Rev. B* **56**, 6805–6809 (1997).
- [12]. Bogdanov, A. N., Röbner, U. K. and Shestakov, A. A. *Phys. Rev. E* **67**, 016602 (2003).
- [13]. Seki, S., Yu, X. Z., Ishiwata, S. and Tokura, Y. *Science* **336**, 198–201 (2012).
- [14]. Yadav, A. K. et al. *Nature* **530**, 198–201 (2016).
- [15]. Ho, T. L. *Phys. Rev. Lett.* **81**, 742–745 (1998).

- [16]. Muhlbauer, S. et al. *Science* **323**, 915–919 (2009).
- [17]. Jiang, W. J. et al. *Phys. Rep.* **704**, 1–49 (2017).
- [18]. Yu, X. Z. et al. *Proc. Natl. Acad. Sci.* **109**, 8856–8860 (2012).
- [19]. Fert, A., Reyren, N. and Cros, V. *Nat. Rev. Mater.* **2**, 17031 (2017).
- [20]. Díaz, S. A., C. Reichhardt, C., Arovas, D. P., Saxena, A. and Reichhardt, C. J. O. *Phys. Rev. Lett.* **120**, 117203 (2018).
- [21]. Bak, P. and Flyvbjerg, H. *Phys. Rev. A* **45**, 2192–2200 (1992).
- [22]. Miguel, J. et al. *Phys. Rev. B* **74**, 094437 (2006).
- [23]. Montoya, S. A. et al. *Phys. Rev. B* **95**, 024415 (2017).
- [24]. Lee, J. C. T. et al. *Appl. Phys. Lett.* **109**, 022402 (2016).
- [25]. Bak, P. and Mukamel, D. *Phys. Rev. B* **19**, 1604–1609 (1979).
- [26]. Bak, P. and von Boehm, J. *Phys. Rev. B* **21**, 5297–5308 (1980).
- [27]. Urbach, J. S., Madison, R. C. and Markert, J. T. *Phys. Rev. Lett.* **75**, 276–279 (1995).
- [28]. Zapperi, S., Cizeau, P., Durin, G. & Stanley, H. E. *Phys. Rev. B* **58**, 6353–6366 (1998).
- [29]. Puppini, E. *Phys. Rev. Lett.* **84**, 5415–5418 (2000).
- [30]. Perkovic, O., Dahmen, K. and Sethna, J. P. *Phys. Rev. Lett.* **75**, 4528–4531 (1995).
- [31]. Ryu, K. S., Akinaga, H. and Shin, S. C. *Nat. Phys.* **3**, 547–550 (2007).
- [32]. Yang, S. and Erskine, J. L. *Phys. Rev. B* **72**, 064433 (2005).
- [33]. Uhl, J. T. et al. *Sci. Rep.* **5**, 16493 (2015).

- [34]. Dahmen, K., Ben-Zion, Y. and Uhl, J. T. *Phys. Rev. Lett.* **102**, 175501 (2009).
- [35]. Singh, A., Lee, J. C. T., Avila, K. E., Chen, Y., Montoya, S. A., Fullerton, E. E., Fischer, P., Dahmen, K. A., Kevan, S. D., Sanyal, M. K. and Roy, S. *Nat. Comm.* **10**:1988 (2019).
- [36]. Yu, X. Z., Kanazawa, N., Onose, Y., Kimoto, K., Zhang, W. Z., Ishiwata, S., Matsui, Y. and Tokura, Y. *Nature Materials*, **10**, 106 (2010).
- [37]. Pázmándi, F., Zaránd, G. & Zimányi, G. T. *Phys. Rev. Lett.* **83**, 1034 (1999).
- [38]. Yu, X. Z. et al. *Nature* **564**, 95 (2018).

Modulated periodicities and Devil's staircase in an amorphous magnetic thin film

Self-organization of magnetic domains on surfaces and interfaces has attracted considerable recent interest because it manifest in regular atomic scale structures, important in both fundamental and technological aspect.

Self organized structures appear in nature whenever a system spontaneously chooses a preferred structure size and geometry due to minimization of energy. Behaviour of magnetic domains is a basic instance of complexity in materials science which has been the subject of a long and abiding series of research in condensed matter physics. Understanding the nature of magnetic domains gives insight into fundamental interactions that give rise to different magnetic phases. Resonant X-ray magnetic scattering offers a versatile technique to probe the magnetic structure in Fourier space and provides the ensemble average properties of the magnetic domains. Further, by using coherence property of the incident X-ray photons we can study the speckle pattern due to the interference of randomly phase shifted waves that are scattered by the domains. The speckle patterns are fingerprints of the domain structure and therefore reveal heterogeneity of the magnetic texture.

4.1 Introduction

Stripe patterns appear in a wide variety of materials, extending from biological to strongly correlated electron systems. The common mechanism behind stripe formation in most system is a natural tendency to balance two or more different phases that appear because of competing interactions. In case of ferromagnetic thin films, the competition between short-range exchange and long-range dipole–dipole interactions results in periodic stripes in which the magnetization self organises in up and down magnetized bands. In antiferromagnets, however, due to absence of finite magnetization that could facilitate long-range interactions between magnetic domains, the stripe formation is not expected. In some cases like in biological membranes, stripe modulation may also appear due to the coupling between different order parameters that is governed primarily by short-range forces. Similar mechanisms can also appear in antiferromagnets and may be active in other strongly correlated electron systems like in high-temperature superconductors, where the competition between charge-stripe ordering and superconductivity has become increasingly evident.

In a seminal work by Kooz and Enz in 1960 on single crystal of bulk $\text{BaFe}_{12}\text{O}_{19}$ by using optical Faraday effect the domain configuration and magnetization process was studied in presence of external applied magnetic field. They developed a theoretical formalism to understand the behaviour of magnetic domains in applied fields [1].

Magnetic domains for a long time have played a dominant role in data storage devices due to the presence of the domain structure. In such devices the magnetic structure is generally confined in the nanometer length regime for energy efficient applications. Newer techniques has paved way to exploit the strong magneto-optical contrast at certain absorption edges which in turns gives deeper insight into the study of magnetic structures in real space:

transmission X-ray microscopy (TXRM) [2-4] and photoelectron emission microscopy (PEEM) have been able to image magnetic structures with resolutions in the 10 nm range [5-8]. On the other hand techniques like X-ray resonant magnetic scattering (XRMS), probes the magnetic structure in reciprocal space and presents the ensemble averaged properties of the magnetic structure [9-10]. In this chapter we discuss new aspects of X-ray resonant magnetic scattering through a detailed analysis of data on the evolution of stripe domains in amorphous Fe/Gd films under perpendicularly applied magnetic fields.

Stripe domains are meandering domain patterns found in thin films displaying perpendicular anisotropy (PMA), in which the magnetization self-organizes in alternating up and down magnetized bands. They result from the competition between the local exchange and anisotropy interactions that favour a single saturated domain state with the long ranged demagnetizing dipolar field that tends to break up this single domain, at the cost of the creation of domain walls. Given the right combination of thickness and magnetic properties, highly correlated up and down domains form. In their seminal work on stripe domains, Kooy and Enz [1] found accurate expressions for the width of the up and down domains in perpendicular fields, assuming infinitely thin domain walls. However, when the film thickness is comparable to the domain period, the structure of the domain wall has to be considered. Thus, closure domains can form, further minimizing the dipolar energy [16] and altering the domain wall energy. To some extent, these effects have been incorporated in extensions of the Kooy and Enz model [11-15]. Alternatively, the true domain structure can be calculated accurately using micromagnetic finite element methods which, however, require the stripe period as an input parameter. Given this situation, high resolution experimental data are required to further test these models.

4.2 Commensurate phases, incommensurate phases and the Devil's staircase

Modulated structures with periods which are incommensurable (or high-order commensurable) with the basic lattice are quite common in condensed-matter physics. The structure may be another lattice, a periodic lattice distortion, a helical or sinusoidal magnetic structure, or a charge density wave in one, two or three dimensions.

Let us consider a model as shown in figure 4.1 which consists of an array of atoms connected with harmonic springs interacting through a periodic potential of period b . A simple example will be an interacting gas atoms adsorbed on a crystalline substrate. Despite its extreme simplicity the model exhibits most of the features which will be discussed in the subsequent part.

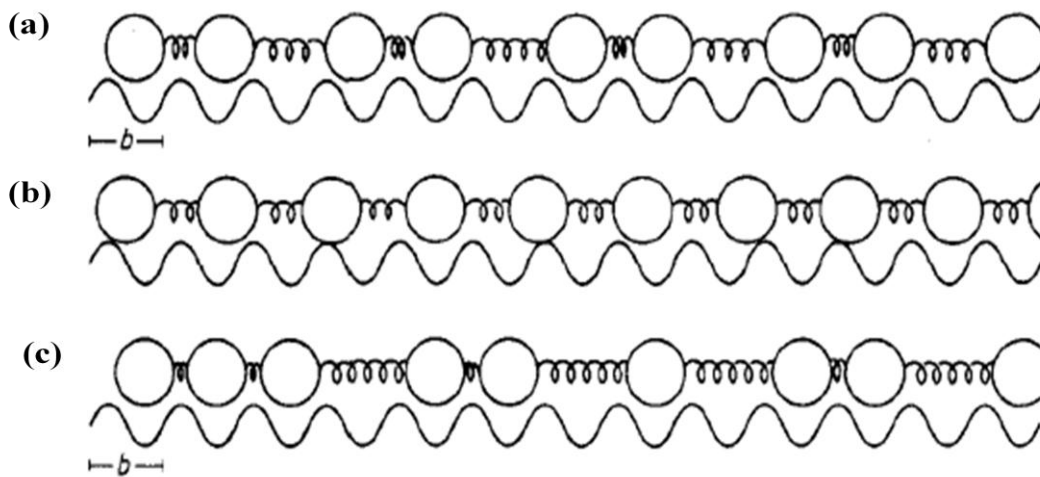


Figure 4.1: The one-dimensional FVdM model. The springs represent interactions between atoms, the wavy line the periodic potential. (a) Commensurate structure, (b) incommensurate structure, (c) chaotic structure.

The model with a cosine potential was initially introduced by Frenkel and Kontorowa (1938) [21], and it was latter studied extensively by several authors, in particular by Frank and Van

der Merwe (1949) [17], Theodorou and Rice (1978) [18], Aubry (1979) [60], Greene (1979) [19] and Bak (1981) [20].

The Hamiltonian of the model may be taken to be:

$$H = \sum_n \frac{1}{2b^2} (x_{n+1} + x_n + a_0)^2 + V(1 - \cos \frac{2\pi}{b} x_n) \quad (4.1)$$

where x_n gives the position of the n th atom. If the periodic potential, V , is absent then the harmonic term would favour a lattice constant a_0 which; in general, may be incommensurable with b . In such condition the adsorbed lattice forms an incommensurate (I) structure (Fig. 4.1(b)). In a diffraction experiment this results in the formation of Bragg spots (or sheets) at positions $Q = 2\pi N/a_0$, where N is a integer. These spots doesn't coincide with the Bragg spots formed due to the periodic potential at positions $G = 2\pi M/b$, where M is another integer. If the potential is dominant enough it may favour the lattice to relax into a commensurate (C) structure in which the average lattice spacing, a , will be a simple rational fraction of the period b . Figure 4.1(a) depicts such a situation where $2a = 3b$. This results in the atoms gaining potential energy at the cost of the elastic energy. The diffraction pattern due to the substrate and the adsorbed layer has an infinite number of coinciding Bragg peaks (sheets).

Even in the case where the potential is not sufficiently strong to force the chain into a commensurate structure, the potential will always try to modulate the chain. The atoms will move towards the minima position. The average periodicity may advance to a simple commensurate value, but still remain incommensurate. In the most general case of incommensurate structure the position of the n th atom may be written [22, 60] in the form:

$$x_n = na + \alpha + f(na + \alpha) \quad (4.2)$$

where α represents a phase and f is continuous and periodic function of period b . Here a being the average distance between atoms (which in general is different from a_0) and f

represents the modulation of the chain owing to the potential. Since the energy is independent of α , the chain is not locked to the potential. The symmetry of incommensurate systems, as well as the continuous symmetry related to α , has been explained in the elegant work of Janner and Janssen (1977). The Bragg peaks are at positions

$$Q = \frac{2\pi M}{b} + \frac{2\pi N}{a} \quad (4.3)$$

The spots at non-vanishing N thus form satellites around the diffraction spots from the basic lattice. Experimentally it is not possible to differentiate between a high-order commensurate structure and an incommensurate structure. Since the commensurate numbers are everywhere dense one may consider that the incommensurate phase will always be unstable with respect to a few nearby high-order commensurate phase. However, the commensurate and incommensurate structures do not satisfy all the stable configurations as there are additional chaotic structures which cannot be explained by the Eq. (4.2). The diffraction pattern corresponding to such condition is not composed of well-defined Bragg spots. It is not hard to imagine that such structures are possible by nature, although an accurate prediction requires some very complex mathematics. For example let us consider the situation where the potential is very strong in contrast to the elastic term. Clearly there exist metastable states where the atoms are distributed in a random way amongst the potential minima. An example of such a structure is shown in Fig. 4.1(c) where the chaotic phase gets ‘pinned’ to the potential. In contrast to the incommensurate phase it is not possible to move the lattice without overcoming a potential barrier. In this respect the chaotic phase is quite similar to the commensurate phase, although the average period is generally incommensurate with the potential. On the other hand a fascinating works shows that if the atoms are charged, the incommensurate phase would be conducting whereas chaotic phase becomes insulating [46, 20].

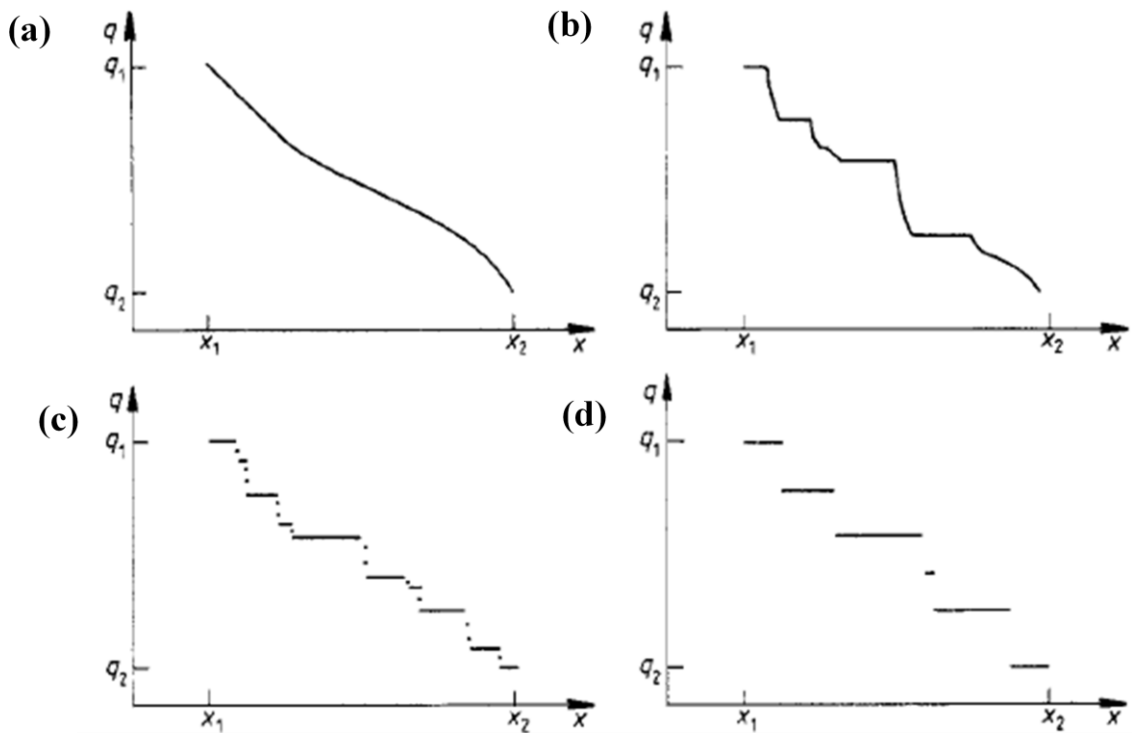


Figure 4.2: Various types of staircase. (a) Continuous behaviour. (b) In-complete devil staircase. (c) Complete devil staircase. (d) Harmless staircase [24].

The model as shown in Fig. 4.1 is a one-dimensional at zero-temperature one. At finite temperature the dimensionality becomes significant, and the prospect of a disordered fluid or paramagnetic phases arises. The incommensurate phases and the global phase diagrams are qualitatively distinct in two or three dimensions. In general, the periodic potential will tend to ‘lock’ the system into a commensurate configuration. How does the periodicity, a (or wavevector $q = 2\pi/a$), varies as some parameter is changed? Figure 4.2 shows the different possible situations which shall be encountered in the following paragraph.

When the parameter say x goes from x_1 to x_2 , q changes from q_1 to q_2 . Figure 4.2(a) shows a simple analytic continuous behaviour. The periodicity happens to pass through an infinite number of commensurate values without locking at any values; this corresponds to a so-called ‘floating’ phase. Such situation may arise in two dimensions also. In Fig. 4.2(b) it is shown that a function locks-in at an infinite number of commensurate values. The value of

$q/2\pi$ remains fixed and rational at an infinity of finite intervals of the variable x . Of course, the stability intervals reduce rapidly as the order of the commensurability increases. If there are some incommensurate phases present between the commensurate phases the function is known as ‘the incomplete devil’s staircase’ [18]. Figure 4.2(c) shows an example of ‘the complete devil’s staircase’ where the locked portions of the function fill up the entire range of the argument x . Even if the function takes only rational values, there are no jumps or first-order like transitions. Figure 4.2(d) shows a “harmless staircase” where q takes only finite number of rational values. The most important ‘devilish’ type system is probably the rare-earth magnet of CeSb, in which up to seven distinct commensurate phases were observed. Figure 4.2 does not provide the complete picture of all the possible situations and it’s not hard to imagine the different types of possible combinations. The phase diagram can comprise of regions showing a complete devil’s staircase, regimes containing an incomplete devil’s staircase and also harmless regimes.

Some examples of commensurate and in-commensurate phases are shown in the figures 4.3 - 4.6 below.

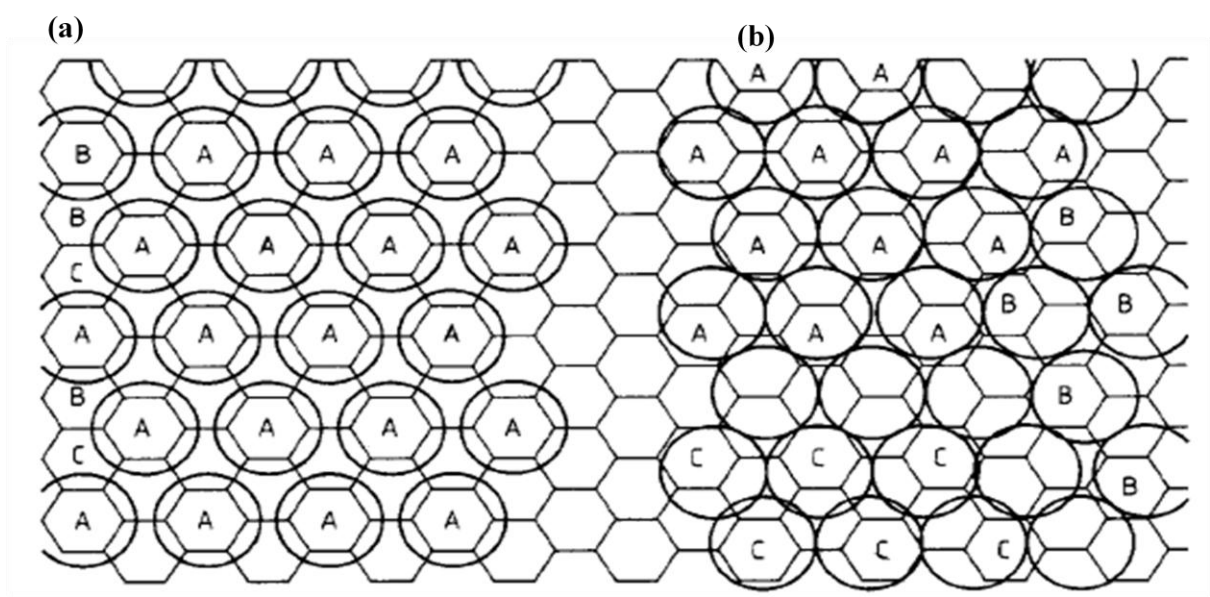


Figure 4.3: Krypton monolayer adsorbed on graphite. (a) Commensurate ' $\sqrt{3}$ structure'. The krypton atoms occupy 1/3 of the graphite honeycomb cells. (b) Incommensurate phase [23].

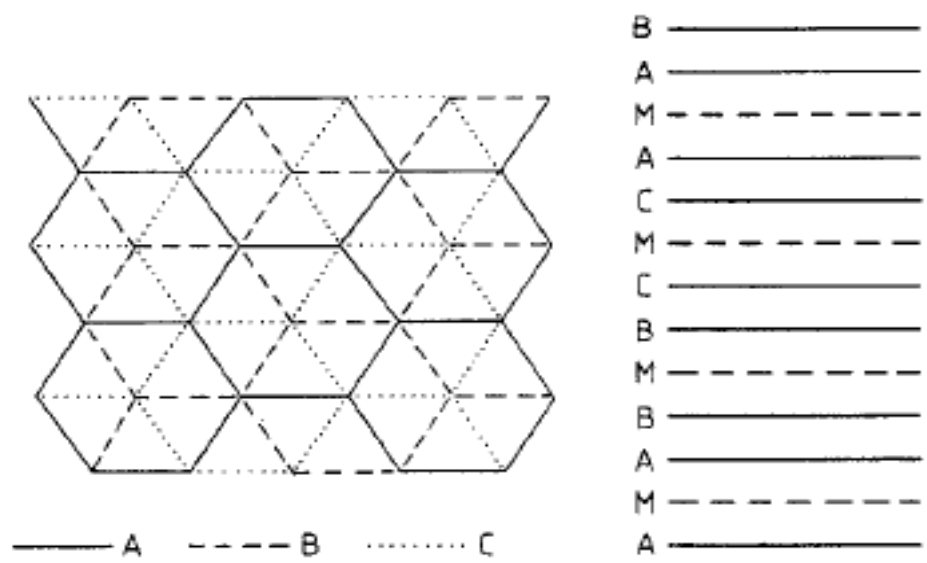


Figure 4.4: Stacking of metal (M) and graphite (A, B, C) layers in stage 2 graphite intercalation compounds such as CsC_{24} . The intralayer ordering may be commensurate or incommensurate as shown in the previous figure [25].

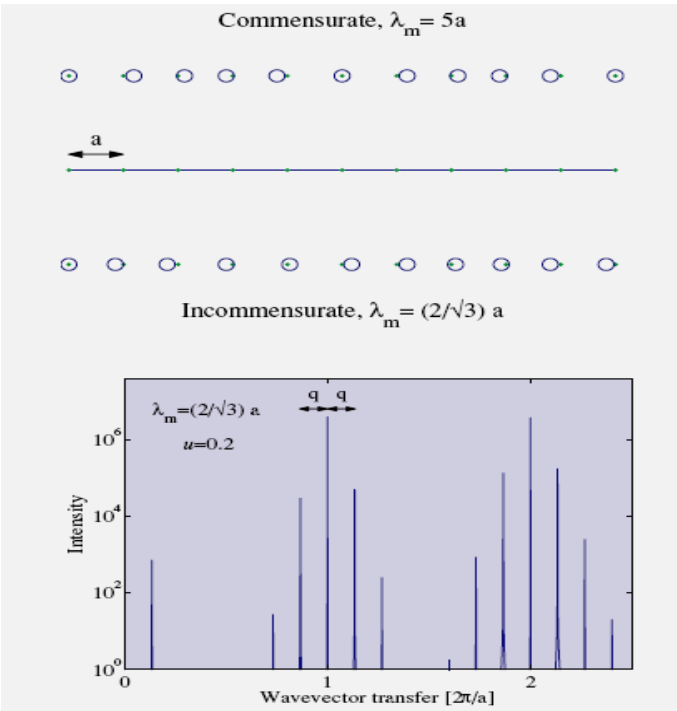


Figure 4.5: Scattering from a 1D incommensurate chain. The top panel shows the position of atoms in a 1D chain with a commensurate, $\lambda_m = 5a$, and an incommensurate, $\lambda_m = (2/\sqrt{3})a$ modulation wavevector. The bottom panel is the calculated scattered intensity for a chain of $N=2000$ atoms, with positions given by Eq. (4.2), a modulation wavelength of $\lambda_m = (2/\sqrt{3})a$, and a displacement amplitude of $u=0.2$. For simplicity it has been assumed that the atomic scattering length is unity, and independent of wavevector transfer Q [59].

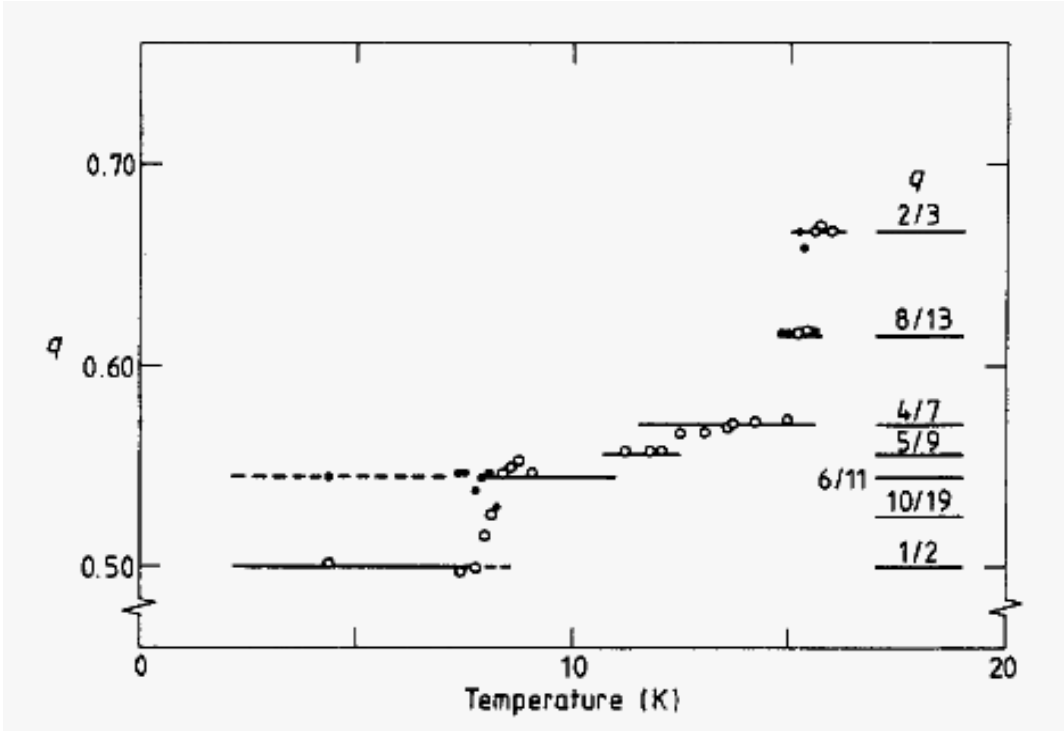


Figure 4.6: Temperature dependence of wavevector for sinusoidally modulated structure of cerium antimonide, CeSb (Fischer et al 1978). •, intense satellite; o, weak satellite [24].

4.3 Modulated periodicities in stripe phase of a Fe/Gd thin film

Modulated periodicities arise out of competition between local attractive potential and long-range repulsive interaction and provide a pathway to topologies and phases with spatially varying order parameter. While prevalent in single crystal and epitaxial systems, observation of modulated phases in amorphous system with perpendicular magnetic anisotropy is rare. Herein we show the wavevector Q due to ordered stripe domains in an amorphous Fe/Gd heterostructure does not change continuously, rather exhibits a staircase structure where the steps are rational fraction of two periodicities, similar to a Devil's staircase. The steps appear randomly with no defined size for height and width. Distribution of the step width and height follow a power law behaviour thereby indicating self-similar nature of the steps. We also observed that thermal fluctuations smear out the steps, consistent with theoretical prediction.

A complex system when subjected to multiple interactions with competing periodicities can exhibit new phases whose ground state is defined by the modulation of the original periodicities. Understanding of modulated structures therefore shed insight into the basic mechanism that produces the non-trivial textures and provides a pathway to discover novel exciting phases. Commensurate and incommensurate phases, such as charge and spin density waves in solids [37], stripes and charge density waves in cuprate superconductors [38, 39], charge ordered state in manganites [40], helical spin structure in magnetic systems [41], skyrmion lattices in quantum materials [42, 43] are some examples of modulated periodicities. In some special cases of interactions the system goes through numerous metastable states and the corresponding wavevector Q shows a complex self-similar staircase

structure resemblance of Devil's staircase [44-47] like structure. As mentioned earlier Devil's staircase has the property that the step width is rational fraction of the two periodicities. Experimentally such a complex metastable states have been observed in diverse systems. For example, in magnetic diffraction due to rare earths [48], charge density waves [49], in phase diagram of Kondo lattice CeSb [50], in evolution of ordered phases in Pb/Si(111) structure [51], in current-voltage characteristics of a niobium Josephson junction [52], spin crossover bimetallic 2D coordination polymer [53], spin valves [32].

For modulated period to exist, it is customary to describe an ordered lattice with a lattice constant a , which gives a diffraction signal at wavevector $Q=2\pi n/a$, where n is an integer. A modulation to the lattice periodicity will give superlattice diffraction peaks at a wavevector $(Q \pm \tau)$ where τ is the modulated wavevector. An interesting question is, how will modulated periodicity manifest for an amorphous material which may have local order but no well defined momentum transfer wavevector Q [46, 54]? In this article we address this question.

The local symmetries and global symmetries in an amorphous system could be different. If these symmetries are in conflict with each other, with their respective ground state energies being near-degenerate, a small perturbation can result in the system follow different pathway and fall into a metastable state. Herein we show using resonant coherent X-ray scattering that the scattering wavevector Q due to ordered stripe domains in an amorphous Fe/Gd heterostructure does not change continuously, rather exhibits a series of distinct field dependent steps. The staircase structure satisfies the criteria of a Devil's staircase. The steps were rational fraction of two periodicities. The steps appear randomly and its width and height has no defined size. Histogram of the step width and height follow a power law behaviour thereby indicating self-similar nature of the steps [58].

A central component to the problem of modulated phases that lead to exhibition of staircase structure is the existence of long range repulsive interaction. In case of 1D-Ising model with long range antiferromagnetic interaction the ground state has a compete Devil's staircase structure [55]. It has been theoretically shown that for an array of magnetic nanostripes with long range antiferromagnetic interaction of the form r^{-p} , the magnetization reversal goes through a number of metastable states and shows a staircase structure [56]. A competition of exchange and dipolar interaction that has different spatial variation can give rise to a conflict in net interaction at a certain positions in space. Such a system is frustrated and is a candidate to exhibit modulated periodicities.

The same sample was used which was already discussed in chapter 3. The Fe and Gd layers are antiferromagnetically coupled making Fe/Gd a ferrimagnet. The sample displays perpendicular magnetic anisotropy and exhibits disordered stripe, aligned stripe and skyrmion phases. Particularly, in the presence of a small applied in-plane field a magnetic phase consisting of bound pairs of unit winding number skyrmions with opposite helicity and aligned polarity is observed [30, 26]. The magnetic phase of the sample can be tuned by varying the applied magnetic field and temperature. Previous studies showed the existence of phase boundaries and underlying critical points in the stripe and skyrmion phases [57].

At resonant condition the X-rays are 10^4 times more sensitive to the magnetization than at non-resonant energies [27]. Resonant coherent X-ray magnetic scattering patterns of the Fe/Gd thin film in the three magnetic phases are shown in Fig. 4.7. The central dark circular region is the beam-stopper to prevent the direct transmitted beam from falling on the CCD camera. The circular fringes surrounding the beam-stop are the Airy patterns and the streaks of intensity surrounding the beam stop are due to scattering from the pinhole edge (refer Fig. 4.7(c)). Intense bright peaks consisting of speckles away from the central region are due to

scattering from the magnetic domains. We start our measurement at the zero field condition and then measured a series of scattering data as a function of applied magnetic field at 85K, 183K, 220K, 236K and 300K temperatures. From our measurements we found that the Fe/Gd thin film comprises of three distinct phases: (i) an ordered stripe phase, (ii) skyrmion phase and (iii) disorder stripe phase at different fields and temperatures.

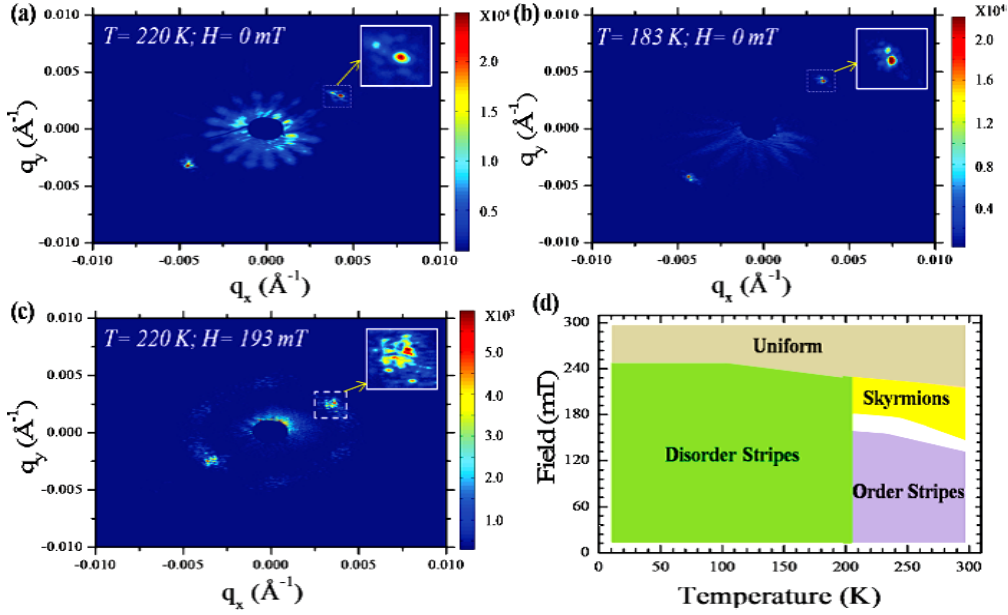


Figure 4.7: Resonant X-ray scattering patterns due to (a) order stripes, (b) disorder stripes and (c) skyrmions. Insets show the enlarged view of the diffraction spot which shows speckle pattern. (d) Temperature Vs. magnetic field phase diagram of the Fe/Gd sample [36].

Formation of well aligned stripes at 220 K is shown in Fig. 4.7(a) with periodicity of $119 \pm 5 \text{ nm}$ at remanence. The intensity profile is dominated with speckles which indicate heterogeneity in the domain morphology (see inset of Fig. 4.7(a)). With further increase in field starting from remanence the periodicity of the stripes starts to increase (See Fig. 4.7(c)) but around 170 mT the symmetry of the diffraction pattern began to change as new peaks in the form of a distorted hexagonal pattern as shown in Fig. 4.7(c) starts to appear. The intensity of the peaks in the skyrmion phase is much less compared to the peaks in the stripe phase. The skyrmion peaks show speckle pattern that indicates domain formation in the skyrmion lattice (see inset of Fig. 4.7(c)). An interesting feature is that due to the topological

protection the periodicity of skyrmions at any field value within the skyrmion phase (refer Fig. 4.7(d)) always remains 180 ± 5 nm.

At sufficiently high fields the diffraction spots becomes faint and finally disappears as the film becomes homogeneously magnetized. Figure 4.7(b) shows the magnetic diffraction pattern at 183K. At sufficiently low field values there are two distinct spots. However, the zero field diffraction peak has a larger FWHM (4 deg) compared to 220K data (2.6 deg) along the azimuthal direction, which indicates that our sample at higher temperature (220K) has a high degree of perfection in the alignment of the stripe system. As the field is increased, instead of an appearance of six-fold diffraction pattern, as was the case in skyrmion phase, the diffraction spots transforms into an arc characteristic of meandering or disordered stripe domains formation. The periodicity of the disorder stripes at remanence is 114 ± 5 nm. As shown in the insets of Fig. 4.7, diffraction patterns are modulated by speckles arising due to presence of domains. The speckle pattern corresponding to a diffracted beam will change whenever the morphology of the domains changes due to variations in magnetic field or temperature.

4.3.1 Experimental details

Resonant coherent X-ray scattering experiments were performed at the Coherent Soft X-ray Science beamline of the Advanced Light Source at Lawrence Berkeley National Laboratory. The beamline was designed to produce linearly polarized coherent soft X-rays. The resonant condition was achieved by tuning the energy of the incident beam to the Fe L3 edge (≈ 707 eV photon energy or 1.75 nm photon wavelength). Since at resonant condition the X-rays are sensitive to the magnetization along the beam propagation direction, we used a normal incidence transmission scattering geometry to enhance the magnetic contrast. A 10 μm pinhole was put in the path of the incident beam to establish transverse coherence in the

beam. Typical transverse coherence length of the beamline is about 5 μm . The existence of Airy fringes and magnetic speckle pattern in the measured data (see Fig. 4.7) clearly demonstrate the coherence of the soft X-ray beam. A charge-coupled device detector was used to record the scattered intensity patterns as a function of magnetic field over entire field cycles and repeated at different temperatures. The schematic of X-ray scattering experiment in transmission geometry is shown in Fig. 4.10(a). A 10 micron pinhole in the beampath and energy of Fe L3 edge (707 eV) was set to establish transverse coherence of the beam and the resonant condition respectively. The magnetic field was placed perpendicular to the sample and the scattered intensity patterns were recorded with a CCD camera placed at a distance of 0.5 m downstream of the sample.

4.3.2 Lorentz TEM data and analysis

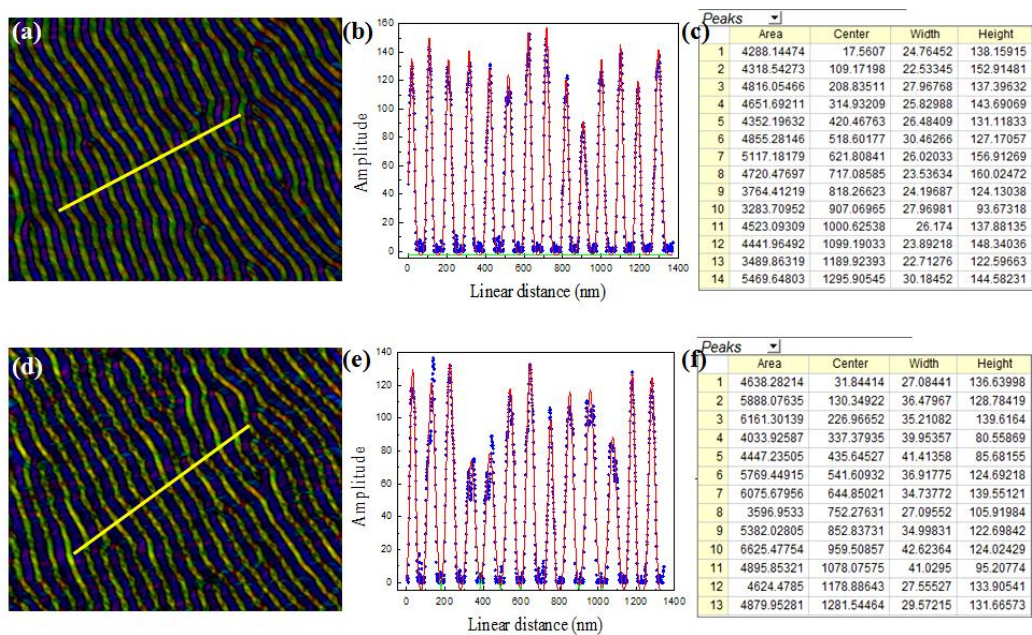


Figure 4.8: (a) & (d) Real space image of magnetic stripe domains using LTEM at fields F_1 and F_2 respectively ($F_2 > F_1$). (b) & (e) Line profile (yellow line in Fig. 4.8a, d) of the stripes at F_1 and F_2 respectively along with the Gaussian fit. (c) & (f) The fitting parameters of the Gaussian profile for all the peaks are listed in the corresponding tables (here width denotes FWHM).

The real space images of magnetic order stripes are shown in Fig. 4.8 above using LTEM. Field/Temperature-dependent in-plane domain morphology images were recorded in Lorentz mode using an FEI Titan equipped with an image aberration corrector at the Center for Advanced Materials Characterization, University of Oregon.

The images show the changes happening in the domain structure as the field is increased from F_1 to F_2 as shown in Fig. 4.8 (a) and 4.8(d). From the parameters derived by fitting a Gaussian profile one can observe that with increase in field the width of the up-domains start increasing (see Fig 4.8(c) and (d)) whereas the width of the reversal domains remains almost constant. The net result is the increase of domain periodicity as evident from the centre to centre distance between two peaks shown in Fig. 4.8(c) and (d).

4.3.3 Experimental Results

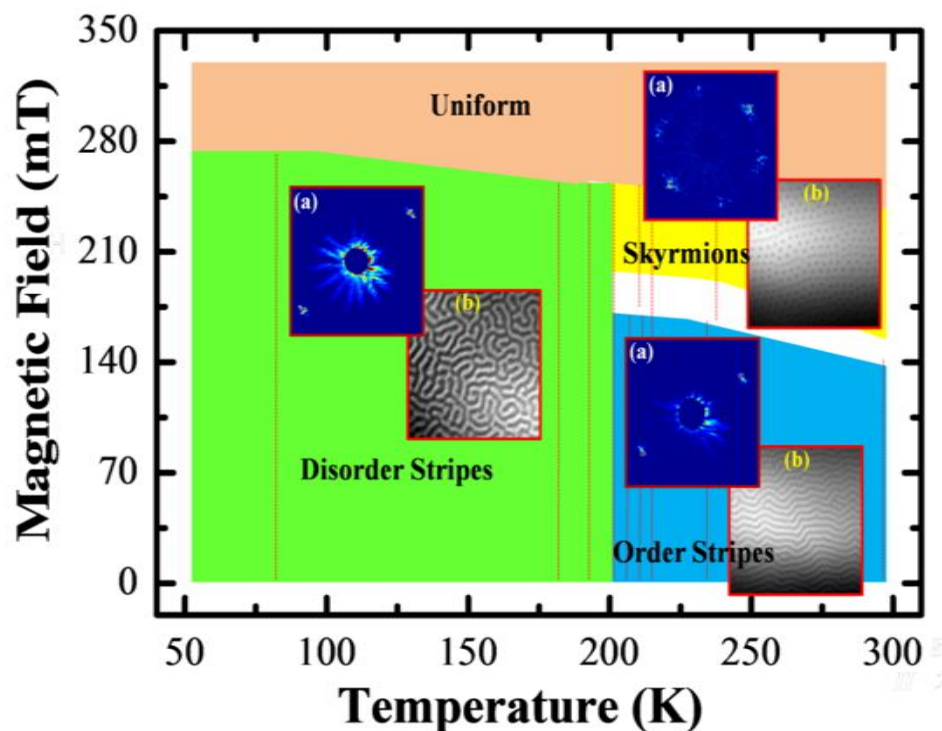


Figure 4.9: The field vs. temperature phase map of the Fe/Gd multilayer films. The reciprocal space image (a) and the X-ray microscopy real space images (b) are shown for the disorder stripe, order stripe and the skyrmion phases. The red dotted lines show the resonant X-ray scattering measurements.

The presence of different magnetic phases, disorder stripes, ordered stripes and skyrmions in the Fe/Gd multilayer films as a function of the magnetic field and temperature is shown in the phase map in Fig. 4.9. The X-ray microscopy real space image and the corresponding reciprocal images measured using resonance soft X-ray scattering (RSXS) at different magnetic phases are shown as the insets corresponding to that particular phase [28]. The disorder stripes phase shows more like a maze pattern whereas the order stripes shows alignment in a particular direction. In both the stripe phases (ordered and disordered) the diffraction image corresponding to the stripes shows two distinct diffraction spots diametrically opposite to the central scattering region. The real space image of skyrmions is represented by the circular dots arranged in a hexagonal lattice. The corresponding diffraction image also shows six Bragg spots in the hexagonal arrangement [31]. The white region in between the skyrmion and order stripe phase in Fig. 4.9 represents a broadened stripe-skyrmion transition and the region corresponding to the uniform magnetization, the magnetic diffraction spots completely disappears. We have selectively chosen the temperatures spanning over different phases in the phase map for the experiments using the RSXS technique which are marked as the red dotted vertical lines and will be discussed next.

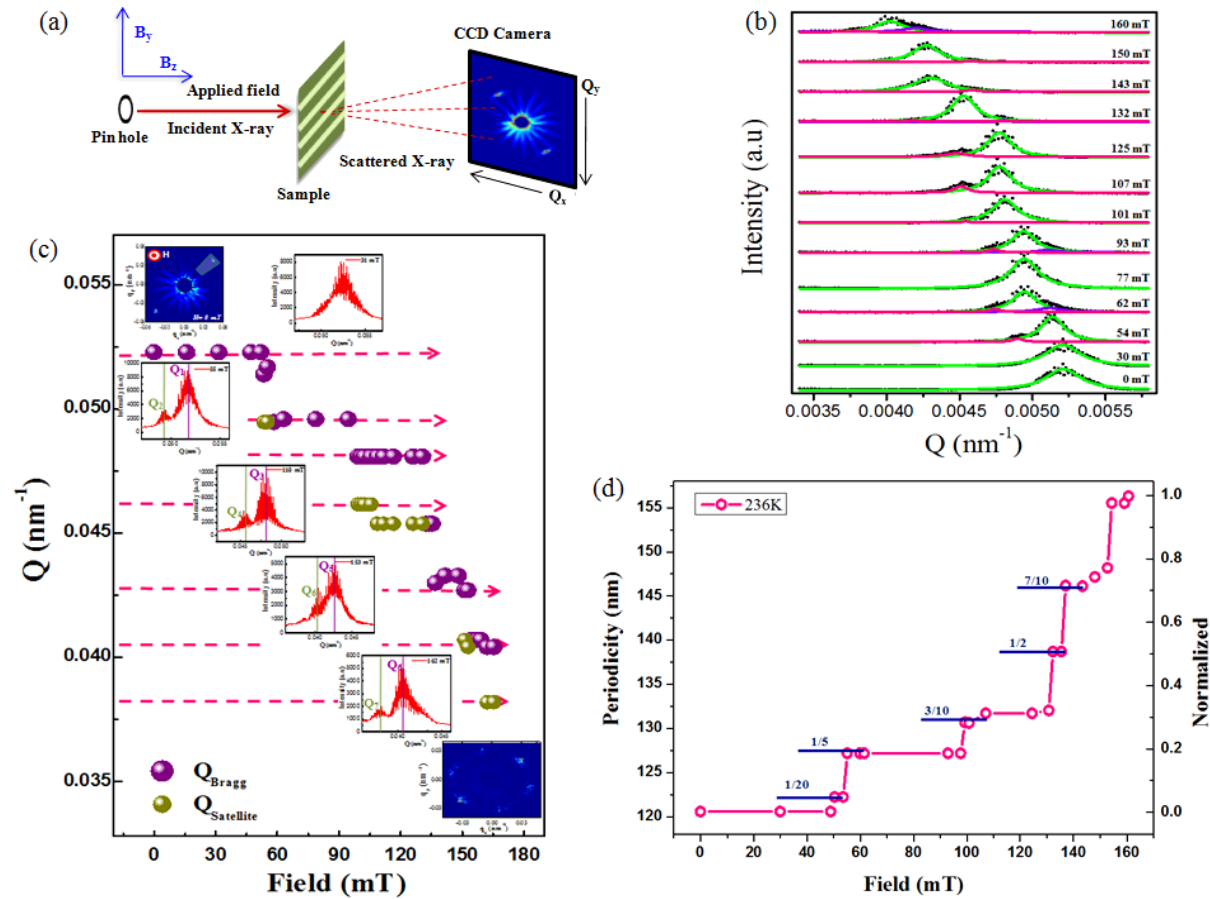


Figure 4.10: (a) Schematic of the experimental setup. (b) Evolution of the stripe phase at 225K at different applied magnetic fields. (c) The changes in the Q value of the diffraction peaks from the stripe phase to skyrmion phase as a function of applied field at 225K. The line profiles are extracted from the images of diffraction spots from the Fe/Gd multilayer structures. Two such images at stripe phase and skyrmion phase are shown at the top left and bottom right position of the figure. (d) The periodicity of the stripes as a function of applied field at 236K. Also shown in the figure are the different rational steps indicating Devil staircase like behaviour.

The evolution of the diffractions spots from the stripe phase to skyrmions as a function of applied field at 225K is shown in Fig. 4.10(c). At zero fields, the multilayer sample is in stripe phase and the diffraction image corresponding to that phase is shown at the top-left corner inset of Fig. 4.10(c). Diagonally opposite two sharp spots in the inset image are due to the diffraction from the stripe magnetic domains whereas the streaks of intensity surrounding the beam stopper is due to the diffraction from the pin hole placed before the sample. The line profile corresponding to the Bragg peak marked in the shaded cone shows a peak at Q_1 ($=0.052 \text{ \AA}^{-1}$) as evident from the profile in the inset next to the image in Fig.

4.10(c). The increase in field leads first to the appearance of a satellite peak at Q_2 (lower than the Bragg peak at Q_1) and subsequently this satellite peak transforms into the main Bragg peak as shown by the symbols in Fig. 4.10(c). The position of the Bragg peak indicates the periodicity in the stripe domains and the intensity is related to the number of domains having such periodicity. First appearance of satellite peak at Q_2 with less intensity and then the merger of the main Bragg peak to this Q_2 at a certain magnetic field indicates that the number of magnetic domains having periodicity $2\pi/Q_1$ decreases with increase in field while the number of domains having periodicity $2\pi/Q_2$ starts increasing and finally all the domains transforms with periodicity $2\pi/Q_2$. This sequence of events, changing Q values from Q_1 to Q_7 with similar mechanism of peak shifts is repeated for higher field values and ultimately ends in a structure when the skyrmion phase emerges which is represented by the six diffraction spots (due to hexagonal ordering) as shown by the image at the bottom-right corner inset of Fig. 4.10(c). It is important to note here that the Q values of the Bragg peaks always change in a discrete random step representing a staircase like phenomena and this change in the position occurs through an evolution of a satellite peak (Q_1 to Q_2 , Q_3 to Q_4 & Q_5 to Q_6). In some cases, direct change in Q values corresponding to the Bragg peaks (Q_2 to Q_3 & Q_4 to Q_5) is also observed.

The periodicity ($2\pi/Q_1$) corresponding to the stripes at remanence is 119 ± 5 nm. As the incident beam is coherent, the intensity profile within the Bragg spot consists of speckles which indicate heterogeneity in the stripe domain structure. Around 170 mT, new peaks are formed in distorted hexagonal pattern start to appear instead of only two diagonally opposite Bragg diffraction peaks indicating a transition to the skyrmion phase. It is to be noted that the intensity of the initial two Bragg peaks is much higher than the other four new peaks in the hexagonal pattern appear in the skyrmion phase. The new skyrmion peaks also show speckles pattern which indicates skyrmion domain structure formation in the spin lattice. The

periodicity of skyrmions at 193 mT is 233 ± 7 nm. At sufficiently high field (H_s) the diffraction pattern disappears as the film becomes uniformly magnetized.

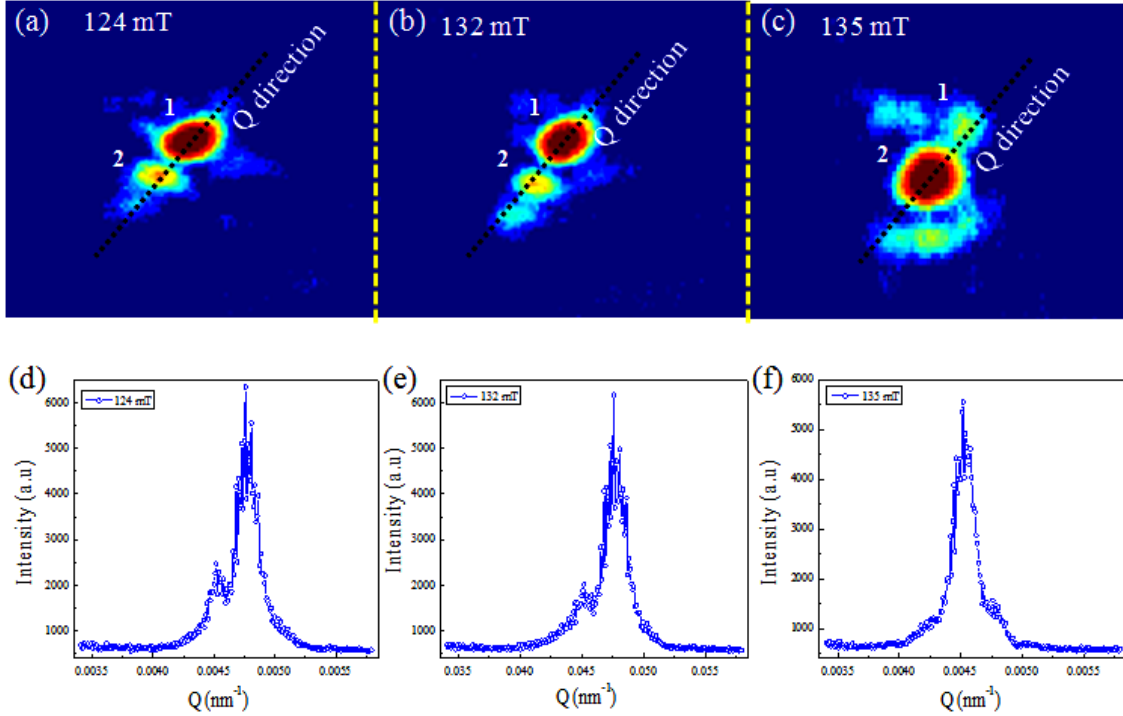


Figure 4.11: Resonant X-ray scattering pattern at different fields (a-c) and the corresponding intensity profile of the diffraction spots as a function of Q .

In figure 4.10(c & d) plotted is the periodicity of the stripes in the order phase at 236K as a function of applied external field from 0 mT to 157.5 mT. We observe steps like behaviour in the periodicity plot as the magnetic field is changed at the rate 1.575 mT/s. We start measuring the periodicity ($2\pi/Q$) at zero field where the periodicity of the stripes is minimum and end our measurement at 157 mT just before the onset of the skyrmion phase where we get the maximum periodicity for the stripes. On the right side of the plot the normalized values are shown. To calculate the normalized values we have first determined the total change in periodicity from 0 mT to 157.5 mT. Then we have subtracted the periodicity at different fields starting at 0 mT from that obtained at 157.5 mT and divided the subtracted values by the total change in periodicity obtained before. So this makes all the

normalized values to lie within zero and one. The position of the different steps corresponds to a particular value of the periodicity and we can allocate different values of these steps from the normalized periodicity values as shown in Fig. 4.10(d). The most interesting thing that we observe from the values is that most of the stairs corresponds to a rational number (nearly five in our case) and the values closely agrees with those that are observed in magnetic materials showing Devil staircase like behaviour [31-35].

In figure 4.11 we have shown the enlarged images of the diffraction pattern from the stripe phase. In the reciprocal pattern presence of two diffraction spots are visible along the q -direction. The corresponding line plots of the intensity profile as a function of q are shown below each of the diffraction patterns taken at different fields. From the pattern it is evident that at 124 mT there are two peaks, one corresponding to the Bragg Peak (label 1) and the other corresponding to the satellite peak (label 2). As the field is increased slowly a changeover takes place whereby the initial Bragg peak moves to the previously formed satellite peak. The line plots in the lower panel clearly shows the transformation. As the Bragg peak shifts its position the initial position doesn't disappear but a small peak remains which latter disappears as the field is increased.

Thus the satellite peak initially formed transforms into a Bragg peak and then again another satellite peak starts forming at a lower q value. This sequence is repeated as described earlier. The transformation incommensurate-commensurate actually gives rise to the staircase type variation of the stripe periodicity as a function of applied field.

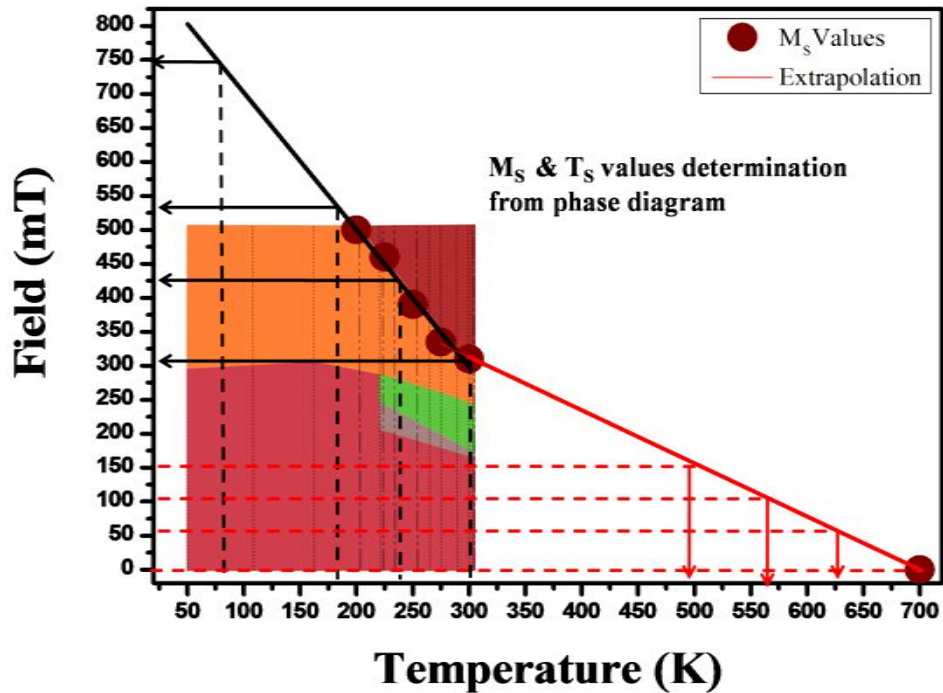


Figure 4.12: Schematic of the extraction of H_s and T_s from the phase boundary of the saturation magnetization in Fe/Gd multilayer films from the phase diagram [28]. The solid black and red lines are the line of extrapolation in the low and high temperature regions respectively. The dotted lines signify the measurement temperatures and fields for the films and the arrows mark the corresponding H_s and T_s .

The estimation process of uniform magnetization at a specific field (H_s) and the same at a temperature (T_s) from the phase boundary of the uniform magnetisation is shown schematically in Fig. 4.12. Previous measurements to map different phases of the Fe/Gd multilayer was limited in the range of 50K to 300K in temperature and 0 mT to 500 mT in field. The simple assumption followed here to calculate the H_s beyond the field of 500 mT was the extrapolation of the slope of the phase boundary at 500 mT to the higher magnetic field region as shown by the black solid line in the Fig. 4.12. The black dotted lines are the temperatures where measurements were done and the corresponding H_s are marked by the arrows. Similarly the phase boundary for uniform magnetisation was extrapolated beyond 300K with an additional constraints, the Curie temperature (700K) for the Fe/Gd multilayers and the T_s were extracted from that line as shown in Fig. 4.12.

The periodicity of the stripe domains can be calculated simply from the position of the Bragg peak following the relation ($\tau_Q = 2\pi/Q$). The variation of the periodicity (τ) of the stripe domains normalised by the periodicity at remanence as a function of H/H_s at different temperatures 85 K, 183K, 236K and 300K are shown in Fig. 4.13(a) to 4.13(d) respectively. The treads in stairs at 85K are longer and also the riser is much bigger in this case. As the system goes from the disorder stripe to the order stripe phase with increase in temperature, both the treads and riser become shorter leading to more number of small steps and ultimately more of a continuous variation with the applied fields. Also it is observed that the rate of change of τ with the variation in field increases with increase in the temperature. The solid lines in Fig. 4.13(a) – 4.13(d) show the fitting of a theoretical model following eq. (4.4) to the experimental data at different temperatures. The theoretical model was initially developed by Kooy, Enz [1] and was later extended by Gehanno *et al* [15] to make it applicable to films with thickness smaller than the domain period. This model gives a relationship between the periodicity of the stripes as a function of the applied field [29].

$$\tau(h) = A_h \sec[\arcsin(B_h h)] \quad (4.4)$$

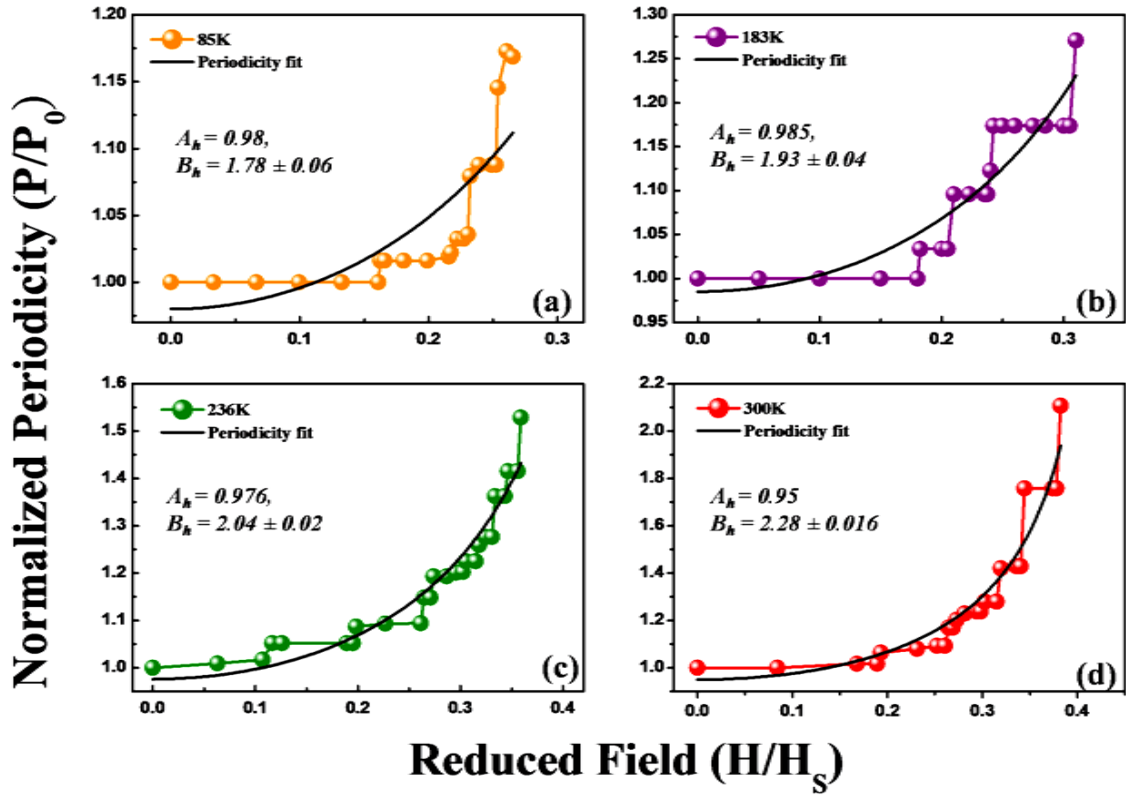


Figure 4.13: The variation of the periodicity of the stripe domains normalised by the periodicity at remanence as a function of reduced fields (H/H_s) at temperatures (a) 85 K, (b) 183K, (c) 236K and (d) 300K.

Here h is the reduced field (H/H_s), A_h and B_h are the terms whose value depends on the film thickness and susceptibility (at zero field) of the material. For a thin film, the ratio of A_h/B_h gives the value of the film thickness (t) at a temperature and the fitted values are shown in the figure. It is clear from the fitting that the theoretical model fits well with our experimental data for the ordered stripes than the disorder stripes.

The variation of the periodicity (τ) of the stripe domains as a function of T/T_s at different fields 0mT, 63mT, 110mT and 150mT are shown in Fig. 4.14(a) - 4.14(d) respectively. Following eq. (4.4), a similar equation has been conjectured just replacing the H/H_s by $t = T/T_s$ as shown in eq. (4.5).

$$\tau(t) = A_t \sec[\arcsin(B_t t)] \quad (4.5)$$

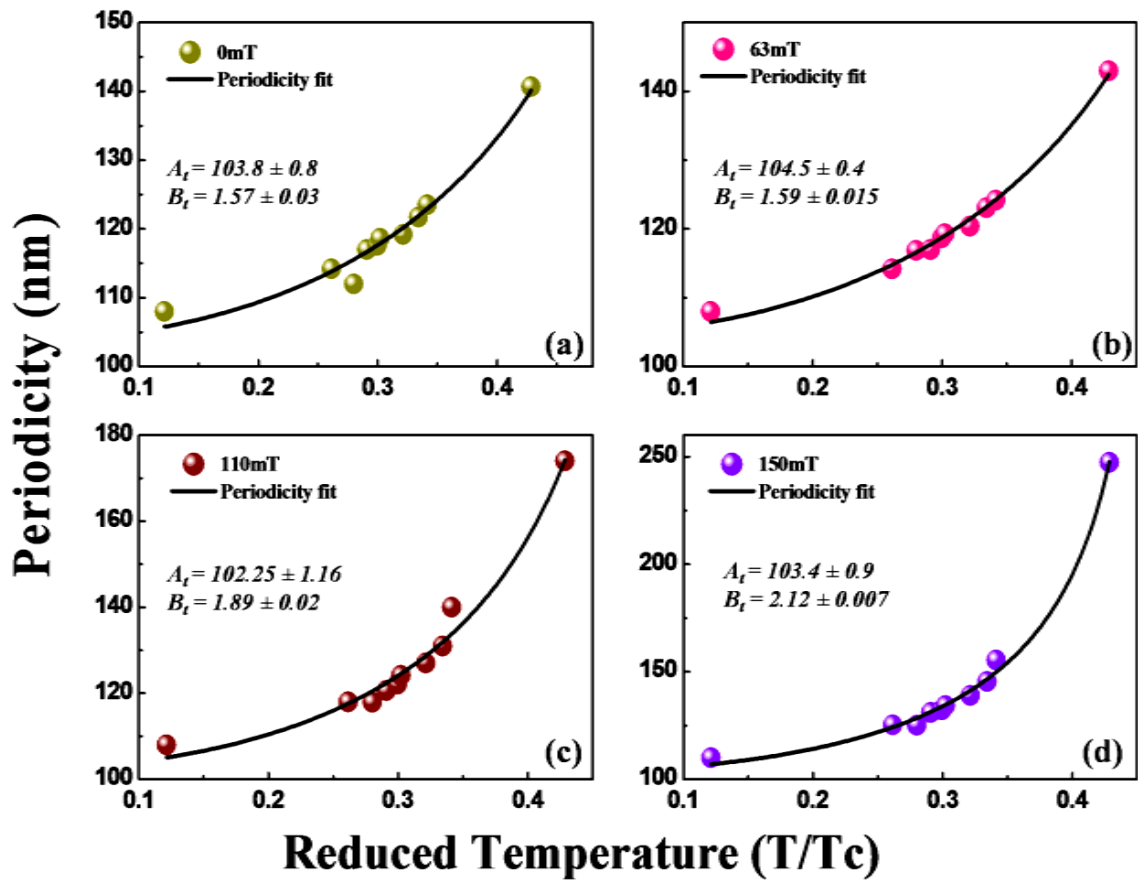


Figure 4.14: The variation of the periodicity of the stripe domains normalised by the periodicity at remanence as a function of reduced fields (T/T_s) at fields (a) 0mT, (b) 63mT, (c) 110mT and (d) 150mT.

The curves in figure 4.14 can be fitted quite well with the eq. (4.5) where the value for T_s at different fields has been extracted following the procedure mentioned in Fig. 4.12. The A_t and B_t are treated as fitting parameters and the ratio (A_t/B_t) also agrees with the estimated value of the film thickness. Although the agreement of the ratio with the thickness is much better at lower fields than the higher field values.

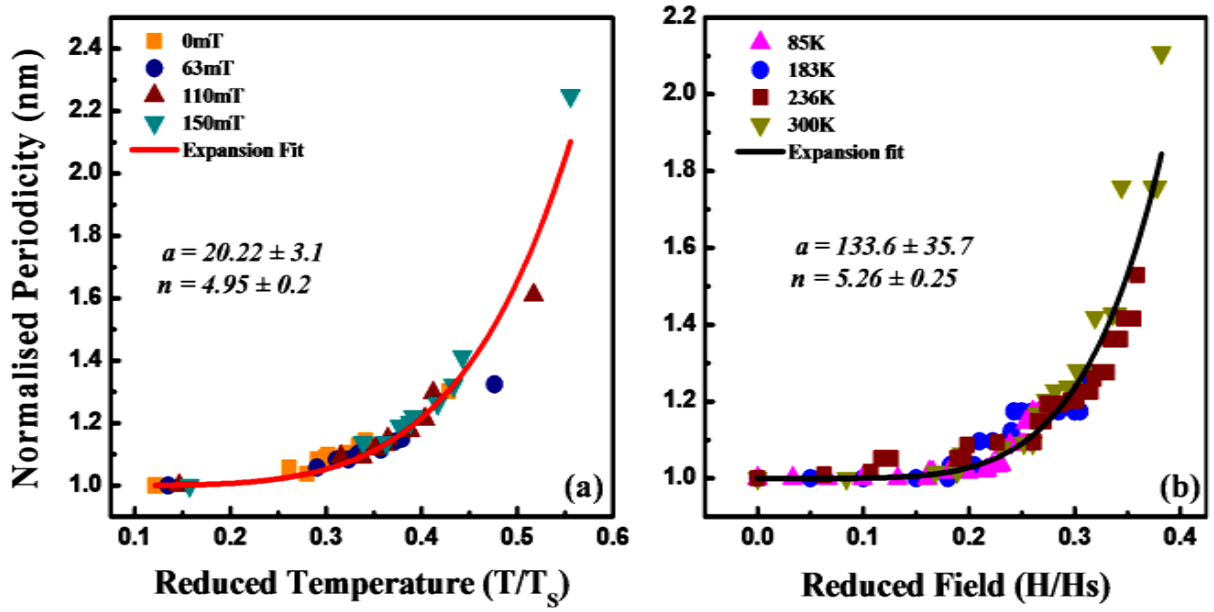


Figure 4.15: The collapse of normalised periodicity (symbols) as a function of (a) reduced temperature (T/T_s) and (b) reduced field (H/H_s). The solid lines are the fit with the expression as described in the text.

The periodicities extracted at different fields and temperatures after normalization can be collapsed to a single curve when plotted against the T/T_s (Fig. 4.15(a)) or H/H_s (Fig. 4.15(b)). The collapsed curve can be fitted with a simple expression similar to thermal expansion of solids as

$$\tau = 1 + a \cdot x^n \quad (4.6)$$

Where x is the reduced temperature (t) for the temperature plot (Fig. 4.15(a)) or the reduced field (h) for the field plot (Fig. 4.15(b)). The values of n higher than 3 in both the cases indicate higher order expansion of spin structure with the field or the temperature.

Distribution of step height and step width of a Devil's staircase

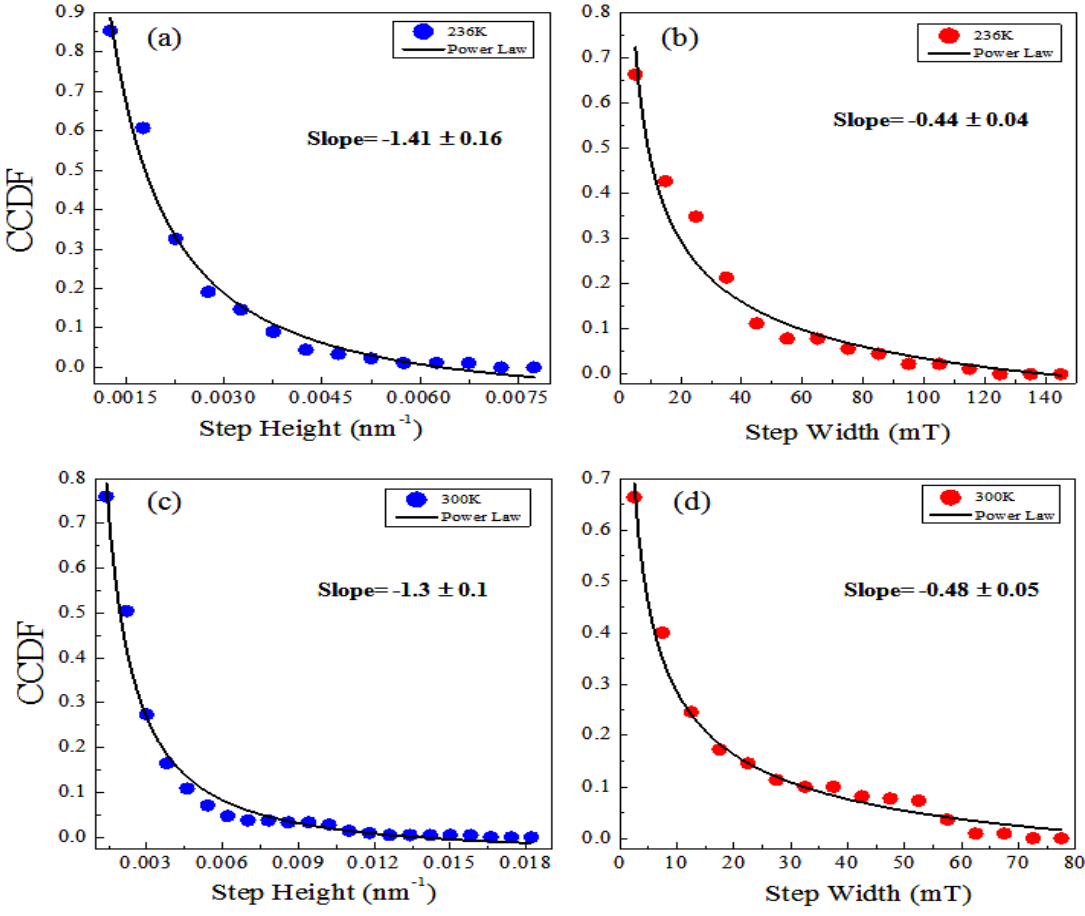


Figure 4.16: Complementary cumulative distribution function (CCDF) of step height at temperatures (a) 236 K, & (c) 300 K and step width at (b) 236 K, & (d) 300 K. The distribution could be fitted with a power law.

Since a staircase comprises of multiple steps each having a step width and step height so we carried out the distribution of these step height and step width at two different temperatures as shown in Fig. 4.16. Here we have plotted the CCDF, the formalism of which has already been described in chapter 3.

The distributions are plotted from over 30 field-loops consisting around 250 data points. We have fitted the distribution function with a simple power law equation of the form:

$$P(x) = A \cdot x^s + y_0, \quad (4.7)$$

where A is the amplitude, s is the exponent and y_0 is the intercept. At $T = 236$ K the value of exponent is -1.41 ± 0.16 and -0.440 ± 0.04 and at $T = 300$ K it is -1.30 ± 0.1 and -0.480 ± 0.05 for ΔQ (step height) and ΔH (step width), respectively. We note that the range of the height and width distribution at $T = 236$ K and 300 K are different, yet, the distributions follows similar power law behaviour confirming the self-similar nature.

A negative slope, similar to earthquakes and stock market fluctuation, imply that there are more numbers of small step width and shorter step size. In fact, from our Q vs Applied Field plots (see Fig. 4.10(c, d)) we have observed that generally steps width (ΔH) at smaller applied fields is associated with shorter heights (ΔQ) and magnitude of both increases with increasing applied field. This implies that as the periodicity of stripe domains changes through different metastable states there is always a tendency of the stripes to favour those states that are more stable, hence more amount of energy is needed to change the periodicity.

While the exponent for ΔQ and ΔH do not change significantly with temperature, the value is different between the height and width distribution. An interesting observation could be made that if we remove the applied field for which the periodicity is locked, then we are left with a set of vertical bars (of ΔQ) that constitutes all sizes that the stripe domains underwent during the field excursion. Similarly, we can determine a set of horizontal bars (of ΔH) where the periodicity does not change that will describe all the magnetization value that the sample can have during a hysteresis loop. A change in Q and/or H causes change in magnetization M , but with different proportionality. We can write, $\Delta Q \approx M^a$ and $\Delta H \approx M^b$. Since the exponent between ΔQ and ΔH differs, we can say that for same change in Q or H , the magnetization changes differently. Further, the ratio $(\Delta Q/\Delta H) \approx (M)^{a-b}$. In case of $a=b$, this would constitute a linear relation between step width and height. The non-equivalent

values between ΔQ and ΔH indicates non-linearity and is likely due to interactions present in the system.

As the temperature is increased the thermal energy starts to compete with the interaction that gives rise to the step jump. Due to difference in spatial variation between the thermal and magnetic energies, temperature changes should change the characteristics of the staircase. For temperatures where $KT \ll E_{\text{step}}$, where E_{step} is the amount of energy needed to make a step jump, the jumps will be sharp. At elevated temperatures fluctuation should smear the steps [56].

4.4 Discussions and Conclusion

If we normalize the change in the periodicity of the stripe phase to vary it between 0 and 1, then a fractional value corresponding to a particular position of the step height can be obtained (see Fig. 4.17(a)). If the value of the normalized periodicity for a particular step is known, then one can construct a schematic of the spin configuration with respect to a known ground state spin configuration. In Fig 4.17(a) we show an example of staircase with normalized periodicity at room temperature. The various rational fractions for each of the staircase are also depicted. To construct a schematic of the spin configuration with respect to a known ground state spin configuration we use the following relationship:

$$\text{Periodicity}_i = \frac{P_i - P_0}{P_N - P_0}, \quad (4.8)$$

where P is the periodicity, the subscript $i = 0, 1, 2, 3, \dots, N$ (field intervals) and each field value corresponds to 1.575 mT. Let us assume that at the coercive field number (0 mT) number of “up” domain equals the number of “down” and that each domain is constituted of four spins. Under an applied field in the up direction, we will also assume that only up

domains increase in size. This means number of blue spins increases and number of red spins remain constant. This is consistent with smaller Q-values with increasing field (as observed in experiments) and LTEM images [Fig. 4.8]. Using relation (4.8), we can get spin configuration for some of the modulated periodicity, viz, $\text{Periodicity}_0 = (8-8)/(12-8) = 0$; $\text{Periodicity}_3 = (9-8)/(12-8) = 1/4$; $\text{Periodicity}_5 = (10-8)/(12-8) = 1/2$; $\text{Periodicity}_N = (12-8)/(12-8) = 1$. Here the numbers denotes the number of spins (adding both up and down spins) in a particular configuration at a given field step. The spin structures are schematically shown in Fig. 4.18(a).

Using normalized periodicity we can also draw a schematic of the magnetic stripe domain pattern (\uparrow =blue colour and \downarrow = red colour) as shown in Fig. 4.17(b). In the ground state up and down domains are of equal width and hence we get a value of zero from the normalized periodicity equation (Eq. 4.8). The domain (spin) configurations are cyclic with respect to the ground state at some particular field values. The cyclic condition holds only in case of a commensurate phase whereas for incommensurate phases this cyclic condition will not hold as is the case for the ratio $1/3$. For simplicity we have shown only three different ratios (Fig. 4.17(b)) comprising of fewer number of stripe periods (one period= $\uparrow+\downarrow$) where the spin configurations are both cyclic and commensurate. The other commensurate phases that are also present in Fig. 4.17(a) will become cyclic with respect to the ground state at higher number of periods which was not possible to show in figure 4.17(b) for availability of space in the horizontal direction.

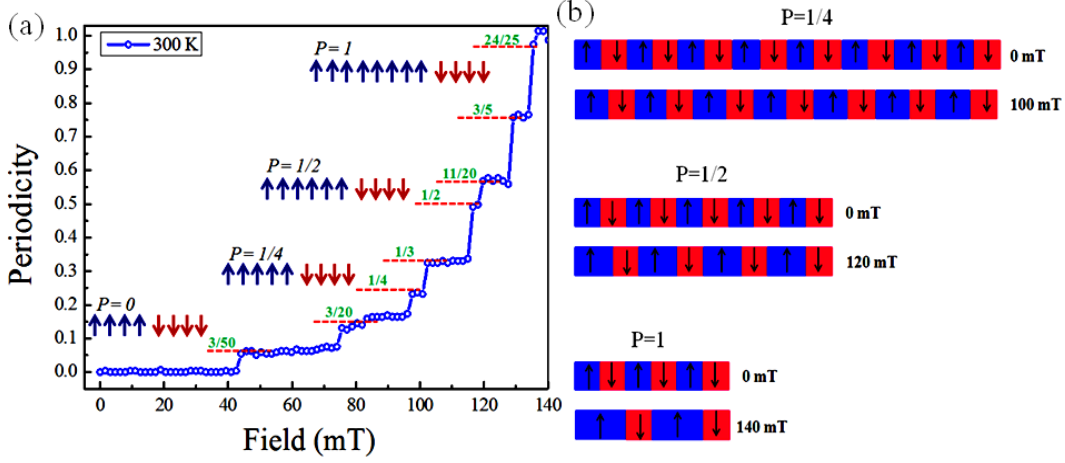


Figure 4.17: (a) Periodicity of the magnetic stripes using Eq. (4.8) as a function of applied magnetic fields at room temperature. Schematic of different spin configurations considering Ising type spins of stripes corresponding to the different rational fractions are shown inside. (b) Ratio of the number of stripes present at different fields with respect to the number of stripes present at zero field (blue region consists of all up spins and red region of all down spins. Blue and red region combined makes for a periodic of the stripes). The spin configurations in the blue and red regions at a particular field is given as in figure 4.17(a) with $P=0$ at 0mT, $P=1/4$ at 100mT, $P=1/2$ at 120mT and $P=1$ at 140mT as calculated from equation 4.8.

We showed existence of remarkably distinct staircase structure in an amorphous magnetic system. Our study confirms the theoretical prediction that periodicity and modulated structures do not necessarily need a crystalline sample. It could be that the aligned stripe in the Fe/Gd sample sets the basic periodicity and other modulated periodicities follows. An obvious next question would be to determine generality of Devil's staircase in other perpendicular anisotropy magnetic system where aligned stripes do not form. We also confirmed the theoretical prediction that thermal fluctuation smears the steps. Indeed, one of the important consequences of our study is that stripe domains in an amorphous magnetic system show many similarities with stripe found in other quantum system although the lengthscale of the interaction are very different. Since there could be infinite numbers of rational fractions between two rational fractions, it means that resolution permitting, more steps between any two steps could be observed. Since modulated periodicities are intricately linked to textures, discovery of new modulated wavevector can lead to discoveries of new quantum phases.

References:

- [1]. Kooy, C. and Enz, U. *Philips. Res. Repts.* **15**, 7-29, (1960).
- [2]. Fischer, P., Eimüller, T., Schütz, G. and Denbeaux, G. *Struct. Chem.* **14**, 39 (2003).
- [3]. Eimüller, T., Fischer, P., Köhler, M., Scholz, M., Guttman, P., Denbeaux, G., Glück, S., Bayreuther, G., Schmahl, G., Attwood, D. *et al.*, *Appl. Phys. A: Mater. Sci. Process.* **73**, 697 (2001).
- [4]. Köhler, M., Zweck, J., Bayreuther, G., Fischer, P., Schütz, G., Denbeaux, G. and Attwood, D. *J. Magn. Magn. Mater.* **240**, 79 (2002).
- [5]. Nolting, F., Scholl, A., Stöhr, J., Seo, J. W., Fompeyrine, J., Siegwart, H., Locquet, J. P., Anders, S., Lüning, J., Fullerton, E. E. *et al.*, *Nature* **405**, 767 (2000).
- [6]. Ohldag, H., Scholl, A., Nolting, F., Anders, S., Hillebrecht, F. U. and Stöhr, J. *Phys. Rev. Lett.* **86**, 2878 (2001).
- [7]. Vogel, J., Kuch, W., Bonfim, M., Camarero, J., Pennec, Y., Offi, F., Fukumoto, K., Kirschner, J., Fontaine, A. and Pizzini, S. *Appl. Phys. Lett.* **82**, 2299 (2003).
- [8]. Kuch, W., Chelaru, L. I., Offi, F., Wang, J., Kotsugi, M. and Kirschner, J. *Phys. Rev. Lett.* **92**, 017201 (2004).
- [9]. Eisebitt, S., Lörger, M., Eberhardt, W., Lüning, J., Stöhr, J., Rettner, C. T., Hellwig, O., Fullerton, E. E. and Denbeaux, G. *Phys. Rev. B* **68**, 104419 (2003).
- [10]. Jaouen, N., Tonnerre, J. M., Raoux, D., Bontempi, E., Ortega, L., Müenzenberg, M., Felsch, W., Rogalev, A., Dürr, H. A., Dudzik, E. *et al.*, *Phys. Rev. B* **66**, 134420 (2002).

- [11]. Lisfi, A. and Lodder, J. C. *J. Phys.: Condens. Matter* **14**, 12339 (2002).
- [12]. Druyvesteyn, W. F., Dorleijn, J. W. F. and Rijnierse, P. J. *J. Appl. Phys.* **44**, 2397 (1973).
- [13]. Cape, J. A. and Lehman, G. W. *J. Appl. Phys.* **42**, 5732 (1971).
- [14]. Kaplan, B. and Gehring, G. A. *J. Magn. Magn. Mater.* **128**, 111 (1993).
- [15]. Gehanno, V., Samson, Y., Marty, A., Gilles, B. and Chamberod, A. J. *Magn. Magn. Mater.* **172**, 26 (1997).
- [16]. Kittel, C., *Phys. Rev.* **70**, 965 (1946).
- [17]. Frank, F. C. and Van der Merwe, J. H. *Proc. R. Soc.* **198** 205, 216 (1949).
- [18]. Theodorou, G. and Rice, T. M. *Phys. Rev. B* **18**, 2840 (1978).
- [19]. Greene, J. M. *J. Math. Phys.* **20**, 1183 (1979).
- [20]. Aharony, A. and Bak, P. *Phys. Rev. B* **23**, 4770 (1981).
- [21]. Frenkel, Y. I. and Kontorowa, T. *Zh. Eksp. Teor. Fir.* **8**, 1340 (1938).
- [22]. Janner, A. and Janssen, T. *Phys. Rev. B* **15**, 643(1977).
- [23]. Coppersmith, S. N., Fisher, D. S., Halperin, B. I., Lee, P. A. and Brinkman, W. F. *Phys. Rev. Lett.* **46**, 549 (1981).
- [24]. Fischer, P., Lebech, B., Meier, G., Rainford, B. D. and Vogt, O. *J. Phys. C: Solid St. Phys.* **11**, 345 (1978).
- [25]. Nielsen, M., Als-Nielsen, J., Bohr, J. and McTague, J. P. *Phys. Rev. Lett.* **47**, 582(1981).

- [26]. Montoya, S. A., Couture, S., Chess, J. J., Lee, J. C. T., Kent, N., Im, M.-Y., Kevan, S. D., Fischer, P., McMorran, B. J., Roy, S., Lomakin, V. and Fullerton, E. E. *Phys. Rev. B* **95**, 224405 (2017).
- [27]. Blume, M., *J. Appl. Phys.* **57**, 3615 (1985).
- [28]. Montoya, S. A., Couture, S., Chess, J. J., Lee, J. C. T., Kent, N., Henze, D., Sinha, S. K., Im, M.-Y., Kevan, S. D., Fischer, P., McMorran, B. J., Lomakin, V., Roy, S. and Fullerton, E. E. *Phys. Rev. B* **95**, 024415 (2017).
- [29]. Miguel, J., Peters J. F., *et al*, *Phys. Rev B* **74**, 094437 (2006).
- [30]. Lee, J. C. T., Chess, J. J., Montoya, S. A., Shi, X., Tamura, N., Mishra, S. K., Fischer, P., McMorran, B. J., Sinha, S. K., Fullerton, E. E., Kevan, S. D. and Roy, S. *Appl. Phys. Lett.* **109**, 022402 (2016).
- [31]. Chen, K. W., Lai, Y., Chiu, Y. C., Steven, S., Besara, T., Graf, D., Siegrist, T., Albrecht-Schmitt, T. E., Balicas, L. and Baumbach, R. E. *Phys. Rev. B* **96**, 014421 (2017).
- [32]. Matsuda, T., Partzsch, S., Tsuyama, T., Schierle, E., Weschke, E., Geck, J., Saito, T., Ishiwata, S., Tokura, Y. and Wadati, H. *Phys. Rev. Lett.* **114**, 236403 (2015).
- [33]. Takigawa, M., Horvatić, M., Waki, T., Krämer, S., Berthier, C., Lévy-Bertrand, F., Sheikin, I., Kageyama, H., Ueda, Y. and Mila, F. *Phys. Rev. Lett.* **110**, 067210 (2013).
- [34]. Fraerman, A. A. and Sapozhnikov, M. V. *Phys. Rev. B* **65**, 184433 (2002).
- [35]. Hupalo, M., Schmalian, J. and Tringides, M. C. *Phys. Rev. Lett.* **90**, 216106 (2003).
- [36]. **Singh, A.**, Sanyal, M. K., Lee, J. C. T., Chen, Y., Montoya, S., Fullerton, E. E. and Roy, S. *AIP Conference Proceedings* **1942**, 130028 (2018).

- [37]. Gruner, G. *Density Waves In Solids* (CRC Press, 2000).
- [38]. Emery, V. J. Kivelson, S. A. and Tranquada, J. M. *Proceedings of the National Academy of Sciences* **96**, 8814 (1999).
- [39]. Chang, J. *et al.*, *Nature Physics* **8**, 871 (2012).
- [40]. Chen, C. H. and Cheong, S. W. *Phys. Rev. Lett.* **76**, 4042 (1996).
- [41]. Binz, B. and Vishwanath, A. *Phys. Rev. B* **74**, 214408 (2006).
- [42]. Mühlbauer, S., Binz, B., Jonietz, F., Pfleiderer, C., Rosch, A., Neubauer, A., Georgii, R. and Böni, P. *Science* **323**, 915 (2009).
- [43]. Langner, M. C. *et al.*, *Phys. Rev. Lett.* **112**, 167202 (2014).
- [44]. Bak, P. and von Boehm, J. *Phys. Rev. B* **21**, 5297 (1980).
- [45]. Reichhardt, C. and Nori, F. *Phys. Rev. Lett.* **82**, 414 (1999).
- [46]. Aubry, S. J. *Phys. France* **44**, 147 (1983).
- [47]. Bak, P. *Reports on Progress in Physics* **45**, 587 (1982).
- [48]. Fleming, R. M., Moncton, D. E., McWhan, D. B. and DiSalvo, *Phys. Rev. Lett.* **45**, 576 (1980).
- [49]. Brown, S. E., Mozurkewich, G. and Grüner, G. *Phys. Rev. Lett.* **52**, 2277 (1984).
- [50]. Chen, K. W. *et al.*, *Phys. Rev. B* **96**, 014421 (2017).
- [51]. Hupalo, M., Schmalian, J. and Tringides, M. C. *Phys. Rev. Lett.* **90**, 216106 (2003).
- [52]. Ben-Jacob, E., Braiman, Y., Shainsky, R. and Imry, Y. *Appl. Phys. Lett.* **38**, 822 (1981).

- [53]. Trzop, E. *et al.*, *Angewandte Chemie International Edition* **55**, 8675 (2016).
- [54]. Levy, J. C. S. *J. Physique* **46**, 215 (1985).
- [55]. Bak, P. and Bruinsma, R. *Phys. Rev. Lett.* **49**, 249 (1982).
- [56]. Fraerman, A. A. and Sapozhnikov, M. V. *Phys. Rev. B* **65**, 184433 (2002).
- [57]. **Singh, A.**, Lee, J. C. T., Avila, K. E., Chen, Y., Montoya, S. A., Fullerton, E. E., Fischer, P., Dahmen, K. A., Kevan, S. D., Sanyal, M. K. and Roy, S. *Nat. Comm.* **10**, 1988 (2019).
- [58]. **Singh, A.**, Sanyal, M. K., Mukhopadhyay, M. K., Lee, J. C. T., Montoya, S. A., Fullerton, E. E., Kevan, S. D., Fischer, P., and Roy, S. *Submitted* (2019).
- [59]. Als-Nielsen, J. and McMorrow, D. *Elements of Modern X-ray Physics*, (John Wiley and Sons, New York, 2000).
- [60]. Aubry, S. *"Solitons and Condensed Matter Physics"*, Springer, p264 (1979).

Two dimensional magnetic ordering in rare-earth Langmuir-Blodgett films

In a remarkable study it was found that topological order can persist in two-dimension through the formation of vortex structures [1] although thermal fluctuations [2, 3] destroy such conventional long-range ordering. There has been a considerable recent interest in Van-der Waals heterostructures and the possibility of technological application in spintronics devices has produced interesting results pertaining to 2D ferromagnetic ordering and skyrmion like vortex structures [4-6]. Moreover, recent studies have focussed on the vortex formation in anti-ferromagnetic (AFM) phase due to the speciality that AFM-skyrmion will be able to move parallel to the applied current –a major problem [7] in the development of ferromagnetic (FM) skyrmion based devices. Experimentally generation of magnetic vortex structures in AFM materials has not been observed. Although such vortex formation in AFM phase could be imposed [8, 9] from adjacent FM-skyrmions, AFM-skyrmions have not been found experimentally and is of great theoretical interest [10].

Langmuir-Blodgett (LB) films of magnetic ions can provide an ideal platform to investigate vortex structure and dynamics in 2D ferromagnetic and anti-ferromagnetic systems with minimal amount of change in the structural configuration. 2D magnetic materials with such ferromagnetic and anti-ferromagnetic spin arrangement confined within ultrathin films and multilayered structures have always attracted considerable attention for understanding the underlying physics in some other phenomena like superconductivity [11, 12].

The metal-organic multilayer structures with magnetic ions can be formed by LB techniques to investigate 2D magnetic ordering [13-15]. In LB films the magnetic metal ions are separated by approximately 5\AA within a monolayer that form a distorted hexagonal 2D in-plane lattice and in the out-of plane direction the monolayers are separated from each other by 50\AA organic chains (refer to Fig. 5.5) [16-18].

It has been reported that 2D short-range ferromagnetic order with no spontaneous magnetization occurs in gadolinium stearate (Gd-St) LB films when a magnetic field is applied along any in-plane (xy plane) direction, whereas the moments remains paramagnetic down to 2 K if the field is applied along the out-of plane direction (z direction). Higher value of magnetization was observed when the field was applied in the z direction than that obtained in any in-plane direction at any temperature indicating that the z direction is the easy axis [19, 20]. Due to vortex formation in Gd-based LB films, sub-Kelvin polarized neutron reflectivity (PNR) measurements have shown [21] that the saturation moment could never reach the expected $\sim 7\mu_B$ magnetic moment per Gd ions unless the sample is cooled below the Berezinskii-Kosterlitz-Thouless (BKT) transition temperature of 600 mK when a field was applied in the in-plane direction. We show here that spin-vortex dynamics in Ho-based LB films are quite different from Gd-based or Er-based LB films and exhibits anti-ferromagnetic ordering [37].

5.1 Langmuir-Blodgett (LB) multilayer films

Initially the Langmuir trough is thoroughly washed by de-ionized (DI) (Millipore, resistivity $\sim 18.2 \text{ M}\Omega \text{ cm}$) water. Then the empty trough was cleaned with isopropyl alcohol and finally with chloroform using kimwipes (KIMTECH). The Gd-St, Er-St and Ho-St Langmuir monolayer was prepared by gently spreading stearic acid (SA; $\text{CH}_3(\text{CH}_2)_{16}\text{COOH}$) solution prepared by mixing stearic acid in chloroform (concentration $\sim 0.2 \text{ mg/ml}$) on the surface of water (Millipore, resistivity $\sim 18.2 \text{ M}\Omega \text{ cm}$) sub-phase containing 0.5 mM rare-earth ions (dissolved gadolinium acetate, erbium acetate or holmium acetate) by using a gas-tight micro-syringe (Hamiltonian). The trough was placed in a closed chamber on an anti-vibration table and the sub-phase temperature was fixed at 15°C . After spreading the stearic acid solution on the water sub-phase there was a delay of 10 minutes before starting the compression process in order to allow the chloroform to evaporate.

The silicon (100) substrate was first cleaned by sonicating in iso-propyl alcohol then in acetone and finally washed in water. The as-cleaned silicon substrate is then hydrophillized by immersing it inside a solution containing $\text{H}_2\text{O}:\text{NH}_4\text{OH}:\text{H}_2\text{O}_2$ (RCA-I) in the ratio 10:3:3 for 20 minutes at 70°C . After disposing the solution the substrate was further washed thoroughly by DI water. Finally the substrate was dried in order to make the surface of substrate free from any dust and trapped air-bubble by blowing dry N_2 gas before loading it to the sample holder. Presence of such dust and trapped air-bubble on the surface inside the water sub-phase hinders the transfer of Langmuir monolayer onto the substrate surface.

The LB monolayer was compressed at a fixed rate of 8 mm/min to reach the target pressure. The LB films were deposited on a hydrophilic Si substrate at a constant dipping speed of 3 mm/minute for decent transfer ratio and a constant pressure (30 mN/m) was

maintained throughout the entire deposition process by an automated differential feedback arrangement. During the dipping process the substrate was held at the top position for 6 minutes during the upward stroke for the initial layer. After that it was made to hold at the top position for 30 seconds during the upward stroke and at the bottom position for 10 seconds during the downward stroke.

The deposition of a LB multilayer film involves dipping of a substrate through a Langmuir monolayer formed on the water sub-phase, by keeping constant surface pressure during transfer of molecules from air-water interface to the substrate. The first monolayer gets deposited during the water-to-air (up-stroke) on a hydrophilic substrate. Then a series of air-to-water (down-stroke) and up-stroke deposit bilayers on the substrate [17]. The first layer forming on the hydrophilic substrate during the first upstroke is an asymmetric molecular layer having metal-heads on the substrate and the hydrocarbon tails pointing upwards as shown in Fig. 5.5(a). The symmetric bi-layer deposited in the subsequent down-stroke-up-stroke cycles have hydrocarbon tails pointed in opposite directions (see Fig. 5.5(a)) [16-18]. We have shown representative X-ray data of Gd-St, Er-St and Ho-St in Fig. 5.6(b) having different odd number of layers.

We have obtained the total thickness of the film from the separation between two Kiessig fringes in the reflectivity data (see Fig. 5.6(c)). The bi-layer periodicity is obtained from the separation between two Bragg peaks (see Fig. 5.6(b)). The number of layers that were deposited in the LB trough matched with the total-thickness obtained from the reflectivity data for all the three LB films [16].

X-ray reflectivity (XRR) and X-ray grazing incidence diffraction (GID) measurements were performed at the Indian beamline in Photon Factory, KEK, Japan with a focused beam of energy 11keV to characterize the out-of plane and in-plane structure of the

deposited multilayer LB films. Since the synchrotron (Photon Factory) uses a bending magnet the focused beam is of diameter 0.6 mm. In order to minimize the effects of radiation damage on the sample we focus the beam away from the sample along the horizontal direction (~ 1.5 meter). The incident slit size was fixed at 0.2 mm X 1.5 mm (H X V).

The magnetization measurements were carried out using a 7-T Quantum Design (MPMS 3) SQUID VSM as a function of magnetic field and temperature down to 2.2 K. Magnetization isotherm measurements (M vs H at a constant temperature) over all four quadrants including the virgin curve were measured as a function of magnetic field up to ± 50 kOe. All the data presented here were collected by applying field in the in-plane direction of the samples.

The magnetization isotherm measurements were carried out first by cooling the sample from 300K to the desired temperature of measurement under zero magnetic field condition. M vs T magnetization measurements were also carried out over the temperature range 5K to 100K by applying a magnetic field of 500 Oe (in-plane) during the warming cycle from 5K.

Langmuir monolayer studies

Isotherm study

A schematic of the experimental set-up and a typical pressure-area (π -A) isotherm of the Gd-St Langmuir monolayer at the air-water interface is presented in the Fig. 5.1. The region of flat plateau and high compressibility in the isotherm is the ‘gaseous’ phase. The phase of low compressibility is identified as ‘liquid expanded’ (LE) phase followed by the ‘liquid condensed’ (LC) phase. The ‘kink’ in the isotherm during transition (LE to LC) manifests the second order phase transition [33]. Beyond this phase the available area per

molecule reaches to a limit and the monolayer goes into the ‘collapsed’ phase (C). The area per molecule of Gd-St just before collapsed phase was obtained as $\sim 22 \text{ \AA}^2$.

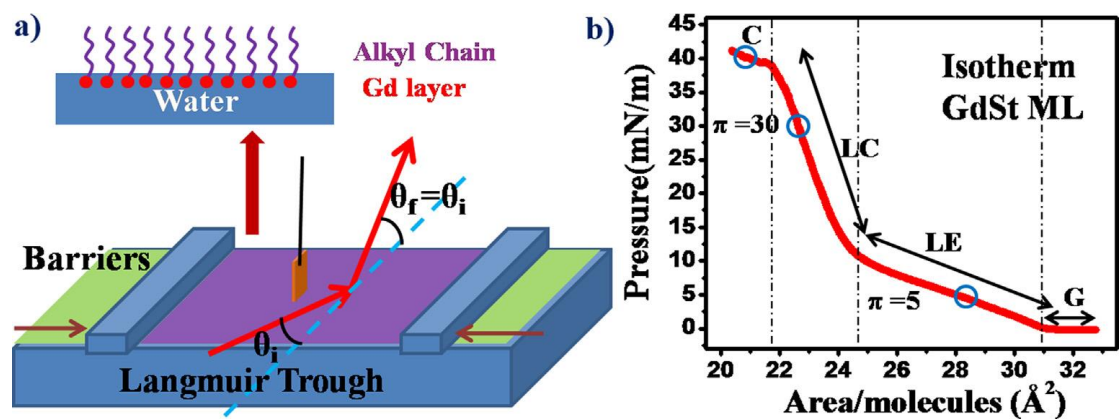


Figure 5.1: (a) Schematic of the experimental set-up and the scattering geometry including incident and scattered X-ray beam directions are indicated. (b) Typical π -A isotherm of Gd-St Langmuir monolayer at the air-water interface is presented (refer text for details) [18].

X-ray reflectivity study

The collected reflectivity in an X-ray detector from the liquid surface can be written as [32, 34]

$$R(q_z) = R_P(q_z) S(q_z, q_{xy}) \tag{5.1}$$

where, $R_P(q_z)$ is the reflectivity as considered in Parratt Formalism [35] and $S(q_z, q_{xy})$ is the contribution of diffuse scattering that depends primarily on the capillary wave fluctuations [32, 34, 36]. To avoid inclusion of diffuse scattering contribution $S(q_z, q_{xy})$ in the fitting of measured data [31], we have divided measured reflectivity ($R_M(q_z)$) by that of the pure water surface ($R_W(q_z)$). The obtained data was multiplied by theoretical Fresnel reflectivity ($R_f(q_z)$) of water surface to generate reflectivity profiles ($R(q_z)$) as given below.

$$R(q_z) \approx \frac{R_M(q_z)}{R_W(q_z)} R_f(q_z) \tag{5.2}$$

The electron densities (ρ), thicknesses (d) and interfacial roughness (σ) along the depth of the film are then extracted from the fitting of the corrected reflectivity data ($R(q_z)$) by using Parratt formalism [35]. This is valid when the measured reflectivity of the LB film on the

water surface can be treated uncorrelated as the reflectivity of the water surface plus reflectivity from the LB film which usually is the case for fatty acid molecules where the correlations between the water surface and Langmuir film are negligible. The measured and fitted reflectivity profiles (RP) are shown in Fig. 5.2(a) and the corresponding R/R_f profiles are shown in Fig. 5.2(b) for better clarity. The fitting was performed by considering a simple box model having two sub-layers of thickness d_1 and d_2 representing organic-tails and head-ions, respectively. The extracted electron density profiles (EDPs) of the Gd-St monolayers along the depth are shown in the Fig. 5.2(c). The higher electron density than that of water corresponds to the Gd-ions coupled with carboxyl group of stearic acid and the lower electron density implies the hydrocarbon tail ($C_{17}H_{35}$) of stearic acid. The reflectivity is proportional to the square of the Fourier transform of the derivative of the electron density (dp/dz) (refer Fig. 5.2(d)). The amplitude of negative peak is $0.31 \text{ el}/\text{\AA}^3$ – the electron density-difference of head-layer ($0.64 \text{ el}/\text{\AA}^3$) and water ($0.33 \text{ el}/\text{\AA}^3$). The positive peak is appearing due to the electron density of the organic tail. The obtained fitted parameters ρ , d and σ of the sublayers at different surface pressures, are provided in Table 5.1 and the corresponding theoretical values in the bottom row (calculated by assuming standard bond lengths). The electron density (ED) of a tail (ρ_1) with 137 electrons in the cross-sectional area of 21 \AA^2 is $0.33 \text{ el}/\text{\AA}^3$ [20, 21] and in the first layer of LB films near the substrate, tails form asymmetric configuration and in upper layers of LB films tails get attached from two-sides of gadolinium forming symmetric configuration. The symmetric configuration has larger ($\sim 8.3 \text{ \AA}$) box-size as compared to that of asymmetric configuration ($\sim 5.5 \text{ \AA}$) giving the ED of the complex-head part (ρ_2) with 59 electrons (one COO and half of Gd+OH), for same cross-sectional area of a tail become $0.51 \text{ el}/\text{\AA}^3$ and $0.34 \text{ el}/\text{\AA}^3$ for asymmetric and symmetric configurations, respectively. The sublayer electron densities (ρ_1 and ρ_2) increase with increasing surface pressure due to more compact packing of the molecules. The obtained thickness of the

stearate tails implies a tilt of 22° at $\pi=30$ mN/m, while it reduces to 16° at collapsed phase (Table 5.1). The reduction in ρ_2 at the collapsed phase can be attributed to the buckling on the monolayer. The increase of interfacial roughness (σ) and decrease of ρ_2 in the box (Fig. 5.2(c)) indicates a diffusion of the head-part along vertical directions due to this buckling.

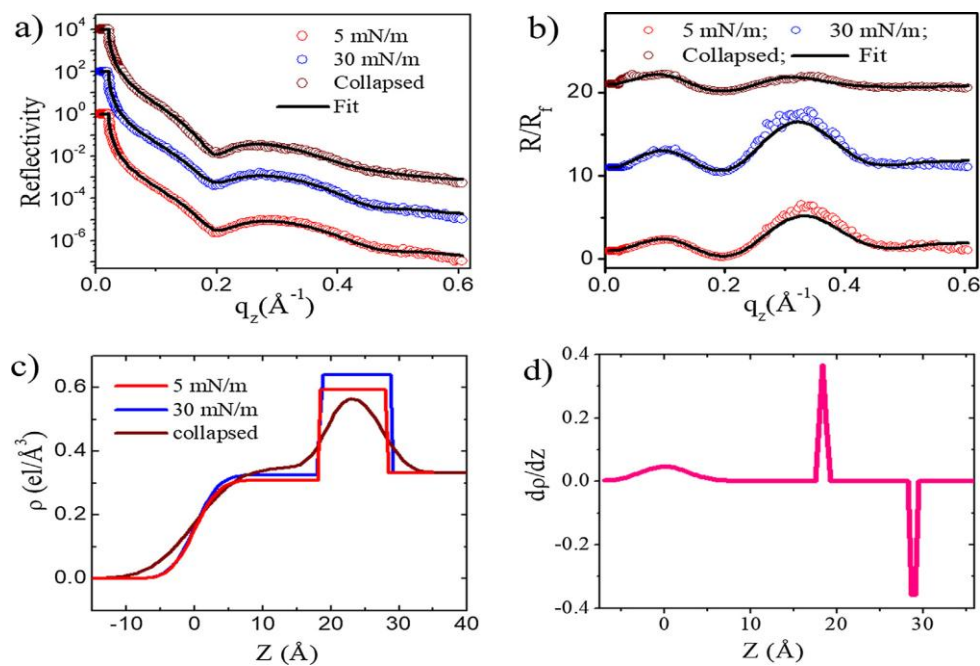


Figure 5.2: (a) XRR profiles of Gd-St Langmuir monolayer on the water surface. (b) Corresponding R/R_f profiles. The profiles are shifted vertically for clarity. (c) Extracted electron density (ρ) profiles after fitting (line color same). (d) Derivative plot of EDP for $\pi=30$ mN/m [18].

GIXD study

A typical GIXD profiles of Gd-St monolayers on the water surface ($\pi=15$ mN/m) are presented in Fig. 5.3(a) (q_z integrated intensity profile) and Fig. 5.3(b) (measured q_{xy} - q_z intensity map). We could detect only broad peak, having a clear asymmetry in the lower q_{xy} -region, due to the variation in tilt angles and small domain size. The q_z -integrated profile could not be fitted with one Lorentzian shaped peak and two peaks were required to represent the data (refer Fig. 5.3(a)). These peaks were found to be located at $1.52 \pm 0.01 \text{ \AA}^{-1}$ and $1.47 \pm 0.03 \text{ \AA}^{-1}$, which are attributed to an in-plane ordering of the Gd-St hydrocarbon tails and indexed as (11) and (02) in a centred rectangular cell with two chains per unit cell [5,10]. The associated lattice parameters are $a_r=5.0 \text{ \AA}$ and $b_r=8.3 \text{ \AA}$ and the unit cell area 41.4 \AA^2 , which

correspond to an area of two tails (20.7 \AA^2 per tail). We estimated the tilt angle (τ) of the tails from the fitting of intensity distribution along (11) and (02) diffraction rods shown in Figs. 5.3(c) and 5.3(d) respectively. The (11) peak is located at $q_z=0 \text{ \AA}^{-1}$ and a sinc function fit give a width of 0.92 corresponding to a layer thickness about 22 \AA . The (02) peak could not be fitted with a single sinc function centered at $q_z=0$ (black dashed line) and a second sinc function was required for this peak at $q_z=0.59 \text{ \AA}^{-1}$ along out-of-plane direction. The presence of stronger degenerate peak (11) at higher q_{xy} value and existence of non-zero q_z value of non-degenerate peak (02) indicate next-nearest-neighbour (NNN) tilt of rod-shaped molecular tails though we could not detect expected shift in (11) peak at half of the above q_z value for NNN-tilt due to weak statistics. The tilt (τ) angle was estimated to be 22° following well-known formalism [5] and this value is consistent with the XRR results.

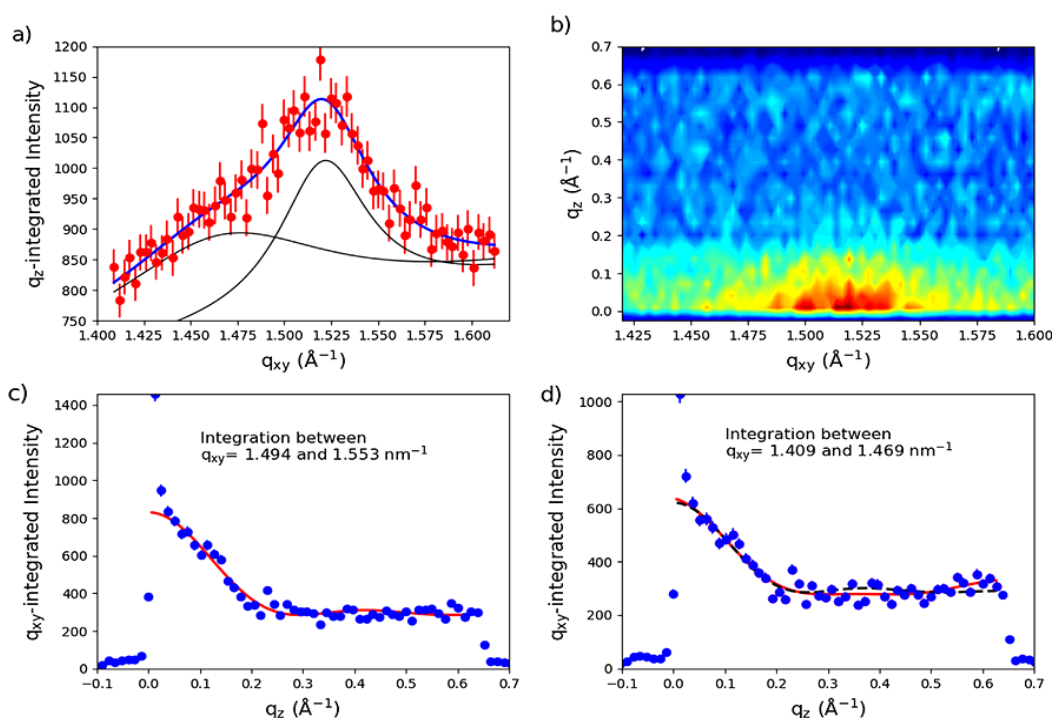


Figure 5.3: (a) q_z -Integrated intensity profile of GIXD spectra as a function of q_{xy} of GdSt Langmuir monolayer; the profile is fitted by a linear background and two Lorentzian shape peaks, (b) q_{xy} - q_z map of GIXD spectra. (c) and (d) Intensity profile of the (02) and (11) peaks along q_z direction along with their fits [18].

Table 5.1

Parameters for GdSt Langmuir film on water; symmetric configuration are in bracket.[18]

Surface Pressure π (mN/m)	Tail (hydrocarbon)		Head (Gd-carboxylate)		Interface roughness (Å)		Tilt-Angle (°)
	d_1 (Å)	ρ_1 (el/Å ³)	d_2 (Å)	ρ_2 (el/Å ³)	air-tail	tail-head	
5	18.3 ± 0.1	0.31 ± 0.03	9.8 ± 1.0	0.59 ± 0.05	2.8 ± 0.1	0	23
30	18.4 ± 0.1	0.32 ± 0.03	10.6 ± 1.0	0.64 ± 0.05	2.8 ± 0.1	0	22
Collapsed	19.1 ± 0.1	0.35 ± 0.03	8.7 ± 1.0	0.59 ± 0.05	5.1 ± 0.1	2.4 ± 0.1	16
Theoretical	19.9	0.33	5.5 (8.3)	0.67 (0.51)	-	-	0

5.2 LB multilayer studies

The metal-organic multilayer structures comprising of rare-earth magnetic ions formed by LB technique is used to investigate the 2D magnetic ordering [13-15]. In LB films the magnetic metal ions are separated by approximately 5Å within a monolayer that form a distorted hexagonal 2D in-plane lattice and in the out-of plane direction the monolayers are separated from each other by 50Å organic chains (refer to Fig. 5.5) [16-18].

5.2.1 X-ray reflectivity (XRR) study

XRR profiles of 1 and 9 monolayer GdSt LB films are depicted in Figs. 5.4(a) and 5.4(b), respectively. The extracted EDP of 1 monolayer film indicate head and tail thickness (see Fig. 5.4(c)) as 5.4 Å and 19.3 Å with corresponding electron densities of 0.51 el/Å³ and 0.32 el/Å³ - these are close to theoretical values (Table 5.1). The XRR data of 9 monolayer film (Fig. 5.4(b)) was fitted using a model [18, 23] that has an asymmetric layer on the substrate and four bi-layers of symmetric molecules with interfacial roughness and a small gap (1.2 Å) between end-points (CH₃) of the organic tails. The obtained electron densities (Fig. 5.4(d)) of the head and tail regions are found to be 0.57 el/Å³ and 0.33 el/Å³ with corresponding thicknesses as 8.1 Å and 20.0 Å respectively. For the asymmetric layer, just

above the substrate, the tail-region were found to be same but the density and thickness for the head-region were $0.44 \text{ el}/\text{\AA}^3$ and 6.0 \AA .

The multilayer film shows excellent periodicity in the out-of-plane direction with efficient deposition of 9 monolayers. The representative AFM images of both the LB films (inset of Figs. 5.4(a) and 5.4(b)) give an average thickness to be about 30 \AA and 260 \AA respectively, confirming with the XRR results.

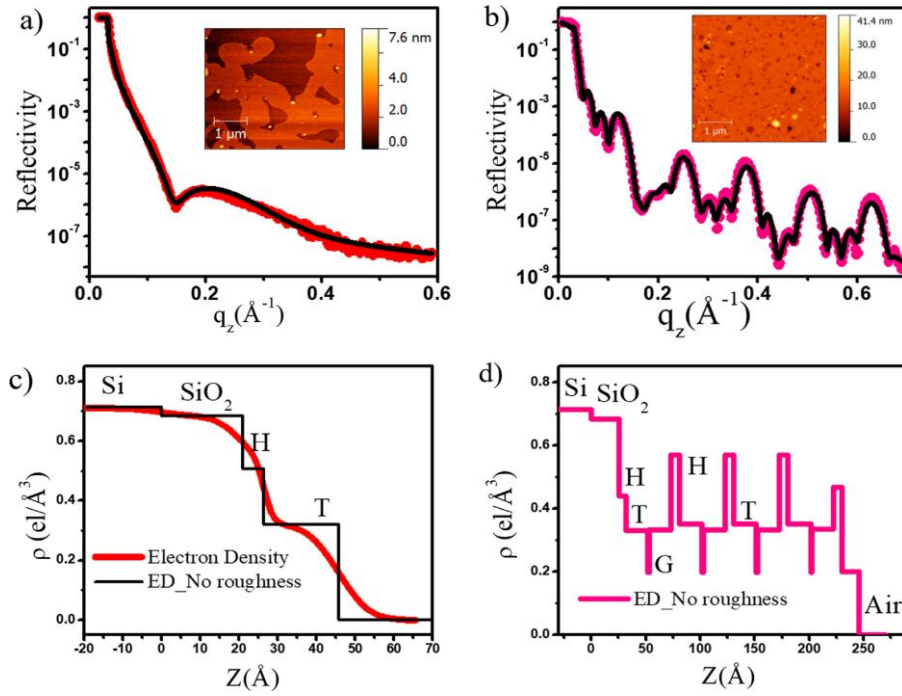


Figure 5.4: XRR profiles of Gd-St LB films (a) monolayer (ML), (b) multilayer (9-ML) and their fits (black solid line). Corresponding AFM tomography images of Gd-St LB films are in the insets. Extracted EDPs for (c) monolayer and (d) multilayer (without any roughness convolution) films [18].

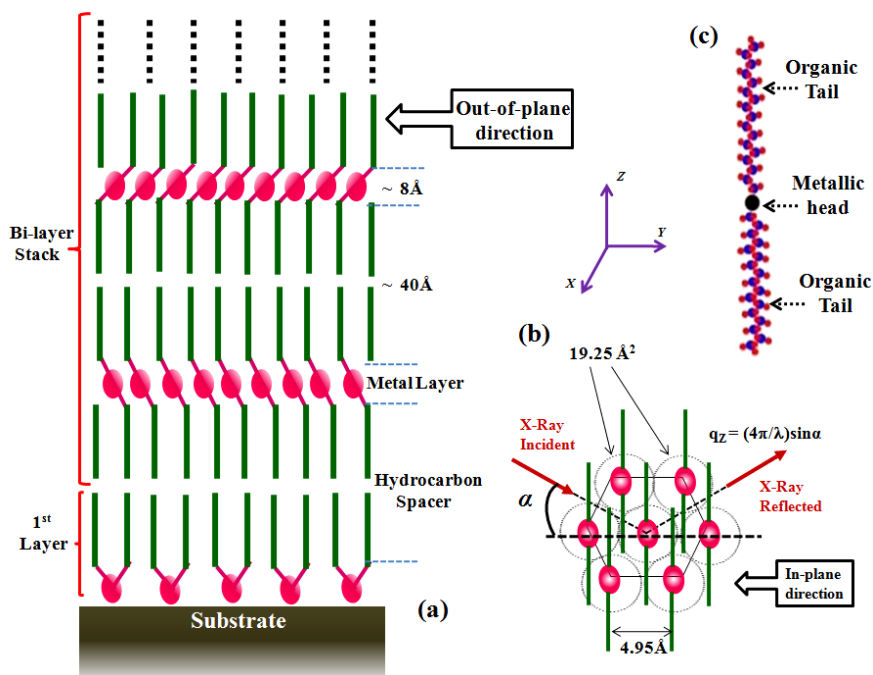


Figure 5.5: Schematic diagram of the (a) out-of-plane and (b) in-plane structure of multilayer Rare-earth (Gd,Er & Ho) Stearate Langmuir-Blodgett films is shown with the scattering geometry employed for the X-Ray measurements. All the molecules are in the same plane with the X-ray incident on the plane at an angle α . The x-z plane is the scattering plane and the magnetic field is applied along the +y direction. λ and α are the wavelengths of the radiation and the angle of incidence, respectively. (c) Shows a single RE-St amphiphilic molecule where the central RE ion is connected to two hydrocarbon chains [37].

In order to determine the out-of plane structure of a monolayer or multilayer, the X-ray reflectivity (XRR) technique is generally used. We have carried out the XRR technique to determine the film thickness, periodicity, electron density and interfacial roughness of the multi-layered LB films. X-ray reflectivity (XRR) and grazing incidence X-ray diffraction (GIXD) measurements were performed at the Indian beamline in Photon Factory, KEK, Japan with a focused photon beam of size 0.6 mm diameter at energy 11keV to characterize the out-of plane and in-plane structure of the deposited multilayer LB films. The GID part will be discussed in the next section. The schematic of the scattering geometry of XRR is shown in Fig. 5.5(c). In Fig. 5.6 (b & c) we have shown the measured and calculated specular X-ray reflectivity data of multilayer rare earth LB films of Ho, Er and Gd respectively. In this data the presence of both Bragg peaks and Kiessig fringes (see Fig. 5.6(c)) corresponding to out-of-plane head-head distance and total film thickness, respectively, are evident. For films

with large number of layers, Bragg peaks become strong and Kiessig fringes could not be resolved properly (see Figs. 5.6(b) and 5.6(c)). The measured data matches quite well with the theoretical reflectivity values calculated from the electron-density profile (refer upper insets) according to the Parratt formalism for all the three films [24]. The electron density of the organic tail and the metallic head group for Ho-St, Er-St and Gd-St is given in Table 5.2.

Table 5.2: X-ray reflectivity fitting parameters as used in Fig. 5.6. Each film is composed of first monolayer on the substrate followed by several bilayers stack having same parameters as shown below [37].

Film	First Monolayer				Bi-Layer Stack			
	Head		Tail		Head		Tail	
	d(Å)	$\rho(\text{el}/\text{\AA})$	d (Å)	$\rho(\text{el}/\text{\AA})$	d(Å)	$\rho(\text{el}/\text{\AA})$	d (Å)	$\rho(\text{el}/\text{\AA})$
Ho-St	6.0±0.1	0.42±0.05	25 ± 0.1	0.30±0.05	6.8±0.1	0.52±0.05	19.5±0.1	0.32±0.05
Er-St	5.8±0.1	0.45±0.05	21.2±0.1	0.29 ±0.05	7.9±0.1	~ 0.64±0.05	20±0.1	~ 0.3±0.05
Gd-St	5.8±0.1	0.34±0.05	18± 0.1	0.29 ±0.05	7.5±0.1	0.57±0.05	19.6±0.1	0.37±0.05

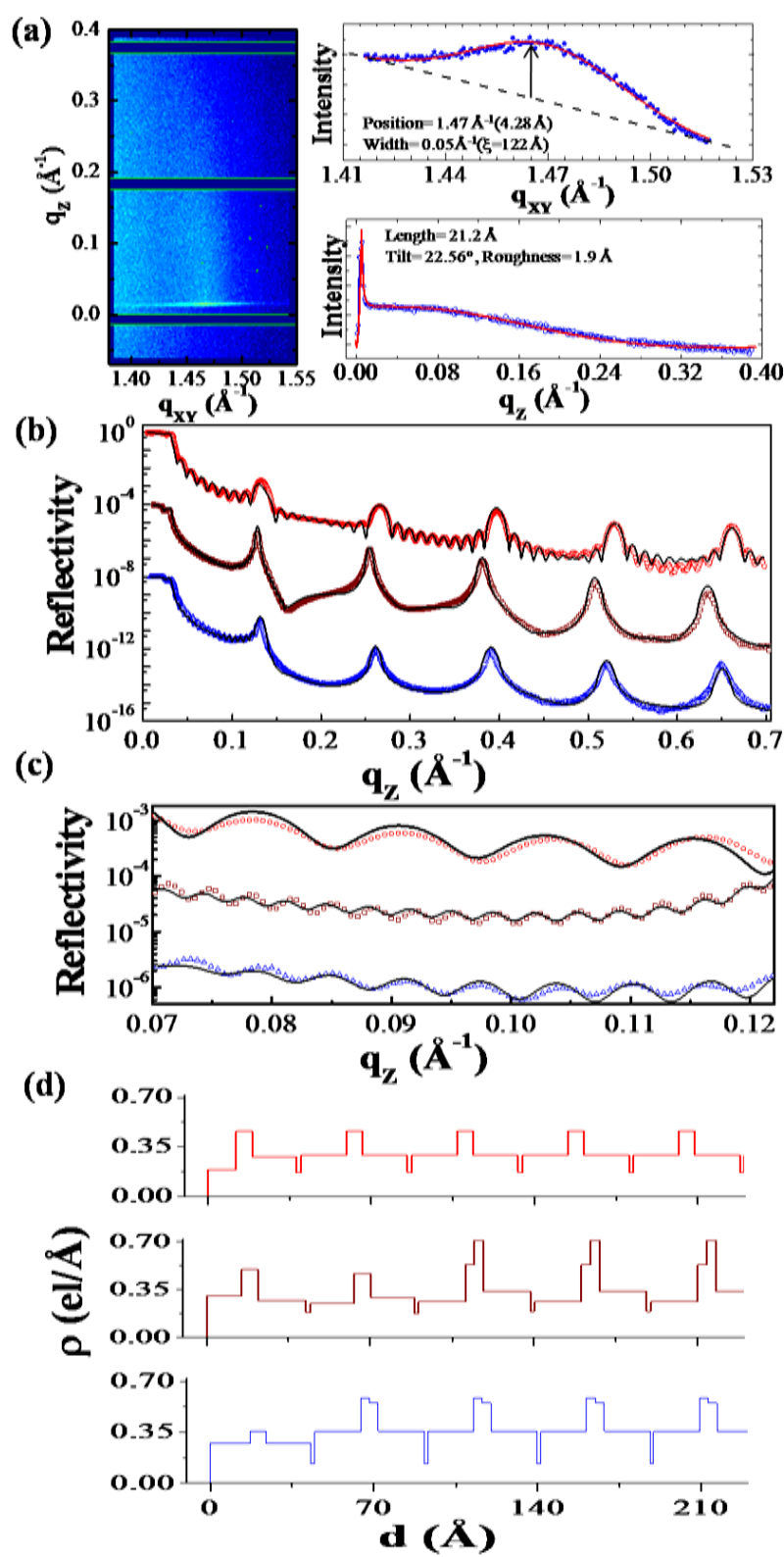


Figure 5.6: (a) Grazing Incidence Diffraction image of Gd-St (21ML) with the extracted q_{xy} and q_z plots along with their fits (red lines). Specular X-Ray reflectivity of (b) Ho-St LB film (open circle) with 21 monolayers, Er-St LB film (open square) with 71 monolayers and Gd-St LB film (open triangle) with 41 monolayers - the plots are shifted vertically for clarity. (c) Enlarged view of Kiessig fringes (with fit). (d) The electron density profile as a function of depth for initial few layers upto 220 \AA . Open coloured circles are experimental data points and solid lines are the fitted curves [37].

5.2.2 Grazing incidence X-ray diffraction (GIXD) study

To determine the in-plane structure of the multi-layer LB films we have done grazing incidence X-ray diffraction (GIXD). A typical GID image collected in Pilatus (1M) 2D detector along with its extracted line profile for Gd-St multilayer LB film (21ML) is presented in Fig. 5.6(a). The extracted data and corresponding fits (shown in red line) after background subtraction (shown by the dotted line) are given in Fig. 5.6(a). The q_{xy} GID plot show a broad peak which was fitted by the Gaussian function to obtain the peak center (refer arrow in the figure). From the peak position in the GID plot along the in-plane direction we have calculated the in-plane separation between two consecutive rare-earth (Gd) atoms to be 4.95 Å. From this value of separation the calculated mean area occupied by each head comes out to be 19.25 Å². The calculated electron density of the head group (Gd-2COO) approaches to the value of 0.69 el/Å³ while the value of the organic tail group comes around 0.35 el/Å³.

The organic tails in the LB films are not point like objects and the molecular degrees of freedom are tilt, orientation of the molecular structures and lattice distortion. The tilt and tilt azimuth of the unit-cell, can be measured from the Bragg rod (q_z) scan, keeping q_{xy} fixed. The data was fitted with the profile [22, 23]

$$I_{zz} = |V(q_z, q_c) S_q(L, \theta, q_z, q_x)|^2 D_{wf}(q_z, \sigma) \quad (5.3)$$

Where V is the Vineyard function, S_q is the structure factor with L , θ being the length and tilt angle of each tail and D_{wf} is the Debye-Waller factor that depends on the interfacial roughness (σ). After fitting with the above intensity profile the length, tilt angle and roughness comes out to be 22.2 Å, 22.56° and 1.9 Å respectively. From the length and tilt angle of the organic tail one can estimate the out-of plane tail length to be 19.58 Å which is close to the value obtained from the fitting of the reflectivity data.

5.3 Magnetization measurements

It has been already reported that 2D short-range ferromagnetic order with no spontaneous magnetization occur in the gadolinium stearate (Gd-St) LB films when a magnetic field is applied along any in-plane (xy plane) direction, whereas the moments remains paramagnetic down to 2 K if the field is applied along the out-of plane direction (z direction). Higher value of magnetization was observed when the field was applied in the z direction than that obtained in any in-plane direction at any temperature indicating that the z direction is the easy axis [19, 20]. Due to vortex formation in Gd-based LB films, sub-Kelvin polarized neutron reflectivity (PNR) measurements have shown [21] that the saturation moment could never reach the expected $\sim 7\mu_B$ magnetic moment per Gd ions unless the sample is cooled below the Berezinskii-Kosterlitz-Thouless (BKT) transition temperature of 600 mK and a field was applied in the in-plane direction. We show here Ho-based LB films are quite different from Gd-based films and exhibit anti-ferromagnetic ordering.

Now we present the as-measured magnetization (M) data as a function of field (H) measured at 2.2K temperature (T) for a Ho-St LB film (refer Fig. 5.7(a)). The diamagnetic signal measured from silicon substrate is also presented in this figure. In Fig. 5.7(b) we have shown typical data of Ho-St obtained after subtracting silicon background. Similar measurements were carried out for all the three types of LB films namely Ho-St, Er-St and Gd-St. We observe field-induced saturation-magnetization in the in-plane direction for all the three types of films as reported [19-21] earlier for the Gd-St films. The Gd-St LB films exhibited temperature dependent saturation moment (M_S) and we find Er-St LB films are also showing similar trends (refer Figs. 5.7(c) and 5.7(d)). However, for the Ho-St LB films all the magnetization curves measured at different temperatures saturated at almost the same value of magnetization (refer Fig. 5.7(b)).

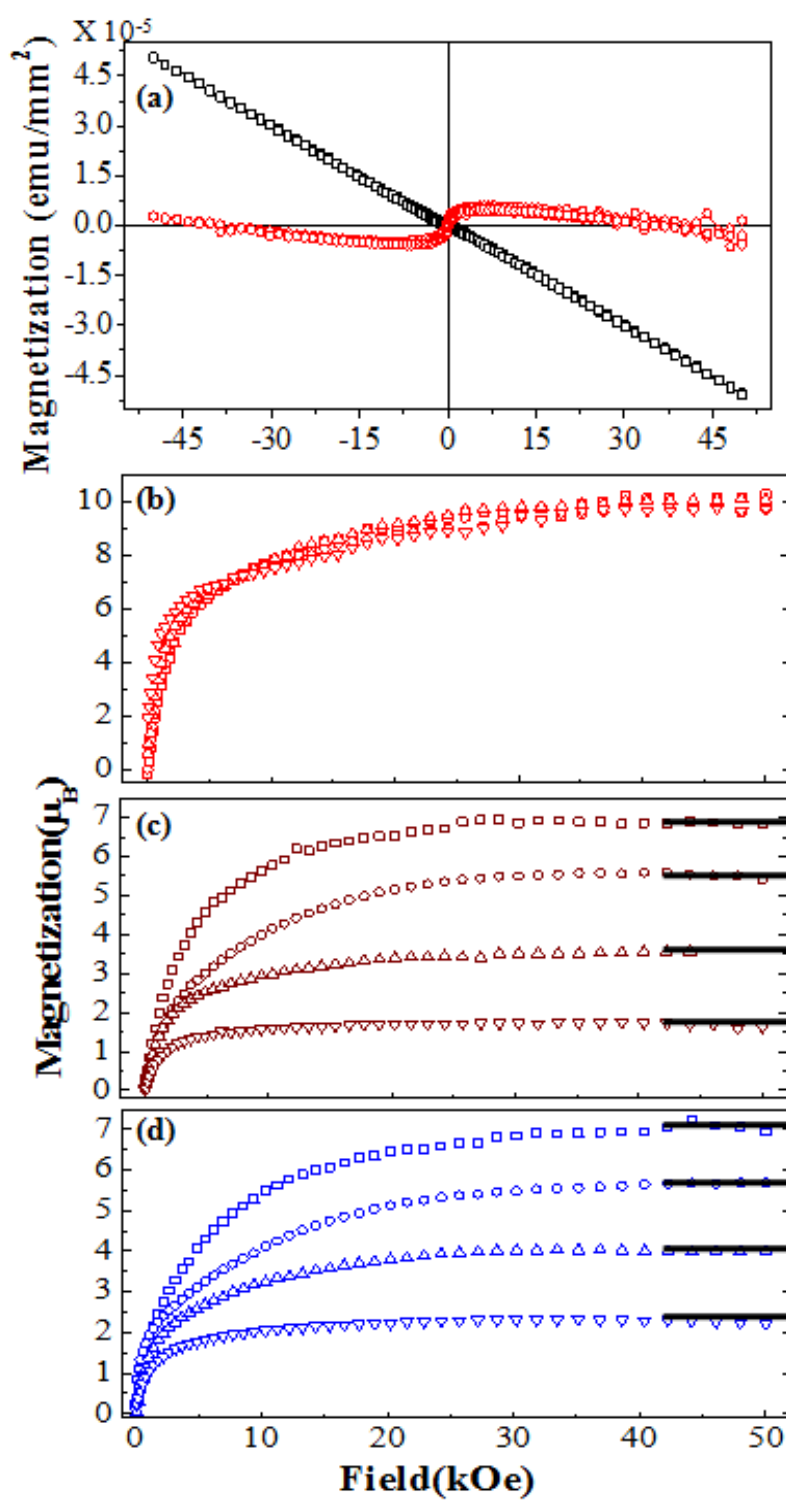


Figure 5.7: (a) Raw data of in-plane magnetization as a function of applied magnetic field taken at 2.2 K for 41 ML Ho-St LB film (open red square) and for bare Si substrate at 2.2K used here (open black square). The in-plane magnetization data after substrate correction in terms of Bohr magneton per unit Rare-earth atom at 2.2K (open square), 5K (open circles), 10K (open up-triangles) and 20K (open down-triangles) for (b) Ho-St LB film with 39 monolayers (red symbol) (c) Er-St LB film with 37 monolayers (violet symbol) and (d) Gd-St LB film with 41 monolayers (blue symbol). The black horizontal lines show the value of the respective saturation magnetization [37].

We have compared the low-field M-H data collected for three different types of films in details. The magnetization data of Ho-St, plotted against (H/T) in log-linear scale clearly show reduction in magnetization as the temperature is lowered indicating anti-ferromagnetic in-plane ordering. It should be noted here that anti-ferromagnetism in manganese stearate (Mn-St) powders, reported [25-27] earlier, the magnetization exhibited increase with the lowering of the temperature, indicating presence of ferromagnetic clusters.

In Fig. 5.14(b) and 5.14(c) we have plotted magnetization data collected at different temperatures to compare the behavior of Ho-St and Er-St LB films. The data for Ho-St clearly showed reduction in M with lowering of T in data taken with lower field values as expected in AFM ordering. The Er-St data do not show such trend; it shows reduction in M with increasing T as observed in the behavior of saturation moments (M_S). In Fig. 5.13(d) we have shown variation of M_S values (refer Fig. 5.13) with temperature for Ho-St, Er-St and Gd-St LB films in log-linear plots.

Substrate correction

All the raw M-H and M-T data were substrate corrected before further analysis were done. M-H silicon substrate data has already been shown in Fig. 5.7(a) (black open squares). All M-T (refer Fig. 5.15(a)) sample data was also substrate corrected using bare Si(100) M-T data and also taking into account the minor contribution of the trace amount of Fe impurities present in all the Si substrate material which was experimentally verified from the SIMS measurement data. The next section details the measurements done for Si (100) substrate to correct the raw M-T data for all the three different LB multilayer systems studied here.

5.4 Substrate magnetization and Secondary Ion Mass Spectrometry (SIMS)

We have carried out magnetization of the silicon bare substrates that we have used for depositing the LB multilayer films of Ho-St, Er-St and Gd-St. The M-H data for silicon substrate is already shown in Fig. 5.7(a) (black open circles) and shows the typical diamagnetic behaviour. In Fig. 5.8 below we have shown raw M-T plots of both sample and substrate from 260 mK to 100K temperature.

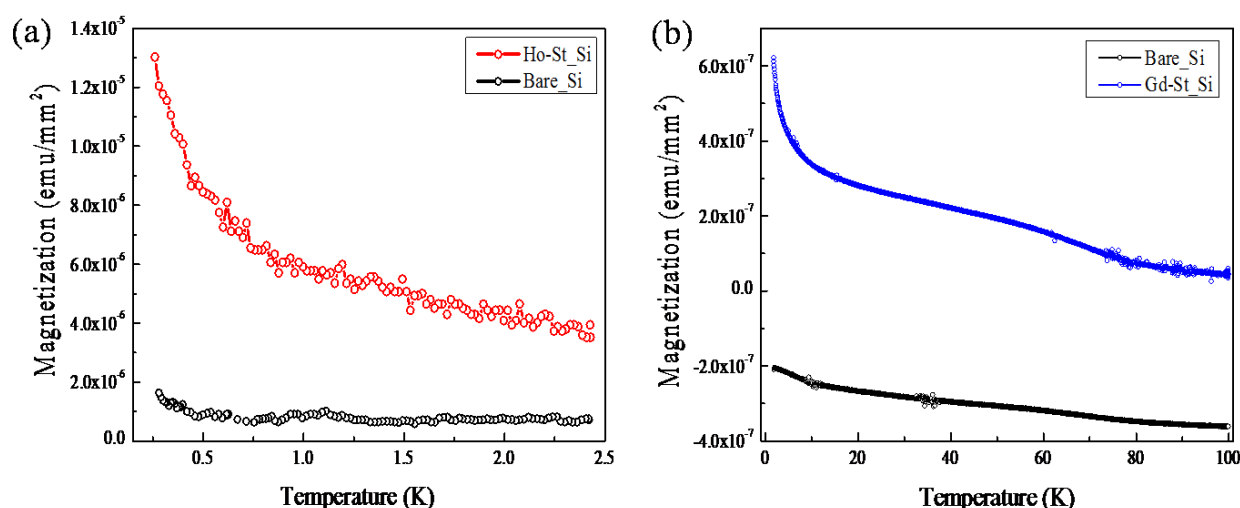


Figure 5.8: Raw magnetization data as a function of temperature, (a) Ho-St on Si (open red circles) and bare Si (open black circles) from 260 mK to 2.4 K and (b) Gd-St on Si (open blue circles) and bare Si (open black circles) from 2.2 K to 100 K.

The high temperature (2.2K to 100K) measurements were done in SQUID VSM at Rutherford Appleton Laboratory (UK) whilst the low temperature magnetization (260mK to 2.4K) measurements were done using an instrument in Sakakibara Lab at ISSP (Japan). In the high temperature plot there is a slight up-ward raising trend of the silicon data at low temperatures although the value is negative whereas in the low temperature plot it is almost flat but the value is positive. In order to check the consistency of this raw magnetization data

we have further carried out SIMS measurement to identify the presence of any magnetic impurities present in the silicon substrate. Before going into the experimental results we have first presented a brief introduction along with a schematic (see Fig. 5.9) of the SIMS instrument.

Secondary-ion mass spectrometry (SIMS) is generally used to analyze the composition of solid surfaces and thin films by sputtering the surface of the sample with a focused primary ion beam and thereby collecting and analyzing ejected secondary ions. The mass/charge ratios of these secondary ions are measured by a mass spectrometer to determine the elemental, isotopic, or molecular composition of the surface to a depth of 1 to 2 nm (See Fig. 5.9). Due to large variation in ionization probabilities corresponding to different materials, SIMS is usually considered to be a qualitative technique, although quantization is achievable with the use of standards. SIMS is the most sensitive surface analysis tool, with elemental detection limits ranging from parts per million to parts per billion.

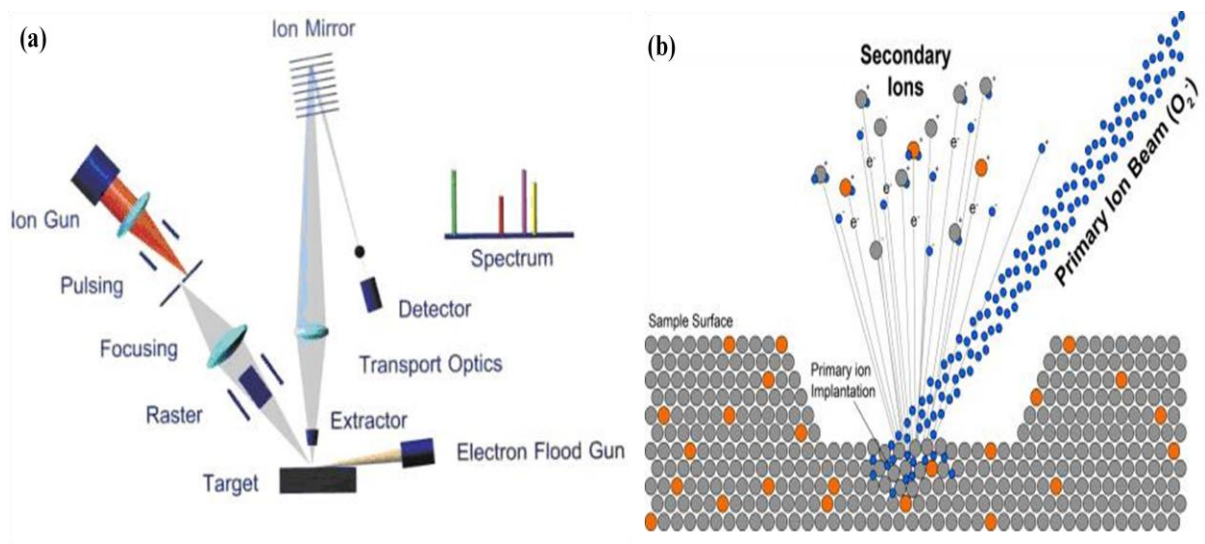


Figure 5.9: (a) Image comprising of the different components of the SIMS instrument. (b) Sputtering mechanism from a sample using O_2 ion beam [34].

SIMS measurements of LB multilayer samples

In order to check the presence of trace amount of magnetic elements present in the Si substrate on which multilayered LB films of Gd-St, Er-St and Ho-St were deposited was studied by using secondary ion mass spectrometer (SIMS) technique available at Saha Institute of Nuclear Physics (See Fig. 5.10 and Fig. 5.11). Apart from the constituents elements like Er, Gd or Ho along with Si which are already present we also probed for the presence of any magnetic impurities in the substrate like Fe, Co and Ni. First we did the mass spectrum of all the three distinct type of LB films as shown in figure 5.12. Then from the mass spectrum data we specified our region of interest and performed counts/second as a function of time measurements for the different atomic masses observed in the samples. Finally we calculated the depth of sputtered region in each sample by using Dektak instrument and plotted the composition profile as function of depth. The energy of the primary ion beam was 5 Kev with the chamber pressure at 4×10^{-7} torr. The size of the beam was around $100 \times 100 \text{ nm}^2$.



Figure 5.10: Image of the SIMS instrument used for calculating the composition profile of the rare-earth based LB films at Saha Institute of Nuclear Physics, Kolkata, India.

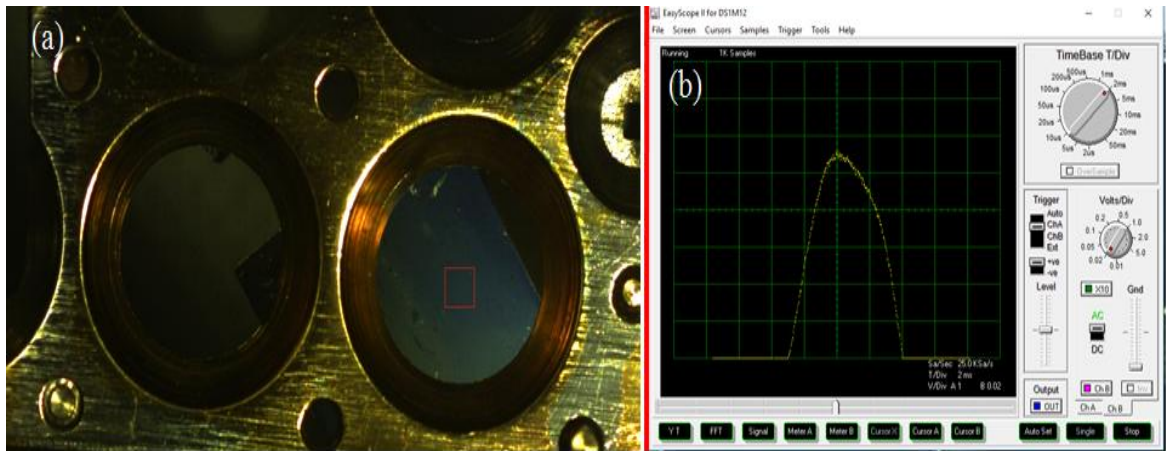


Figure 5.11: (a) Image of the sample holder along with samples inside it. The red box shows the region to be studied. (b) Instrumental parameters of the ion beam (O_2) at the time of measurement.

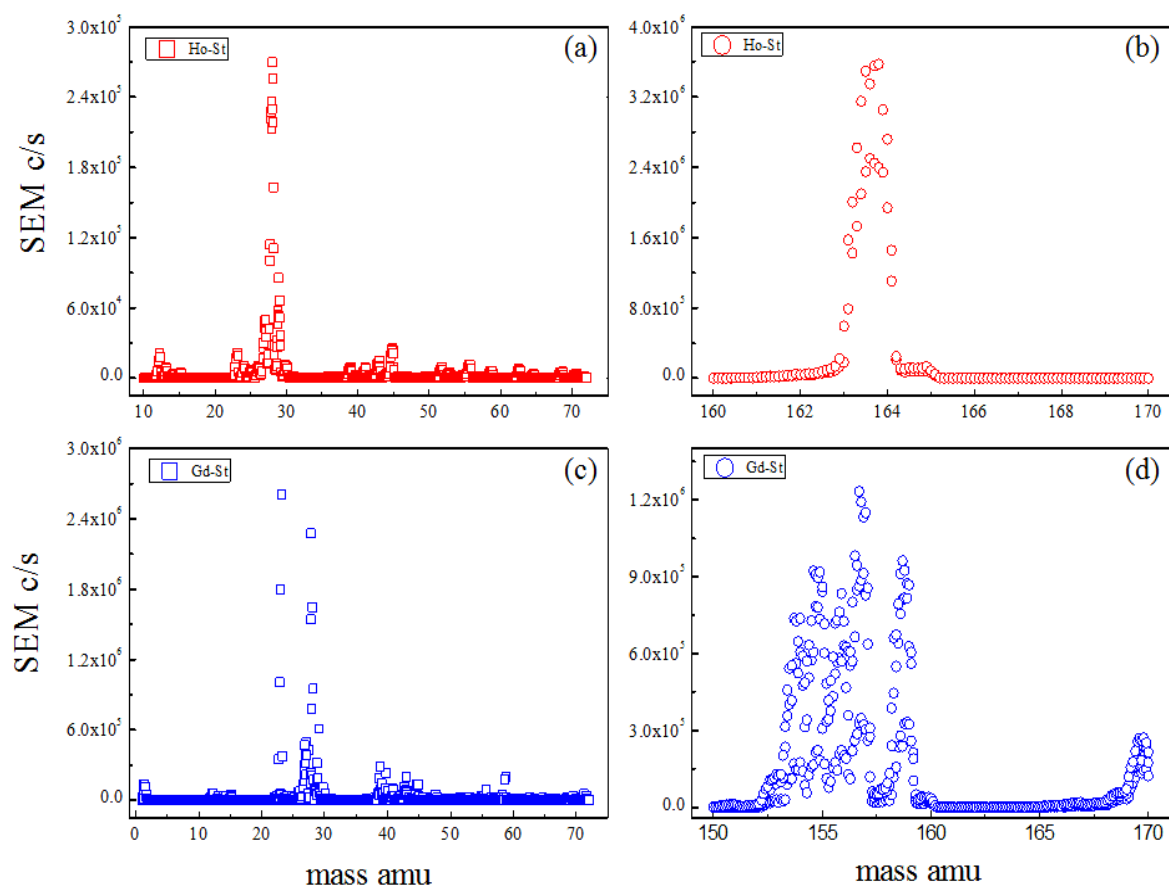


Figure 5.12: Mass spectrum of Ho-St (red symbol) and Gd-St (blue symbol) LB films from mass number (a, c) 0 to 70 and (b, d) 150 (Gd) or 160 (Ho) to 170 respectively.

Table 5.3: Constituent elements and their corresponding Mass number considered for SIMS measurements as observed from Mass spectrum results (see Fig. 5.12)

	Ho/Er/Gd	Silicon	Iron	Nickel	Cobalt
Ho-St	164.9 (Ho)	28 .0	55.9	57.9	58.9
Er-St	166.9 (Er)	28 .0	55.9	57.9	58.9
Gd-St	157.25 (Gd)	28 .0	55.9	57.9	58.9

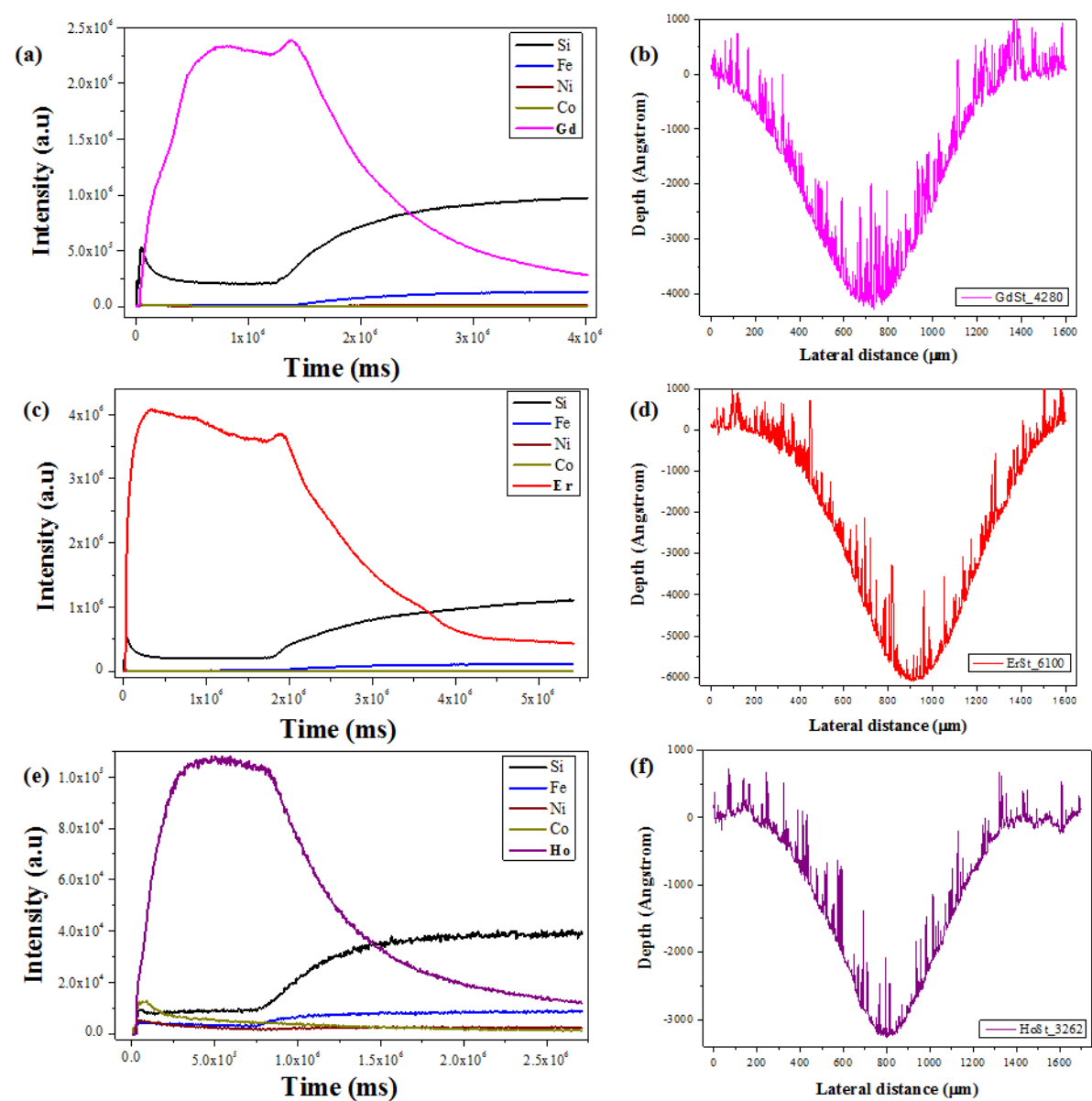


Figure 5.13: Intensity vs time profile in SIMS measurement of (a) Gd based LB film, (c) Er based LB film and (e) Ho based LB film. Depth vs Lateral distance profile as observed in Dektak instrument for (b) Gd based LB film, (d) Er based LB film and (f) Ho based LB film. All the samples were deposited on Si (100) substrates.

From Fig. 5.13 one can observe that apart from the dominant contribution coming due to the sample and substrate constituents in each of the three samples there is also some additional amount of Iron (Fe) contribution present in each of the three samples. Careful observation of Fig. 5.13 (a, c & e) illustrates that the Fe contribution is very small and is coming from the silicon (100) substrate where it is assumed to be present as impurities whereas that of Ni and Co is almost negligible. Although the percentage of Fe impurity is small in comparison to the sample still the amount varies slightly from one sample to another. The other magnetic impurities that we have considered was Cobalt (Co) and Nickel (Ni), which are insignificant or almost absent in all the three cases. From Fig. 5.13 (b, d & f) we have calculated the height of depth up to which the film was sputtered by subtracting the minima point from zero. The plot of the Intensity as a function of depth of the sputtered region as obtained from figure 5.13 for all the three different LB films of Gd-St, Er-St and Ho-St are shown in figure 5.14.

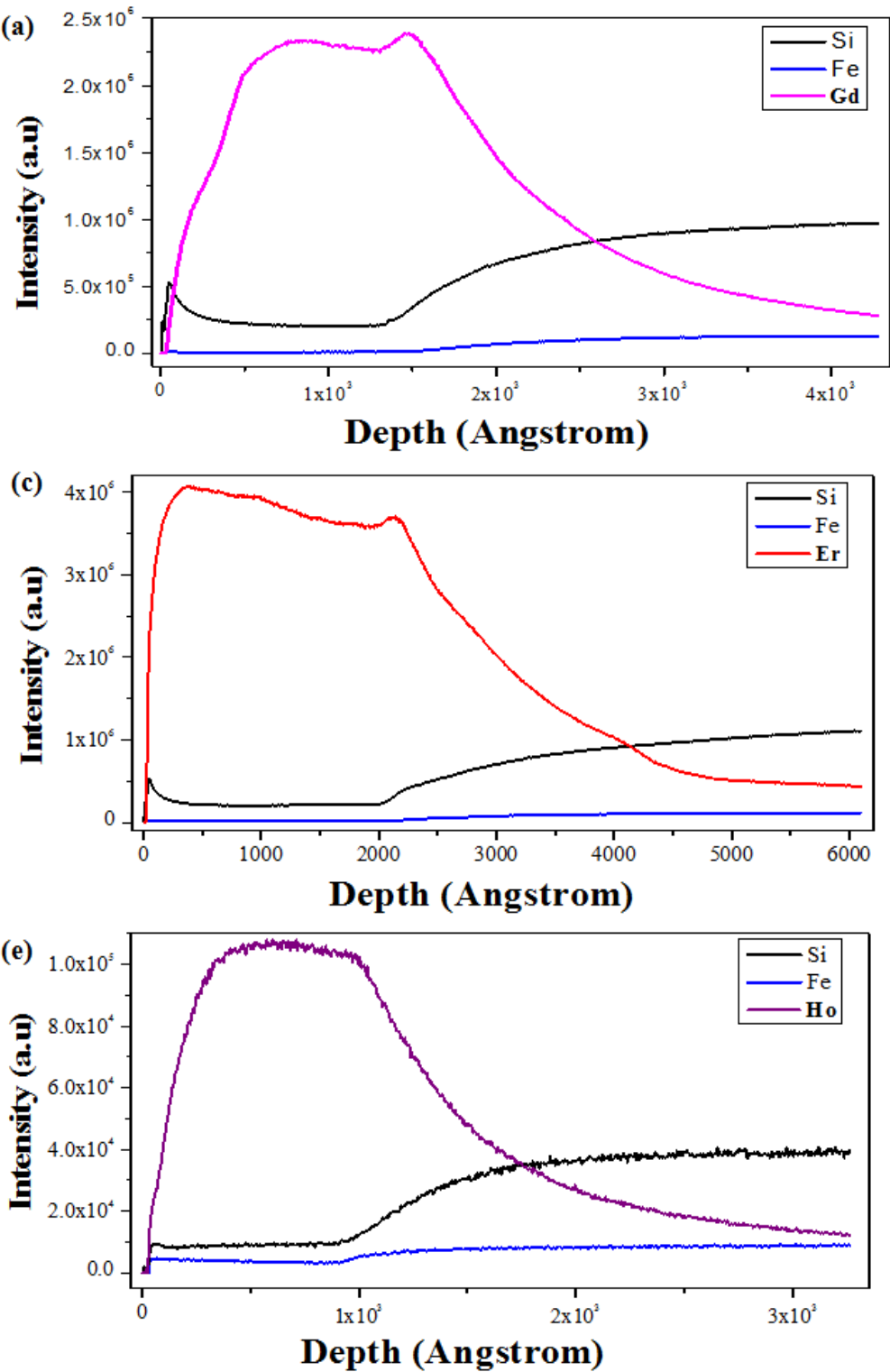


Figure 5.14: Plot of composition profile as a function of depth for (a) Gd-St LB film, (b) Er-St LB film and (c) Ho-St LB film.

5.5 Anti-ferromagnetic ordering in Ho-St LB multilayer films

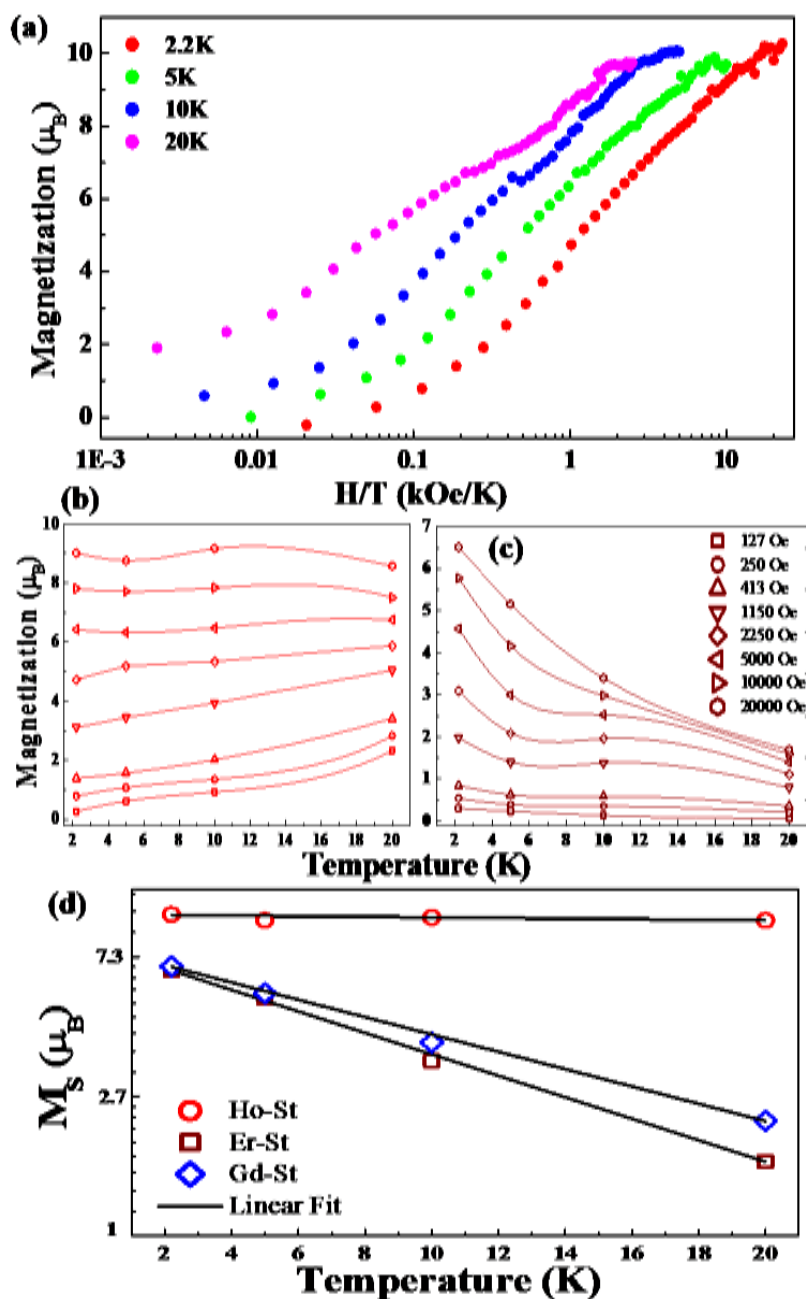


Figure 5.15: (a) Magnetization data in terms of Bohr magneton for Ho-St LB film with 39 monolayers as a function of H/T (log scale) measured at 2.2 K (red), 5K (green), 10K (blue) and 20K (pink). Magnetization value as a function of temperature at different field values (shown within Fig. 4(c)) derived from M-H curves for (b) Ho-St (red colour) and (c) Er-St LB films (violet colour). (d) Log-linear plot of the saturation magnetization M_s expressed in Bohr magneton per RE (Gd, Er or Ho) ion as a function temperature and solid black line is the linear fit [37].

The saturation magnetization (M_S) of Gd-St and Er-St LB films decay exponentially with temperature giving a relation ($\ln M_S = 0.66-S*T$). Here M_S is expressed in the unit of μ_B/ion . The value of the slope, S , obtained from linear fit and was found to be 0.077 and 0.062 for Er-St and Gd-St respectively. The exponential decay in the value of the saturation magnetization, M_S , is known to be due to the existence of vortex structure in Gd-St [21] and we observe similar trend in Er-St data. Ho-St shows almost temperature independent, giving a very small value of S , 0.0023, saturation moment (M_S) of $\sim 10.2\mu_B$ - this is close to the theoretical value $10.5\mu_B$. The saturation value of Er-St and Gd-St at the lowest observed temperature (2.2K) is $\sim 6.7\mu_B$ and $\sim 6.9\mu_B$ respectively. The theoretically predicted value of Er-St and Gd-St is around $9\mu_B$ and $7\mu_B$ respectively. The mismatch in experimental and theoretical value is primarily due to error in calculation of the number of molecules.

We now present the M vs T curves (refer Fig. 5.15(a)) for all the three types of films, measured with an applied field of 500 Oe applied along the in-plane direction. The Er-St and Gd-St LB films showed similar trends in M - T data. The anti-ferromagnetic characteristics in the Ho-St data became clear in the of $1/\chi$ vs T plot (refer Fig. 5.15(b)).

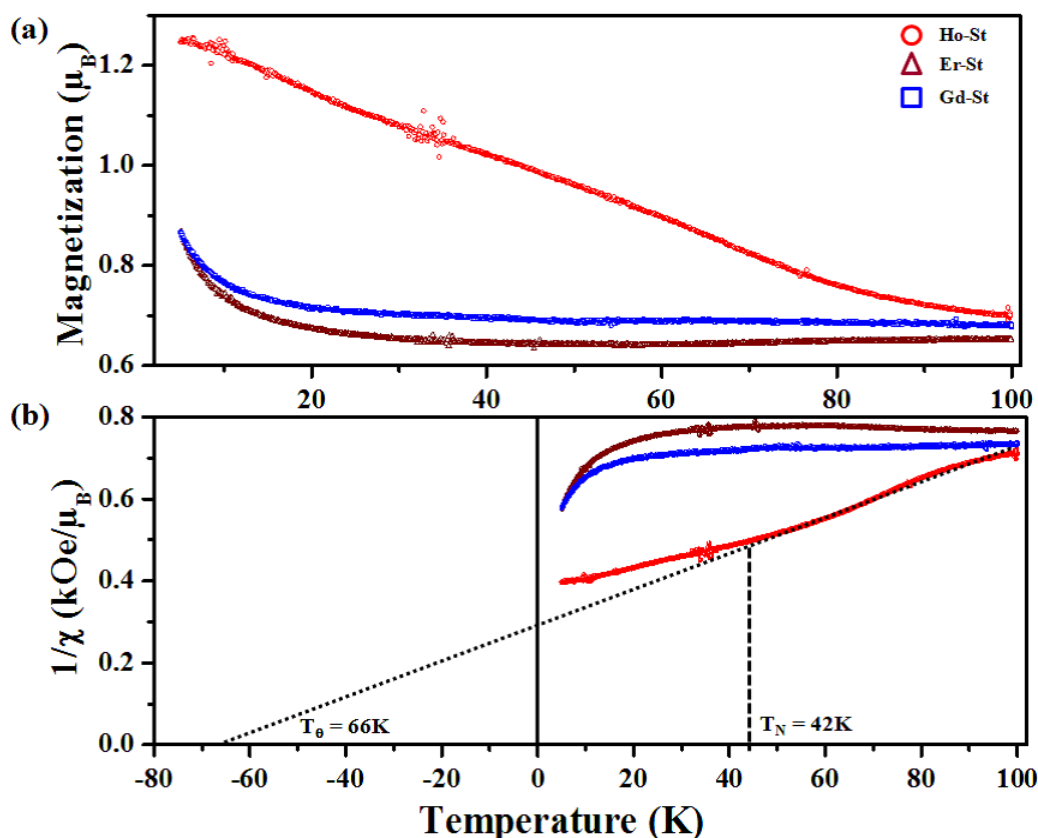


Figure 5.16: (a) The in-plane magnetization data for Ho-St (open red circles), Er-St (open violet triangles) and Gd-St (open blue squares) LB films measured as a function of temperature T with an applied field H of 0.5 kOe. (b) Curie-Weiss plot of the inverse susceptibility vs temperature of Ho-St. The extrapolation of the high temperature data is shown by the dotted line which intercepts at a negative temperature [37].

By fitting a straight-line to the higher temperature data of the form $1/\chi = (T - \theta)/C$ we get $C = 1.275$ emu-K/mole-Oe, and an intercept at a negative temperature $\theta = -66$ K, as expected in anti-ferromagnetic ordering (refer Fig. 5.16(b)) for the Ho-St LB films. The value of Neel-temperature T_N for this film was obtained as 42K. It should be mentioned here that similar M-T plots were obtained earlier [25, 26] for Mn-St powders giving θ and T_N of -41.6K and 10K respectively. These measurements were not done with LB film, hence in-plane component could not be separated. The value of θ in Mn-St was obtained as -26K in a systematic study of 3d transition-metal based LB films.

5.6 Conclusion

Magnetic properties of rare-earth elements mainly in lanthanide series are generally determined by the localized 4f orbital and spin moments. The exchange interaction mediated by the hybridized 6s and 5d conduction electrons results in the long-range magnetic ordering. Moreover dipole-dipole long-range interaction exists among ions and that will be dominating in the in-plane direction due to reduced distance within a monolayer.

Here we have presented the structural and magnetic properties of rare-earth based LB films of holmium, erbium and gadolinium. The earlier studies on gadolinium based LB film have already shown the existence of vortex structures [21] showing BKT transition temperature of 600 mK. Below this temperature vortex and anti-vortex pairs were bound and can be annihilated by magnetic field yielding total moment of $\sim 7\mu_B$ per Gd-ions. In higher temperature vortices are generated spontaneously giving lower M_S values.

Gd-St LB films have shown exponential decay of M_S as a function of temperature below 30K [19]. We find similar behaviour of Er-St (refer Fig. 5.15(d)). At higher temperatures (refer Fig. 5.16) for both Gd-St and Er-St magnetization remain almost independent of temperature perhaps due to spontaneous generation of vortices. On the other hand magnetization exhibit continuous rise as the temperature is lowered (refer Fig. 5.16) for Ho-St LB films and $1/\chi$ vs T plot clearly showing an anti-ferromagnetic behavior. The M vs H data at various temperatures shown in figure 5.15(a) and figure 5.15(b) also indicate anti-ferromagnetic ordering in Ho-St LB films. The saturation magnetization data of Ho-St LB films was also found to be quite different (refer Fig. 5.15(d)) from that of Gd-St and Er-St. One can get the maximum saturation moment as predicted theoretically for Ho-St LB films but not for Er-St and Gd-St LB films unless the sample is cooled below BKT transition

temperature. Although further neutron scattering measurements at sub-Kelvin temperature will be required, but the results presented here clearly show that Ho-St LB films are exhibiting anti-ferromagnetic order at low applied fields and vortex dynamics in Ho-St LB films is quite different from that observed in Gd-St LB films although these are iso-structural.

We observe different magnetic behaviour of Ho-St LB films from both M-H and M-T data using SQUID VSM in the temperature range from 2.2K to 100K with field applied along the in-plane direction. Ferromagnetic behaviour in Gd-St LB films as previously reported is observed in Er-St films also. Whereas Ho-St LB film shows anti-ferromagnetic behaviour although the lattice structure of all the films are identical. The anti-ferromagnetic ordering temperature and Neel temperature is calculated to be 66K and 42K respectively. Neutron and X-ray scattering experiments have shown that magnetic structure of Holmium [28] is quite different from that of Gadolinium [29] and Erbium [30], we plan to extend the present study on LB films having these rare-earth ions further using scattering techniques.

References:

- [1]. Kosterlitz, J. M. and Thouless, D. J. *J. Phys. C* **6**, 1181 (1973).
- [2]. Mermin, N. D. and Wagner, H. *Phys. Rev. Lett.* **17**, 1133 (1966).
- [3]. Bruno, P. *Phys. Rev. Lett.* **87**, 137203 (2001).
- [4]. Gong, C., Li, L., Li, Z., Ji, H., Stern, A., Xia, Y., Cao, T., Bao, W., Wang, C., Wang, Y., Qiu, Z. Q., Cava, R. J., Louie, S. G., Xia, J. and Zhang, X. *Nature* **546**, 265 (2017).
- [5]. Huang, B., Clark, G., Navarro-Moratalla, E., Klein, D. R., Cheng, R., Seyler, K. L., Zhong, D., Schmidgall, E., McGuire, M. A., Cobden, D. H., Yao, W., Xiao, D., Jarillo-Herrero, P. and Xu, X. *Nature* **546**, 270 (2017).
- [6]. Singh, A., Lee, J. C. T., Avila, K. E., Chen, Y., Montoya, S. A., Fullerton, E. E., Fischer, P., Dahmen, K. A., Kevan, S. D., Sanyal, M. K. and Roy, S. *Nat. Comm.* **10**, 1988 (2019).
- [7]. Zhang, X., Zhou, Y. and Ezawa, M. *Sci. Rep.* **6**, 24795 (2016).
- [8]. Chmiel, F. P., Waterfield, P. N., Johnson, R. D., Lamirand, A. D., Schad, J., van der Laan, G., Harris, D. T., Irwin, J., Rzechowski, M. S., Eom, C-B. and Radaelli, P. G. *Nat. Mat.* **17**, 581 (2018).
- [9]. Sort, J., Buchanan, K. S., Novosad, V., Hoffmann, A., Salazar-Alvarez, G., Bollero, A., Baró, M. D., Dieny, B. and Nogués, J. *Phys. Rev. Lett.* **97**, 067201 (2006).
- [10]. Lvanov, B. A. and Sheka, D. D. *Zh. Éksp Teor. Fiz.* **107**, 1626 (1995).
- [11]. Shirane, G., Endoh, Y., Birgeneau, R. J., Kastner, M. A., Hidaka, Y., Oda, M., Suzuki, M. and Murakami, T. *Phys. Rev. Lett.* **59**, 14 (1987).

- [12]. Vaknin, D., Sinha, S. K., Moncton, D. E., Johnston, D. C., Newsam, J. M., Safinya, C. R. and King, H. E. Jr. *Phys. Rev. Lett.* **58**, 26. (1987).
- [13]. Gambardella, P., Dallmeyer, A., Maiti, K., Malagoli, M. C., Eberhardt, W., Kern, K. and Carbone, C. *Nature (London)* **416**, 301 (2002).
- [14]. Schneider, C. M. and Kirschner, J. *Handbook of Surface Science* 511-668 (Elsevier, Amsterdam) (2000).
- [15]. Pomerantz, M., Dacol, F. H. and Segmüller, A. *Phys. Rev. Lett.* **40**, 246 (1978).
- [16]. Basu, J. K. and Sanyal, M. K. *Phys. Rep.* **363**, 1 (2002).
- [17]. Sanyal, M. K., Mukhopadhyay, M. K., Mukherjee, M., Datta, A., Basu, J. K. and Penfold, J. *Phys. Rev. B* **65**, 033409 (2002).
- [18]. Maiti, S., Sanyal, M. K., Mukhopadhyay, M. K., **Singh, A.**, Mukherjee, S., Datta, A. and Fontaine, P. *Chem. Phys. Lett.* **712**, 177 (2018).
- [19]. Mukhopadhyay, M. K., Sanyal, M. K., Mukadam, M. D., Yusuf, S. M. and Basu, J. K. *Phys. Rev. B* **68**, 174427 (2003).
- [20]. Mukhopadhyay, M. K., Sanyal, M. K., Sakakibara, T., Leiner, V. R., Dalgliesh, M. and Langridge, S. *Phys. Rev. B* **74**, 014402 (2006).
- [21]. Gayen, S., Sanyal, M. K., Sarma, A., Wolff, M., Zhernenkov, K. and Zabel, H. *Phys. Rev. B* **82**, 174429 (2010).
- [22]. Vineyard, G. H. *Phys. Rev. B* **26**, 4146 (1982).
- [23]. Grenzer, J., Darowski, N., Pietsch, U., Daniel, A., Renon, S., Reithmaier, J. P. and Forchel, A. *Appl. Phys. Lett.* **77**, 4277 (2000).

- [24.] Parratt, L. G. *Phys. Rev.* **95**, 359 (1954).
- [25.] Pomerantz, M. and Aviram, A. *Solid State Commun.* **20**, 9 (1976).
- [26.] Aviram, A. and Pomerantz, M. *Solid State Commun.* **41**, 297 (1982).
- [27.] Ando, Y., Hiroike, T., Miyashita, T. and Miyazaki, T. *Thin Solid Films* **278**, 144 (1996).
- [28.] Helgesen, G., Hill, J. P., Thurston, T. R., Gibbs, D., Kwo, J. and Hong, M. *Phys. Rev. B* **50**, 2990 (1994).
- [29.] Will, G., Nathans, R. and Alperin, H. A. *Journal of Applied Physics* **35**, 1045 (1964).
- [30.] Sanyal, M. K., Gibbs, D., Bohr, J. and Wulff, M. *Phys. Rev. B* **49**, 1079 (1994).
- [31.] Sanyal, M.K., Sinha, S.K., Huang, K.G. and Ocko, B.M. *Phys. Rev. Lett.* **66**, 628 (1991).
- [32.] Kaganer, V.M., Moehwald, H. and Dutta, P. *Rev. Mod. Phys.* **71**, 779 (1999).
- [33.] Braslau, A., Pershan, P.S., Swislow, G., Ocko, B.M., Als-Nielsen, J., *Phys. Rev. A* **35**, 2457 (1988).
- [34.] <https://www.cameca.com/products/sims/technique>
- [35.] Maiti, S., Sanyal, M. K., Varghese, N., Satpati, B., Dasgupta, D., Daillant, J., Carriere, D., Konovolov, O. and Rao, C. N. R. *J. Phys.: Condens. Matter* **25**, 395401 (2013).
- [36.] Maiti, S., Sanyal, M. K., Jana, M. K., Runge, B., Murphy, B. M., Biswas, K. and Rao, C. N. R., *J.Phys. Condens. Matter* **29**, 095101 (2016).
- [37.] Singh, A., Mukhopadhyay, M. K., Sanyal, M. K., Stenning, G. and Langridge, S. Accepted in *J. Phys.: Condens. Matter*, **39**, 495803 (2019).

Summary and outlook

In this thesis, we mainly demonstrate the use of resonant coherent X-ray scattering, X-ray reflectivity, grazing incidence X-ray diffraction and magnetization measurement techniques to study the behaviour of low dimensional magnetic structures in a Fe/Gd thin film and rare-earth based Langmuir-Blodgett multilayer films under the application of external magnetic field at different temperatures.

In the first chapter, the introductory materials relevant for the scientific investigations are described in details. After the basic magnetic interactions required describing the usual family of magnetic materials, we have mainly focused on magnetism in low dimensional systems, as this topic is specifically related to the investigations carried out in this thesis work. With the help of magnetocrystalline anisotropy, we finally discuss about more complex and novel magnetic pattern formations that are reported in two-dimensional systems. In the second chapter, we have provided a comprehensive description of all the experimental techniques used in this Ph.D research work, reported in the thesis.

Research results obtained and their analysis and interpretations of a Fe (0.34 nm)/Gd (0.4 nm) multilayer (80) film and rare-earth (Gd, Er and Ho) LB multilayer films were presented in the following three chapters. The works are summarized here and possible future research directions are given.

In Chapter 3, we show using coherent X-ray resonance scattering technique that the domain fluctuations in one-dimensional (1D) magnetic stripe-phase are dramatically reduced in topologically protected two-dimensional (2D) skyrmion phase. Results of this study with a thin film of Fe/Gd also show that the stripe and skyrmion phases follow different universality class. One of the important conclusions of this chapter is that the skyrmion phase unlike the other phases hardly shows any significant extent of sudden or large changes in the periodicity, orientation or number density of the distorted hexagonal lattice. Future studies using this novel X-based metrology will be directed towards understanding the nature of the disorder–order transition particularly that involves meron and skyrmion spin textures. Definitely, study of fluctuations as a function of time will enable us to determine “correlation function” that may shed light into formation of skyrmions. It will be important to perform similar studies on a Dzyaloshinskii–Moriya based skyrmion system and evaluate the critical nature of the helical and skyrmion state. Beyond magnetic systems, our X-ray based technique can be readily applied to a wide variety of materials system, such as liquid crystals, polymers, ferroelectrics to directly study stochasticity and scaling behaviour at the nanometer length regime.

In Chapter 4, we study the behaviour of the magnetic stripe periodicity in a amorphous magnetic Fe/Gd thin film (as used in chapter 3) using resonant X-ray scattering techniques as a function of magnetic field at different temperatures. We observe that the periodicity of the stripe phase with applied magnetic-field revealed a transition from discrete, staircase like behaviour at low temperatures to a smooth, continuous curve as we approach

room temperature. This nature is remanence of Devil's staircase like behaviour observed in very few systems till date. We also assign different rational number ratios to different steps height using a formulation for deriving normalized periodicity. Using this formulation and with the Lorentz TEM we have shown the representative spin configuration consisting of up and down spin states at different rational values. Finally we have shown that these spin configurations are commensurate with the basic ground state spin configuration of the system. Thus we conclude that distinct staircase structure can exist also in amorphous magnetic system with thermal fluctuations smearing out the steps, confirming theoretical predictions. This reciprocal based technique can be applied to other magnetic system showing Devil staircase behaviour to demonstrate the real space spin configurations for different metastable states.

In chapter 5 we describe the structural and magnetic properties of multi-layered films grown by Langmuir-Blodgett (LB) method which also provide an ideal platform to study 2D magnetic structures. Through systematic X-ray reflectivity and magnetization studies of rare-earth LB films, it was shown that with similar structural configuration a ferromagnetic to anti-ferromagnetic crossover occurs as the rare earth ions of gadolinium or erbium are replaced by holmium ions in LB films. The result of the magnetization study shows that the saturation moment of a Ho based LB film is found to be almost independent of temperature indicating the absence of spin vortex structures. In future we plan to extend the present study on LB films having these rare-earth ions further using neutron scattering techniques and magnetization studies at sub-Kelvin temperature range. Also in future it would be interesting to study two-dimensional melting or order to disorder transition in these rare-earth Langmuir-Blodgett multilayer films.

